

UNIVERSITA' DEGLI STUDI DI GENOVA

Istituto Italiano di Tecnologia

Universität Regensburg

PhD School in Sciences and Technologies of Chemistry
and Materials

Curriculum of Scienze e Tecnologie Chimiche
XXIX Cycle



NANOPARTICLES FOR TECHNOLOGICAL APPLICATIONS

Doctoral thesis by
Sharif Najafshirtari

Supervisors:

Dr. Massimo Colombo
Prof. Liberato Manna
Prof. Fabio Canepa
Prof. Oliver Reiser

January 2017

Acknowledgment

I would like to acknowledge the EU-ITN network Mag(net)icFun to provide the funding for my works, also sincerely appreciate Prof. Liberato Manna and Prof. Oliver Reiser who gave me the opportunity to work within the highly scientific and international environment of IIT and Universität Regensburg. I am really grateful to Dr. Massimo Colombo for his insightful guidance and supervision in all steps of the work.

I would also like to express my gratitude to Dr. Mahdi Goharrokhi, who paved my path in pursuing of knowledge and to whom I will be forever grateful. In particular, I would like to thank my family for all the supports I have received from them in all stages of my life.

And finally to my dearest, Ati ...

List of Publications:

- 1) **Sharif Najafishirtari**, Pablo Guardia, Alice Scarpellini, Mirko Prato, Sergio Marras, Liberato Manna, Massimo Colombo; “The effect of Au domain size on the CO oxidation catalytic activity of colloidal Au-FeOx dumbbell-like heterodimers”; Journal of Catalysis 338 (2016) 115–123. **This paper was selected as Editor-in-Chief’s Featured Article in June 2016.**
- 2) **Sharif Najafishirtari**, Rosaria Brescia, Pablo Guardia, Sergio Marras, Liberato Manna, Massimo Colombo; “Nanoscale Transformations of Alumina-Supported AuCu Ordered Phase Nanocrystals and Their Activity in CO Oxidation”; ACS Catalysis 2015, 5, 2154–2163.
- 3) **Sharif Najafishirtari**, Tathiana Midori Kokumai, Sergio Marras, Priscila Destro, Mirko Prato, Alice Scarpellini, Rosaria Brescia, Aidin Lak, Teresa Pellegrino, Daniela Zanchet, Liberato Manna, Massimo Colombo; “Dumbbell-like $\text{Au}_{0.5}\text{Cu}_{0.5}\text{@Fe}_3\text{O}_4$ Nanocrystals: Synthesis, Characterization and Catalytic Activity in CO Oxidation”; ACS applied Materials and Interfaces, **2016**, 8 (42), pp 28624–28632.
- 4) **Sharif Najafishirtari**, Alice Scarpellini, Sergio Marras, Mirko Prato, Clara Guglieri, Liberato Manna, Massimo Colombo; “Metal-support interaction in Au catalysis: the effect of the morphology of a nano-oxide domain in CO oxidation activity”; Manuscript under preparation.
- 5) Zahra Hosseinpour, Alice Scarpellini, **Sharif Najafishirtari**, Sergio Marras, Massimo Colombo, Abdolali Alemi, Michaël De Volder, Chandramohan George, and Vladimir Lesnyak; “Morphology Dependent Electrochemical Properties of CuS Hierarchical Super-Structures”; ChemPhysChem 2015, 16, 3418–3424.

International Conferences

- 1) 8th International Conference on Environmental Catalysis, Place: Asheville (US), Date: 24/08/2014-27/08/2014, Contribution: Poster. **“CO oxidation over dumbbell like Au@FeOx nanoparticles: catalytic activity, thermal stability and effect of gold domain size”** Sharif Najafishirtari, Massimo Colombo, Alice Scarpellini, Mirko Prato, Liberato Manna.
- 2) 24th North American Meeting (NAM) of the Catalysis Society, Place: Pittsburgh Pennsylvania (United States), Date: 14/06/2015-19/06/2015, Contribution: Poster. **“Nanoscale transformations of alumina-supported AuCu ordered phase nanoparticles upon CO oxidation”** Sharif Najafishirtari, Rosaria Brescia, Massimo Colombo, Liberato Manna.
- 3) 7th International Conference Gold2015, Place: Cardiff (UK), Date: 26/07/2015-29/07/2015, Contribution: Poster. **“AuCu ordered tetragonal phase nanocrystals: the effects of nanoscale transformations on CO oxidation catalytic activity”** Sharif Najafishirtari, Rosaria Brescia, Pablo Guardia, Sergio Marras, Liberato Manna, Massimo Colombo.
- 4) 16th International Congress on Catalysis (ICC 16), Place: Beijing (China), Date: 03/07/2016-08/07/2016, Contribution: Poster. **“AuCu@FeOx dumbbell like heterodimers as catalysts for the CO oxidation: when support size matters”**; Sharif Najafishirtari, Alice Scarpellini, Mirko Prato, Sergio Marras, Priscila Destro, Tathiana Midori, Daniela Zanchet, Liberato Manna, Massimo Colombo.

Table of Contents

Chapter I	1
Introduction.....	1
1.1. Outline	2
1.2. Colloidal Synthesis: Basic Principles	2
1.3. Application of Colloidal NCs in Catalysis	4
1.4. Experimental and Methods	10
1.4.1. Colloidal synthesis of NCs	10
1.4.2. Catalyst preparation.....	11
1.4.3. Characterization techniques	12
1.4.3.1. Electron microscopy (EM).....	12
1.4.3.2. X-ray diffraction (XRD)	13
1.4.3.3. X-ray spectroscopy	14
1.4.3.4. Diffuse Reflectance Infrared Fourier Transform Spectroscopy (DRIFT)	15
1.4.3.5. Inductively coupled plasma-optical emission spectroscopy (ICP-OES)	16
1.5. Summary of the Results.....	16
1.5.1. Au-Iron oxide Heterodimers	17
1.5.2. AuCu Bimetallic NCs.....	17
1.5.3. AuCu-Iron oxide nanodumbbell NCs.....	18
1.5.4. AuCu-Iron oxide NCs: The Effect of Hollow Oxide Domain on The Activity	19
1.5.5. Application of colloidal NCs in Liquid Phase Reactions	19
References.....	20

Chapter II. The effect of Au domain size on the CO oxidation catalytic activity of colloidal Au–FeOx dumbbell-like heterodimers.

Chapter III. Nanoscale Transformations of Alumina-Supported AuCu Ordered Phase Nanocrystals and Their Activity in CO Oxidation.

Chapter IV. Dumbbell-like $\text{Au}_{0.5}\text{Cu}_{0.5}@\text{Fe}_3\text{O}_4$ Nanocrystals: Synthesis, Characterization, and Catalytic Activity in CO Oxidation.

Chapter V. Metal-support interaction in Au catalysis: the effect of the morphology of a nano-oxide domain in CO oxidation activity.

Appendix I. Application of NCs in liquid phase hydrogenation of model compounds.

Chapter I

Introduction

1.1. Outline

This thesis is dedicated to the preparation of catalytic nanomaterials and nanocomposites with well-defined morphological properties, aiming at establishing a so-called structure-activity correlation for a given reaction, namely the oxidation of carbon monoxide (CO). Colloidal synthesis was applied as the main route to prepare the desired nanocrystals (NCs) which were then deposited on a number of supports to prepare the catalysts. The catalytic properties of these materials were then evaluated in CO oxidation as a model reaction. The NCs and catalysts were extensively characterized by many advanced technique to build up a relationship between the properties of the materials and their catalytic function. Within this context, the basics of the colloidal chemistry will be firstly discussed in this chapter, followed by a general description of the applied experimental methods and a brief summary about the results and achievements of the present thesis work. In the next chapters of the thesis, the finalized results regarding catalytic applications and structure-activity correlations for a number of NCs are be reported.

1.2. Colloidal Synthesis: Basic Principles

Colloidal synthesis is among the established procedures to produce NCs with outstanding properties for wide range of applications in the fields of electronics [1], biology [2,3], energy [4,5] and data storage [6], chemical conversion [7] and etc. The synthesis is typically done in presence of an organic medium containing the chemical precursors, solvents, ligands and/or reactive agents to initiate, terminate or generally speaking to manipulate the formation of the NCs from the precursors. It should be mentioned that in this system, the same component can have multiple roles, acting as a solvent, as stabilizer or as a reducing agent of the metal precursors [8]. The process of colloidal NCs formation can be thought as an inorganic polymerization: in this process the monomers are formed from the chemical transformation of precursors, occurring either by their thermal decomposition or by the addition of a secondary chemical agent. The formation process includes the initial formation of seeds i.e. nucleation followed by the subsequent growth by further attachment of the monomers present in the synthesis mixture. The growth step is greatly affected by the organic surfactants which act as stabilizing, directing or capping agents bounded to the surface of the formed NCs [9].

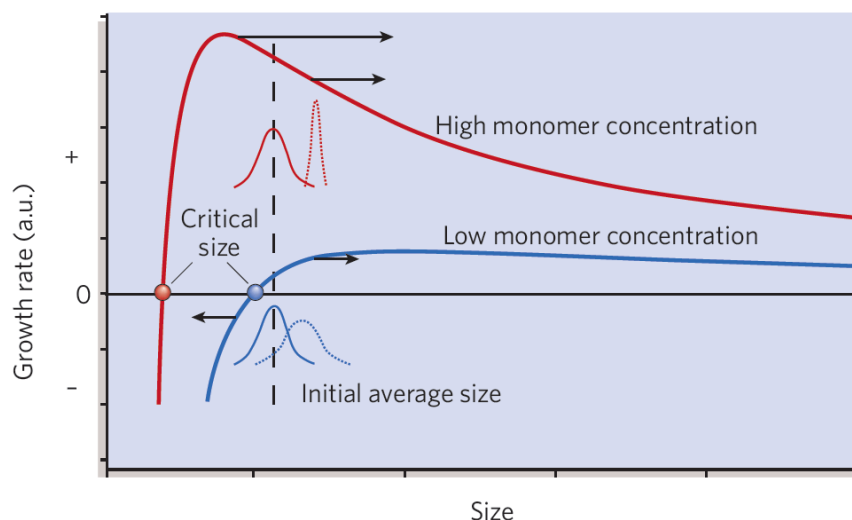


Figure 1. The growth rate vs NCs size and depiction of size distribution focusing; Reprinted by permission from Macmillan Publishers Ltd: Nature, [9], Copyright (2004).

By the help of colloidal synthesis, it is practically possible to design and synthesize uniform NCs with fascinating properties through controlling their composition and morphological aspects such as size and shape. Each of these features can be tuned by the manipulation of the synthesis conditions in the kinetically-controlled NC growth of the colloidal synthesis method. For instance, to control the size it is important to keep the conditions in a way to have a so called focusing synthesis mode. This mode is practically defined by the concentration of the monomers in solution. Indeed, at any given concentration of the monomer, a critical size for NCs growth exists. If the concentration is high, the critical size is small and all the NCs grow in a way that the smaller particles would grow faster than the larger ones. Therefore and as a result of different growth rate of the particles having different size, the final NCs' sizes would converge to a similar value, and the distribution would be narrower. This is referred to as the focusing mode. On the opposite, if the monomer concentration is below a critical threshold, the smaller NCs will be dissolved and recrystallized onto the larger particles and as a result, the size distribution would be broader. Obtaining nearly monodisperse particles would be achieved then by terminating the synthesis while it is under the focusing regime. Indeed, if the reaction is not terminated, all particles will eventually continue to grow at the same rate causing the broad size distribution to be maintained. These two modes are depicted in Figure 1. It should be noted that depending on the termination point of the reaction, there could be still some or many monomers left in the system that would affect the yield of the synthesis.

The control of NCs' shape is usually achieved by means of the so-called capping agents. Exploiting the different affinity of the same molecule to different facets of a NC, enables the control of the growth rate at targeted facets. There are several strategies to manipulate the shape of the colloidal NCs as graphically illustrated in Figure 2. Generally speaking, the high-energy facets grow faster than low energy facets in a kinetic regime (Figure 2a). However, a ligand with different adhesion properties to different facets can be used to selectively manipulate the growth rate at the targeted facet, resulting in the formation of rod- or disk-shaped nanocrystals (Figure 2b). Sequential elimination of high energy facets could result in more complex shapes. The persistent growth of an intermediate-energy facet eventually eliminates the initial high-energy facet, forming complex structures (Figure 2c). Finally, in case of having more than one crystal structures, surface energies of the facets of different NCs can be manipulated to favor the attachment of targeted facets and obtain more complex nanostructures such as tetrapods (Figure 2d).

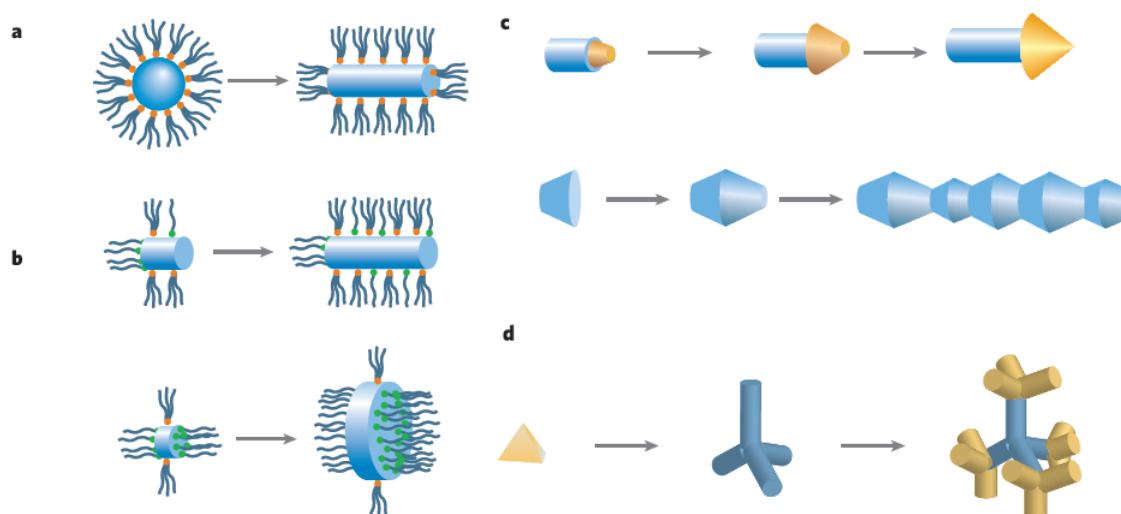


Figure 2. Illustration of different NCs shapes obtained from colloidal synthesis. The yellow and green dots in a and b represent metal coordinating groups with different affinities to nanocrystal facets; Reprinted by permission from Macmillan Publishers Ltd: Nature, [9], Copyright (2004).

1.3. Application of Colloidal NCs in Catalysis

Among the many applications of the colloidal NCs that have been explored, catalysis is of great importance. Heterogeneous catalysis is among the earliest known applications of nanomaterials, although this has been clearly recognized only few decades ago. Indeed, in the design and application of this class of materials, one deals with the manipulation of materials at nanoscale. There are a number

of nanoscale properties that influence the performances of heterogeneous catalysts. For instance, the metal-support interaction or the size of the metal active sites in metal supported catalysts are among the nanoscale properties defining the final catalytic performance. In addition, the sintering of the metallic active sites during the catalyst activation or even the course of reaction is among the phenomena occurring at nanoscale which should be thought of and carefully examined in the design and application of the heterogeneous catalysts. In the field of catalyst synthesis, one aims for a specific composition and structure of synthesized materials, which in turn define the desired specific catalytic properties in terms of activity, selectivity, and stability [10-12]. However, conventional methods for catalyst preparation typically result in a material with a relevant level of inhomogeneity in terms of properties at nanoscale.

Take the case of metal supported catalysts for instance. Such catalysts have been typically comprised of micrometer-sized grains of support with high surface area (metal oxides, active carbon, zeolites and etc.), decorated with clusters or nanosized metal (and/or metal oxide) domains as the active sites [13-18]. In this class of materials, the activity is significantly defined by the size, shape, dispersion and interaction of the metal species with the support. However, the conventionally-prepared industrial catalysts usually consist of metal nanoparticles with considerable variations in size and shape, which makes it difficult to understand the fundamental catalytic properties of such materials [19]. More specifically, in case of the Au catalysts for CO oxidation and despite of numerous studies, it is still debated what really controls the activity of the catalysts. The accurate and precise analysis of the origin of CO oxidation activity is indeed a challenging task considering the vast structural transformations that the support and the Au active species can undergo during the preparation and/or activation of the catalyst [20]. Moreover, it has been shown that the observed activity of the Au catalysts can be mainly related to the presence of sub-nanometer Au species on the support, not observable by traditional imaging techniques [21], which can result in an increase in the population of low-coordinated Au atoms subsequently enhancing the activity [22]. On the other hand, the interaction of the metals with the support and the position at which the former one is interacting with the latter one (e.g. kinks, steps, terrace and etc.) are also greatly responsible for the catalytic properties. This parameter has also a huge variance in case of traditional catalysts. The situation can become even more complicated if the support itself is active in the reaction and participates in the reaction pathways. This phenomenon can happen for example in the case of reducible supports used in the preparation of oxidation catalysts. Last but not least is the fact that the active sites can be transformed during the reaction itself, and their structural

properties might be altered upon exposure to different environments [10,23]. This is very important for example in case of bimetallic catalysts, as the surface chemistry of the active sites is directly related to the local elemental coordination of the mixed species in the system under reactive environment. Therefore, it is very important to develop reliable model catalysts for fundamental understanding of the catalytic properties.

In the attempt to understand and rationalize the catalytic properties of materials, single crystal surfaces have been used for a long time as model systems [24]. However, the deviation from the real case is considerable using these systems. More importantly, using single crystal as model catalyst we can only study the nature of the surface chemistry of the metal active sites while their interaction with the support as well as their size effects are substantially neglected or anyway intrinsically limited. The application of colloidal synthesis methods in the catalyst preparation, on the other hand, provides a unique tool to study in details the properties of metal active sites. [12,25]. These methods offer indeed the possibility of: (a) size and shape tuning to study the effect of size and find about the most active facet of the NCs, (b) composition tuning for evaluation of the synergies between different constituents especially in case of bimetallic or composite catalysts, and (c) design of architecture for careful examination of metal-support interaction. The successful application of colloidal chemistry and NCs as model systems in studies related to catalysis have been already reported in literature. Few examples are given hereafter.

Studying the effect of the NCs size by means of colloidal chemistry, Kuhn et al. [25] have prepared mesoporous SBA-15 supported Pt NCs from 0.8 to 5 nm and evaluated their activities in the hydrogenation of pyrrole, a cyclic unsaturated N-containing compound. They observed that ring saturation and ring opening reactions can take place using this catalyst. The latter was largely favored in presence of the larger NCs, thus affecting the selectivity for the desired product (see Figure 3). The shape dependency of the activities for a similar catalysts and reaction has been also reported by Tsung et al [26]. In another work, Kang et al. [27] have studied the shape effect of monodisperse Pt nanocrystals by synthesizing different morphologies, including octahedra, icosahedra, cubes, truncated cubes, cuboctahedra, spheres, tetrapods, star-shape octapods, multipods (see Figure 4) and further examined their properties in electrocatalysis, CO oxidation, and liquid-phase electron transfer reaction. They demonstrated that high quality Pt NCs which selectively expose “111” or “100” facets are the ideal model catalyst for such reactions.

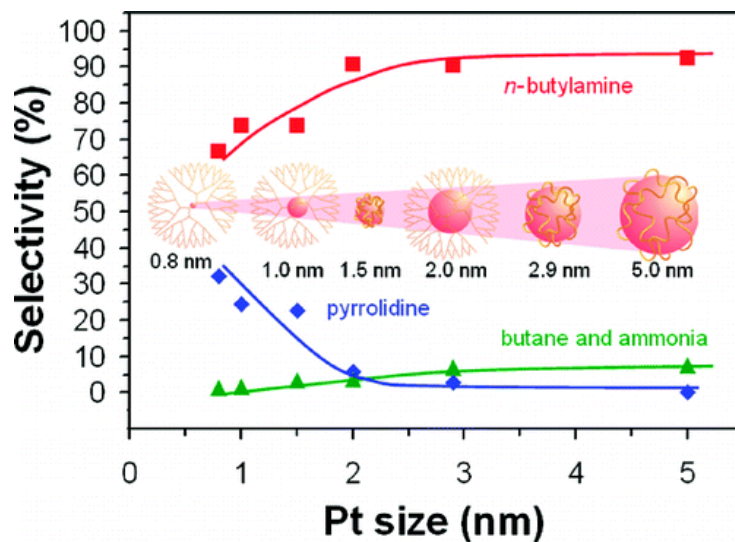


Figure 3. Effect of Pt size on selectivity in pyrrole hydrogenation; Reprinted with the permission from [25]. Copyright (2008) American Chemical Society.

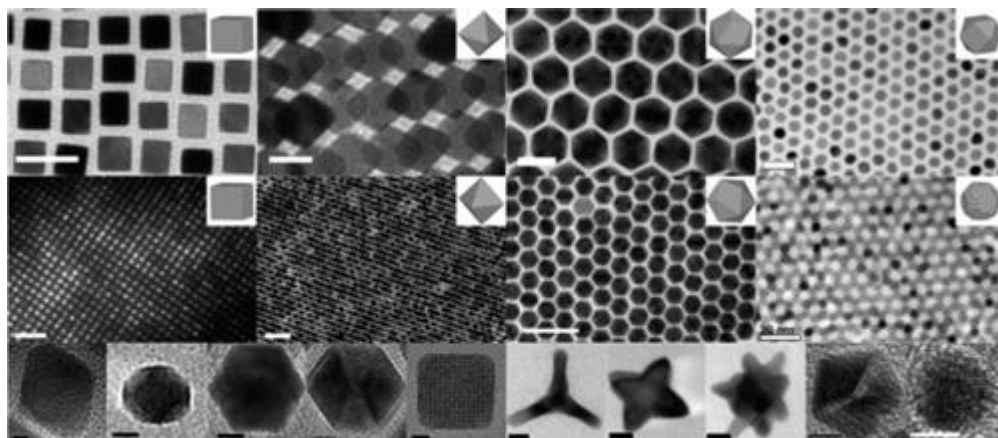


Figure 4. TEM images of Pt NCs with different shapes; Reprinted with the permission from [27]. Copyright (2013) American Chemical Society.

Regarding the effects of compositions, Kumar et al. [28] have successfully prepared AgNi alloy NCs, with different compositions but all having 5-fold twinned morphology. These elements are considered immiscible in form of bulk materials. They have studied and proved that the size, electronic effects and the synergy emanated from the defects of the bimetallic NCs can offer high catalytic activity for reduction reaction of substrates like nitrophenols and nitroaniline or degradation of dyes in liquid phase (see Figure 5). In another work, Lee et al. [29], have shown that uniform and monodispersed PdNi NCs demonstrate an enhanced activity in electrocatalytic oxidation of ethanol compared to commercial Pd catalyst having the same metal size.

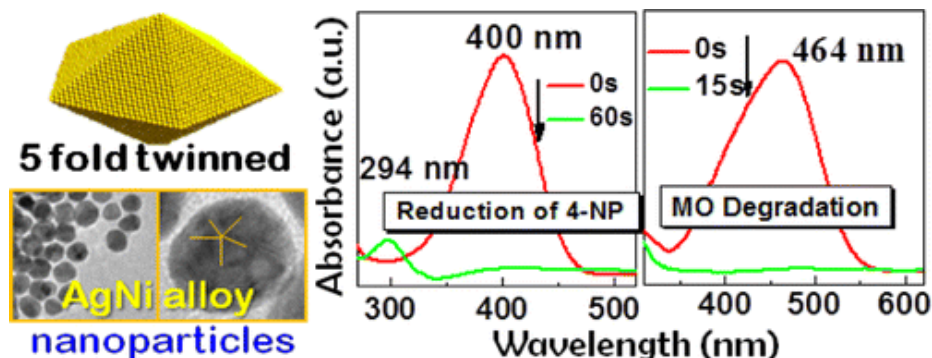


Figure 5. TEM images and catalytic application of AgNi NCs in reduction of 4-nitrophenol (4-NP) and degradation of methyl orange (MO); Reprinted with the permission from [28]. Copyright (2014) American Chemical Society.

To study the supports effect, Comotti et al. have presented a research work on the effect of support in CO oxidation for the Au based catalysts [30]. They prepared the catalyst by deposition of premade colloidal Au NCs having the same size, and in this way they were able to isolate the effect of a number of supports such as TiO_2 , ZrO_2 , Al_2O_3 and ZnO . The studies on the supports effect have been extended further by the synthesis and application of dumbbell-like metal/metal oxide NCs. As shown in Scheme 1, this nanostructure is characterized by an epitaxial connection of a nanosized metallic domain to a nanosized metal oxide domain, in which the metal domain is partially nested [31,32]. With this morphology, it is possible to study different aspects of the catalytic properties, isolating the support effect while having uniform nanosized metal-support entities. A number of works have been published on this class of materials, not only proving its ability to provide insights on the issues of metal-support interaction but indeed to create even more efficient catalysts in terms of activity and stability in some specific reactions [33,34].



Scheme 1. Schematic illustration of a dumbbell-like NC characterized by epitaxial connection of a metal domain (M) to a metal oxide domain (MO_x).

Other morphologies can be also prepared targeting for new composite nanomaterials offering enhanced catalytic properties. For example, Chen et al. [35], have described a methodology to produce

mesoporous nanospheres of cerium oxide and titanium oxide trapping the noble metals such as Ru, Rh, Pd, Pt, Au and Ag. These catalysts have proven to be very efficient in a number of oxidation and reduction reactions. The active sites accessibility is always guaranteed with the porosity of the oxide nanosphere around the metal active sites, while the sintering is prevented due to the efficient containment of the metal NCs. It should be noted that the morphology is different from a simple core-shell and can be considered as a new approach to design metal-supported catalysts. Similar methodology has been also applied to prepare catalytic nanocomposites of Pd-CeO₂ showing high activity in CO oxidation compared to the catalyst prepared by impregnation [36].

There are of course a number of challenges in the process of catalyst preparation from colloidal NCs [37] which should be addressed particularly in case of heterogeneous catalysis. Generally, to prepare a model catalyst from colloidal NCs, a specific volume of the colloidal solution with known concentration is added to a suspension containing the support grains. In this way, the NCs will be deposited onto a support by wet impregnation to achieve the target loading. The concentration of parent solution containing the NCs is usually low to prevent the aggregation of NCs while it is important to keep the conditions so as to maximize the contact of the support grains with the colloidal NCs. These conditions can limit the production throughput of the synthesis method. In addition, one should note that if the sizes of the premade NCs are bigger than the aperture of the support, they cannot easily enter the pores and so they will interact only with the external surface area of the support [37]. This issue is not limiting if the catalyst is to be used as a model material but it would be problematic for the scale up of the catalyst production. More importantly, the NCs are covered with stabilizing ligands that usually needs to be removed, e.g. thermally [38] or chemically [29], in order to fully expose the surface of the metal active sites. This process can be considered as an activation step of the catalyst. However, due to the variety of the capping agents, it will be difficult to generalize a proper method, even though in most cases it is easy to burn them off under oxidizing conditions. It is important to mention though that in some new strategies, the capping agents can be exchanged/modified to manipulate the selectivity of the reactions towards targeted materials [39].

Given all these considerations, my works were dedicated to the synthesis of well-defined colloidal NCs and their application in CO oxidation. In addition to general aspects of NCs synthesis, I developed protocols for NCs based catalyst preparation and activation. In addition, transformations of the NCs upon exposure to different reaction environments were thoroughly studied in the attempt to establish

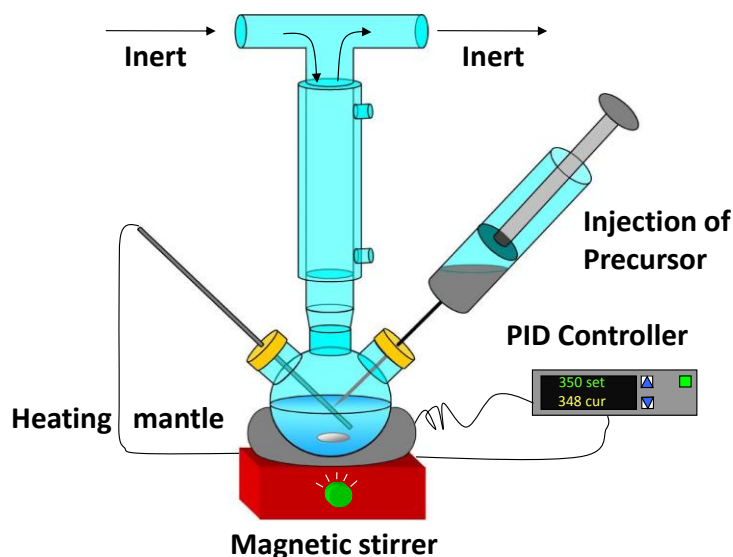
clear structure-activity correlations. The results of this thesis can be used as a guideline for the design, characterization and evaluation of the catalytic activity of these materials, especially NCs with metal-metal oxide nanodumbbell morphology. More specifically, in the study of the structure-activity relationship in CO oxidation, our results can help to understand the true nature of the catalytic active sites of advanced and tailored catalytic materials.

1.4. Experimental and Methods

Typical procedures for material preparation, as well as basic principles of the characterization techniques and methods for the evaluation of the catalytic performances are provided in this section. The scope of this paragraph is to briefly explain the strategies for synthesis and justify the application of selected characterization techniques, giving insights to the different kind of information they can provide. Needless to say, the details and full extent of the experimental works as well as the exact methodologies will be further provided in each chapter.

1.4.1. Colloidal synthesis of NCs

Typically the synthesis of the NCs was performed in a standard 3-neck flask whose volume was selected based on the total volume of the synthesis mixture i.e. solvents, ligands and precursors. The middle neck was connected to a condenser to maintain the reflux conditions while the other two were capped with either plastic septums or glass accessories to isolate the reaction mixture from the external atmosphere. A magnetic bar was used to agitate the mixture under reaction conditions while the temperature was being monitored via a thermocouple inserted into a glass thermos-well provided through one of the flask's necks. When needed, heating was provided by a heating mantel sitting around the flask, while the temperature was regulated by a PID controller. A typical scheme of the synthesis setup is illustrated in Scheme 2. The syntheses protocols were then developed through careful control of each step such as degassing, precursors dissolution and injection, heating ramp rate and profile. At the end of the synthesis, NCs were separated from the reaction mixture by several consecutive washing-centrifugation steps, using solvents such as acetone, ethanol, iso-propanol. Finally the synthesized NCs were dispersed in volatile inert solvents such as hexane, toluene and chloroform and stored either in cold room or glove box.



Scheme 2. Schematic of a typical setup for colloidal synthesis.

1.4.2. Catalyst preparation

The catalysts were typically prepared by deposition of the pre-made colloidal NCs on the supports grains. Usually alumina grains (γ -Al₂O₃ extrudate from Strem Chemicals: SSA = 220 m²/g; average pore diameter = 6.5 nm; previously crushed and sieved to 90 μ m) were dispersed in a solvent identical to the one of colloidal NCs solution and then the specific amount of the colloidal solution, corresponding to the targeted elemental loading, was added to the mixture. Then the suspension was either mixed using a magnetic stirrer and a magnetic bar or sonicated, typically for 2 h, which allowed the contact of NCs and support grains for the deposition. After this step, the solvent was removed by evaporation and the catalyst powder was dried before storing. The catalysts were often calcined/in-situ activated under oxidizing atmosphere to remove the protecting ligands prior to reaction tests. In some cases, silica or other supports were also used within the context of the study. The activities of catalysts were typically measured using a fixed bed micro-reactor coupled with a μ -gas chromatograph to analyze the outlet of the reactor. The arrangement of the catalyst bed in the micro-reactor used in our experiments is illustrated in Figure 6. The inlet of the reactor was connected to a number of mass flow controllers (MFCs) to control the flowrate and composition of inlet gas stream.

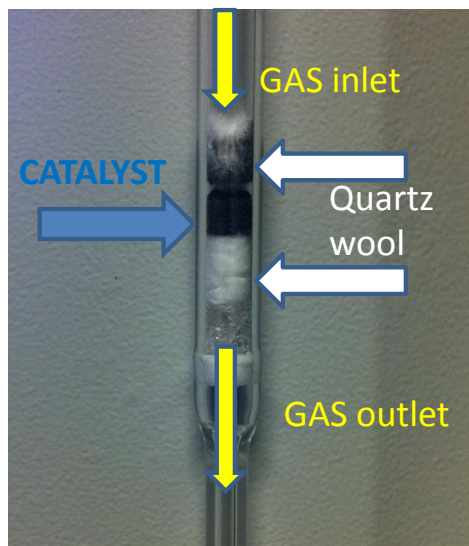


Figure 6. Illustration of the micro-reactor used for catalytic experiments.

1.4.3. Characterization techniques

1.4.3.1. Electron microscopy (EM)

As mentioned in the previous section, by means of colloidal synthesis we are able to manipulate the morphology of NCs. In this regard, it is important to monitor these properties whether during the synthesis of the NCs or after possible transformation they might undergo in the course of the catalytic experiments, in order to fully understand the correlation between the structural and the catalytic properties. Electron microscopy (EM) is a powerful technique vastly used to study the morphological properties of the NCs and heterogeneous catalysts [40-42]. Generally in this technique, the sample is bombarded with a beam of electrons provided by a high voltage electron gun (typical range of 80 to 300 keV). Different interactions can occur between the high energy electrons and the sample which can be monitored, measured and quantified in order to obtain many useful information [43,44]. For instance, a fraction of the electrons will pass through the sample without significant energy losses and can form a two-dimensional projection of the sample on the screen located below the sample. This is referred to as transmission electron microscopy (TEM) i.e. one of the most common EM-based measurements to generate images from the sample. This technique provides an insight about the shape and size of the colloidal NCs but it should be noted that the images are created with a low contrast. High resolution images can be obtained as well using this technique, providing information about the crystallinity of the sample, lattice spacing and the order of atoms within the crystalline domains. On the other hand, the scattered electrons at high angle can be used to produce images with a high contrast

between atoms characterized by a large difference in the atomic number. This technique, called high angle annular dark field scanning transmission electron microscopy (HAADF-STEM), can be used in the characterization of the catalysts, providing useful information about dispersion and morphology of the supported NCs. Moreover, a sample could be excited to release X-ray emission due to specific type of its interaction with the beam. The number and the energy of the emitted X-rays can be detected according to a method known as energy dispersive X-ray spectroscopy (EDS) and be used in elemental analysis of the NCs and catalysts. Finally, a fraction of the electrons in the beam can be diffracted to particular angles defined by the crystalline structure and arrangements of the atoms within the lattice space. This type of interaction can provide information about the crystalline nature of the sample in a similar manner to that of X-ray diffraction (XRD) method described later with respect to the fact that the electrons can be considered as wave packets having defined energies. In the course of our experiments, many of these methods were applied to provide information about size distribution, morphology, elemental composition, elements distribution, and crystallinity of the colloidal NCs as well as their dispersion, transformations, extent of sintering, and change of morphology when the same NCs were supported and used as catalysts.

1.4.3.2. X-ray diffraction (XRD)

XRD is another commonly used technique for characterization of both NCs and heterogeneous catalysts [45-47] which has the ability to detect the crystalline phases present in the system and provide useful structural information. The main principle of this method lies in the fact that when a crystalline material is exposed to an X-ray beam, its constituent arrays of atoms which are ordered in the lattice space, will diffract the beam in directions given by Bragg's law [48] (i.e. $n\lambda = 2d \sin \theta$; where λ is the wavelength of the X-ray, d is the spacing between two lattices, θ is the angle between the incident X-ray and the normal vector of the reflecting plane and n is the order of reflection). XRD patterns can be collected using a stationary source of X-ray and a movable detector which scans the intensity of the diffracted beams as a function of the angle 2θ between the incoming and diffracted beams [49]. Indeed, the angle of diffraction as well as the intensity of the scattered beams are proportional to the positions of the atoms, interatomic distances or generally speaking to the geometry of the atoms in the lattice space which makes XRD a powerful technique for structural analysis. It should be mentioned that in this technique the diffraction is related to the interaction of the incident beam to the electrons rather than the nucleus of the atoms. XRD patterns can be also correlated to provide information about the compositional changes of the NCs [47]. In this regard, we mainly used XRD to characterize the

crystalline structure of the colloidal NCs, to monitor and study the transformations of the supported NCs as well as NCs' supports upon exposure of the catalysts to different environments of the catalytic experiments. Also many useful indirect information were derived from the analysis of the XRD patterns, specifically in the quantification and the determination of the crystalline phases present in our samples.

1.4.3.3. X-ray spectroscopy

A number of X-ray based spectroscopy methods had been also applied in our works such as X-ray absorption fine-structure spectroscopy (XAFS) and X-ray photoelectron spectroscopy (XPS). To perform XAFS measurements, the sample is exposed to a high flux of monochromatic X-ray beam with specific energy provided in synchrotron facilities. Indeed, a part of energy can be absorbed by specific atoms at energies near and above their core-level binding energies. XAFS can be regarded as the modulation of an atom's X-ray absorption probability due to the local chemical and physical state of the atom [50,51]. Data acquisition can be done in two modes i.e. transmission and fluorescence. In transmission mode, the absorption of the incident beam by the sample is measured by two ionization chambers placed before and after the sample, while the beam is passing through the sample. In the fluorescence mode, measurement is done by detecting the photoelectrons emitted after an electron fills up the hole in the pre-excited core. XAFS spectra are indeed sensitive to the oxidation state, coordination chemistry and the interatomic distances around the selected atoms absorbing the energy of the incident beam [51-53]. While not being limited to crystalline materials, it can be used to collect precious information about the nature of the active sites in heterogeneous catalysts [50]. The X-ray absorption spectrum is typically divided into two regions: (1) X-ray absorption near-edge spectroscopy (XANES) characterized by a sharp rise in the absorption coefficient which occurs typically within 30 eV of the main absorption edge and (2) the extended X-ray absorption fine-structure spectroscopy (EXAFS) which addresses the oscillations of the excited photoelectrons around the absorbing atoms and typically extended up to few keV after the absorption edge [51]. Although having the same origin, they are used to derive different structural information. XANES is strongly sensitive to formal oxidation state and coordination chemistry of the absorbing atom and can be qualitatively determined by these parameters. Though no mathematical function exists to describe the XANES region, it can be nevertheless used as a fingerprint to identify the phases present in the sample and monitor their transformations. On the other hand, EXAFS is defined by a simplified yet detailed mathematical function and can be used for quantitative determination of the interatomic distances, coordination

number, disorder and type of neighboring species around the absorbing atom [53]. Both methods have been used in our works to identify the phases present in the NCs and study their structural transformations upon exposure to catalytic conditions to correlate the catalytic and the structural properties. In addition to XAFS, XPS was also applied in our works. Its principle lies in irradiating the sample with an X-ray beam to excite the core electrons to high energy state above the vacuum level. The core-hole then decays through either Auger process or emission of photoelectrons [54] that can be measured much like the XAFS in fluorescence mode. As the XPS spectra are directly proportional to the electronic density of the atoms, they can be used to identify the binding energy of the electrons and therefore provide information about the oxidation states of different elements. Moreover, due to the low energy of the beam and its limitation for diffusion in the structure, they are widely used to identify and characterize the surface species in catalytic materials as well as charge transfer between epitaxially attached phases [55]. We used XPS in our works mainly to provide information about the charge transfer between different phases of the synthesized NCs which would define the catalytic properties of the NCs especially in Redox reactions.

1.4.3.4. Diffuse Reflectance Infrared Fourier Transform Spectroscopy (DRIFT)

Diffuse Reflectance Infrared Fourier Transform Spectroscopy (DRIFT) is another powerful characterization technique in catalysis researches, exploited to identify the active surface species [56]. In principle, the sample is exposed to incident IR beam which will penetrate the sample interacting with it. The interaction usually results in a loss of energy, while the beam would be reflected in different directions afterwards. The diffusely scattered radiation is then collected by an ellipsoidal mirror and focused on the detector, which allows the determination of the absorption spectrum as a function of frequency [57]. . In particular case of catalysis research, a probe molecule such as CO or NO is usually employed in order to identify and study the properties of the active sites. The strength of the adsorbed molecule bonded to the surface species has indeed direct correlation to the catalytic performance of the materials [58,59]. With respect to the dependence of stretching vibrations of the surface bonds with the bond strength [56], we can identify different active sites by correlating the adsorption bands to specific electronic state of the active sites [58]. In our experiments, we mainly used this technique to identify the nature of the surface species in our catalysts, nanoscale transformation of NCs resulting in different surface species as well as evidencing the possible charge transfer between the metal NCs and the bulk or nanosized support.

1.4.3.5. Inductively coupled plasma-optical emission spectroscopy (ICP-OES)

This technique was applied in our work to obtain information about the elemental compositions of the colloidal NCs and loading of the catalysts. This measurement fundamentally relies on a phenomenon in which the excited atoms or ions can emit a radiation decaying to the ground state [60]. The energy of this radiation is defined by Planck's equation: $E = h\nu$; where E is the energy, h is the Planck's constant and ν is the frequency of the radiation. In practice, the solid sample is digested to have it dissolved typically in an acidic liquid. The liquid sample is then pumped and atomized using a nebulizer to form liquid sols i.e. very small droplets of the liquids. These droplets are torched with a plasma flame resulting in dissociation of the sample to its constituting atoms in form of excited ions. Subsequently, the excited ion decay to their ground state emitting a radiation which is monitored by optical detector. The intensity of the emitted radiation at specific wavelength can be correlated to the concentration of the elements of interest in the sample.

1.5. Summary of the Results

In this section, a summary is given about the main results of the PhD research activities that I carried out mainly at the IIT Genova, Nanochemistry Department under the supervision of Prof. Manna and Dr. Colombo. I developed the synthesis protocols for a number of colloidal NCs and applied them in catalytic CO oxidation as a model reaction. Firstly, I focused on the synthesis and the application of dumbbell-like Au-iron oxide NCs and studied the effect of the Au domain size on their activity in CO oxidation. In the next step, I aimed at tuning the composition of the metal domain in such morphology. To achieve such a goal I firstly synthesized intermetallic alloyed NCs of Au and Cu and thoroughly studied their transformations and activity in CO oxidation. Then, the dumbbell-like NCs of AuCu-iron oxide were prepared using the same AuCu NCs, and their activities were benchmarked against bulk magnetite supported AuCu to study the effect of nanosizing of the support. Finally, we focused on tuning the morphology of the iron oxide domain in AuCu-iron oxide dumbbell-like NCs. The objective of the study was to understand the effect of hollow oxide against non-hollow oxide nanosized supports on the CO oxidation activity. To this aim, different batches of AuCu-iron oxide dumbbell-like NCs were prepared, each batch being characterized by a different fraction of core-shell oxide domains. The iron-rich core in the oxide domain would then transform to hollow oxide upon activation of the catalyst. The thesis works resulted in 3 publications and 1 manuscript under preparation as first author plus a co-authorship collaborative paper within the group. Also considering a cotutelle agreement, I

spent 9 months in the group of Prof. Reiser in Institut für Organische Chemie, Institut für Pharmazie und Chemie, Universität Regensburg. My activities there were mainly focused on the application of the NCs supported on magnetic nanobeads for liquid phase reactions.

1.5.1. Au-Iron oxide Heterodimers

At first, a protocol was developed to synthesize dumbbell-like nanocomposites made of a metallic domain epitaxially connected to a metal oxide one. The synthesis work was focused initially on Au@Iron oxide heterostructures: NCs were obtained with various sizes of Au domain (nominally 4, 6 and 10 nm) while the size of the iron oxide domain was kept constant, around ~18 nm. A seeded growth method was employed to form the iron oxide domain on pre-made Au nanoparticles. These NCs were further deposited on alumina supports and their catalytic activities as well as thermal stabilities were evaluated in the oxidation of CO. To benchmark the performances of the synthesized heterostructure, Au catalysts were prepared by their deposition on alumina and iron oxide (having similar sizes as in case of dumbbells) and tested as controlling experiments. The catalyst made of dumbbell NCs of 4 nm Au and iron oxide showed the best performance in CO oxidation suggesting the importance of Au-Iron oxide interface as the active sites of the reaction, being maximized in this sample. Advanced electron microscopy, XPS and IR spectroscopy studies were carried out in order to characterize the NCs and rationalize the observed trends. This work resulted in a publication in Journal of Catalysis (<http://dx.doi.org/10.1016/j.jcat.2016.03.002>; **2016**, 338, pp 115–123) and represent the chapter II of the thesis. The paper was further selected by the editor in chief as a featured article in June 2016 as a paper worthy of extra attention.

1.5.2. AuCu Bimetallic NCs

The research went on focusing on the same nanostructure where the composition of the metallic domain was tuned in order to obtain an intermetallic alloy of AuCu while keeping the size of the metallic domain at ~6 nm. In this regard, procedures for producing firstly AuCu NCs with an atomic ratio of 1:1 and then the corresponding AuCu@FeOx dumbbell nanocomposite were established. The AuCu NCs seeds were the subject of a dedicated study where their transformations upon different pre-treatments (i.e. under oxidizing or reducing atmospheres) and the resulting CO oxidation catalytic activities were studied. Analyses carried out by techniques such as STEM-EDS, XRD, SAED and *in-situ* DRIFTS were applied to characterize the colloidal NCs, to study their transformations and identify the nature of the active sites. The exposure at high temperature (350 °C) to an oxidizing environment

caused phase segregation between Au and Cu and the subsequent migration of Cu species on the support surface, which was found to be detrimental for the CO oxidation reaction. On the other hand, AuCu alloyed NCs were restored when the catalyst was exposed to a reducing environment and the catalytic activity was then significantly enhanced. The CO/O₂ reacting atmosphere also caused changes in the NCs composition and consequently on the reaction rate: for a reduced system the catalytic activity progressively decreased with time on stream, as a consequence of Cu de-alloying and of partial migration on the support surface. On the other hand, when starting from a fully oxidized situation, the reaction environment caused a partial re-alloying of Cu, which in turn resulted in the progressive increase of the catalyst activity. All these transformations were found to be fully reversible. The results of this work were published in ACS Catalysis (doi: 10.1021/cs501923x; **2015**, 5 (4), pp 2154–2163) and represent the chapter III of the thesis.

1.5.3. AuCu-Iron oxide nanodumbbell NCs

The AuCu@FeOx dumbbell-like NCs were also successfully synthesized by means of colloidal synthesis having both Au and Cu localized in the metal domain. These dumbbell NCs were further deposited on alumina support and tested in CO oxidation after oxidative pre-treatment which was essential to remove the protecting ligands and activate the catalyst. The complex transformations of these NCs upon activation was thoroughly studied by means of EDS-STEM and XAFS. The oxidation pre-treatment caused the de-alloying between Au and Cu, with Cu atoms likely being incorporated in the iron oxide domain. The resulted structure-activity correlation was further rationalized by comparison of the activity against iron oxide bulk supported AuCu catalyst as well as alumina supported Au@FeOx nanodumbbell having the same size of the metal and metal oxide domains. The AuCu@FeOx sample displayed CO oxidation reaction rates similar to those measured over a Au@FeOx catalyst having a similar Au domain size, highlighting the dominant role of the Au-iron oxide interface for this reaction. The nanosized support of iron oxide in case of dumbbell NCs provided a strong thermal stability of the metallic domains: the sintering of the Au domains was effectively prevented. This in turn yielded a higher activity of the AuCu@FeOx dumbbells when compared against a bulk Fe₃O₄ supported AuCu NCs catalyst, where extensive sintering occurred. The results of this work were published in ACS Applied Materials & Interfaces (doi:10.1021/acsami.6b09813; **2016**, 8 (42), pp 28624–28632) and represent the chapter IV of the thesis.

1.5.4. AuCu-Iron oxide NCs: The Effect of Hollow Oxide Domain on The Activity

Interestingly in the case of the AuCu@FeOx NCs, we observed the development of a core-shell structure within the oxide domain for a number of NCs, this structure being characterized by an iron rich core. The fraction of NCs with such morphology was found to be tunable by simply adjusting the synthesis conditions. We therefore prepared three samples characterized by an increasing fraction of core-shell particles referred to the total number of NCs in the sample. These dumbbell NCs were further deposited on alumina support as before and tested in CO oxidation after oxidative pre-treatment. After the activation of the catalysts under oxidative atmosphere the iron rich core was transformed to a hollow iron oxide domain, while the Cu atoms were delocalized from the metal domain and dispersed in the iron oxide one. The catalytic properties of these catalysts were studied along with the characterizations trying to find a correlation between the activity and structural properties of such NCs. The characterizations techniques included TEM, STEM-HAADF-EDS, XAFS, XRD, XPS, and CO TPR. The kinetic measurements have been performed on the catalyst suggesting a correlation between the activity and the population of NCs with a hollow oxide domain, while the activation energy remained constant. EXAFS data have been also simulated to understand the structural properties of the fresh NCs and their evolution upon activation. The work resulted in a manuscript under preparation and represents the chapter V of the thesis.

1.5.5. Application of colloidal NCs in Liquid Phase Reactions

Finally and during my stay in Regensburg, I explored the catalytic activities of some of the NCs I had synthesized in IIT for liquid phase hydrogenation and oxidation reactions. In this regard, I developed a procedure to prepare magnetically recyclable catalysts using Turbobeats magnetic nanoparticles (NPs) as support (commercially available carbon-coated Co NPs) and pre-made colloidal NCs. I prepared a number of catalysts and applied them in liquid phase oxidation and hydrogenation reactions. The most promising results were the hydrogenation of cinnamylaldehyde to its corresponding unsaturated (or saturated) alcohol using AuCu (or AuCu@FeOx). We have checked the effect of different parameters on the extent of the reaction and found that the reaction takes place at moderately high pressure of 20 bar, the temperature of 50 °C and 24 h. The method for catalyst preparation is straightforward and can be applied for other colloidal NCs of interest as long as they are stable under harsh conditions of sonication. A collaboration started with the same group to complete and finalize this work. The results of this work are presented in the thesis as an Appendix as it still lacks completion.

References

1. Pietryga, J.M., Y.-S. Park, J. Lim, A.F. Fidler, W.K. Bae, S. Brovelli, and V.I. Klimov, *Spectroscopic and Device Aspects of Nanocrystal Quantum Dots*. Chem. Rev., 2016. **116**(18): p. 10513-10622.
2. Moore, T.L., L. Rodriguez-Lorenzo, V. Hirsch, S. Balog, D. Urban, C. Jud, B. Rothen-Rutishauser, M. Lattuada, and A. Petri-Fink, *Nanoparticle colloidal stability in cell culture media and impact on cellular interactions*. Chem. Soc. Rev., 2015. **44**(17): p. 6287-6305.
3. Gleich, B. and J. Weizenecker, *Tomographic imaging using the nonlinear response of magnetic particles*. Nature, 2005. **435**(7046): p. 1214-1217.
4. Chuang, C.-H.M., P.R. Brown, V. Bulović, and M.G. Bawendi, *Improved performance and stability in quantum dot solar cells through band alignment engineering*. Nat Mater, 2014. **13**(8): p. 796-801.
5. Paoella, A., G. Bertoni, S. Marras, E. Dilella, M. Colombo, M. Prato, A. Riedinger, M. Povia, A. Ansaldi, K. Zaghib, L. Manna, and C. George, *Etched Colloidal LiFePO₄ Nanoplatelets toward High-Rate Capable Li-Ion Battery Electrodes*. Nano Lett., 2014. **14**(12): p. 6828-6835.
6. Ethirajan, A., U. Wiedwald, H.G. Boyen, B. Kern, L. Han, A. Klimmer, F. Weigl, G. Kästle, P. Ziemann, K. Fauth, J. Cai, R.J. Behm, A. Romanyuk, P. Oelhafen, P. Walther, J. Biskupek, and U. Kaiser, *A Micellar Approach to Magnetic Ultrahigh-Density Data-Storage Media: Extending the Limits of Current Colloidal Methods*. Adv. Mater., 2007. **19**(3): p. 406-410.
7. Jia, C.-J. and F. Schuth, *Colloidal metal nanoparticles as a component of designed catalyst*. Phys. Chem. Chem. Phys., 2011. **13**(7): p. 2457-2487.
8. Mourdikoudis, S. and L.M. Liz-Marzán, *Oleylamine in Nanoparticle Synthesis*. Chem. Mater., 2013. **25**(9): p. 1465-1476.
9. Yin, Y. and A.P. Alivisatos, *Colloidal nanocrystal synthesis and the organic-inorganic interface*. Nature, 2005. **437**(7059): p. 664-670.

10. Zhang, S., L. Nguyen, Y. Zhu, S. Zhan, C.-K. Tsung, and F. Tao, *In-Situ Studies of Nanocatalysis*. Acc. Chem. Res., 2013. **46**(8): p. 1731-1739.
11. Gamarra, D., G. Munuera, A.B. Hungria, M. Fernández-García, J.C. Conesa, P.A. Midgley, X.Q. Wang, J.C. Hanson, J.A. Rodríguez, and A. Martínez-Arias, *Structure–Activity Relationship in Nanostructured Copper–Ceria-Based Preferential CO Oxidation Catalysts*. J. Phys. Chem. C, 2007. **111**(29): p. 11026-11038.
12. Li, Y. and G.A. Somorjai, *Nanoscale Advances in Catalysis and Energy Applications*. Nano Lett., 2010. **10**(7): p. 2289-2295.
13. Wu, Z., J. Deng, Y. Liu, S. Xie, Y. Jiang, X. Zhao, J. Yang, H. Arandiyán, G. Guo, and H. Dai, *Three-dimensionally ordered mesoporous Co₃O₄-supported Au–Pd alloy nanoparticles: High-performance catalysts for methane combustion*. J. Catal., 2015. **332**: p. 13-24.
14. Wang, F., L. Xu, J. Zhang, Y. Zhao, H. Li, H.X. Li, K. Wu, G.Q. Xu, and W. Chen, *Tuning the metal-support interaction in catalysts for highly efficient methane dry reforming reaction*. Appl. Catal., B, 2016. **180**: p. 511-520.
15. Wu, Q., C. Zhang, B. Zhang, X. Li, Z. Ying, T. Liu, W. Lin, Y. Yu, H. Cheng, and F. Zhao, *Highly selective Pt/ordered mesoporous TiO₂–SiO₂ catalysts for hydrogenation of cinnamaldehyde: The promoting role of Ti²⁺*. J. Colloid Interface Sci., 2016. **463**: p. 75-82.
16. Julkapli, N.M. and S. Bagheri, *Graphene supported heterogeneous catalysts: An overview*. Int. J. Hydrogen Energy, 2015. **40**(2): p. 948-979.
17. Cheng, N., J. Liu, M.N. Banis, D. Geng, R. Li, S. Ye, S. Knights, and X. Sun, *High stability and activity of Pt electrocatalyst on atomic layer deposited metal oxide/nitrogen-doped graphene hybrid support*. Int. J. Hydrogen Energy, 2014. **39**(28): p. 15967-15974.
18. Sartipi, S., M. Alberts, M.J. Meijerink, T.C. Keller, J. Pérez-Ramírez, J. Gascon, and F. Kapteijn, *Towards Liquid Fuels from Biosyngas: Effect of Zeolite Structure in Hierarchical-Zeolite-Supported Cobalt Catalysts*. ChemSusChem, 2013. **6**(9): p. 1646-1650.

19. Meunier, F.C., *Bridging the Gap between Surface Science and Industrial Catalysis*. ACS Nano, 2008. **2**(12): p. 2441-2444.
20. Guo, Y., D. Gu, Z. Jin, P.-P. Du, R. Si, J. Tao, W.-Q. Xu, Y.-Y. Huang, S. Senanayake, Q.-S. Song, C.-J. Jia, and F. Schuth, *Uniform 2 nm gold nanoparticles supported on iron oxides as active catalysts for CO oxidation reaction: structure-activity relationship*. Nanoscale, 2015. **7**(11): p. 4920-4928.
21. Herzing, A.A., C.J. Kiely, A.F. Carley, P. Landon, and G.J. Hutchings, *Identification of Active Gold Nanoclusters on Iron Oxide Supports for CO Oxidation*. Science, 2008. **321**(5894): p. 1331-1335.
22. Lopez, N., T.V.W. Janssens, B.S. Clausen, Y. Xu, M. Mavrikakis, T. Bligaard, and J.K. Nørskov, *On the origin of the catalytic activity of gold nanoparticles for low-temperature CO oxidation*. J. Catal., 2004. **223**(1): p. 232-235.
23. Tao, F., M.E. Grass, Y. Zhang, D.R. Butcher, J.R. Renzas, Z. Liu, J.Y. Chung, B.S. Mun, M. Salmeron, and G.A. Somorjai, *Reaction-Driven Restructuring of Rh-Pd and Pt-Pd Core-Shell Nanoparticles*. Science, 2008. **322**(5903): p. 932-934.
24. Speder, J., I. Spanos, A. Zana, J.J.K. Kirkensgaard, K. Mortensen, L. Altmann, M. Bäumer, and M. Arenz, *From single crystal model catalysts to systematic studies of supported nanoparticles*. Surf. Sci., 2015. **631**: p. 278-284.
25. Kuhn, J.N., W. Huang, C.-K. Tsung, Y. Zhang, and G.A. Somorjai, *Structure Sensitivity of Carbon–Nitrogen Ring Opening: Impact of Platinum Particle Size from below 1 to 5 nm upon Pyrrole Hydrogenation Product Selectivity over Monodisperse Platinum Nanoparticles Loaded onto Mesoporous Silica*. J. Am. Chem. Soc., 2008. **130**(43): p. 14026-14027.
26. Tsung, C.-K., J.N. Kuhn, W. Huang, C. Aliaga, L.-I. Hung, G.A. Somorjai, and P. Yang, *Sub-10 nm Platinum Nanocrystals with Size and Shape Control: Catalytic Study for Ethylene and Pyrrole Hydrogenation*. J. Am. Chem. Soc., 2009. **131**(16): p. 5816-5822.
27. Kang, Y., M. Li, Y. Cai, M. Cargnello, R.E. Diaz, T.R. Gordon, N.L. Wieder, R.R. Adzic, R.J. Gorte, E.A. Stach, and C.B. Murray, *Heterogeneous Catalysts Need Not Be so “Heterogeneous”*:

Monodisperse Pt Nanocrystals by Combining Shape-Controlled Synthesis and Purification by Colloidal Recrystallization. J. Am. Chem. Soc., 2013. **135**(7): p. 2741-2747.

28. Kumar, M. and S. Deka, *Multiply Twinned AgNi Alloy Nanoparticles as Highly Active Catalyst for Multiple Reduction and Degradation Reactions*. ACS Appl. Mater. Interfaces, 2014. **6**(18): p. 16071-16081.

29. Lee, K., S.W. Kang, S.-U. Lee, K.-H. Park, Y.W. Lee, and S.W. Han, *One-Pot Synthesis of Monodisperse 5 nm Pd–Ni Nanoalloys for Electrocatalytic Ethanol Oxidation*. ACS Appl. Mater. Interfaces, 2012. **4**(8): p. 4208-4214.

30. Comotti, M., W.-C. Li, B. Spliethoff, and F. Schüth, *Support Effect in High Activity Gold Catalysts for CO Oxidation*. J. Am. Chem. Soc., 2006. **128**(3): p. 917-924.

31. Wang, C., C. Xu, H. Zeng, and S. Sun, *Recent Progress in Syntheses and Applications of Dumbbell-like Nanoparticles*. Adv. Mater., 2009. **21**(30): p. 3045-3052.

32. Wang, C., H. Daimon, and S. Sun, *Dumbbell-like Pt–Fe₃O₄ Nanoparticles and Their Enhanced Catalysis for Oxygen Reduction Reaction*. Nano Lett., 2009. **9**(4): p. 1493-1496.

33. George, C., A. Genovese, A. Casu, M. Prato, M. Povia, L. Manna, and T. Montanari, *CO Oxidation on Colloidal Au_{0.80}Pd_{0.20}–Fe_xO_y Dumbbell Nanocrystals*. Nano Lett., 2013. **13**(2): p. 752-757.

34. Sun, X., S. Guo, Y. Liu, and S. Sun, *Dumbbell-like PtPd–Fe₃O₄ Nanoparticles for Enhanced Electrochemical Detection of H₂O₂*. Nano Lett., 2012. **12**(9): p. 4859-4863.

35. Chen, C., C. Nan, D. Wang, Q. Su, H. Duan, X. Liu, L. Zhang, D. Chu, W. Song, Q. Peng, and Y. Li, *Mesoporous Multicomponent Nanocomposite Colloidal Spheres: Ideal High-Temperature Stable Model Catalysts*. Angew. Chem. Int. Ed., 2011. **50**(16): p. 3725-3729.

36. Du, C., G. Lu, Y. Guo, Y. Guo, and X.-q. Gong, *Surfactant-Mediated One-Pot Method To Prepare Pd–CeO₂ Colloidal Assembled Spheres and Their Enhanced Catalytic Performance for CO Oxidation*. ACS Omega, 2016. **1**(1): p. 118-126.

37. Munnik, P., P.E. de Jongh, and K.P. de Jong, *Recent Developments in the Synthesis of Supported Catalysts*. Chem. Rev., 2015. **115**(14): p. 6687-6718.
38. Cargnello, M., C. Chen, B.T. Diroll, V.V.T. Doan-Nguyen, R.J. Gorte, and C.B. Murray, *Efficient Removal of Organic Ligands from Supported Nanocrystals by Fast Thermal Annealing Enables Catalytic Studies on Well-Defined Active Phases*. J. Am. Chem. Soc., 2015. **137**(21): p. 6906-6911.
39. Niu, Z. and Y. Li, *Removal and Utilization of Capping Agents in Nanocatalysis*. Chem. Mater., 2014. **26**(1): p. 72-83.
40. Wang, Z.L., *Transmission Electron Microscopy of Shape-Controlled Nanocrystals and Their Assemblies*. J. Phys. Chem. B, 2000. **104**(6): p. 1153-1175.
41. Yang, J.C., M.W. Small, R.V. Grieshaber, and R.G. Nuzzo, *Recent developments and applications of electron microscopy to heterogeneous catalysis*. Chem. Soc. Rev., 2012. **41**(24): p. 8179-8194.
42. Villa, A., N. Dimitratos, C.E. Chan-Thaw, C. Hammond, G.M. Veith, D. Wang, M. Manzoli, L. Prati, and G.J. Hutchings, *Characterisation of gold catalysts*. Chem. Soc. Rev., 2016. **45**(18): p. 4953-4994.
43. Niemantsverdriet, J.W., *Microscopy and Imaging*, in *Spectroscopy in Catalysis*. 2007, Wiley-VCH Verlag GmbH & Co. KGaA. p. 179-216.
44. Su, D.S., B. Zhang, and R. Schlögl, *Electron Microscopy of Solid Catalysts—Transforming from a Challenge to a Toolbox*. Chem. Rev., 2015. **115**(8): p. 2818-2882.
45. Alayoglu, S. and B. Eichhorn, *Rh–Pt Bimetallic Catalysts: Synthesis, Characterization, and Catalysis of Core–Shell, Alloy, and Monometallic Nanoparticles*. J. Am. Chem. Soc., 2008. **130**(51): p. 17479-17486.
46. Herbert, J.J., P. Senecal, D.J. Martin, W. Bras, S.K. Beaumont, and A.M. Beale, *X-ray spectroscopic and scattering methods applied to the characterisation of cobalt-based Fischer-Tropsch synthesis catalysts*. Catal. Sci. Technol., 2016. **6**(15): p. 5773-5791.

47. Xu, D., S. Bliznakov, Z. Liu, J. Fang, and N. Dimitrov, *Composition-Dependent Electrocatalytic Activity of Pt-Cu Nanocube Catalysts for Formic Acid Oxidation*. Angew. Chem. Int. Ed., 2010. **49**(7): p. 1282-1285.
48. Bragg, W.H. and W.L. Bragg, *The Reflection of X-rays by Crystals*. Proc. R. Soc. London, Ser. A, 1913. **88**(605): p. 428-438.
49. Niemantsverdriet, J.W., *Diffraction and Extended X-Ray Absorption Fine Structure (EXAFS)*, in *Spectroscopy in Catalysis*. 2007, Wiley-VCH Verlag GmbH & Co. KGaA. p. 147-177.
50. Bordiga, S., E. Groppo, G. Agostini, J.A. van Bokhoven, and C. Lamberti, *Reactivity of Surface Species in Heterogeneous Catalysts Probed by In Situ X-ray Absorption Techniques*. Chem. Rev., 2013. **113**(3): p. 1736-1850.
51. Newville, M., *Fundamentals of XAFS*. Rev. Mineral. Geochem., 2014. **78**(1): p. 33-74.
52. Tsuji, K., K. Nakano, Y. Takahashi, K. Hayashi, and C.-U. Ro, *X-ray Spectrometry*. Anal. Chem., 2012. **84**(2): p. 636-668.
53. Calvin, S., *XAFS for Everyone*. 2013: Taylor & Francis.
54. Salmeron, M. and R. Schlögl, *Ambient pressure photoelectron spectroscopy: A new tool for surface science and nanotechnology*. Surf. Sci. Rep., 2008. **63**(4): p. 169-199.
55. Lin, F.-h. and R.-a. Doong, *Characterization of interfacially electronic structures of gold-magnetite heterostructures using X-ray absorption spectroscopy*. J. Colloid Interface Sci., 2014. **417**: p. 325-332.
56. Hadjiivanov, K.I. and G.N. Vayssilov, *Characterization of oxide surfaces and zeolites by carbon monoxide as an IR probe molecule*, in *Advances in Catalysis*. 2002, Academic Press. p. 307-511.
57. Niemantsverdriet, J.W., *Vibrational Spectroscopy*, in *Spectroscopy in Catalysis*. 2007, Wiley-VCH Verlag GmbH & Co. KGaA. p. 217-249.

58. Mihaylov, M., H. Knözinger, K. Hadjiivanov, and B.C. Gates, *Characterization of the Oxidation States of Supported Gold Species by IR Spectroscopy of Adsorbed CO*. Chem. Ing. Tech., 2007. **79**(6): p. 795-806.
59. Venkov, T., K. Hadjiivanov, and D. Klissurski, *IR spectroscopy study of NO adsorption and NO + O₂ co-adsorption on Al₂O₃*. Phys. Chem. Chem. Phys., 2002. **4**(11): p. 2443-2448.
60. Boss, C.B. and K.J. Fredeen, *Concepts, Instrumentation, and Techniques in Inductively Coupled Plasma Optical Emission Spectrometry*. 1997: Perkin-Elmer.

Chapter II¹

The effect of Au domain size on the CO oxidation catalytic activity of colloidal Au–FeOx dumbbell-like heterodimers²

¹ XPS measurements were done by M. Prato; SEM by S. Marras, TEM by A. Scarpellini; All other activities including experimental, results interpretation and manuscript preparation were performed by S. Najafshirvari under supervision of P. Guardia (for synthesis) and M. Colombo (for all characterizations, catalytic experiments and results interpretation) and L. Manna (for manuscript preparation).

² Reprinted from Journal of Catalysis, 338, S. Najafshirvari et al., The effect of Au domain size on the CO oxidation catalytic activity of colloidal Au–FeOx dumbbell-like heterodimers, 115-123, Copyright (2016), with permission from Elsevier.



The effect of Au domain size on the CO oxidation catalytic activity of colloidal Au–FeOx dumbbell-like heterodimers



Sharif Najafshirtari^a, Pablo Guardia^{a,b}, Alice Scarpellini^a, Mirko Prato^a, Sergio Marras^a, Liberato Manna^a, Massimo Colombo^{a,*}

^a Department of Nanochemistry, Istituto Italiano di Tecnologia, Via Morego 30, 16163 Genova, Italy

^b Centro de Tecnología Química de Cataluña, Carrer de Marcel·lí Domingo s/n, 43007 Tarragona, Spain

ARTICLE INFO

Article history:

Received 23 January 2016

Revised 29 February 2016

Accepted 2 March 2016

Keywords:

CO oxidation

Heterodimers

Nanocatalyst

Gold nanoparticles

Dumbbell

Iron oxide

ABSTRACT

Au@FeOx dumbbell nanocrystals (NCs) with different sizes of the Au domain (i.e. 4 nm, 6 nm and 10 nm) were successfully synthesized by means of a colloidal synthesis procedure. They were then deposited on γ -alumina and tested in CO oxidation. The use of alumina minimized the contribution of the Au-support interaction in the CO oxidation, thus enabling us to clearly identify a synergy between the Au and the iron oxide that eventually resulted in an enhanced activity in CO oxidation, good sintering resistance and good stability of the catalytic performances. Among the three gold sizes tested, the dumbbells with 4 nm Au domains were found to be the most active ones. Nevertheless, we found that the activity of the 4 nm dumbbells was significantly hampered by the limited exposure of the Au or of the Au/iron oxide interface to the reacting environment.

© 2016 Elsevier Inc. All rights reserved.

1. Introduction

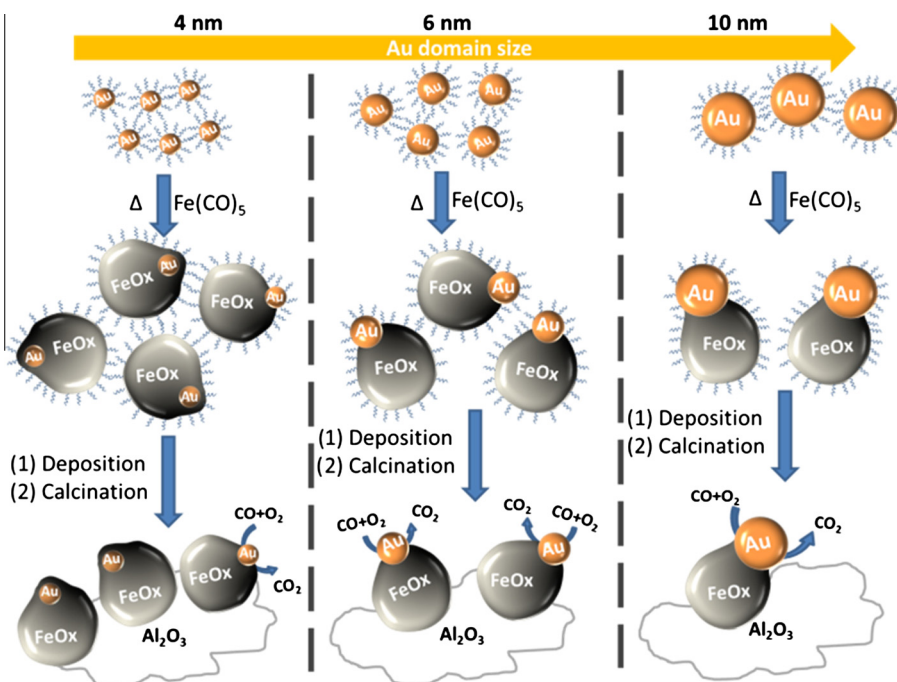
After the early work of Bond on activation of H₂ and mono-olefin hydrogenation using gold as catalyst [1], and the pioneering work of Haruta in low temperature CO oxidation [2–4], catalysis by Au has been extensively studied [5,6]. In this regard, CO oxidation has often been selected as a probe reaction to study the catalytic properties of Au catalysts [2,7–9]. Among the different Au based catalysts studied in the literature, iron oxide-supported Au catalysts are one of the most active systems for low-temperature CO oxidation [10,11] and dumbbell like Au@FeOx heterodimers represent an interesting example of Au based nanostructured materials for catalytic and biomedical applications [12,13]. In the nano-dumbbell morphology each gold nanoparticle is connected to an oxide domain of few nanometers size, which acts as a nano-sized support. Interesting effects of nano-sized supports have been reported for example by Carrettin et al. [14], who studied the synthesis of phenols using gold nanoparticles supported on nanocrystalline CeO₂. Compared to conventionally prepared catalysts, the nano-dumbbell structure is characterized by a strong epitaxial connection between the metal and the metal oxide domains, which eventually results in an enhanced charge transfer across the inter-

face between the metal and the metal oxide [12,15–17]. Another interesting property of the dumbbell morphology is the fact that the metal domain is typically nested or anchored in the oxide domain; this morphology ensures structural stability and a high resistance to sintering of the metal domains [18–20], which is one of the main causes of deactivation in traditional catalysts. Sun et al. [12] pioneered the synthesis of dumbbell nanocrystals (NCs) and different groups studied their application as low-temperature CO oxidation catalysts [18,21]. However, Yin et al. [21] and Wu et al. [18] showed that the catalytic activity of Au@FeOx dumbbells strongly depends on the support on which the NCs are deposited. Eventually the catalytic activity can be dominated by the interface between the Au and the support, leading to contradictory results on the actual role of the Au/FeOx interaction in the dumbbell morphology. Therefore, a deeper understanding of the correlation between the physicochemical properties of the Au@FeOx dumbbell structures and their catalytic activity in CO oxidation is yet to be achieved [22]. In addition, the effect of the gold domain size on the catalytic activity of this class of nanostructured materials is still to be addressed.

In this work, colloidal Au@FeOx dumbbell NCs were synthesized starting from Au seeds having different, well-defined sizes (Scheme 1 Top and Center). The colloidal Au seeds as well as the Au@FeOx dumbbell-like NCs were deposited onto alumina and systematically studied as CO oxidation catalysts (Scheme 1 Bottom).

* Corresponding author.

E-mail address: massimo.colombo@iit.it (M. Colombo).



Scheme 1. Sketch of the dumbbells synthesis, colloidal deposition and catalytic test in CO oxidation. (Top) Au seeds with different sizes were firstly prepared by means of a colloidal synthesis procedure; (Center) the Au NCs were used as seeds to prepare Au@FeOx dumbbell like NCs; and (Bottom) the dumbbell shaped NCs were deposited on alumina, calcined in air to remove organic ligands and tested in the CO oxidation reaction.

The choice of alumina, a non-reducible oxide, allowed us to minimize the contribution of Au-support interactions in the CO oxidation and highlighted the synergy between the Au and the FeOx domains: our results revealed an enhanced CO oxidation activity in comparison with Au/Al₂O₃ catalysts prepared using the same Au seeds. The catalysts, after being loaded in the micro-reactor, were initially activated in an oxidative atmosphere to remove the protecting ligands. Then the activity data were collected in the CO/O₂ mixture during heating and cooling transients. A high temperature oxidative pre-treatment was performed before each test in order to restore the initial activity of the catalysts without causing deterioration of the dumbbells structures or their dispersion. Among the tested dumbbell catalysts, Au@FeOx NCs with 4 nm Au domains were found to be the most active ones, even though their activity was negatively affected by the limited exposure of Au domains and thus of the Au–FeOx interface to the reactive atmosphere.

2. Experimental

2.1. Synthesis of NCs

2.1.1. Chemicals

Oleylamine (OIAM, 70%), HAuCl₄·3H₂O, 1,2,3,4-tetrahydronaphthalene (Tetralin®), Octadecene (ODE, 90%), Oleic acid (OIAc, 90%), Iron pentacarbonyl (Fe(CO)₅, >99.99% trace metals basis), Tert-butylamine-borane complex (TBAB 97%) and solvents (Ethanol, 2-isopropanol, chloroform and n-hexane) were purchased from Sigma Aldrich. γ-Al₂O₃ extrudate was purchased from Strem Chemicals. All chemicals were used as received.

2.1.2. Au NCs synthesis

Au NCs were synthesized using a reported procedure [21] with some modifications in the synthesis temperature and the washing procedure. Briefly, to prepare Au NCs of ~3 nm in size, 100 mg of HAuCl₄·3H₂O was first dissolved in a mixture of 10 ml of OIAM

and 10 ml of Tetralin®, then degassed in N₂ atmosphere for 30 min. 44 mg of the reducing agent, TBAB, was dissolved by sonication in a mixture of 1 ml OIAM and 1 ml of Tetralin® and then injected into the Au precursor mixture under stirring at the temperature of 21 °C. The mixture was kept under stirring for 1 h, washed twice with a mixture of isopropanol and ethanol (4:1 vol. ratio), centrifuged and dispersed in 10 ml of hexane. Larger Au NCs of 5.4 nm in size were synthesized using the same procedure except that the temperature was lowered and kept at 0 °C using an ice bath. The Au NCs having the largest size in our study (i.e. 10.5 nm) were synthesized by means of a thermal decomposition procedure. Typically, 20 ml of ODE, 1.5 ml of OIAM and 1.5 ml of OIAc were mixed and degassed for 30 min at 120 °C using N₂. Then, a solution of 40 mg of Au precursor in 0.7 ml of OIAM and 2 ml of ODE was injected into the solvent mixture; the temperature was raised to 150 °C and kept there for 30 min. The product was washed with isopropanol and ethanol, centrifuged and dispersed in 10 ml of hexane.

2.1.3. Synthesis of Au@FeOx and FeOx NCs

Dumbbell shaped NCs were synthesized by a seed mediated growth approach. The pre-made Au NCs, obtained as previously described, were used as seeds and iron pentacarbonyl was used as the iron source. Typically, 8 mg of the Au NCs seeds was mixed with a solvent mixture of 20 ml of ODE, 3 ml of OIAM and 1 ml of OIAc and degassed under vacuum at 80 °C for 1 h to remove hexane. Then, a solution of Fe precursor in 1 ml of already degassed ODE was injected in the solution at 150 °C while the temperature was raised to 205 °C. The mixture was stirred for 1.5 h and then it was heated up to 300 °C and kept there for 1 h. The products were washed once with a mixture of isopropanol and ethanol (4:1 vol. ratio), centrifuged and dispersed in 10 ml of chloroform. The amount of Fe precursor in the synthesis was adjusted considering the different number of Au seeds having different sizes (using less Fe precursor in case of larger Au seeds). FeOx NCs were also synthesized using the same procedure as the dumbbells

NCs. In this case no Au seeds were added to the synthesis mixture.

2.1.4. Catalysts preparation

The alumina supported catalysts were prepared by colloidal deposition. Typically, a specified weight of γ - Al_2O_3 powder (manually crushed and sieved to 90 μm) was dispersed in hexane (in case of Au catalyst) or chloroform (in case of dumbbells) and then a proper amount of colloidal solution (targeting 1 wt.% Au loading) was added to it. The suspension was mixed for 2 h (either with a magnetic stirrer in case of Au catalysts or sonication in case of dumbbells). Subsequently, the suspension was dried under dry air and the resulting powder was calcined in static air at 200 °C for 13 h. Another alumina supported catalyst was also prepared based on FeOx NCs, to be used for control experiments. The loading of Fe was set to 8 wt.%, corresponding to the highest iron loading of the dumbbell catalysts. The colloidal deposition procedure was similar to the one just described in case of the dumbbell samples.

2.2. Catalytic experiments

The activity of the catalysts for CO oxidation was measured using a micro reactor system coupled with a micro-Gas Chromatograph (μ -GC) equipped with three modules working in parallel (each consisting of an injector, a column and a thermal conductivity detector) to analyze CO, O_2 and CO_2 (SRA Instruments model R-3000). Typically, the catalyst powder was diluted with alumina (2:1 weight ratio) and loaded into a quartz reactor (internal diameter ID = 8 mm). The feed gas was a mixture of 1% v/v CO and 6% v/v O_2 balanced with He with a flow rate of 80 Ncc/min corresponding to a gas hourly space velocity of 3,000,000 Ncc/h/(g Au). After being loaded in the micro-reactor, the catalysts were initially in-situ activated at 350 °C for 10 h in 6% v/v O_2 (balance He) to remove the ligands from the surface of deposited NCs. The successful removal of the ligands using this treatment was checked by connecting the outlet stream of the reactor to a Mass Spectrometer (Pfeiffer Vacuum Omnistar GSD 320), as shown in Fig. S1(a). Additionally, catalytic activity measurements after pre-treatment at higher temperatures (i.e. 400 °C) did not result in any activity improvement (Fig. S1(b)). For the activity measurements, the reactor was heated from room temperature (RT) to 300 °C with a heating rate of 2 °C/min and kept at 300 °C for 30 min, then cooled down to 100 °C with the same rate and kept at 100 °C for 30 min. Transient activity data were collected every 4 min during the mentioned cycle of catalytic test. Before each test cycle, the catalyst bed was exposed to a stream of 6% v/v O_2 in He at 350 °C for 1 h. The heating rate used in the activation and in the oxidizing pre-treatment was set to 5 °C/min. In case of kinetic measurements, the space velocity was increased to $4.8\text{E}+7$ Ncc/h/(g Au) in order to keep the CO conversion below 10% and work under differential reactor conditions. Reaction rates were evaluated after 2 h on stream at constant temperature. CO and CO_2 outlet concentrations were measured by a NDIR analyzer (ABB Uras 26).

2.3. Characterization

2.3.1. Transmission electron microscopy (TEM)

Overview bright-field TEM (BFTEM) images were acquired on the various samples deposited on standard carbon coated Cu grids using a Jeol JEM-1011 instrument with a thermionic W source operated at 100 kV. High angle annular dark field (HAADF) scanning TEM (STEM) images and high resolution (HR) TEM images were collected using a FEI Tecnai G2 F20 instrument equipped with a Schottky field emission (FEG) electron source, operating at 200 kV acceleration voltage.

2.3.2. Scanning electron microscopy (SEM)

High Resolution Scanning Electron Microscopy (HRSEM) analysis was performed to check the visual dispersion of the dumbbell NCs on the support. Backscattered electron (BSE) images having compositional contrast were collected using a JEOL JSM-7500FA instrument, equipped with a cold field emission gun (single crystal $\langle 310 \rangle$ emitter), a 2-segments solid state annular BSE detector and operating at 10 kV. Samples were prepared by depositing a small amount of catalysts powder on an ultra-smooth silicon wafer.

2.3.3. Elemental analysis

The chemical composition of the colloidal NCs as well as the metal loadings of the catalysts was measured by Inductively Coupled Plasma Optical Emission Spectroscopy (ICP-OES) using a iCAP 6000 Thermo Scientific spectrometer. A specific weight (in case of powder catalyst) or volume (in case of colloidal solutions) was digested in HCl/HNO_3 3:1 (v/v) overnight, diluted with deionized water (14 μS) and filtered using PTFE filter before measurement.

2.3.4. Temperature programmed reduction (TPR)

TPR measurements were performed on ~100 mg of the catalyst unloaded from the reactor using a Quantachrome Autosorb iQ equipped with a VICI® micro thermal conductivity detector (TCD). For the 10 nm Au@FeOx sample, the mass was increased to ~250 mg. Au@FeOx dumbbell as well as the FeOx catalysts was loaded into a quartz U-tube (ID = 12 mm) and exposed to a mixture of 5% v/v O_2 in He at 350 °C for 3 h. Then the tube was cooled down and, after stabilizing the temperature to 40 °C, the gas flow was switched to a mixture of 5% v/v H_2 in Ar. The system was heated up to 900 °C at a rate of 20 °C/min while the TCD signal was being monitored.

2.3.5. In-situ diffuse reflectance infrared fourier transform spectroscopy (DRIFTS)

Spectra were collected using a Vertex 70 infrared spectrometer (Brüker Optics) equipped with a DRIFTS cell (Praying Mantis, Harrick) and a Mercury Cadmium Telluride detector (MCT), cooled with liquid nitrogen. The outlet of the DRIFTS cell was connected to an on-line mass spectrometer (Pfeiffer Vacuum Omnistar GSD 320). Using a 4 port selector valve, the inlet gas was switched between two different gas streams, one used for purging and/or pre-treatments and the other containing the probe species. The loaded sample was pre-treated in oxidizing atmosphere prior to the test using the same conditions as those of the catalytic experiments, except for the heating rate which was set to 20 °C/min. After pre-treatment, the cell was cooled down to RT. After stabilization of the signal at RT, the background spectrum was collected while the pretreatment gas mixture was flowing. Then, the flowing gas was switched to a mixture containing either 0.2% v/v CO and balance He or 1% v/v CO, 6% v/v O_2 and balance He. Spectra were collected every 10 s for the first 100 s of adsorption. The process was monitored for further 35 min, by collecting a spectrum every 5 min. Each test was performed at least two times to verify the reproducibility of the measurement.

2.3.6. X-ray photoelectron spectroscopy (XPS)

XPS was performed on a Kratos Axis Ultra DLD spectrometer, using a monochromatic Al $\text{K}\alpha$ source (15 kV, 20 mA). High resolution narrow scans were performed at constant pass energy of 10 eV and steps of 0.1 eV. The photoelectrons were detected at a take-off angle $\Phi = 0^\circ$ with respect to the surface normal. The pressure in the analysis chamber was maintained below 7×10^{-9} Torr for data acquisition. The data were converted to VAMAS format and processed using CasaXPS software, version 2.3.16. The binding energy (BE) scale was internally referenced to the C 1 s peak (BE for C-C = 284.8 eV).

2.3.7. Iodine (I_2) etching

Gold was etched from the Au@FeOx dumbbells using iodine at low temperature. Briefly, a small volume of dumbbell colloidal solution (containing 0.2 mg of Au) was added to 5 ml of 3 mg/ml solution of I_2 in hexane and stored in closed cap vials. The solution was stirred at 50 °C for 24 h, washed with ethanol and separated by centrifugation.

3. Results and discussion

Typical BFTEM images of the Au NCs seeds along with their size distribution profiles are shown in Fig. S2, while BFTEM images of the final colloidal Au@FeOx NCs are shown in Fig. 1(a)–(c). The mean sizes of the Au and FeOx domains were statistically evaluated by graphical measurement of more than 100 NCs and the resulting size distribution profiles are shown in Fig. 1. A limited enlargement of the Au domain size in the dumbbells, likely related to particles coalescence or Ostwald ripening during the synthesis procedure, was observed in comparison with the starting seeds for the smallest (from 3.1 ± 0.4 to 4.2 ± 0.7 nm) and intermediate gold sizes (from 5.4 ± 0.6 to 6.6 ± 1.0 nm). No statistically relevant difference was observed in case of the largest gold seeds (from 10.5 ± 1.8 to 10.6 ± 1.7 nm). The mean size of the oxide domain was found to be 18.1 ± 3.0 and 18.4 ± 4.0 nm using 3.1 and 5.4 nm Au seeds, respectively, and 23.6 ± 5.5 nm when using the 10.5 nm Au seeds. For the sake of simplicity, the dumbbell NCs are labeled hereafter as 4 nm Au@FeOx, 6 nm Au@FeOx and 10 nm Au@FeOx. We can conclude that it is possible to tune the size of Au domain in dumbbell shaped NCs by using seeds of different sizes. It should be mentioned however that flower shaped NCs were also observed, especially in case of 3.1 nm Au seeds. The formation of flower shaped NCs when smaller Au NCs were used could be due to different crystallinity of the Au seeds but also to the higher amount of Fe precursor that was added into the solution when smaller Au NCs were used as seeds. In the case of 3.1 nm Au seeds, we observed indeed a tradeoff between the number of free Au NCs and the number of flower-shaped Au@FeOx NCs. The former were prevailing when using a low amount of Fe precursor (see Fig. S3) while the latter were preferentially observed when higher amounts of $Fe(CO)_5$ were used in the synthesis, as evident in Fig. 1(a).

The alumina supported catalysts were further prepared by colloidal deposition. HRSEM images in Fig. S4 show that the dumbbell NCs were quite well dispersed on the alumina support and no signs of Au aggregation were observed after the calcination process. The loadings of Au and Fe in each catalyst sample were measured by ICP and are reported in Table 1. The concentration of Au was close to 1 wt.% in all cases, while the Fe loading was different among the samples. This trend can be easily explained considering that at a fixed Au mass, the number of deposited NCs increased with decreasing the size of Au. Considering that the sizes of FeOx domain in all samples were similar, the Fe loading increased by decreasing the Au size, in line with what is summarized in Table 1.

The catalysts were analyzed by TEM after the activation process detailed in the Experimental section, which represents the hardest set of conditions that the catalyst underwent during the experiments of the present work. As shown in Fig. S5 for the case of 4 nm Au@FeOx on alumina catalyst, no sintering was observed, while the morphology of the dumbbell NCs was preserved. These data proved that the FeOx domain was stable at temperatures up to 350 °C under oxidizing atmosphere and it also prevented Au from sintering. The same results were observed for the other dumbbell catalytic samples (results not shown).

A series of transient catalytic tests were conducted on the samples after the initial in-situ activation. The evolution of the activity in CO oxidation for the 4 nm Au@FeOx on alumina support is

shown in Fig. 2. The trend highlighted by the black squares, which represents the CO conversion as a function of temperature for one cycle of reaction, indicated that the catalyst had limited activity at room temperature. CO conversion evolved as the temperature was raised, reaching 100% conversion at ~ 230 °C. By comparing the black squares and red circles in Fig. 2, representing two different cycles of reaction, we concluded that the activity trend of the catalyst was reproducible, proving the stability of the catalyst. Moreover, both tests highlighted a hysteresis in the activity between the heating and cooling phases, in a way that the activity during the cooling phase was higher than in the heating phase. This behavior might be related to the formation of surface carbonates species. It is well-known indeed that carbonates can be formed during Au catalyzed CO oxidation reaction and that they can cause the deactivation of the catalyst [23]. The accumulation of surface carbonates at low temperatures during the heating phase of the experiment was confirmed by DRIFTS measurements (Fig. S6), which clearly showed the fast development of strong absorption bands in the carbonates region (1300 – 1800 cm^{-1}) [24]. The formation of these species could justify the lower activity in comparison with the cooling transient of the test. To further support this hypothesis, the catalyst activity was measured using a different gas feed mixture consisting of 1% v/v CO, 6% v/v O_2 and 5% v/v CO_2 . Before the test, the sample was pre-treated according to the oxidative treatment described previously. As shown in Fig. 2 (the pink triangles), the catalyst's activity was lower in the presence of CO_2 , while the hysteresis was eliminated. Both trends are consistent with carbonates poisoning, favored by the increased concentration of CO_2 in the gas mixture. If no regeneration was performed between two consecutive tests (see Fig. S7) the hysteresis was still observed. This result is in line with DRIFTS data, which showed the fast buildup of carbonates over the clean catalyst surface. Further indication of surface poisoning was provided by testing the catalyst at a constant temperature of 100 °C during 12 h of time on stream, using a gas feed mixture of 1% v/v CO and 6% v/v O_2 . As shown in the inset of Fig. 2, the catalyst activity dropped from $\sim 23\%$ (conversion at 100 °C during the cooling phase of the transient tests) to $\sim 14\%$, approaching the conversion at 100 °C measured during the heating phase of transient tests, i.e. $\sim 10\%$.

The same hysteresis was observed also when using the 6 nm and 10 nm Au@FeOx samples. In order to compare the catalytic activity of the dumbbells with different gold domain size, we performed kinetic measurements. Fig. 3 shows the Arrhenius plots of the CO oxidation rate for the various samples. Among the three samples, the dumbbell catalyst having 4 nm Au domain size was the most active one, in agreement with literature reports on Au catalyzed CO oxidation [9,25,26]. Interestingly, the activity over the three samples showed a double regime, one below 140 °C, characterized by lower activation energies in the range 14–20 kJ/mol (see Table 2), and one at higher temperatures, characterized by higher activation energies, in the range 26–40 kJ/mol. Such a trend is in line with the observed carbonates poisoning, which results in the decrease of the apparent activation energy, similar to what observed over Pt/ Al_2O_3 catalysts [27]. It should be mentioned, however, that the same trend could be also consistent with the onset of different reaction mechanisms in different temperature windows. Table 2 reports also the turnover frequencies (TOFs) evaluated at 80 °C for the three samples. For 6 nm and 10 nm Au@FeOx dumbbell samples, the calculated values are comparable to those reported in the literature for Au supported on bulk iron oxide [28]. In case of the 4 nm Au@FeOx sample, the calculated value is instead significantly smaller compared to what can be found in the literature, where values in the range 3 – 6 s^{-1} have been reported [28].

As control experiments, catalysts containing only Au NCs seeds (with different sizes) were prepared and used for kinetic measure-

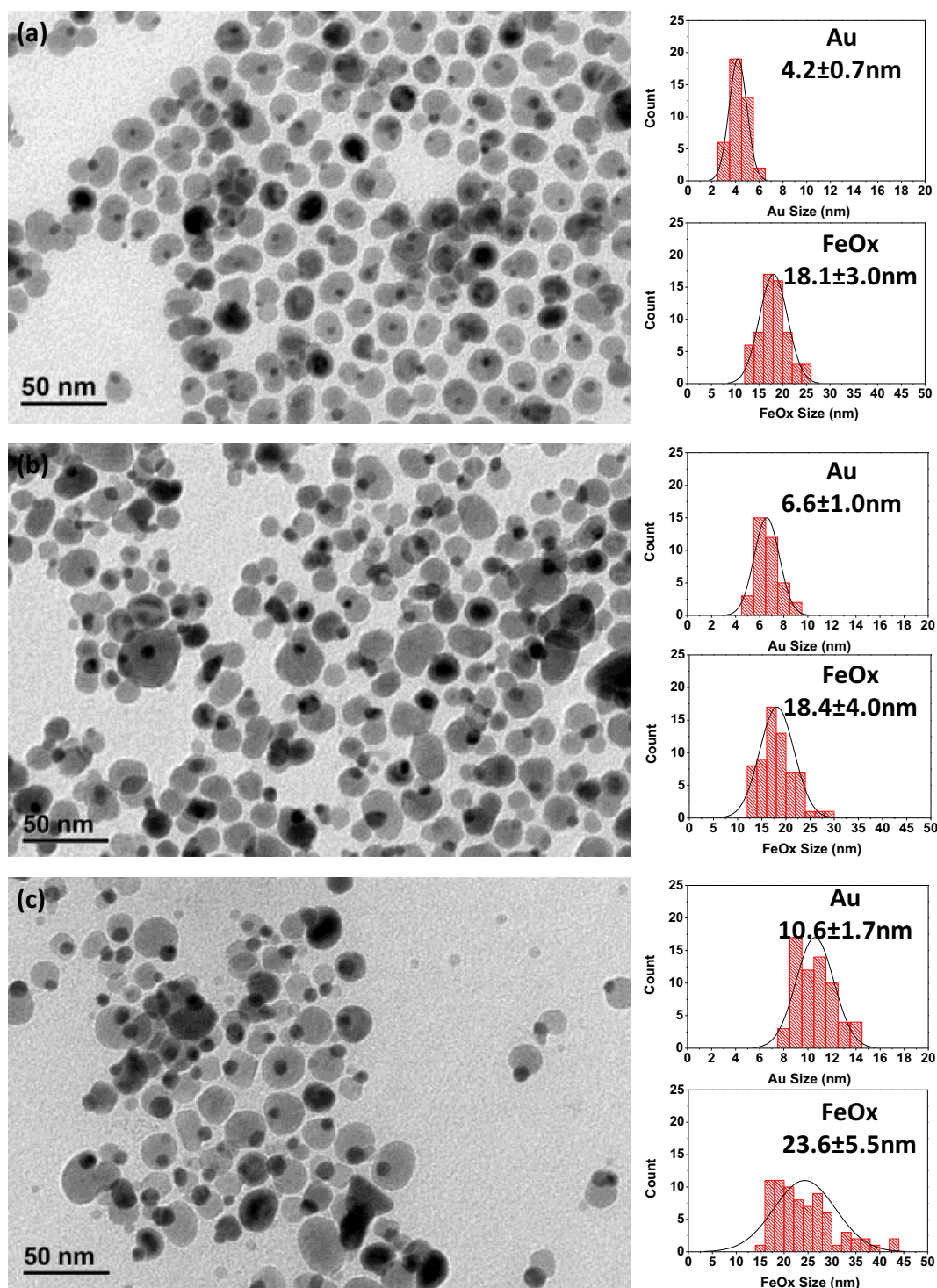


Fig. 1. BFTEM images of synthesized Au@FeOx dumbbell-like NCs: (a) 4 nm, (b) 6 nm, (c) 10 nm Au@FeOx with their corresponding size distribution profiles for Au and FeOx domains.

ments. Samples were prepared using the same Au NCs used as seeds in the synthesis of the corresponding dumbbell like structures. A significant enhancement of the CO oxidation rate was observed for all dumbbells catalysts (see Fig. S8) compared to the corresponding Au/Al₂O₃ ones. In another control experiment a catalyst sample was prepared using bare FeOx NCs, in order to evaluate their contribution to the CO oxidation catalytic activity. As shown in Fig. S9 the sample exhibited negligible catalytic activity at temperatures lower than 200 °C, where 90% conversion was

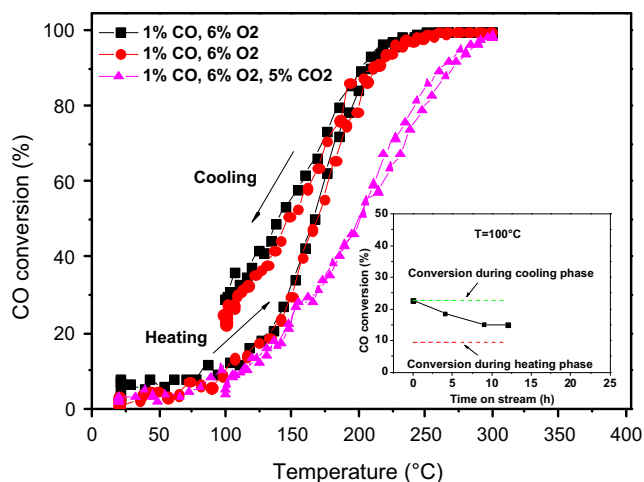
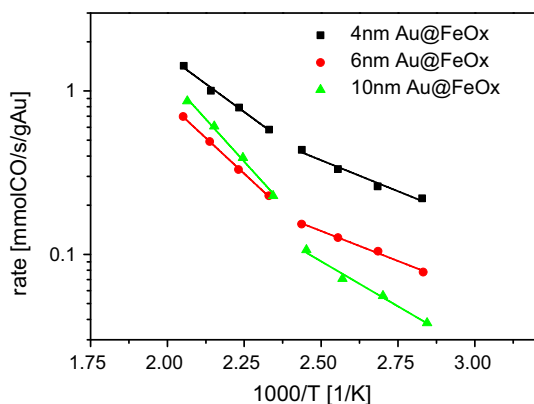
already achieved using the dumbbell catalysts. These results highlighted how the activity enhancement observed for the dumbbells catalysts was the result of the synergy created between the Au and the FeOx in the dumbbells and not by the interaction between the Au and the Al₂O₃ support.

In order to shed more light on such a synergy and understand the reasons of the activity trend observed as a function of the Au domain size, the dumbbells as well as the FeOx catalysts were firstly characterized by TPR experiments [29]. These measure-

Table 1

Au and Fe loadings of calcined Au@FeOx dumbbell catalysts.

Catalyst	Au loading (%)	Fe loading (%)
4 nm Au@FeOx	0.94	7.71
6 nm Au@FeOx	1.02	3.61
10 nm Au@FeOx	0.87	1.08

**Fig. 2.** Catalytic activity of 4 nm Au@FeOx dumbbells and CO₂ effect. Black solid squares and red circles represent two different cycles at the same conditions. Inset: CO conversion at 100 °C as a function of time on stream. The catalyst was treated in oxidative atmosphere of 6% v/v O₂ in He, at 350 °C for 1 h before each test.**Fig. 3.** Comparison of the CO oxidation rate among the Au@FeOx dumbbells having different Au domain size.

ments were carried out in order to understand the effect of the Au presence on the reducibility of the FeOx domain. We firstly used a commercial Fe₃O₄ powder as reference. As shown in Fig. 4, there were two main regions in which the reference Fe₃O₄ sample was reduced: the first one ($T < 500$ °C) can be correlated to the reduction of Fe₂O₃ to Fe₃O₄, and the second one to the Fe₃O₄ multiple steps reduction to Fe⁰ ($T > 500$ °C), as also reported in the literature [24,29–31]. The presence of Fe₂O₃ is justified by the oxidizing pre-treatment included in the TPR test protocol (see the Experimental section). The FeOx/Al₂O₃ catalyst had a similar reduction profile: one additional shoulder in the first reduction region ($T < 400$ °C) could be noticed, while the high temperature region ($T > 400$ °C) was similar to the one observed over the Fe₃O₄ standard. The shift of the reduction peaks toward lower temperatures highlights how nano-sizing the oxide domain positively affected its reducibility. Reducing the mass loading of FeOx NCs obviously resulted in a simple decrease of peaks' intensities (results not shown).

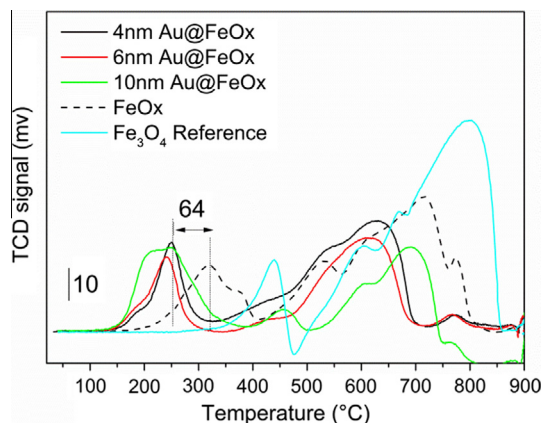
Table 2

Apparent activation energies and turnover frequencies (TOF, calculated at 80 °C) of the CO oxidation reaction over the Au@FeOx dumbbells having different Au domain size. Details about TOF calculation are given in SI.

Catalyst	T range (°C)	Ea (kJ/mol)	TOF (s ⁻¹)
4 nm Au@FeOx	80–140	15 ± 1	0.31
	150–220	28 ± 2	
6 nm Au@FeOx	80–140	14 ± 1	0.17
	150–220	31 ± 2	
10 nm Au@FeOx	80–140	21 ± 1	0.14
	150–220	40 ± 2	

When the dumbbell catalysts were exposed to a reducing atmosphere of 5% v/v H₂ in Ar during the TPR test, the Fe reduction peaks were significantly shifted toward lower temperatures. This suggested the facilitation of Fe reduction in the presence of Au. As an example, for the case of 4 nm Au@FeOx, the first intense peak was shifted by 64 °C toward lower temperatures compared to the FeOx/Al₂O₃ catalyst. A comparable shift was observed for the three dumbbells catalysts tested in our experiments, regardless of the sizes of the Au domain. Nonetheless, for the 10 nm Au@FeOx sample, the shape of the low temperature reduction peak ($T < 400$ °C) was slightly different from that observed for the 4 nm and 6 nm dumbbells. The intensity of the shoulder below 200 °C was indeed much stronger in case of the 10 nm Au@FeOx sample.

Monitoring the adsorption of CO by IR spectroscopy has been reported to be a useful tool to study the charge state of supported Au catalysts [32]. We thus performed CO DRIFTS tests in order to understand whether the difference between the catalytic activity of the dumbbell samples could be the result of a different Au charge state. The spectra were collected during 35 min of exposure to diluted CO mixture in He as described in the Experimental section. The DRIFT spectra in the carbonyl region for dumbbells consisting of 4, 6 and 10 nm Au domains are shown in Fig. 5(a)–(c), respectively. A carbonyl band was detected for all three dumbbell catalysts at the wave number of ~ 2184 cm⁻¹, which then shifted to the lower wave number of 2182 cm⁻¹ by exposure time, in line with the increase of surface coverage [33]. This band was attributed to Au^{δ+}, [32] highlighting thus an electron transfer from the Au domains to the FeOx ones. As a complementary test, monometallic Au catalysts were also checked and a band was observed at lower wave numbers of 2116 (4 nm Au), 2141 (6 nm Au) and 2141 cm⁻¹ (10 nm Au), suggesting that the Au domains were more positively

**Fig. 4.** TPR profiles of 4 nm Au@FeOx (black line), 6 nm Au@FeOx (red line), 10 nm Au@FeOx (green line), FeOx/Al₂O₃ catalyst (black dashed line) and Fe₃O₄ standard (light blue line). The samples were pre-treated at 350 °C for 3 h before exposure to 5% v/v H₂ in Ar. The signal was collected while heating the catalysts from room temperature to 900 °C at a rate of 20 °C/min.

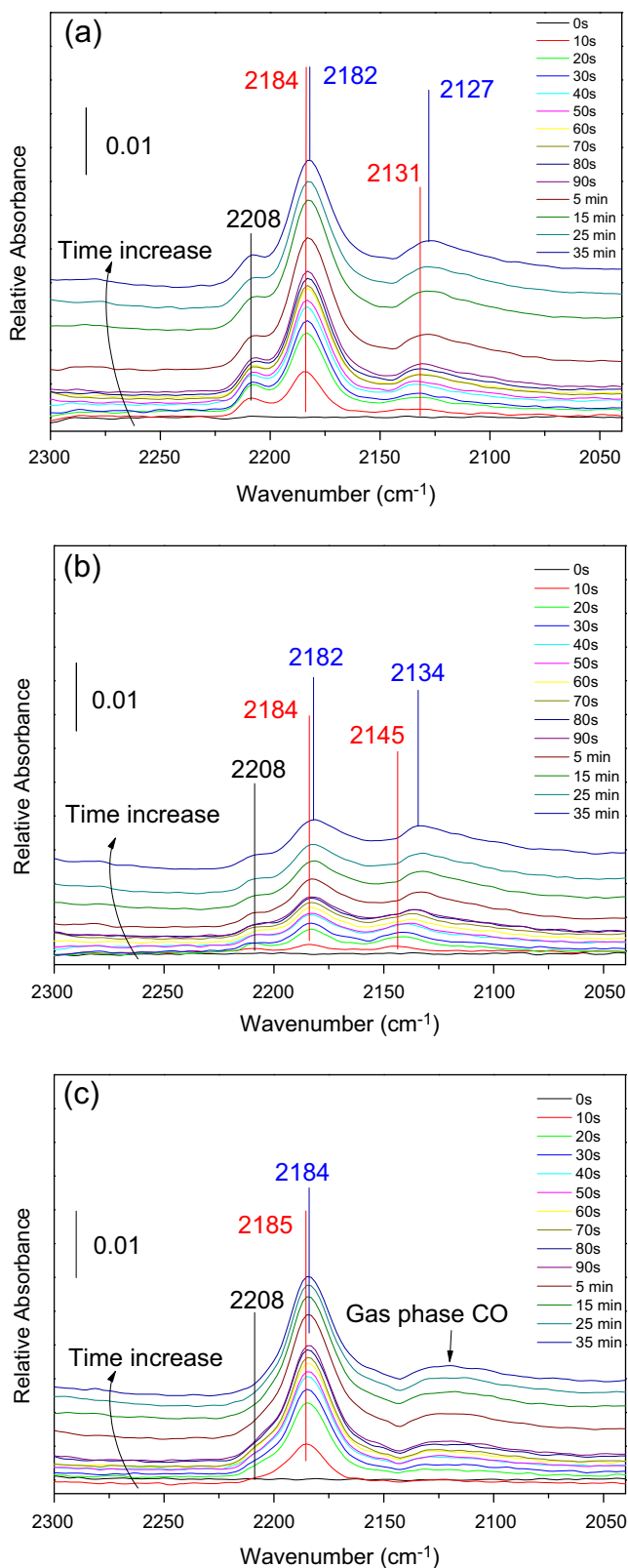


Fig. 5. DRIFTS spectra in the carbonyl region recorded during the adsorption of CO at RT after oxidizing pre-treatment in 6% v/v O₂ in He, at 350 °C for 1 h, (a) 4 nm Au@FeOx (b) 6 nm Au@FeOx and (c) 10 nm Au@FeOx.

charged in case of the dumbbells [32] (see Fig. S10 for details). Another band was detected for the 4 and 6 nm Au@FeOx dumbbells in the wave number range of 2127–2145 cm⁻¹ which suggests that there could be different Au adsorption sites in case of

dumbbell catalysts; some in vicinity of FeOx domain and some only coordinated by Au atoms with different adsorption strengths. Such a band was not detected in case of 10 nm Au@FeOx dumbbells, while a broad band associated with gas-phase CO could be observed.

Another band was detected for the 4 and 6 nm Au@FeOx dumbbells at a wave number of 2208 cm⁻¹ which did not shift throughout the exposure time (Fig. 5a and b). This band was attributed to Fe²⁺ as the formation of carbonyl band on low coordinated Fe²⁺ is reported in the literature [34]. Indeed, the FeOx/Al₂O₃ catalyst was also checked through the same procedure and the only band observed was at 2208 cm⁻¹ (see Fig. S11 for details). It should be noted that for 10 nm Au@FeOx, having the lowest Fe loading, this band was hardly observed. Accumulation of CO in the gas phase was also observed for all tests (i.e. absorption at the wave number of 2125–2145 cm⁻¹). A summary of the band assignments is given in Table 3. To sum up, CO-DRIFTS results showed positively charged gold species on all dumbbell catalysts. However, no significant differences among different Au sizes could be observed.

In addition to DRIFTS measurements, the prepared colloidal dumbbell NCs (not supported on alumina) were further characterized by X-ray Photoelectron Spectroscopy (XPS). The XPS spectra of the dumbbells were compared with those of the Au seeds and of the FeOx NCs. As detailed in SI (Fig. S12 and related discussion), XPS data supported our hypothesis on charge transfer from the Au to the iron oxide domain for all dumbbell samples. Also with this technique, no significant difference as a function of the Au domain size could be observed, in line with the DRIFTS data.

The dumbbell NCs were further analyzed by HRTEM to study the exposure of the Au domain to the surrounding environment. As shown in Fig. 6(a), the Au domain was found to be almost entirely covered by a layer of iron oxide in a considerable fraction of the 4 nm Au@FeOx dumbbell NCs. On the opposite, the Au domain was fully exposed in case of 6 or 10 nm Au@FeOx, as shown in Fig. 6(b) and (c).

Further indirect indication of the exposure of the Au domain to the reacting environment was provided by Iodine (I₂) etching, following the procedure detailed in the Experimental section. This method was already reported by some of us in order to selectively etch the gold domain of Au@FeOx dumbbell like NCs [35]. As shown in Fig. 6(d)–(f), it could be seen that in the case of 6 and 10 nm dumbbells, a limited number of the Au domains were still attached to FeOx, while in the case of the 4 nm Au domain size, most of the metallic domains were still present, as shown also by lower resolution images in Fig. S13. These data highlight that the layer of iron oxide observed by the HRTEM analyses prevented most of the gold domains in the 4 nm Au@FeOx dumbbells from being exposed to the reacting environment and thus taking part in the CO oxidation reaction [36]. The presence of an iron oxide layer covering the metallic domain could be explained considering the synthesis conditions and mechanism. As already proposed in the literature [12,35], a shell of iron oxide is initially formed around the Au seeds at ~200 °C. This initial shell undergoes a transformation when the solution is annealed at 300 °C, which results in the formation of a domain at the edge of the Au particle while the shell is dissolved. When the Au seed is as small as 4 nm, the applied thermal annealing could not effectively and completely push the Au to the edge of the iron oxide domain. Even though we cannot provide a quantitative estimation, the coating of the Au domain in the 4 nm Au@FeOx NCs can justify the measured TOF

Table 3

Summary of the carbonyl bands assignment for CO DRIFT spectra.

Band assignment	Au ^{δ+}	Fe ²⁺	CO in gas phase
Wave number (cm ⁻¹)	2182–2184	2208	2127–2145

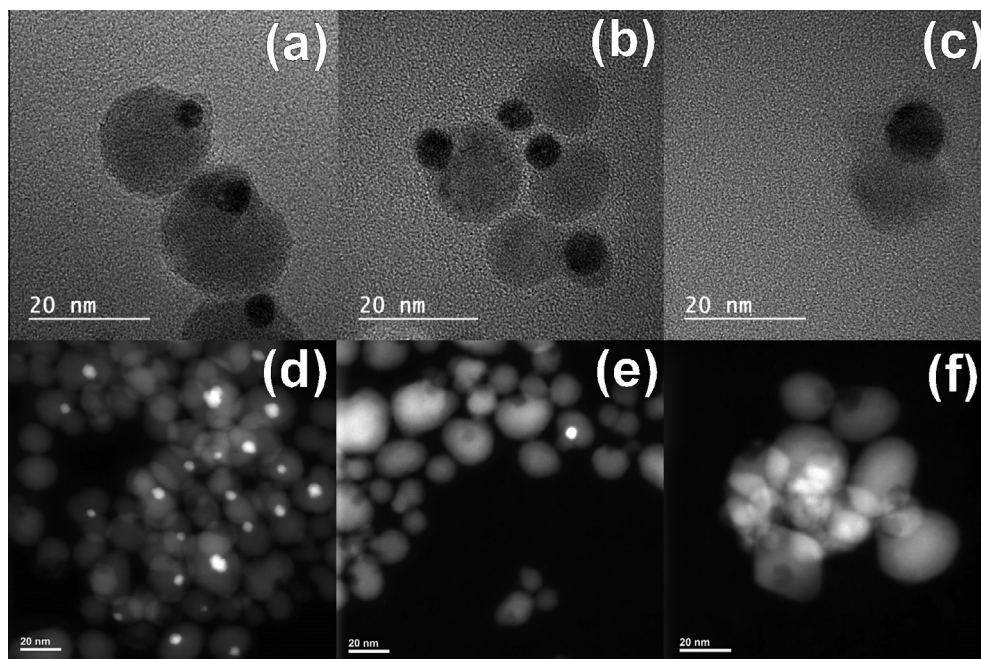


Fig. 6. (a)–(c): HRTEM images of as synthesized Au@FeOx dumbbell-like NCs: (a) 4 nm, (b) 6 nm, (c) 10 nm Au@FeOx. (d)–(f): HAADF-STEM images of Au@FeOx dumbbell-like NCs after I_2 etching treatment for 24 h at 50 °C: (d) 4 nm, (e) 6 nm, and (f) 10 nm Au@FeOx dumbbells.

value, which was significantly lower compared to what reported in the literature.

4. Conclusion

In this work, Au@FeOx dumbbell NCs with different sizes of the Au domain were successfully prepared and further tested as catalytic materials in CO oxidation. Compared to Au/Al₂O₃ catalysts prepared from the same gold seeds, dumbbell-like Au@FeOx NCs featured better performances in CO oxidation, highlighting a synergy between the Au and the FeOx domain in the dumbbell structure. Independently from the size of the Au domain, a hysteresis was observed between the heating and cooling phases of the transient activity tests: such a phenomenon was attributed to the accumulation of carbonate species at low temperature during the heating phase of the experiment. The different size of the gold domain resulted in different catalytic activity toward CO oxidation. In line with literature reports on Au catalyzed CO oxidation, the dumbbell catalyst with the smallest Au domain size (i.e. 4 nm) showed the highest activity. We studied the charge transfer between the Au and the FeOx domain, the effect of Au presence on the reducibility of the FeOx domain and the effective exposure of the Au surface to the reacting environment for all dumbbell catalysts. The different Au size did not result in significant differences neither of charge transfer nor of iron oxide reducibility. On the other hand, we found out that in case of the smallest Au size (i.e. 4 nm), a significant fraction of the Au domains were actually covered by an iron oxide layer, while for the 6 and 10 nm Au@FeOx dumbbells the Au domains were clearly exposed to the reacting environment. We therefore concluded that in case of 4 nm Au@FeOx dumbbells, the limited exposure of the Au surface and thus of the Au–iron oxide interface to the reacting environment prevented the full exploitation of the oxidation capability of the dumbbells catalyst. The present work provides useful insights into the correlation between the physicochemical properties of the Au@FeOx dumbbell structures and their catalytic function. The results presented herein could therefore help the rational design

of metal@metal-oxide dumbbell like heterodimers and their application in heterogeneous catalytic processes.

Acknowledgments

The authors acknowledge financial support from the European Union through the EU-ITN network Mag(net)icFun (PITNGA-2012-290248) and from the Italian FIRB grant “Ossidi Nanostrutturati” (contract #RBAP115AYN). P.G. acknowledges the People Program (Marie Curie Actions) of the FP7/2007-2013 European Union Program (TECNIOspring grant agreement no. 600388) and the Agency for Business Competitiveness of the Government of Catalonia, ACCIÓ.

Appendix A. Supplementary material

Supplementary data associated with this article can be found, in the online version, at <http://dx.doi.org/10.1016/j.jcat.2016.03.002>.

References

- [1] G.C. Bond, P.A. Sermon, G. Webb, D.A. Buchanan, P.B. Wells, Hydrogenation over supported gold catalysts, *J. Chem. Soc., Chem. Commun.* (1973) 444–445.
- [2] M. Haruta, N. Yamada, T. Kobayashi, S. Iijima, Gold catalysts prepared by coprecipitation for low-temperature oxidation of hydrogen and of carbon monoxide, *J. Catal.* 115 (1989) 301–309.
- [3] T. Takei, T. Akita, I. Nakamura, T. Fujitani, M. Okumura, K. Okazaki, J. Huang, T. Ishida, M. Haruta, Chapter one – heterogeneous catalysis by gold, in: C.G. Bruce, C.J. Friederike (Eds.), *Advances in Catalysis*, Academic Press, 2012, pp. 1–126.
- [4] G.J. Hutchings, M. Haruta, A golden age of catalysis: a perspective, *Appl. Catal. A* 291 (2005) 2–5.
- [5] A.S.K. Hashmi, G.J. Hutchings, Gold catalysis, *Angew. Chem. Int. Ed.* 45 (2006) 7896–7936.
- [6] G.J. Hutchings, Catalysis by gold, *Catal. Today* 100 (2005) 55–61.
- [7] R.J.H. Grisel, B.E. Nieuwenhuys, A comparative study of the oxidation of CO and CH₄ over Au/MOx/Al₂O₃ catalysts, *Catal. Today* 64 (2001) 69–81.
- [8] M. Haruta, S. Tsubota, T. Kobayashi, H. Kageyama, M.J. Genet, B. Delmon, Low-temperature oxidation of CO over gold supported on TiO₂, α -Fe₂O₃, and Co₃O₄, *J. Catal.* 144 (1993) 175–192.

- [9] M. Valden, X. Lai, D.W. Goodman, Onset of catalytic activity of gold clusters on Titania with the appearance of nonmetallic properties, *Science* 281 (1998) 1647–1650.
- [10] N. Lopez, T.V.W. Janssens, B.S. Clausen, Y. Xu, M. Mavrikakis, T. Bligaard, J.K. Nørskov, On the origin of the catalytic activity of gold nanoparticles for low-temperature CO oxidation, *J. Catal.* 223 (2004) 232–235.
- [11] H.-Y. Lin, Y.-W. Chen, Low-temperature CO oxidation on Au/FexOy catalysts, *Ind. Eng. Chem. Res.* 44 (2005) 4569–4576.
- [12] H. Yu, M. Chen, P.M. Rice, S.X. Wang, R.L. White, S. Sun, Dumbbell-like Bifunctional Au–Fe₃O₄ nanoparticles, *Nano Lett.* 5 (2005) 379–382.
- [13] Y. Sheng, J. Xue, Synthesis and properties of Au–Fe₃O₄ heterostructured nanoparticles, *J. Colloid Interface Sci.* 374 (2012) 96–101.
- [14] S. Carrettin, M.C. Blanco, A. Corma, A.S.K. Hashmi, Heterogeneous gold-catalysed synthesis of phenols, *Adv. Synth. Catal.* 348 (2006) 1283–1288.
- [15] C. Wang, H. Yin, S. Dai, S. Sun, A general approach to noble metal–metal oxide dumbbell nanoparticles and their catalytic application for CO oxidation, *Chem. Mater.* 22 (2010) 3277–3282.
- [16] C. George, A. Genovese, A. Casu, M. Prato, M. Povia, L. Manna, T. Montanari, CO Oxidation on colloidal Au_{0.80}Pd_{0.20}–FexOy dumbbell nanocrystals, *Nano Lett.* 13 (2013) 752–757.
- [17] J. Zhao, H. Liu, S. Ye, Y. Cui, N. Xue, L. Peng, X. Guo, W. Ding, Half-encapsulated Au nanoparticles by nano iron oxide: promoted performance of the aerobic oxidation of 1-phenylethanol, *Nanoscale* 5 (2013) 9546–9552.
- [18] B. Wu, H. Zhang, C. Chen, S. Lin, N. Zheng, Interfacial activation of catalytically inert Au (6.7 nm)-Fe₃O₄ dumbbell nanoparticles for CO oxidation, *Nano Res.* 2 (2010) 975–983.
- [19] N. Ta, J. Liu, S. Chenna, P.A. Crozier, Y. Li, A. Chen, W. Shen, Stabilized gold nanoparticles on ceria nanorods by strong interfacial anchoring, *J. Am. Chem. Soc.* 134 (2012) 20585–20588.
- [20] X. Liu, M.-H. Liu, Y.-C. Luo, C.-Y. Mou, S.D. Lin, H. Cheng, J.-M. Chen, J.-F. Lee, T.-S. Lin, Strong metal-support interactions between gold nanoparticles and ZnO nanorods in CO oxidation, *J. Am. Chem. Soc.* 134 (2012) 10251–10258.
- [21] S. Peng, Y. Lee, C. Wang, H. Yin, S. Dai, S. Sun, A facile synthesis of monodisperse Au nanoparticles and their catalysis of CO oxidation, *Nano Res.* 1 (2008) 229–234.
- [22] Z. Ma, S. Dai, Design of novel structured gold nanocatalysts, *ACS Catal.* 1 (2011) 805–818.
- [23] J. Saavedra, C. Powell, B. Panthi, C.J. Pursell, B.D. Chandler, CO oxidation over Au/TiO₂ catalyst: pretreatment effects, catalyst deactivation, and carbonates production, *J. Catal.* 307 (2013) 37–47.
- [24] B. Aejjelts Averink Silberova, G. Mul, M. Makkee, J.A. Moulijn, DRIFTS study of the water–gas shift reaction over Au/Fe₂O₃, *J. Catal.* 243 (2006) 171–182.
- [25] M. Haruta, Size- and support-dependency in the catalysis of gold, *Catal. Today* 36 (1997) 153–166.
- [26] M. Haruta, When gold is not noble: catalysis by nanoparticles, *Chem. Rec.* 3 (2003) 75–87.
- [27] U. Oran, D. Uner, Mechanisms of CO oxidation reaction and effect of chlorine ions on the CO oxidation reaction over Pt/CeO₂ and Pt/CeO₂/γ-Al₂O₃ catalysts, *Appl. Catal. B* 54 (2004) 183–191.
- [28] M.M. Schubert, S. Hackenberg, A.C. van Veen, M. Muhler, V. Plzak, R.J. Behm, CO Oxidation over supported gold catalysts—“Inert” and “Active” support materials and their role for the oxygen supply during reaction, *J. Catal.* 197 (2001) 113–122.
- [29] Y. Guo, D. Gu, Z. Jin, P.-P. Du, R. Si, J. Tao, W.-Q. Xu, Y.-Y. Huang, S. Senanayake, Q.-S. Song, C.-J. Jia, F. Schuth, Uniform 2 nm gold nanoparticles supported on iron oxides as active catalysts for CO oxidation reaction: structure-activity relationship, *Nanoscale* 7 (2015) 4920–4928.
- [30] A. Sárkány, Z. Schay, K. Frey, É. Széles, I. Sajó, Some features of acetylene hydrogenation on Au–iron oxide catalyst, *Appl. Catal. A: Gener.* 380 (2010) 133–141.
- [31] J. Huang, W.-L. Dai, K. Fan, Remarkable support crystal phase effect in Au/FeOx catalyzed oxidation of 1,4-butanediol to γ-butyrolactone, *J. Catal.* 266 (2009) 228–235.
- [32] M. Mihaylov, H. Knözinger, K. Hadjiivanov, B.C. Gates, Characterization of the oxidation states of supported gold species by IR spectroscopy of adsorbed CO, *Chem. Ing. Tech.* 79 (2007) 795–806.
- [33] J.C. Clark, S. Dai, S.H. Overbury, Operando studies of desorption, reaction and carbonate formation during CO oxidation by Au/TiO₂ catalysts, *Catal. Today* 126 (2007) 135–142.
- [34] S.A. Jimenez-Lam, Z. Martinez-Ramirez, I.A. Santos-López, B.E. Handy, M.G. Cárdenas-Galindo, J.C. Fierro-Gonzalez, Role of iron carbonyls in the inhibition of oxygen activation for the oxidation of CO catalyzed by iron oxide-supported gold, *ChemPhysChem* 13 (2012) 4173–4179.
- [35] C. George, D. Dorfs, G. Bertoni, A. Falqui, A. Genovese, T. Pellegrino, A. Roig, A. Quarta, R. Comparelli, M.L. Curri, R. Cingolani, L. Manna, A cast-mold approach to iron oxide and Pt/iron oxide nanocontainers and nanoparticles with a reactive concave surface, *J. Am. Chem. Soc.* 133 (2011) 2205–2217.
- [36] T. Yan, D.W. Redman, W.-Y. Yu, D.W. Flaherty, J.A. Rodriguez, C.B. Mullins, CO oxidation on inverse Fe₂O₃/Au(111) model catalysts, *J. Catal.* 294 (2012) 216–222.

Supporting Information

The effect of Au domain size on the CO oxidation catalytic activity of colloidal Au-FeOx dumbbell-like heterodimers

Sharif Najafshirtari^a, Pablo Guardia^{a,b}, Alice Scarpellini^a, Mirko Prato^a, Sergio Marras^a, Liberato Manna^a, Massimo Colombo^{a}*

a) Department of Nanochemistry, Istituto Italiano di Tecnologia, Via Morego 30, 16163, Genova, Italy

b) Centro de Tecnologia Quimica de Catalunya, Carrer de Marcel·lí Domingo s/n, 43007 Tarragona, Spain

massimo.colombo@iit.it (corresponding author email)

Keywords: CO oxidation, heterodimers, nanocatalyst, gold nanoparticles, dumbbell, iron oxide

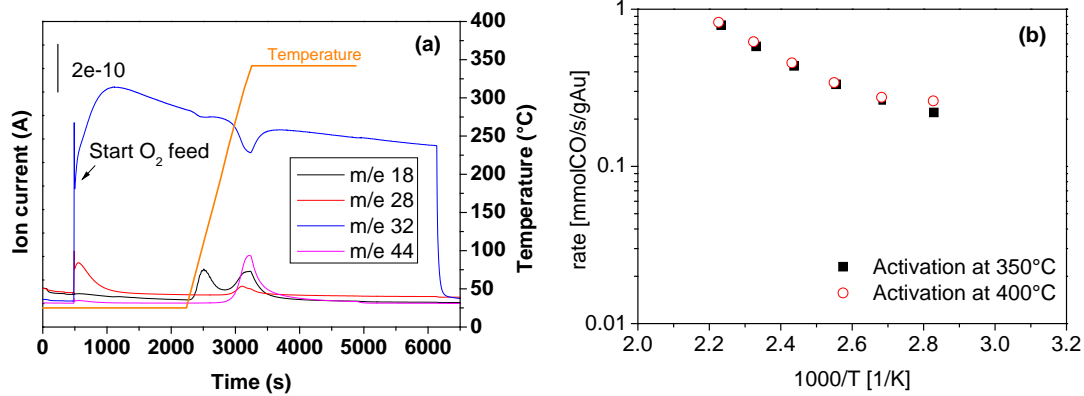


Figure S1. a) Time evolution of Mass Spectrometer (MS) signals at reactor outlet during the in-situ activation procedure. b) Comparison of CO oxidation rate after pre-treatment at 350 °C and 400 °C for the 4 nm Au@FeOx dumbbell sample.

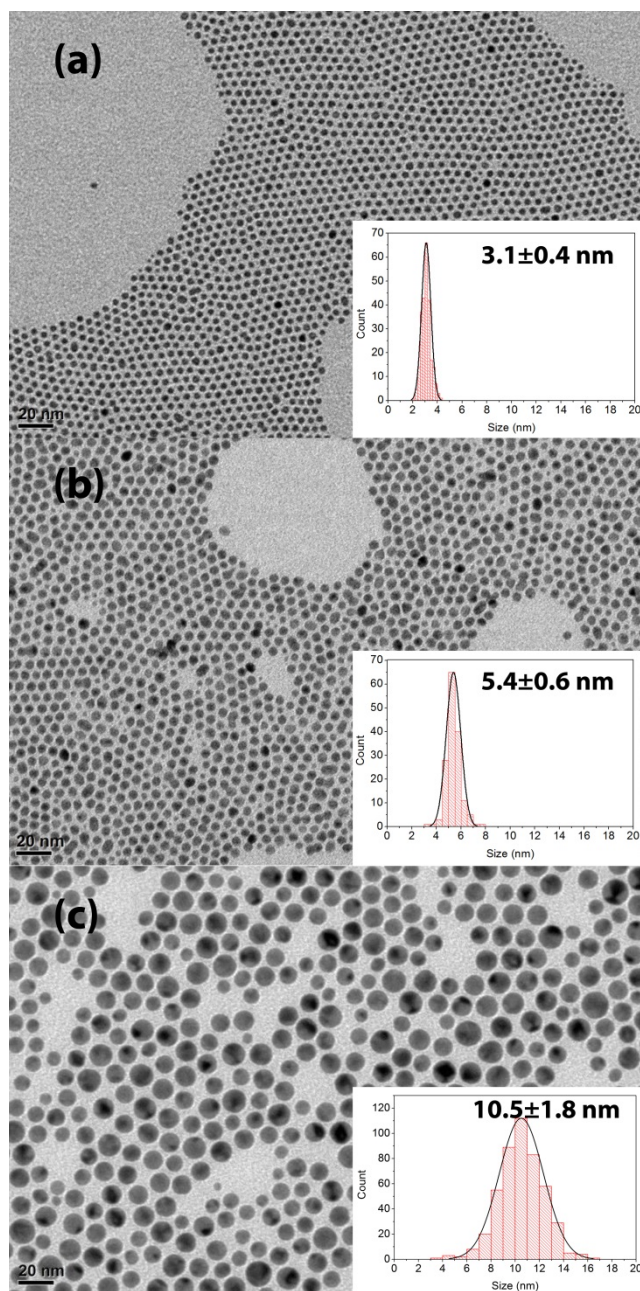


Figure S2. Typical BFTEM image of the colloidal Au NCs having different sizes of (a) 3.1 nm (b) 5.4 nm and (c) 10.5 nm with their corresponding size distribution profiles as insets.

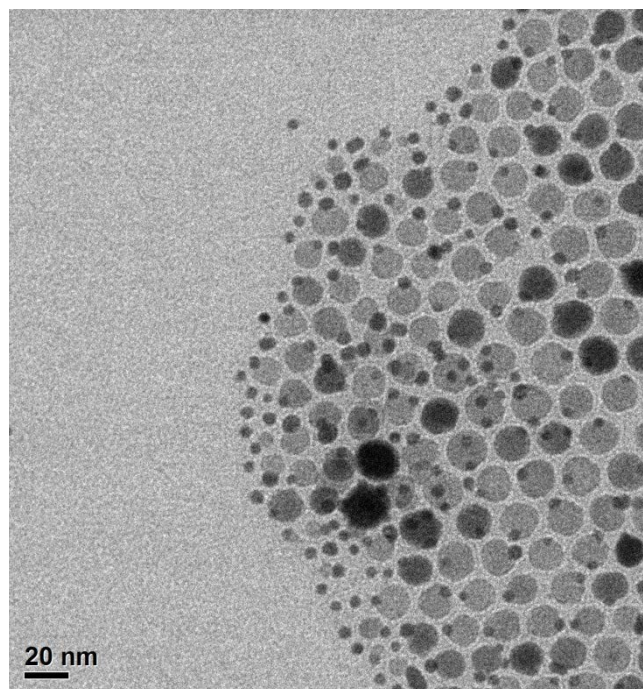


Figure S3. Typical BFTEM image of a Au@FeOx sample synthesized from 3.1 nm Au seeds using a lower Fe/Au ratio.

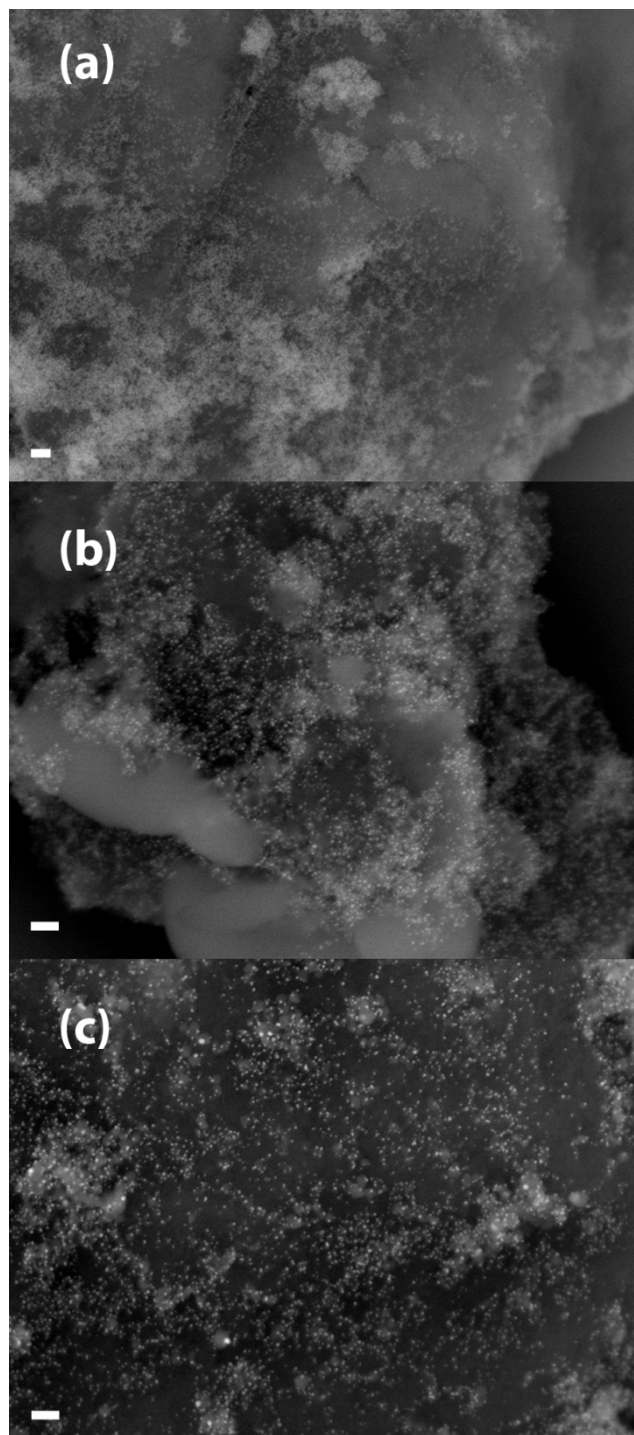


Figure S4. BSE-HRSEM images of the dumbbell catalysts after calcination (a) 4 nm Au@FeOx, (b) 6 nm Au@FeOx and (c) 10 nm Au@FeOx; scale bar is 100 nm. The brighter dots correspond to the Au domains.

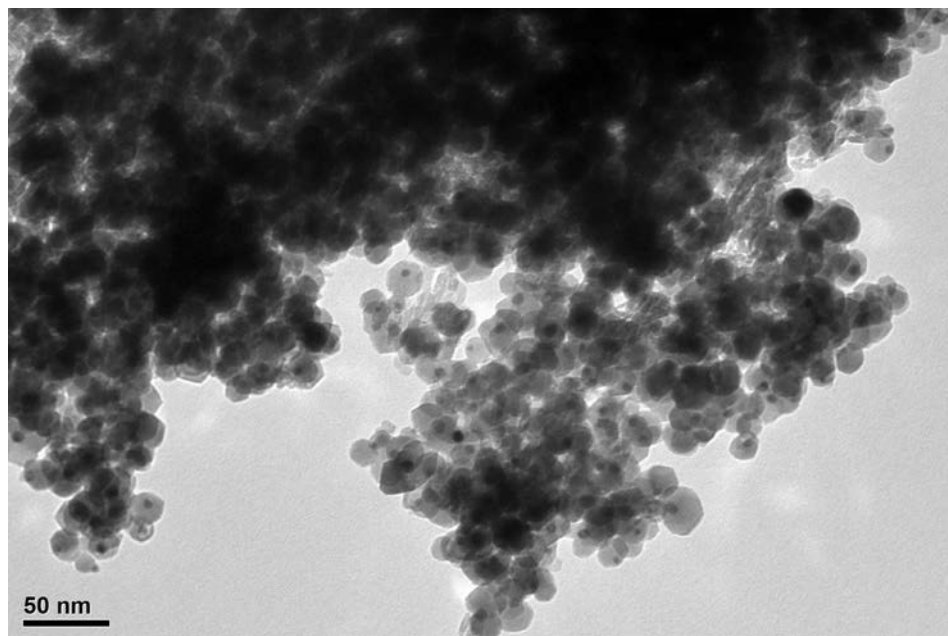


Figure S5. BFTEM images of the 4 nm Au@FeOx dumbbell catalyst after activation.

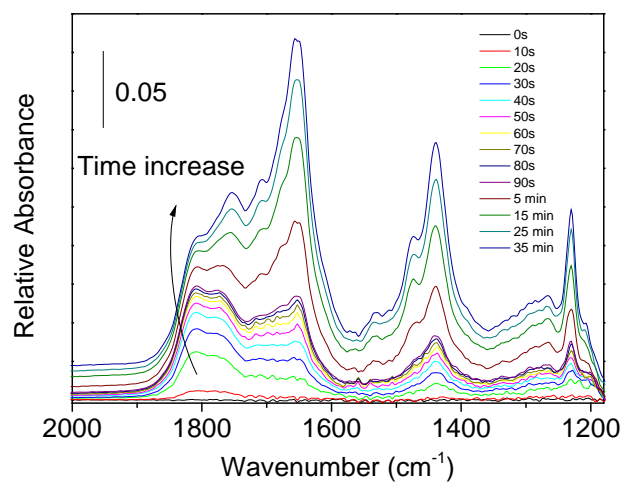


Figure S6. DRIFTS spectra in the carbonates region recorded during the exposure at RT to a 1% v/v CO, 6% v/v /O₂ (balance He) atmosphere. Before recording the spectra the sample was subject to an oxidizing pre-treatment in 6% v/v O₂ in He, at 350 °C for 1 h.

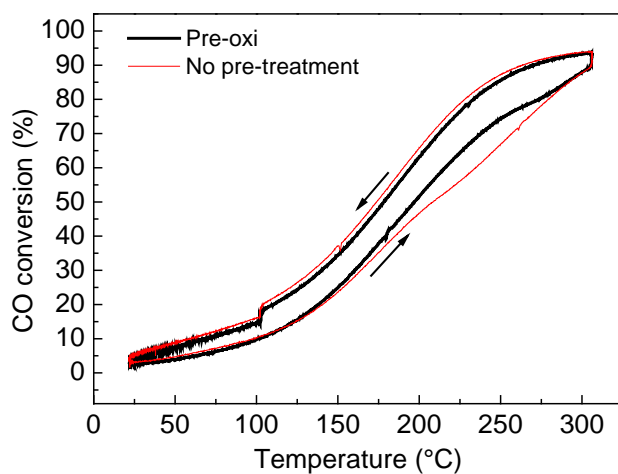


Figure S7. Catalytic activity of 4 nm Au@FeOx dumbbells. Black thick solid line: before the catalytic test the sample was exposed to an oxidizing pre-treatment in 6% v/v O₂ in He, at 350 °C for 1 h. Red thin line: the catalytic test was performed after cooling the sample to room temperature in reaction atmosphere. No further pre-treatment was performed before the catalytic test. GHSV = 2.4E+7 Ncc/h/(g Au). Arrows indicate the heating-up and cooling-down procedure.

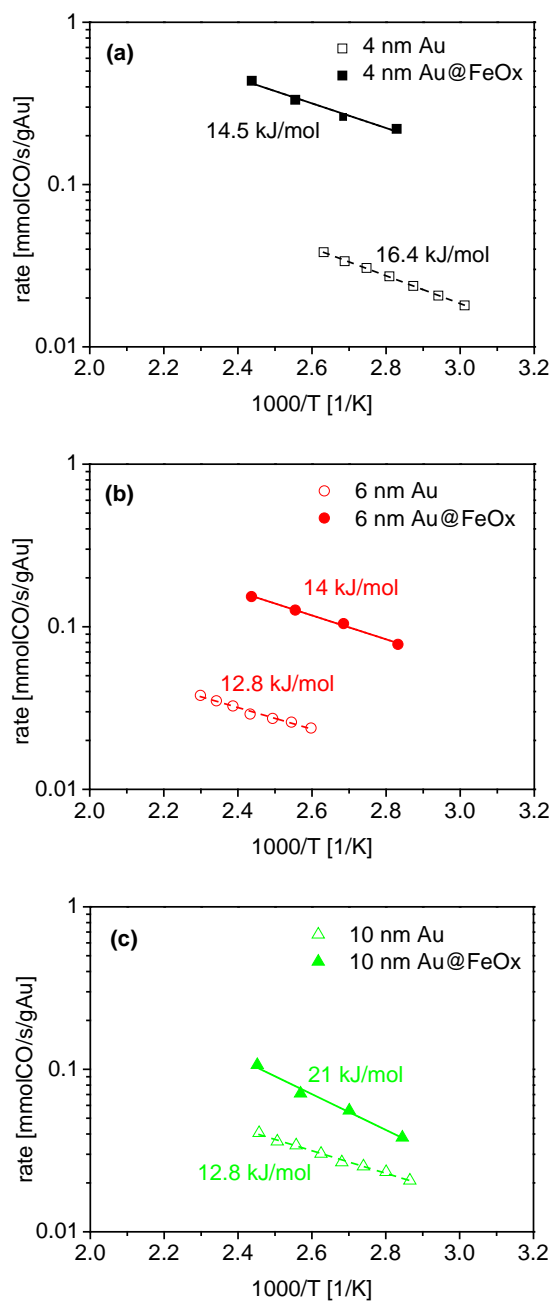


Figure S8. Comparison of the CO oxidation rate of the alumina supported Au@FeOx dumbbell and Au catalysts. (a) 4 nm Au@FeOx Vs. 4 nm Au, (b) 6 nm Au@FeOx Vs. 6 nm Au and (c) 10 nm Au@FeOx Vs. 10 nm Au.

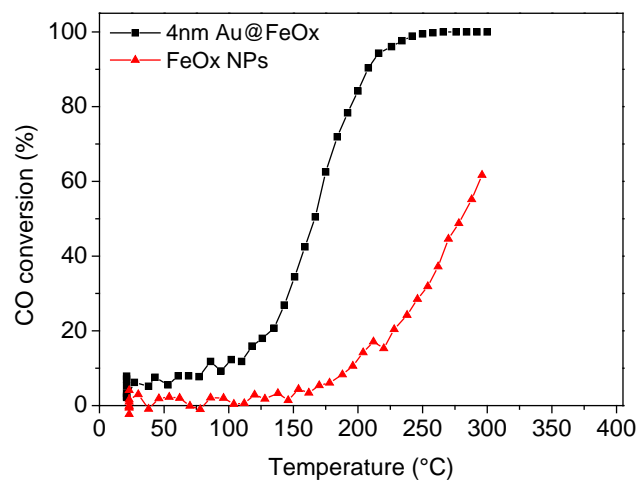


Figure S9. Comparison of the CO conversion of alumina supported 4 nm Au@FeOx dumbbell and 8 wt. % FeOx catalyst. GHSV = $3\text{E}+4$ Ncc/h/(g Cat)

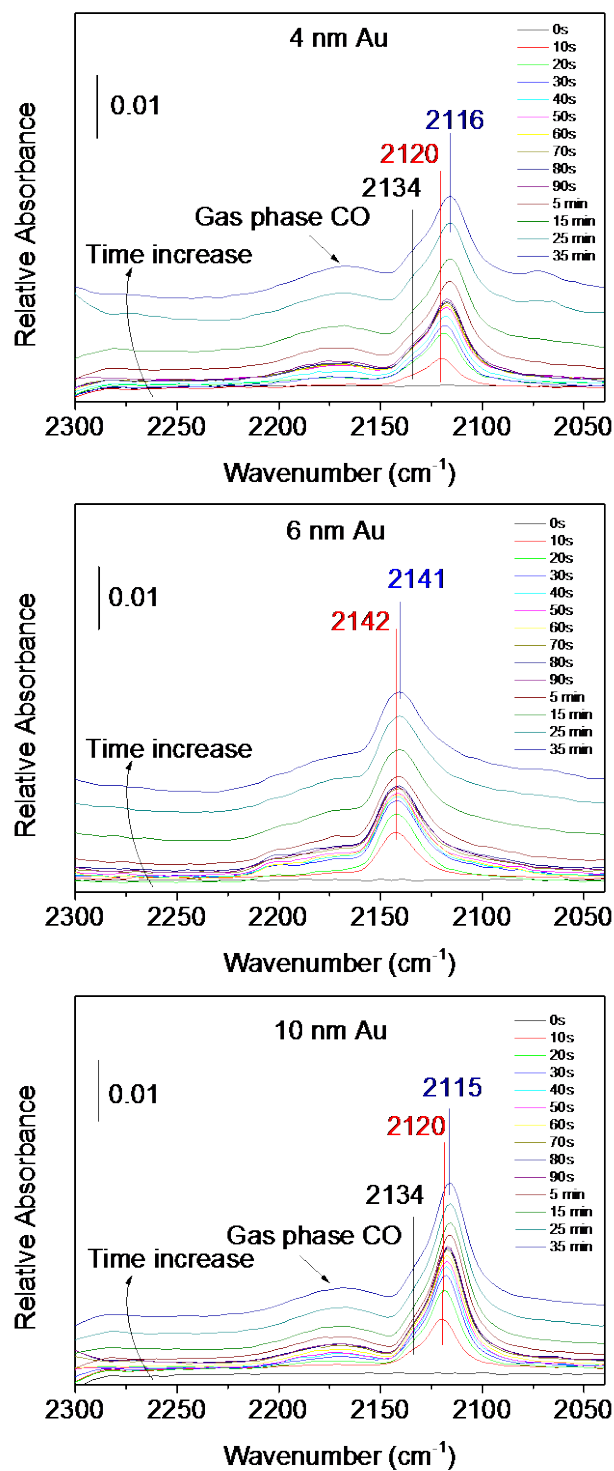


Figure S10. DRIFTS spectra in the carbonyl region obtained during the adsorption of CO at room temperature on alumina supported 1 wt.% Au catalysts after oxidizing pre-treatment in 6% v/v O₂ in He, at 350 °C for 1 h.

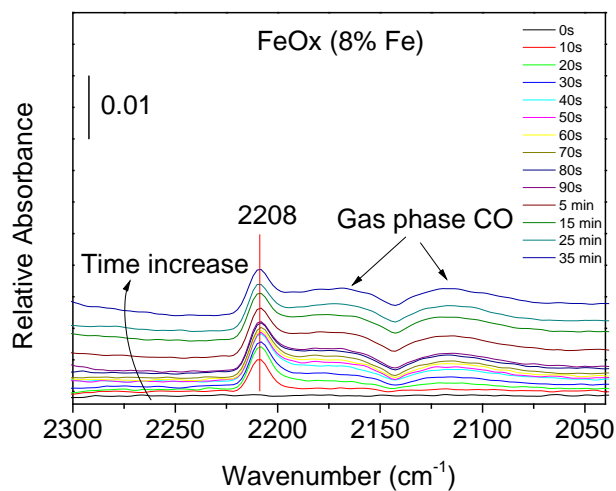


Figure S11. DRIFTS spectra in the carbonyl region obtained during the adsorption of CO at room temperature on alumina supported FeOx catalyst (8 wt.% Fe) after oxidizing pre-treatment in 6% v/v O₂ in He, at 350 °C for 1 h.

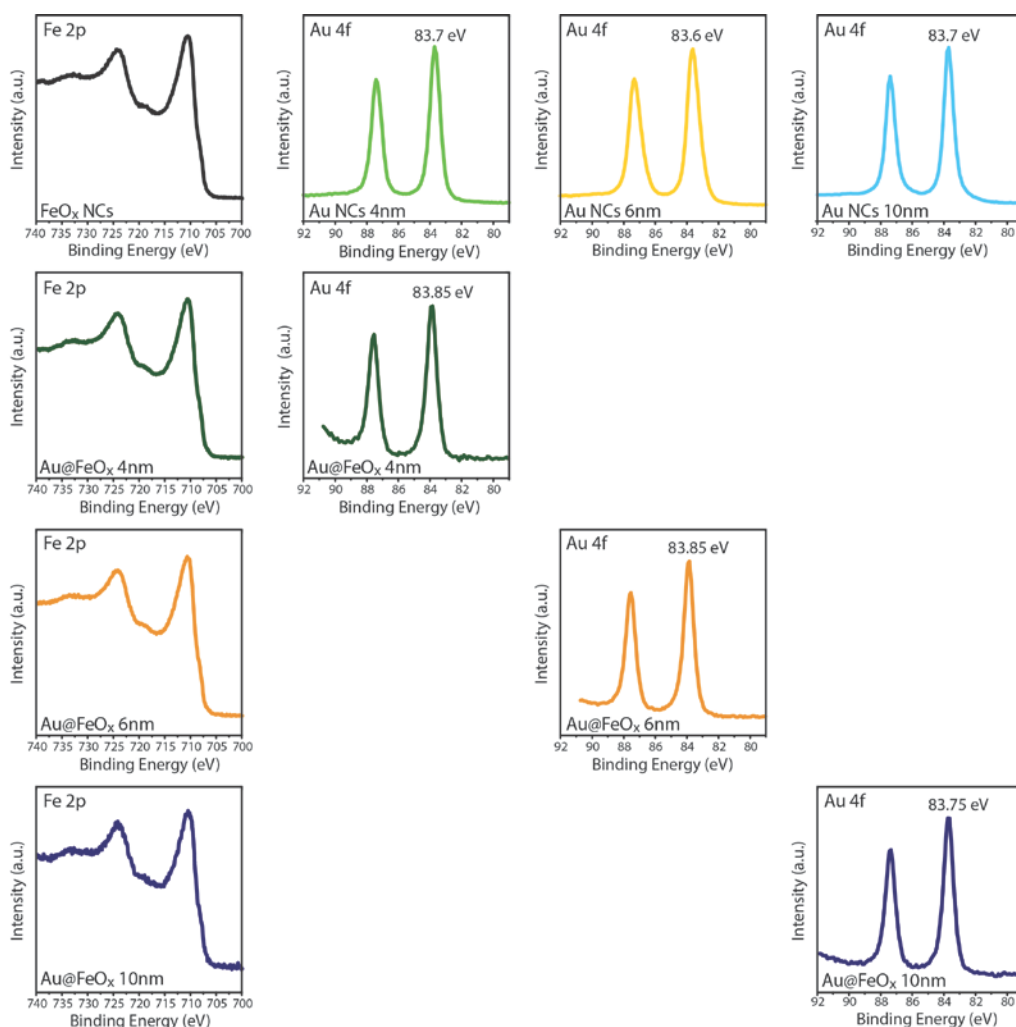


Figure S12. Comparison of Fe 2p and Au 4f XPS spectra collected on not-supported Au@FeO_x dumbbells, Au seeds and FeO_x NCs.

In the first row of the Figure S9, the Fe 2p and Au 4f core level XPS spectra for FeO_x NCs and Au NCs of different sizes are represented. Au 4f_{7/2} component was observed at binding energy values of 83.6-83.7 (± 0.2) eV for all sizes of Au, corresponding to the presence of metallic Au [1]. Fe 2p profile instead is indicative of the presence of Fe³⁺ in the sample, since the main peak – satellite distance is approx. 8 eV [2]. The presence of a shoulder at 708 eV suggests that Fe⁰ could also be present in the sample, likely in the core of the FeO_x domain, since the samples have been exposed to air. By

comparison, the XPS spectra collected on the dumbbells show an almost unchanged Fe 2p profile and a tiny shift to higher binding energy of the Au 4f peaks, suggesting that there is electron transfer from the Au domain to the FeO_x domain [3]. The shift towards higher binding energy was slightly more pronounced for 6 nm Au@FeO_x compared to the other dumbbells.

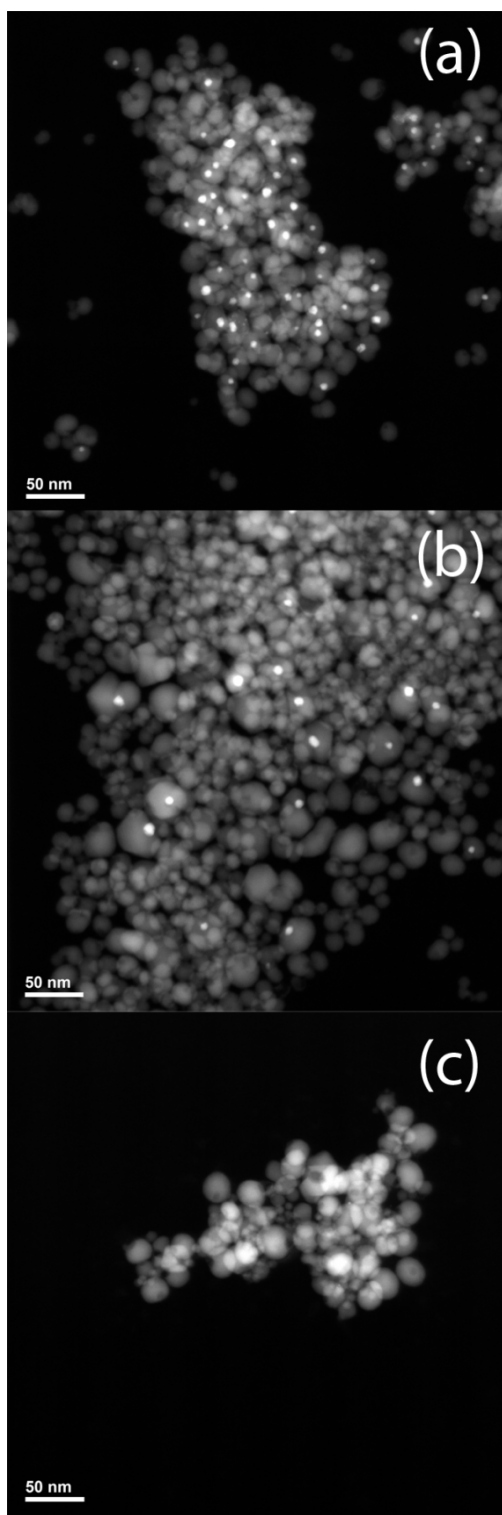


Figure S13. HAADF-STEM images of the Au leached dimers, (a) 4 nm (b) 6 nm and (c) 10 nm Au@FeOx dimer samples. The sample were treated with Iodine in hexane solution for 24 h.

Evaluation of Turn over Frequency (TOF):

We report the rate of reaction as:

$$\frac{molCO_2\text{produced}}{s} = \frac{CO_{\text{feed}} (N_{cc}/\text{min}) \cdot CO_{\text{conversion}}}{60 (s/\text{min}) \cdot 22.414 (cc/mol)}$$

We assumed spherical gold NPs and considered that only half of the sphere was exposed to the reacting atmosphere (i.e. half of the sphere is embedded in the iron oxide domain). The content of gold was measured by ICP. We consider bulk gold density and the area occupied by surface gold atoms to be $1.9 \text{ E-}5 \text{ mol/m}^2$ [4]. TOF was thus calculated as:

$$TOF = \frac{molCO_2\text{produced}}{s} \cdot \frac{1}{molAu}$$

REFERENCES

- [1] Shen, C.; Hui, C.; Yang, T.; Xiao, C.; Tian, J.; Bao, L.; Chen, S.; Ding, H.; Gao, H., *Chem. Mater.* **2008**, *20*, 6939-6944.
- [2] Grosvenor, A. P.; Kobe, B. A.; Biesinger, M. C.; McIntyre, N. S., *Surf. Interface Anal.* **2004**, *36*, 1564-1574.
- [3] Lin, F.-h.; Doong, R.-a., *J. Colloid Interface Sci.* **2014**, *417*, 325-332.
- [4] Güttel, R.; Paul, M.; Galeano, C.; Schüth, F., *J. Catal.* **2012**, *289*, 100-104

Chapter III¹

Nanoscale Transformations of Alumina-Supported AuCu Ordered Phase Nanocrystals and Their Activity in CO Oxidation²

¹ TEM and EDS measurements were done by R. Brescia; SEM and XRD by S. Marras; All other activities including experimental, results interpretation and manuscript preparation were performed by S. Najafshirvari under supervision of P. Guardia (for synthesis) and M. Colombo (for all characterizations, catalytic experiments, and results interpretation) and L. Manna (for manuscript preparation).

² Reprinted with permission from S. Najafshirvari et al., ACS Catal., 2015, 5 (4), pp 2154–2163. Copyright (2015) American Chemical Society.

Nanoscale Transformations of Alumina-Supported AuCu Ordered Phase Nanocrystals and Their Activity in CO Oxidation

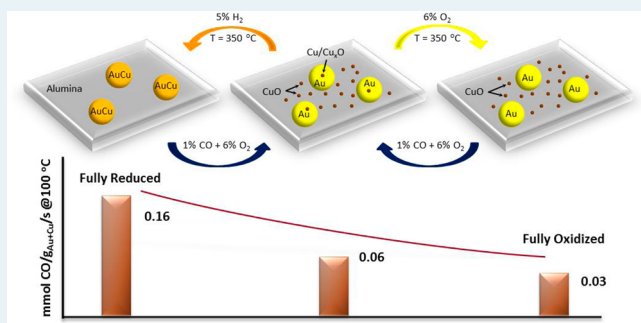
Sharif Najafshirtari, Rosaria Brescia, Pablo Guardia,[†] Sergio Marras, Liberato Manna,* and Massimo Colombo*

Department of Nanochemistry, Istituto Italiano di Tecnologia, Via Morego 30, 16163 Genova, Italy

Supporting Information

ABSTRACT: In this work we applied colloidal preparation methods to synthesize AuCu nanocrystals (NCs) in the ordered tetragonal phase with an atomic composition close to 50:50. We deposited the NCs on a support (Al_2O_3), studied their transformations upon different redox treatments, and evaluated their catalytic activity in the CO oxidation reaction. The combined analyses by energy dispersive X-ray spectroscopy (EDX)-scanning transmission electron microscopy (STEM), selected area electron diffraction (SAED), and in situ diffuse reflectance infrared Fourier transform spectroscopy (DRIFTS) highlighted a phase segregation between gold and copper upon the high-temperature (350 °C) oxidizing treatment. While gold remained localized in the NCs, copper was finely dispersed on the support, likely in the form of oxide clusters. AuCu alloyed NCs, this time in the form of solid solution, face-centered cubic phase, were then restored upon a reducing treatment at the same temperature, and their catalytic activity was significantly enhanced in comparison to that of the oxidized system. The composition of the NCs and consequently the CO oxidation reaction rate were also affected by the CO/O_2 reacting atmosphere: regardless of the pretreatment, the same catalytic activity was approached over time on stream at temperatures as low as 100 °C. Consistently, the same situation was observed on the catalyst surface as probed by EDX-STEM, SAED, and DRIFTS. All of these transformations were found to be fully reversible.

KEYWORDS: AuCu, bimetallic nanocrystals, nanoalloy, CO oxidation, DRIFTS



1. INTRODUCTION

Bimetallic nanocrystals (NCs) have caught researchers' attention in catalysis over the past decade.¹ While conventional preparation methods have been extensively applied to provide bimetallic catalysts with enhanced performances, the use of NCs in catalyst preparation offers the additional possibility to finely tune the size and the composition of the metallic active sites and to exploit synergetic effects between different metals.^{1a} Such a synergy is usually the result of electronic or structural modifications of the active sites arising from interactions among metals (such as alloying) at the nanoscale, which can eventually result in a material with enhanced catalytic properties.^{1c} Bimetallic catalysts composed of Au and a secondary metal are among the most widely studied materials in heterogeneous catalysis, with particular interest in CO oxidation.² The presence of a base metal such as Ag, Ni, Co, or $\text{Cu}^{2a,3}$ can indeed facilitate electron transfer to oxygen molecules while maintaining good CO adsorption capacity in comparison to monometallic Au and thus enhancing the catalytic activity.^{3f} As an example, catalysts based on Au–Cu alloys have been reported to be promising and effective in low-temperature CO oxidation, as they exhibit higher activity and resistance against sintering in comparison to monometallic Au catalysts.^{3a,b,d,4} On the other hand, the effect of redox treatments on bimetallic

AuCu catalysts and the resulting changes in the catalytic activity toward CO oxidation are still debated in the scientific literature, and conflicting results have been reported.

Liu et al.^{4b} prepared a Au–Cu/SBA-15 catalyst by means of consecutive reduction of Au and Cu precursors and studied the structural changes of the prepared catalyst in different conditions. They reported that, when Cu was in the form of an oxide and was attached to the Au NCs as a layer or patches of CuO, the catalyst was highly active in the CO oxidation. In contrast, the catalyst was inactive when Cu in the metallic state was alloyed with Au. The effectiveness of Cu oxide species in the bimetallic Au–Cu catalyst used in oxidation reactions has been reported in other works as well.^{3d,e,4a,b,5} Mozer et al.^{3c} studied the effect of Cu loading on the CO oxidation activity of an alumina-supported Au catalyst prepared by deposition–precipitation. The authors showed that there was a correlation between activity and Cu loading. While low amounts of copper were beneficial for the CO oxidation activity, high copper contents caused blocking of the Au active sites, thus decreasing the catalytic activity. Sandoval et al.^{3d} prepared a Au–Cu/ TiO_2

Received: December 2, 2014

Revised: February 6, 2015

catalyst by sequential deposition–precipitation and studied the effect of the Au/Cu ratio and of the activation treatment. They reported the highest activity in CO oxidation for the catalyst with a Au:Cu ratio of 1:0.9 after activation in air at 300 °C and attributed the high activity to the formation of an Au/CuO/TiO₂ structure. Bauer and co-workers⁵ studied the effect of different pretreatments on the CO oxidation activity of AuCu catalysts formed by reduction and diffusion of Cu into Au NCs already supported on silica. They observed that the activity of ordered AuCu alloy NCs, formed by reducing the catalyst under an H₂ atmosphere, was negligible at room temperature but started increasing when the temperature reached the level at which the segregation of Cu and the formation of amorphous Cu oxide occurred. Consistently, a much higher CO oxidation activity was observed when the sample was pretreated in O₂ at high temperatures.

A different scenario was described by Yin et al.,⁶ who thoroughly investigated the properties of AuCu alloyed NCs synthesized by both wet chemical methods and nanoscale alloying. They reported the activity of such NCs supported on carbon and silica in the CO oxidation. The catalyst with a Au₅₁Cu₄₉ composition, supported on C, was more active when exposed to a reducing treatment than to an oxidizing one, although for copper-rich NCs (Au₁₁Cu₈₉/C), the difference was not as significant. They claimed that the formation of a large number of surface oxygenated Cu species after the oxidizing pretreatment blocked the surface of Au NCs, thus inhibiting the CO oxidation. They did not observe phase segregation between Au and Cu.

Most of the reports mentioned above referred to AuCu catalysts that were obtained according to conventional preparation methods: for example, coprecipitation or coimpregnation. Although these methods are relatively simple and scalable, their main drawback is that they are often characterized by a poor control over NCs size and composition. Considering the complex transformations that nanoalloys undergo upon activation treatments and catalysis, a strong heterogeneity of the synthesized material can yield drastically different results. In order to overcome this limitation, in this work we followed colloidal preparation methods to synthesize size-tunable AuCu NCs of well-defined composition (Scheme 1 left, center left, and center right sketches). Colloidal synthesis indeed allowed the fine tuning of the NC size, shape, and composition at a level which is typically not achievable with classical catalyst preparation methods.⁷ By means of colloidal

deposition we effectively prepared an alumina-supported catalyst and studied the effect of different activation treatments on catalyst morphology, composition, and CO oxidation catalytic activity (Scheme 1, right image).

The exposure at high temperature (350 °C) to an oxidizing environment caused a phase segregation between gold and copper, which was found to be detrimental for the CO oxidation reaction. On the other hand, AuCu alloyed NCs were restored when the catalyst was exposed to a reducing environment and the catalytic activity was then significantly enhanced. The CO/O₂ reacting atmosphere also caused changes in the NC composition and consequently in the reaction rate: for a reduced system the catalytic activity progressively decreased with time on stream, as a consequence of Cu dealloying and of partial migration on the support surface. On the other hand, when starting from a fully oxidized situation, the reaction environment caused a partial realloying of Cu, which in turn resulted in the progressive increase of the catalyst activity. All of these transformations were found to be fully reversible.

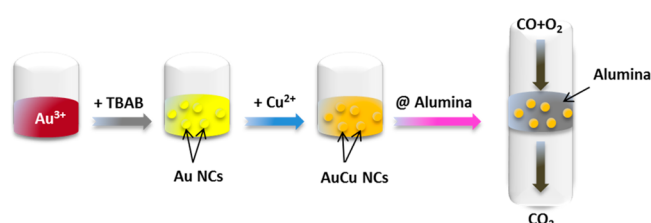
2. RESULTS

2.1. Characterization of the as-Synthesized AuCu NCs.

Colloidal Au NCs were prepared by fast reduction of Au³⁺ at room temperature⁸ and were kept suspended in hexane (see the Experimental Section). The uniformity of the as-synthesized NCs was verified by transmission electron microscopy (TEM, see Figure S1 in the Supporting Information). The size distribution was obtained by statistical size measurement including 450 particles (see the inset of Figure S1), which yielded an average particle size of 3.1 ± 0.4 nm, confirming a monodispersed size distribution, considering the criterion of having $\sigma \leq 15\%$.⁹ These NCs were further used to prepare the AuCu NCs (atomic Au:Cu = 50:50) through a seed-based diffusion mechanism:¹⁰ according to Chen et al.,¹⁰ Cu²⁺ ions were reduced to highly active Cu⁰ atoms or clusters by a mild reducing agent, i.e. oleylamine (OAm), and reacted with the surface of Au NCs. The Cu atoms diffused then from the surface of the Au NCs to their interior, resulting in the formation of a AuCu solid solution. OAm acted also as a stabilizing agent.¹¹ The size distribution of the as-synthesized AuCu NCs was estimated in a manner similar to that for the Au seeds, by measuring the sizes of 450 particles (Figure 1). Having a mean size of 6.1 ± 1.0 nm, it was concluded that the size distribution was narrow, according to the criterion of $\sigma \leq 20\%$.⁹ Elemental mapping by means of scanning TEM-energy-dispersive X-ray spectroscopy (STEM-EDX) over several NCs indicated a homogeneous distribution of Au and Cu within each NC (see Figure 1e–h).

The composition of the alloy NCs was quantitatively analyzed by inductively coupled plasma atomic emission spectroscopy (ICP-AES) and scanning electron microscopy (SEM)-EDX: the first technique gave an atomic Au:Cu ratio of 53:47, while the second technique gave a ratio of 48:52 (see Figure S2 in the Supporting Information). Both values were close to the desired target of Au:Cu = 50:50. The ratio between the amount of copper in the final product and the amount of copper in the precursors was around 95%, thus highlighting the high yield of the applied synthesis protocol. X-ray diffraction patterns collected from the NCs (Figure 1d) were in agreement with a body-centered-tetragonal structure, corresponding to an ordered AuCu alloy, which was previously reported for Au:Cu atomic ratios of around 1.^{10,12} SAED patterns collected from

Scheme 1. Sketch of Seeded Growth Protocol for AuCu Colloidal NC Synthesis, Preparation of the Catalyst, and CO Oxidation Catalytic Tests: (Left) Reduction of the Starting Au³⁺ Precursor in Solution To Form (Center Left) Au NCs and Addition of a Cu²⁺ Precursor Leading to (Center Right) the Formation of AuCu NCs, Which Are Then Mixed with Alumina Grains To Prepare (Right) the Final Catalyst for the CO Oxidation Reaction



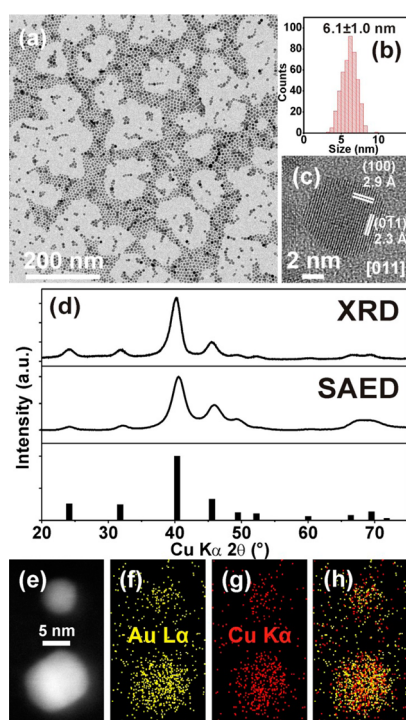


Figure 1. (a) Typical bright-field (BF)-TEM image of the as-prepared AuCu colloidal NCs. (b) Size distribution histogram obtained by measuring 450 NCs. (c) High-resolution TEM (HRTEM) image of a single AuCu NC matching with the [011] zone axis of tetragonal AuCu (JCPDS No. 01-071-5024). (d) X-ray diffraction (XRD) and azimuthally integrated, background-subtracted, selected area electron diffraction (SAED) pattern of as-prepared AuCu alloy NCs. Experimental data are compared with the database powder XRD pattern for tetragonal AuCu (JCPDS No. 01-071-5024). (e–h) High-angle annular dark field-scanning TEM (HAADF-STEM) image and corresponding quantitative EDX maps (intensity proportional to atomic percent) for Au and Cu, showing homogeneous distribution of the two elements for NCs in the starting colloidal sample. The noise observed outside the NCs is caused by irradiation-induced carbon contamination, caused by the presence of residual organics.

areas including hundreds of NCs of the same sample agree with the XRD results (Figure 1d). On the basis of the results of structural characterization, it can be additionally concluded that NC sintering must have occurred during the AuCu synthesis, likely during the annealing step at 280 °C, which is essential to obtain an ordered AuCu alloy, as demonstrated by Chen et al.¹⁰ In the absence of NC sintering, the starting Au NCs with an average size of 3.1 nm would indeed evolve to ~3.7 nm AuCu NCs and not to 6.1 nm, as measured for the synthesized AuCu NCs (see the Supporting Information for additional details on calculations). Further evidence of alloy formation was provided by comparison of the visible light absorption spectra of the Au and AuCu NCs, shown in Figure S3 in the Supporting Information. Consistent with alloy formation, the plasmon peak of Au at 520 nm was shifted toward the plasmon peak of Cu at 561 nm by about 27 nm in the case of the AuCu (atomic Au:Cu = 50:50) alloy NCs, in line with what has been reported in the literature.^{10,13}

2.2. Catalytic Activity Results. To evaluate the catalytic activity of the synthesized AuCu NCs in the CO oxidation, the NCs were deposited on γ -Al₂O₃ and exposed to different activation treatments prior to catalytic tests, following the procedures described in detail in the Experimental Section. The

transient activity of 1 wt % AuCu/Al₂O₃ catalyst in CO oxidation for three runs, each of them performed after the oxidizing pretreatment, is shown in Figure 2a. On investigation

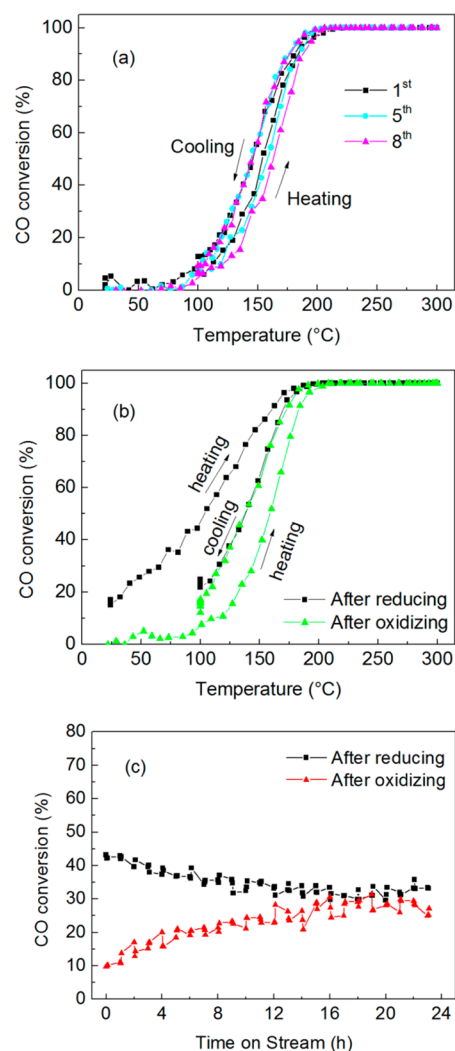


Figure 2. Catalytic activity data for the 1 wt % AuCu/Al₂O₃ catalyst in CO oxidation: (a) catalytic activity during three reaction cycles (first, fifth, and eighth) after the oxidizing pretreatment; (b) catalytic activity after oxidizing and reducing pretreatments; (c) steady-state activity data at a constant temperature of 100 °C after oxidizing and reducing pretreatments. Conditions: CO 1% v/v; O₂ 6% v/v; GHSV = 3000000 Ncc/(h (g of AuCu)).

of the black square dots (first test after the initial activation procedure described in the Experimental Section), it can be noted that, during the heating phase of the experiments, the catalyst was almost inactive at low temperature and then the conversion gradually increased with temperature and reached 100% at a temperature of ~200 °C. During the cooling phase of the test, the catalytic activity decreased with temperature, resulting in a small but evident hysteresis, so that the activity at a given temperature during the cooling phase was higher than that in the heating phase. Figure 2a reports the first, fifth, and eighth reaction cycles performed after the oxidizing pretreatment on the same catalyst batch. A comparison among the three curves provides useful information about the stability of the catalyst with time on stream and about the effectiveness of the oxidizing pretreatments to restore the same surface

situation after the catalytic tests. Indeed, the catalyst was initially activated under an oxidizing atmosphere after being loaded in the reactor, and then various series of tests were performed, exposing the catalyst to different pretreatments, i.e. oxidizing and reducing without any specific order, always followed by a reaction cycle. Regardless of the history of the sample, the activity toward CO oxidation after oxidizing pretreatment was extremely stable and reproducible, as supported by the data displayed in Figure 2a. Moreover, we observed a clear indication of synergy between Au and Cu by comparing the alumina-supported AuCu catalyst against a monometallic Au/Al₂O₃ catalyst (see Figure S4 in the Supporting Information). Even though we employed smaller Au NCs, which should be more active in CO oxidation, the synergy between Au and Cu led to a superior performance for the 6 nm AuCu NCs catalyst, especially at temperatures above 100 °C.

When the catalyst was pretreated according to the reducing protocol described in the Experimental Section, the catalytic activity in CO oxidation dramatically changed (Figure 2b). The sample exhibited about 15% conversion already at room temperature, corresponding to a significantly higher activity in comparison with that observed after the oxidizing pretreatment. The CO conversion then increased with temperature, approaching 100% at about 200 °C. During the following cooling phase of the test, the reduced sample exhibited a lower activity in comparison to the heating transient, resulting in a reverse hysteresis in comparison to the same sample after the oxidizing pretreatment. Interestingly, the catalytic activities during the cooling transients of both reduced and oxidized catalysts converged. When the sample was then heated again in a second reaction cycle without any further pretreatment, the catalytic activity in CO oxidation almost overlapped with that of the prior cooling transient (see Figure S5 in the Supporting Information), thus resulting in a performance closer to that observed after an oxidizing pretreatment.

In addition to the transient tests, the catalyst was also tested in CO oxidation at a constant temperature of 100 °C for 24 h (Figure 2c). The catalyst lost ~25% of its initial activity when the test followed the reducing pretreatment, approaching a conversion value of ~30% after 24 h of time on stream. The oxidized catalyst instead gained activity during 24 h of exposure to CO/O₂ atmosphere, eventually approaching the same conversion value as the reduced catalyst after 24 h.

To benchmark the catalytic activity of the prepared sample, we evaluated the initial CO oxidation rate at 25 °C after reducing pretreatment. As shown in Table 1, the synthesized

Table 1. Comparison of CO Oxidation Rates for AuCu Catalysts

catalyst	temp (°C)	CO oxidation rate (mol of CO/(g _{Au} /h))	source
AuCu/Al ₂ O ₃	25	0.30	this work
AuCu/TiO ₂	20	0.27	ref 3d
AuCu/SiO ₂	25	0.43	ref 3a

catalyst sample, when pretreated according to the reducing protocol, exhibited a CO oxidation rate which was comparable to those reported for AuCu/TiO₂^{3d} and AuCu/SiO₂^{3a} catalysts under similar conditions.

2.3. Characterization of the AuCu/Al₂O₃ Catalyst. In order to shed light on the catalytic activity changes observed

upon the applied pretreatments, as well as upon exposure to reaction atmosphere, we characterized the AuCu/Al₂O₃ catalyst by means of TEM and CO/NO adsorption in situ diffuse reflectance infrared Fourier transform spectroscopy (DRIFTS) at three different stages: namely, after oxidation pretreatment, after reducing pretreatment, and after a reaction cycle. Overview STEM-HAADF images of the catalyst in the three mentioned conditions are reported in Figure S6 in the Supporting Information. For the three conditions, we observed a homogeneous distribution of the NCs on the surface of the alumina grains, with no evident differences in the NC sizes for the different treatments. Despite the presence of few larger particles, highlighted by the asymmetric size distribution reported in Figure S6d–f, we can conclude that the initial size distribution of the NCs was essentially preserved. Additionally, the extremely stable catalytic activity measured during the entire catalyst testing period indirectly proved the absence of significant sintering phenomena with time on stream, in line with what has already been reported in the literature on the effect of Cu in increasing the stability and sintering resistance of AuCu catalysts.^{3a–d,4a}

Furthermore, the transformations of the AuCu NCs were followed locally after oxidizing or reducing pretreatments and after one cycle of reaction by STEM-EDX (see Figure 3a–c). After oxidizing activation, Au was localized within the NCs while a diffuse signal from Cu was observed over all of the alumina support. This result is in contrast with the speculation of Sandoval et al.^{3d} about the migration of Cu atoms and the

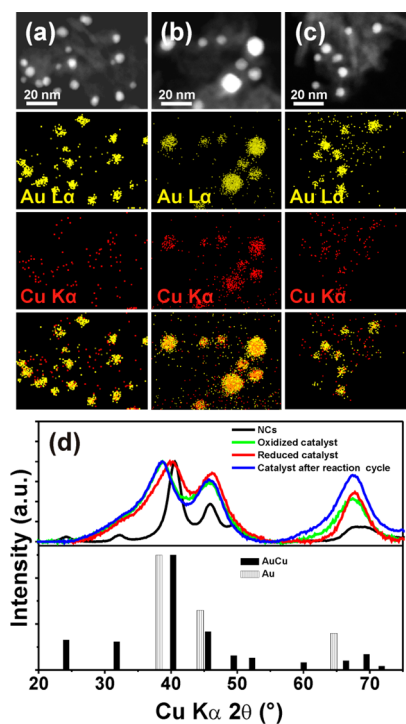


Figure 3. HAADF-STEM images and corresponding quantitative EDX maps (intensity proportional to atomic percent) for Au and Cu after (a) oxidizing pretreatment, (b) reducing pretreatment, and (c) reaction cycle. (d) Azimuthally integrated, background-subtracted SAED patterns of the 1 wt % AuCu/Al₂O₃ catalyst after oxidation, after reduction, and after one cycle of reaction, in comparison to AuCu colloidal NCs. The experimental patterns are compared to database powder XRD patterns for Au (JCPDS No. 00-004-0784) and AuCu (JCPDS No. 01-071-5024).

following formation and accumulation of Cu oxide under the Au particles after such oxidizing treatment. In contrast, both Au and Cu are localized within the particles after the reducing pretreatment, with a weak Cu signal detected on the support. After one cycle of reaction, an intermediate condition was observed, with Au clearly localized within the NCs and a slightly higher concentration of Cu within the NCs with respect to the support.

XRD analyses of the catalyst at the three different stages did not lead to conclusive results on the accompanying structural transformations involving the NCs, due to the proximity of the high-intensity peaks from γ - Al_2O_3 to the significant features from the metallic NCs and to the low volume fraction of the latter species (see Figure S7 in the Supporting Information). Because of its local character, SAED could instead follow the structural transformations for alumina grains characterized by a relatively high NC loading, albeit with a resolution and precision lower than those of XRD. SAED analyses of the catalyst in the three different stages, in comparison with the pattern obtained on the parent colloidal NCs, are reported in Figure 3d. After oxidizing activation, the diffraction peak positions matched those of Au, while after the following reducing pretreatment a cell contraction was observed. The comparison with the pattern obtained from the parent colloidal particles showed that the initial order of the AuCu tetragonal phase was lost at this stage, while the reduction treatment led to bimetallic NCs in a less ordered solid solution phase (face-centered cubic (fcc) structure), with about 46 atomic % Cu. Within the precision of SAED, no significant differences were observed in the patterns between the catalyst after the oxidizing treatment and after one cycle of reaction, suggesting that in the latter case the Cu atoms were not incorporated in the fcc structure of the Au NCs.

While TEM characterization provided useful information on the evolution of NC composition and structure upon the different treatments, DRIFTS tests were performed to track the evolution of metal oxidation states on the same samples. To do this, we selected two probe molecules, CO and NO, and studied their interaction with the catalyst surface. CO has indeed been reported to form carbonyl species on $\text{Au}^{\delta+}$, Au^0 , Cu^0 , and Cu^+ ,¹⁴ while NO forms stable nitrosyl species selectively on Cu^{2+} .^{14a} Figure 4a,b shows respectively the IR spectra in the carbonyl region after 10 s and 42 min of exposure to the carbon monoxide mixture at room temperature (for the same sample pretreated under either an oxidizing or a reducing atmosphere), while Figure 4c reports the IR spectra in the same region after 40 min of purging at room temperature under a He atmosphere. As can be seen, after 10 s of exposure (Figure 4a), the reduced sample exhibited a main peak at 2130 cm^{-1} with a shoulder at 2102 cm^{-1} , while the oxidized sample had only one peak at the bigger wavenumber of 2137 cm^{-1} . Considering that Cu^{2+} does not form carbonyl species at room temperature, the only band observed at 2137 cm^{-1} over the oxidized sample can be reasonably assigned to $\text{Au}^{\delta+}$ -CO species.¹⁵ This assignment was confirmed by performing CO adsorption on the monometallic Au/ Al_2O_3 catalyst (see Figure S9a in the Supporting Information): a band was observed at 2142 cm^{-1} on the oxidized Au catalyst, in line with what was observed over the oxidized AuCu/ Al_2O_3 catalyst. For the latter sample, the presence of Cu^+ carbonyl species was ruled out by monitoring the desorption phase of the experiment: Cu^+ is indeed reported to form carbonyl species that are stable at room temperature upon evacuation in the 2122 – 2132 cm^{-1} region.^{3d,14a,b} After 40

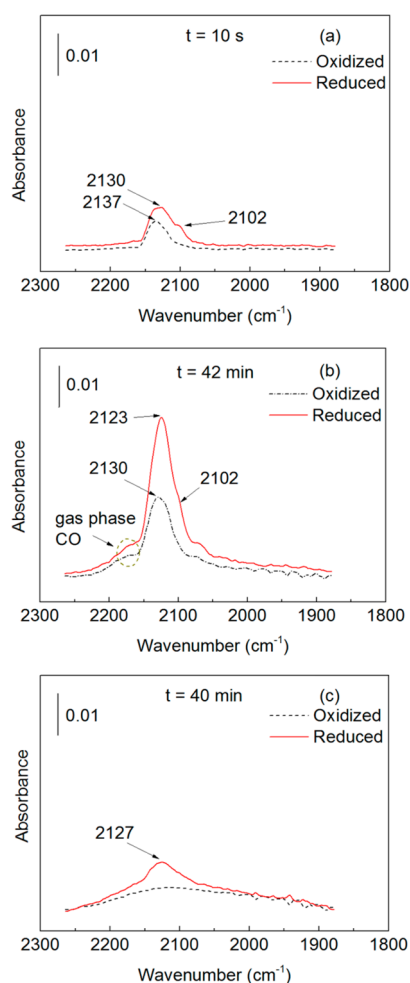


Figure 4. DRIFTS spectra in the carbonyl region recorded during the adsorption (a, b) and desorption (c) of CO at room temperature on the 1 wt % AuCu/ Al_2O_3 catalyst. The sample was either oxidized (black dashed curves) or reduced (red curves) prior to the test. Spectra were taken after (a) 10 s and (b) 42 min of exposure to the probe gas (0.2% v/v CO, balance He) and after (c) 40 min of purging under a He atmosphere.

min of purging in He, no residual carbonyl band could be observed, as shown in Figure 4c, indicating the absence of any Cu^+ species.

When the monometallic Au/ Al_2O_3 catalyst underwent the reducing pretreatment, the following CO adsorption test resulted in the shift of the carbonyl band to 2116 cm^{-1} (see Figure S9b in the Supporting Information), in line with the shift reported in the literature from $\text{Au}^{\delta+}$ to Au^0 .^{3d,15} The shoulder at 2102 cm^{-1} on the reduced AuCu/ Al_2O_3 catalyst can thus be attributed to Au^0 , while the bands at 2130 and 2123 cm^{-1} in the case of the reduced catalyst can be assigned to Cu^+ or Cu^0 , as they are both known to form carbonyl species at room temperature between 2122 and 2132 cm^{-1} .^{14a,c,16} The dominant presence of Cu^0 is supported by SAED, which proves AuCu alloy formation. However, the presence of residual Cu^+ species was confirmed by monitoring the desorption phase of the experiment: as reported in Figure 4c, the reduced sample showed a residual carbonyl band even after 40 min of purging at room temperature, consistent with the formation of stable Cu^+ carbonyls.^{14a} The reduced sample also exhibited higher intensities for the carbonyl bands, which can be a qualitative

indication of higher capacity of the reduced sample for CO adsorption.

A comparison between the initial absorption after 10 s of exposure (Figure 4a) with the final absorption after 42 min (Figure 4b) indicates that, regardless of the type of pretreatment, the main peaks were slightly shifted to lower wavenumber by $\sim 8\text{--}10\text{ cm}^{-1}$, while the intensities of carbonyl species increased. Both trends are consistent with the increase of CO surface coverage with exposure time. The accumulation of CO in the gas phase is also evident by observing the evolution of the absorption at $\sim 2170\text{ cm}^{-1}$.

NO adsorption at room temperature was studied to detect the presence of Cu^{2+} on the surface of the catalyst after different pretreatments. The formation of nitrosyl species was monitored following the evolution of IR spectra in the $1800\text{--}2250\text{ cm}^{-1}$ range during 42 min of exposure to 650 ppm of NO in He. After 10 s of exposure, the absorption spectrum of the reduced catalyst (Figure 5a) was still almost flat, indicating no

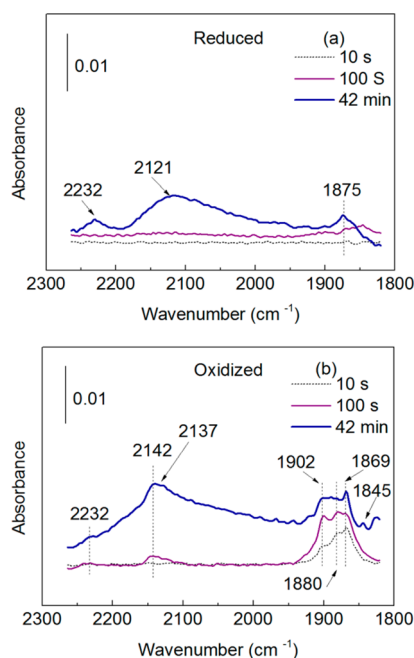


Figure 5. DRIFTS spectra in the nitrosyl region obtained during the adsorption of NO at room temperature on the 1 wt % AuCu/ Al_2O_3 catalyst. Spectra were taken after 10 s, 100 s, and 42 min of exposure to the probe gas on the same sample that was either reduced (a) or oxidized (b) prior to the test. Probe gas composition: 650 ppm of NO, balance He.

adsorbed NO species and thus no Cu^{2+} on the catalyst surface. This is line with the reduction of Cu species inferred from the TPR test (see Figure S8 in the Supporting Information). However, after prolonged exposure to the NO stream, three main bands centered at around 1875, 2121, and 2232 cm^{-1} appeared. The first band can be assigned to Cu^{2+} nitrosyl species^{14a} and the second and the third bands to the formation of respectively NO^+ and N_2O adsorbed on the alumina surface.^{14a,17} The formation of these species is consistent with the presence of NO_2 contamination in the NO stream. Such a contamination likely arises from the disproportionation reaction of NO ($3\text{NO} \leftrightarrow \text{N}_2\text{O} + \text{NO}_2$), which leads to the formation of N_2O and NO_2 (with the latter known to be a strong oxidizing agent) and which justifies the formation of

Cu^{2+} nitrosyl species.^{14a,18} NO DRIFTS on monometallic Au/ Al_2O_3 catalyst (see Figure S10 in the Supporting Information) evidenced the same broad band at 2121 cm^{-1} for both oxidized and reduced catalysts, in line with the presence of NO_2 contamination, while no nitrosyl formation was detected on the same sample.

A different scenario was observed when the oxidized catalyst was exposed to NO. Figure 5b indeed shows several peaks in the region of $1910\text{--}1840\text{ cm}^{-1}$ already after 10 s of exposure to NO, indicating the formation of different Cu^{2+} nitrosyl species.^{14a,18b} With longer exposure time, the intensity of the nitrosyl bands increased, accompanied by the formation of new features at around 2140 and 2232 cm^{-1} . In line with the assignments on the prereduced sample, these bands are assigned respectively to NO^+ and N_2O species.^{14a,18b} The absence of nitrosyl species on Au was verified by means of a control experiment as specified above.

IR spectra were also taken after a CO oxidation reaction cycle, which was performed following an oxidizing or reducing pretreatment. Spectra of CO adsorption at room temperature after 100 s of exposure to the probe stream are shown in Figure 6. The oxidized and reduced catalysts after a CO oxidation

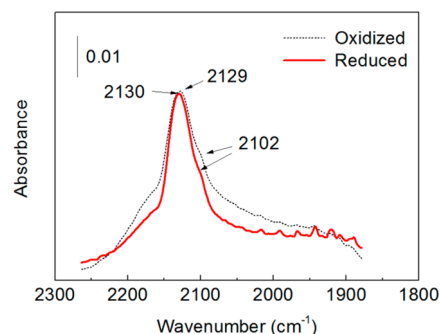


Figure 6. DRIFTS spectra in the carbonyl region obtained during the adsorption of CO at room temperature on the 1 wt % AuCu/ Al_2O_3 catalyst. The sample was first either oxidized (black dashed curves) or reduced (red curves) and then exposed to a CO/ O_2 reaction cycle prior to the adsorption test. Spectra were taken after 100 s of exposure to the probe gas (0.2% v/v CO, balance He).

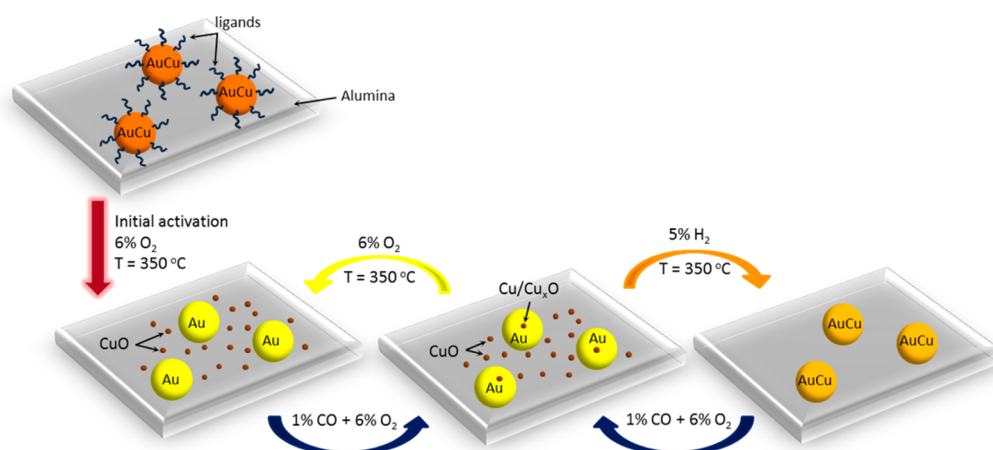
reaction cycle have very similar spectral features: in both cases we observe one peak at $\sim 2130\text{ cm}^{-1}$, already attributed to $\text{Au}^{\delta+}/\text{Cu}^+/\text{Cu}^0$ carbonyls, as well as a shoulder at 2102 cm^{-1} , which is attributed to CO adsorption on Au^0 . The various infrared band assignments are summarized in Scheme 2.

These results are in line with the catalytic activity tests. We have indeed shown that the CO oxidation catalytic activity of the catalyst after one cycle of reaction converged to the same value during the cooling phase of the transient reaction test,

Scheme 2. Infrared Band Assignments for Carbonyl and Nitrosyl Species Identified on the Catalyst Surface by Means of in Situ Diffuse Reflectance Infrared Fourier Transform Spectroscopy (DRIFTS)

	CO	CO	CO	NO
	Au^0	$\text{Au}^{\delta+}$	Cu^0/Cu^+	Cu^{2+}
After oxidation	Not Detected	$2130\text{--}2137\text{ cm}^{-1}$	Not Detected	$1845\text{--}1902\text{ cm}^{-1}$
After reduction	2102 cm^{-1}	Not Detected	$2123\text{--}2130\text{ cm}^{-1}$	Not Detected

Scheme 3. Sketch of the AuCu NC Transformations as a Function of the Activation Treatment and Reaction Environment: (Top) Starting AuCu NCs after Colloidal Deposition; (Bottom Left) after Oxidizing Pretreatment; (Bottom Center) after Reaction Cycle; (Bottom Right) after Reducing Pretreatment



regardless of oxidizing or reducing pretreatments (Figure 2). Consistently, DRIFTS tests indicated that the same surface species were detected after a reaction cycle, independently from the initial condition of the catalyst.

3. DISCUSSION

The supported bimetallic AuCu NCs underwent structural changes upon exposure to different gas atmospheres. On the basis of our TEM and DRIFTS studies, we can deduce that exposing the catalytic system to reducing or oxidizing environments led to two opposite scenarios: while a reducing treatment led to the formation of AuCu disordered alloy NCs (Scheme 3, bottom right image), a strongly oxidizing treatment caused a phase segregation between gold and copper. While gold remained localized in NC entities, copper was finely dispersed on the support (in this case Al_2O_3), likely in the form of oxide clusters (Scheme 3, bottom left image). The presence of Cu^{2+} (e.g., CuO) was supported by combined CO and NO adsorption DRIFTS studies. We observed the formation of different Cu^{2+} –nitrosyl species, indicating the existence of different Cu^{2+} sites on the surface. Considering the high dispersion of Cu on the support surface, different nitrosyl species can result from oxide clusters localized in different chemical environments (e.g., CuO localized on or close to Au NCs, isolated CuO clusters on Al_2O_3).

The different situations observed on the catalyst surface after oxidizing or reducing pretreatments resulted in a dramatic change of the catalyst performance, indicating a strong structure/activity relationship for the studied catalytic system. The phase segregation between Au and Cu and the migration of the latter on the alumina support observed after the oxidizing pretreatment was found to be detrimental to the catalytic activity in CO oxidation. This is in line with many literature reports on Au-catalyzed CO oxidation, where the presence of an interface between gold and a reducible metal oxide is considered as the catalytically active region of the catalyst surface.^{7,19} In agreement with this interpretation, the intimate contact between Au and Cu in the alloyed NCs obtained with a reducing treatment (Scheme 3, bottom right image) boosted the CO conversion.^{3a,d} Our data support the hypothesis that exposure to the reactive atmosphere (mostly oxidizing due to the presence of a large excess of O_2) resulted in the sudden

formation of CuO clusters/patches in intimate contact with the Au surface: the adsorption and activation of oxygen provided by Cu then enhanced the catalytic activity.^{2a,3a,b,4b} Increasing the temperature under the same atmosphere then resulted in the progressive migration of Cu on the support and the subsequent decrease of catalytic activity (Scheme 3, bottom center image). In contrast, when starting from a fully oxidized situation (Scheme 3, bottom left image), exposure to the reactive atmosphere (partially reducing due to the presence of CO) resulted in the partial back-migration of Cu to the Au NCs (Scheme 3, bottom center image), leading then to a slightly enhanced activity during the cooling transient of the test. In agreement with this interpretation, the performance of the same sample in a second reaction cycle, carried out without the application of any pretreatment, almost overlaps with that observed during the cooling transient of the first cycle (Figure S5 in the Supporting Information). Interestingly, these structural changes were significant at temperatures as low as 100 °C, even though their kinetics were slow: indeed after 18–20 h at 100 °C under the same reaction atmosphere, the same catalytic activity was approached, regardless of the initial situation of the catalyst surface. Consistently, the same situation was observed on the catalyst surface, as probed by CO adsorption monitored by DRIFTS.

The reproducibility of the catalytic activity data during noninterrupted cycles of pretreatment/test proved both the stability of the synthesized material and the effectiveness of the applied pretreatments in restoring the same surface situation, independently from the catalyst pretreatment/test history.

The observed process of phase segregation caused by exposure to different atmospheres has often been reported in the case of bimetallic catalysts.²⁰ This segregation was shown to be size and support dependent;^{20c} thus, different results can be expected by changing the size of the NCs and the support where the NCs are deposited. The observed process of copper migration on the alumina surface, evidently driven by temperature and gas composition, can also be strongly influenced by the support material, thus leading to different situations even when applying the same pretreatment protocols. These aspects need to be further explored in future works, in order to rationalize the effect of different pretreatments on the catalytic activity of AuCu catalysts.

4. CONCLUSIONS

We studied the transformations that colloidal AuCu ordered phase NCs supported on Al_2O_3 underwent upon different redox treatments and correlated such changes with the catalytic activity in the CO oxidation reaction. By means of different characterization techniques we highlighted a phase segregation between gold and copper upon a high-temperature (350 °C) oxidizing treatment. Copper was found to be finely dispersed on the support, likely in the form of oxide clusters, while gold remained localized in the NCs. The weak interaction between the two metals resulted in poor CO oxidation activity. However, a high-temperature (350 °C) reducing treatment was able to restore the AuCu alloyed NCs, albeit in the form of a solid solution, face-centered cubic phase. The intimate contact between the two metals was most likely the reason for a significant enhancement of the CO oxidation catalytic activity. We also observed that the CO/O_2 reacting atmosphere affected the composition of the NCs: as a result, also the CO oxidation reaction rate changed with time on stream, even at temperatures as low as 100 °C. These transformations were fully reversible, with alloyed AuCu NCs restored upon the high-temperature reducing treatment, regardless of the catalyst history.

5. EXPERIMENTAL SECTION

5.1. NC Synthesis and Catalyst Preparation. Au NCs (3 nm) were synthesized using the procedure reported in ref 8 with some modifications, specifically in the synthesis temperature and washing procedure. Typically, 100 mg of $\text{HAuCl}_4 \cdot 3\text{H}_2\text{O}$ (Sigma-Aldrich) was mixed with 10 mL of oleylamine (OAm, Sigma-Aldrich 70%) and 10 mL of 1,2,3,4-tetrahydronaphthalene (Tetralin, Sigma-Aldrich) and degassed under an inert atmosphere of N_2 for 30 min. Then, 0.5 mmol of *tert*-butylamine–borane complex (TBAB, Sigma-Aldrich), 1 mL of OAm, and 1 mL of Tetralin were mixed and sonicated until a clear solution was formed. The solution was injected into the Au precursor mixture at 21 °C, and stirring was maintained for 1 h. After the reaction, a solution of 2-propanol and ethanol (4/1 v/v) was added and the particles were precipitated by centrifugation. The supernatant was discarded and the precipitate dispersed in hexane. This washing procedure was repeated one more time before the NCs were dispersed in 10 mL of hexane. The colloidal solution was stable for at least 2 months, as observed by TEM analyses (not reported).

The as-prepared 3 nm Au NCs were used as seeds to synthesize AuCu NCs (target Au/Cu = 50/50 atomic ratio). Typically, 7 mg of CuCl_2 dihydrate (99+%, Alfa Aesar) was dissolved in a mixture of 3 mL of OAm and 0.5 mL of oleic acid (OAc, Sigma-Aldrich), and this mixture was magnetically stirred under a N_2 blanket at 100 °C until the copper salt was completely dissolved. Then 8 mg of Au NCs was added to the bluish solution of the Cu precursor and subjected to vacuum at 80 °C for 1 h to remove the hexane. Subsequently, the temperature of the mixture was increased to 280 °C with a heating rate of 5 °C/min under an N_2 atmosphere. After 1 h at this temperature, the solution was cooled to room temperature, diluted with 2 mL of anhydrous toluene, and transferred to a glovebox (Ar atmosphere). Here the NCs were washed twice by addition of a 2-propanol/methanol solution (1/3 v/v) and centrifugation. The final product was collected and dispersed in 2 mL of anhydrous hexane. The alumina-supported AuCu catalyst was prepared by colloidal deposition, which is known

to preserve the particle size distribution of the parent colloidal NCs after deposition.⁷ Typically, the AuCu colloidal solution (target AuCu NCs load 1 wt %) was added to $\gamma\text{-Al}_2\text{O}_3$ powder (extrudate from Sigma-Aldrich, crushed and sieved to 90 μm mean particles size, BET specific surface area 190 m^2/g), dispersed in hexane, and magnetically stirred for 2 h. Subsequently, the suspension was dried under an N_2 atmosphere and the resulting powder was calcined at 200 °C for 13 h.

5.2. Catalytic Experiments. The catalytic activity of the catalysts for CO oxidation was measured using a micro reactor system coupled with a micro-gas chromatograph ($\mu\text{-GC}$) equipped with three thermal conductivity detectors (TCD) to analyze CO, O_2 , and CO_2 (SRA Instruments Model R-3000). Typically, the catalyst powder was diluted with alumina (2/1 weight ratio) and loaded into a quartz reactor. The feed gas was a mixture of 1% v/v CO and 6% v/v O_2 balanced with He with a flow rate of 80 Ncc/min corresponding to a gas hourly space velocity of 3000000 Ncc/(h (g of Au + Cu)). After loading, the catalyst was initially activated at 350 °C for 10 h in 6% v/v O_2 in He to remove organic ligands present on the NC surface. Independent thermogravimetric analysis (TGA; see Figure S11 in the Supporting Information) showed that weight loss due to organic ligand removal was completed at 350 °C. For the activity measurements, the reactor was heated from room temperature to 300 °C with a heating rate of 2 °C/min, kept at 300 °C for 30 min, and then cooled to 100 °C with the same rate and kept at 100 °C for 30 min. Transient activity data were collected every 4 min during the mentioned cycle of the catalytic test. In addition to the first activation treatment to remove organic ligands, before each test the catalyst was exposed to either a reducing (5% v/v H_2 in He) or an oxidizing (6% v/v O_2 in He) atmosphere at a temperature of 350 °C for 1 h. The heating rate used in activation, reducing, and oxidizing pretreatments was set to 5 °C/min. Long-term steady-state catalytic activity data were also collected after reducing and after oxidizing pretreatments: in both cases, the pretreated catalyst was exposed to the reactants at a constant temperature of 100 °C for 24 h using the same feed gas composition and space velocity of the transient tests. Three measurements were performed on the outlet stream every 1 h to monitor the evolution of the catalytic activity with time on stream.

5.3. Characterization. **5.3.1. TEM.** Overview BF-TEM and SAED patterns were acquired on various samples using a JEOL JEM-1011 microscope with a thermionic W source operated at 100 kV. The SAED patterns were acquired at constant camera length after mechanically adjusting the height of the sample to the eucentric height and after carefully focusing the NC images. In the same session, the diffraction camera length and the system distortions were calibrated using a nanocrystalline Au sputtered film on a standard C-covered Cu grid. The elaboration of SAED patterns (beam-stop removal, centering, azimuthal integration, and background subtraction) was carried out using the PASAD software.²¹

HRTEM and HAADF-STEM analyses were performed using a JEOL JEM-2200FS microscope equipped with a Schottky emitter operated at 200 kV, a CEOS spherical aberration corrector of the objective lens, and an in-column Omega filter. Compositional analysis of the AuCu alloy NCs deposited on alumina was carried out by EDX performed in STEM mode with a Bruker Quantax 400 system with a 60 mm^2 silicon-drift detector (SDD). Quantification of the Au/Cu atomic ratio from the collected EDX spectra by the Cliff–Lorimer ratio

method systematically led to overestimation of the Au content due to a spurious Au fluorescence signal originating within the detecting system. In any case the Cliff–Lorimer ratio method was applied to obtain semiquantitative intensity scaling in the two-dimensional elemental maps. For TEM analyses, ~10 mg of the catalyst powder samples was suspended in 1 mL of anhydrous chloroform and mildly sonicated. About 100 μ L of the supernatant was then deposited onto a carbon-coated metal grid. For EDX analyses, non-Cu grids (W for the oxidized catalyst, Mo for the remaining samples) and an analytical holder with a Be cup were used. For the as-synthesized NCs, about 100 μ L of diluted AuCu colloidal solution was deposited onto the carbon support film.

5.3.2. HRSEM-EDX. Analyses were carried out using a JEOL JSM-7500FA instrument, equipped with an Oxford X-max LN₂-free SDD, with 80 mm² of sensor active area and 129 eV of energy resolution at 5.9 keV (Mn K α). Samples were prepared by drop-casting the alloy NC solution on an ultrasmooth silicon wafer. The extended Pouchou and Pichoir (XPP) matrix correction algorithm included in the Oxford AZtec software was used to analyze the data.

5.3.3. Elemental Analysis. The chemical composition of the colloidal NCs as well as the metal loadings of the catalyst were measured by ICP-AES using a Varian Vista AX spectrometer. Samples were dissolved in HCl/HNO₃ 3/1 (v/v) overnight, diluted with deionized water (14 μ S), and filtered using a PTFE filter before measurement.

5.3.4. XRD. Measurements were performed using a Rigaku SmartLab X-ray diffractometer equipped with a 9 kW Cu K α (λ = 1.542 Å) rotating anode, operating at 40 kV and 150 mA. A Göbel mirror was used to convert the divergent X-ray beam into a parallel beam and to suppress the Cu K β radiation (λ = 1.392 Å). A zero diffraction silicon substrate was used to collect XRD spectra on both colloidal NCs solutions and catalyst powdered samples. The diffraction patterns were collected at room temperature over an angular range of 10–85°, with a step size of 0.05°. XRD data analysis was carried out using PDXL 2.1 software from Rigaku.

5.3.5. In Situ DRIFTS. Spectra were collected using a Vertex 70 infrared spectrometer (Brüker Optics) equipped with a DRIFTS cell (Praying Mantis, Harrick) and a MCT detector, cooled with liquid nitrogen. The outlet of the DRIFTS cell was connected to an online mass spectrometer (Omnistar, Pfeiffer). Using a four-port selector valve, it was possible to switch between two different gas streams, one used for purging and/or pretreatments and the other containing the probe species. The loaded sample was pretreated under oxidizing or reducing atmospheres prior to the test. The pretreatments followed the same conditions used in the case of catalytic experiments, except for the heating rate, which was set to 20 °C/min. After each pretreatment, the cell was cooled to room temperature. Once the temperature was stabilized, the background spectrum was collected while the pretreatment mixture was continuously flowed. Then, the flowing gas was switched to a mixture containing either 0.2% v/v CO or 650 ppm of NO with a balance of He. Spectra were collected every 10 s for the first 100 s of adsorption. The process was monitored for a further 40 min, collecting a spectrum every 10 min. After that, the flow was switched to a He stream to purge the catalyst and desorption spectra were collected during 40 min of purging with inert gas. Each test was repeated at least two times to verify the reproducibility of the measurement. The spectra of CO adsorption at room temperature was also collected after

performing one cycle of reaction in the DRIFTS cell, using the same feed composition and flow rate as in the case of catalytic experiments. When NO was used as the probe molecule, a reducing treatment at high temperature (5% H₂, balance He at 350 °C) was always performed after the adsorption test to clean the surface from nitrite/nitrate species. Then, the desired pretreatment and the following adsorption test were performed.

■ ASSOCIATED CONTENT

Supporting Information

The following file is available free of charge on the ACS Publications website at DOI: 10.1021/cs501923x.

BF-TEM of as-prepared Au NCs, SEM EDX maps of AuCu NCs, calculation of AuCu NC size on the basis of starting Au NC size, optical absorption characterization of Au and AuCu NCs, comparison of activity for 3 nm Au/Al₂O₃ vs 6 nm AuCu/Al₂O₃, activity of the AuCu catalyst after one cycle of reaction without performing any pretreatment, overview HAADF-STEM images, XRD pattern and TPR measurement on the AuCu/Al₂O₃ catalyst sample, CO and NO DRIFTS on the Au/Al₂O₃ catalyst sample, and TGA data of the AuCu NCs in air ([PDF](#))

■ AUTHOR INFORMATION

Corresponding Authors

*E-mail for L.M.: liberato.manna@iit.it.

*E-mail for M.C.: massimo.colombo@iit.it

Present Address

[†](For P.G.) Catalonia Energy Research Institute – IREC, Jardí de les Dones de Negre 1, Sant Adria del Besos, Spain

Notes

The authors declare no competing financial interest.

■ ACKNOWLEDGMENTS

The authors acknowledge financial support from European Union through the EU-ITN network Mag(net)icFun (PITN-GA-2012–290248) and the Italian FIRB grant “Ossidi Nanostrutturati” (contract #RBAP115AYN).

■ REFERENCES

- (1) (a) Tao, F. *Chem. Soc. Rev.* **2012**, *41*, 7977–7979. (b) Jiang, H.-L.; Xu, Q. *J. Mater. Chem.* **2011**, *21*, 13705–13725. (c) Sankar, M.; Dimitratos, N.; Miedziak, P. J.; Wells, P. P.; Kiely, C. J.; Hutchings, G. J. *Chem. Soc. Rev.* **2012**, *41*, 8099–8139.
- (2) (a) Wang, A.; Liu, X. Y.; Mou, C.-Y.; Zhang, T. *J. Catal.* **2013**, *308*, 258–271. (b) Bracey, C. L.; Ellis, P. R.; Hutchings, G. J. *Chem. Soc. Rev.* **2009**, *38*, 2231–43.
- (3) (a) Liu, X.; Wang, A.; Wang, X.; Mou, C. Y.; Zhang, T. *Chem. Commun.* **2008**, 3187–9. (b) Liu, X.; Wang, A.; Zhang, T.; Su, D.-S.; Mou, C.-Y. *Catal. Today* **2011**, *160*, 103–108. (c) Mozer, T. S.; Dziuba, D. A.; Vieira, C. T. P.; Passos, F. B. *J. Power Sources* **2009**, *187*, 209–215. (d) Sandoval, A.; Louis, C.; Zanella, R. *Appl. Catal., B* **2013**, *140–141*, 363–377. (e) Bauer, J. C.; Mullins, D. R.; Oyola, Y.; Overbury, S. H.; Dai, S. *Catal. Lett.* **2013**, *143*, 926–935. (f) Liu, J.-H.; Wang, A.-Q.; Chi, Y.-S.; Lin, H.-P.; Mou, C.-Y. *J. Phys. Chem. B* **2004**, *109*, 40–43.
- (4) (a) Li, X.; Fang, S. S. S.; Teo, J.; Foo, Y. L.; Borgna, A.; Lin, M.; Zhong, Z. *ACS Catal.* **2012**, *2*, 360–369. (b) Liu, X.; Wang, A.; Li, L.; Zhang, T.; Mou, C.-Y.; Lee, J.-F. *J. Catal.* **2011**, *278*, 288–296. (c) Petkov, V.; Shastri, S.; Shan, S.; Joseph, P.; Luo, J.; Zhong, C.-J.; Nakamura, T.; Herbani, Y.; Sato, S. *J. Phys. Chem. C* **2013**, *117*, 22131–22141.

- (5) Bauer, J. C.; Mullins, D.; Li, M.; Wu, Z.; Payzant, E. A.; Overbury, S. H.; Dai, S. *Phys. Chem. Chem. Phys.* **2011**, *13*, 2571–81.
- (6) Yin, J.; Shan, S.; Yang, L.; Mott, D.; Malis, O.; Petkov, V.; Cai, F.; Shan, N. M.; Luo, J.; Chen, B. H.; Engelhard, M.; Zhong, C.-J. *Chem. Mater.* **2012**, *24*, 4662–4674.
- (7) Comotti, M.; Li, W.-C.; Spliethoff, B.; Schüth, F. *J. Am. Chem. Soc.* **2005**, *128*, 917–924.
- (8) Peng, S.; Lee, Y.; Wang, C.; Yin, H.; Dai, S.; Sun, S. *Nano Res.* **2008**, *1*, 229–234.
- (9) Jia, C.-J.; Schuth, F. *Phys. Chem. Chem. Phys.* **2011**, *13*, 2457–2487.
- (10) Chen, W.; Yu, R.; Li, L.; Wang, A.; Peng, Q.; Li, Y. *Angew. Chem., Int. Ed. Engl.* **2010**, *49*, 2917–21.
- (11) Mourdikoudis, S.; Liz-Marzán, L. M. *Chem. Mater.* **2013**, *25*, 1465–1476.
- (12) Okamoto, H.; Chakrabarti, D. J.; Laughlin, D. E.; Massalski, T. *B. J. Phase Equilib.* **1987**, *8*, 454–474.
- (13) (a) Motl, N. E.; Ewusi-Annan, E.; Sines, I. T.; Jensen, L.; Schaak, R. E. *J. Phys. Chem. C* **2010**, *114*, 19263–19269. (b) Sra, A. K.; Schaak, R. E. *J. Am. Chem. Soc.* **2004**, *126*, 6667–6672.
- (14) (a) Hadjiivanov, K.; Knözinger, H. *Phys. Chem. Chem. Phys.* **2001**, *3*, 1132–1137. (b) Venkov, T.; Hadjiivanov, K. *Catal. Commun.* **2003**, *4*, 209–213. (c) Dulaurent, O.; Courtois, X.; Perrichon, V.; Bianchi, D. *J. Phys. Chem. B* **2000**, *104*, 6001–6011.
- (15) Mihaylov, M.; Knözinger, H.; Hadjiivanov, K.; Gates, B. C. *Chem. Ing. Technol.* **2007**, *79*, 795–806.
- (16) (a) Praliaud, H.; Mikhailenko, S.; Chajar, Z.; Primet, M. *Appl. Catal., B* **1998**, *16*, 359–374. (b) Dandekar, A.; Vannice, M. A. *J. Catal.* **1998**, *178*, 621–639.
- (17) (a) Venkov, T.; Hadjiivanov, K.; Klissurski, D. *Phys. Chem. Chem. Phys.* **2002**, *4*, 2443–2448. (b) Morterra, C.; Boccuzzi, F.; Coluccia, S.; Ghiotti, G. *J. Catal.* **1980**, *65*, 231–234. (c) Parres-Esclapez, S.; Such-Basañez, I.; Illán-Gómez, M. J.; Salinas-Martínez de Lecea, C.; Bueno-López, A. *J. Catal.* **2010**, *276*, 390–401.
- (18) (a) Shimokawabe, M.; Okumura, K.; Ono, H.; Takezawa, N. *React. Kinet. Catal. Lett.* **2001**, *73*, 267–274. (b) Hadjiivanov, K.; Saussey, J.; Freysz, J. L.; Lavalley, J. C. *Catal. Lett.* **1998**, *52*, 103–108.
- (19) (a) Lopez, N. *J. Catal.* **2004**, *223*, 232–235. (b) Schubert, M. M.; Hackenberg, S.; van Veen, A. C.; Muhler, M.; Plzak, V.; Behm, R. *J. J. Catal.* **2001**, *197*, 113–122.
- (20) (a) Ma, T.; Fu, Q.; Su, H.-Y.; Liu, H.-Y.; Cui, Y.; Wang, Z.; Mu, R.-T.; Li, W.-X.; Bao, X.-H. *ChemPhysChem* **2009**, *10*, 1013–1016. (b) Mayrhofer, K. J. J.; Juhart, V.; Hartl, K.; Hanzlik, M.; Arenz, M. *Angew. Chem., Int. Ed.* **2009**, *48*, 3529–3531. (c) Guisbiers, G.; Mejia-Rosales, S.; Khanal, S.; Ruiz-Zepeda, F.; Whetten, R. L.; José-Yacamán, M. *Nano Lett.* **2014**, *14*, 6718–6726.
- (21) Gammer, C.; Mangler, C.; Rentenberger, C.; Karthaler, H. P. *Scr. Mater.* **2010**, *63*, 312–315.

Supporting information

Nanoscale Transformations of Alumina-Supported AuCu Ordered Phase Nanocrystals and Their Activity in CO Oxidation

Sharif Najafshirtari^a, Rosaria Brescia^a, Pablo Guardia^{a,†}, Sergio Marras^a, Liberato Manna^{a},
Massimo Colombo^{a*}*

a) Department of Nanochemistry, Istituto Italiano di Tecnologia, Via Morego 30, 16163, Genova Italy

† Current address: Catalonia Energy Research Institute – IREC, Jardí de les Dones de Negre 1, Sant
Adria del Besos, Spain

liberato.manna@iit.it; massimo.colombo@iit.it (corresponding authors emails)

keywords: AuCu, bimetallic nanocrystals, nanoalloy, CO oxidation, DRIFTS

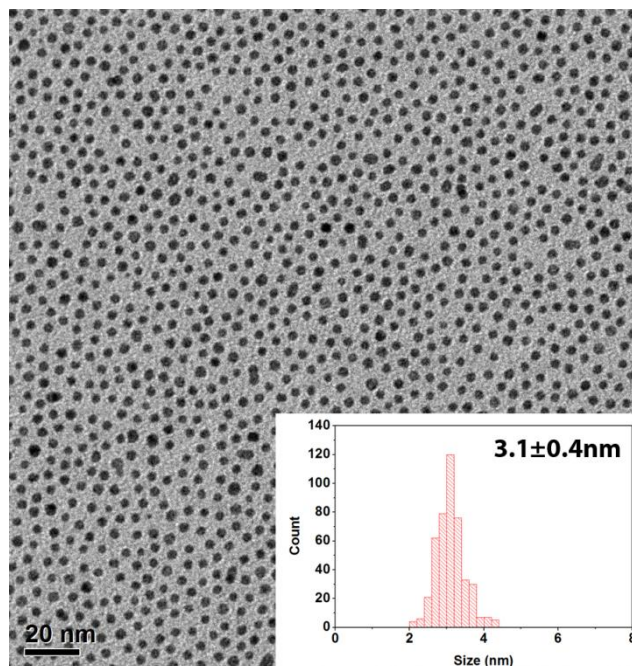


Figure S1. Typical BF-TEM image of the as-prepared Au colloidal NCs with the size distribution histogram in the inset.

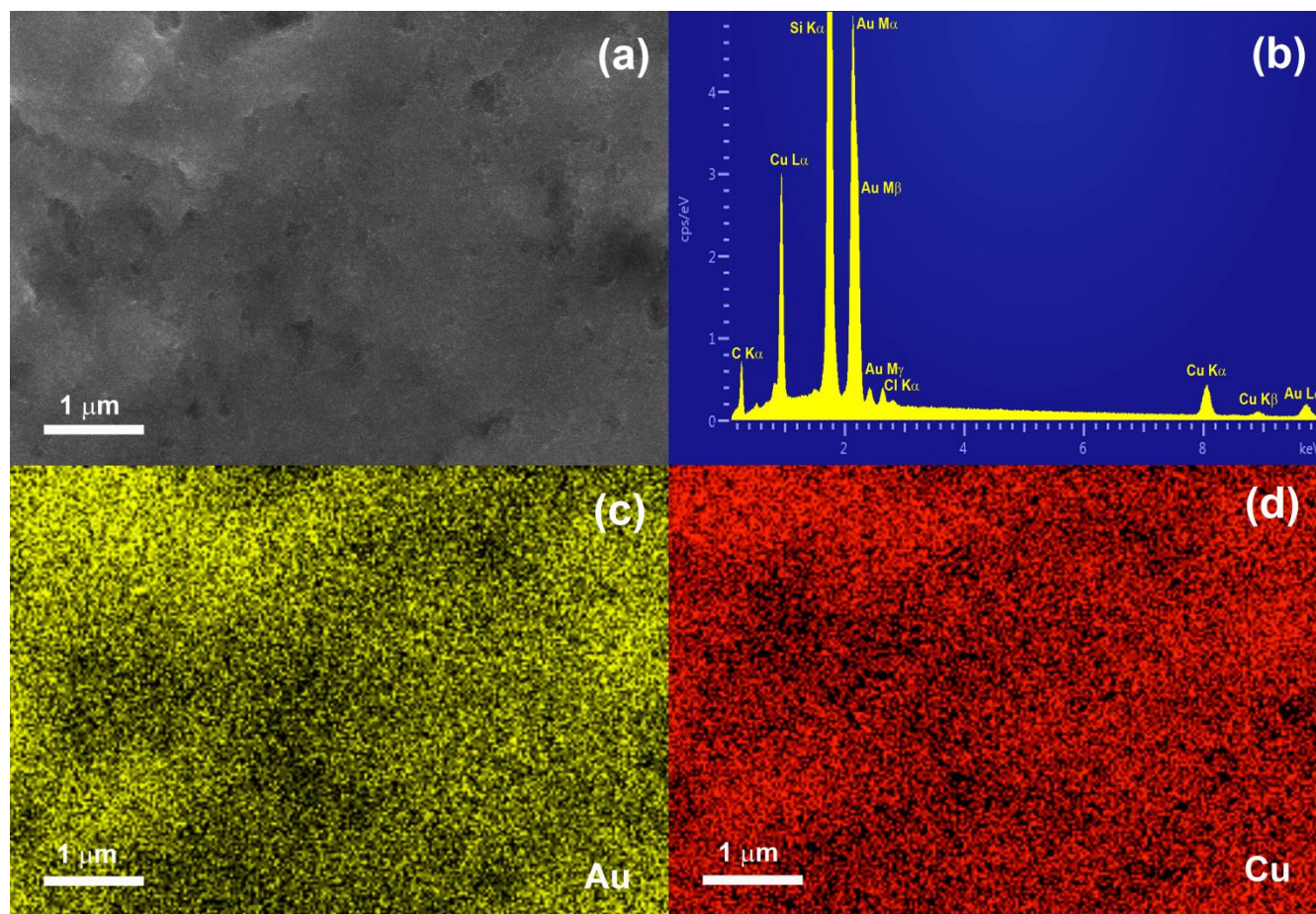


Figure S2. SEM EDX maps for quantitative analysis of alloy AuCu NCs composition. (a) Sample area used for the quantitative analysis. (b) EDX spectrum; elemental maps showing the distribution for Au (c) and Cu (d).

Calculation of AuCu NCs size based on starting Au seeds size

We estimated the enlargement of the Au NCs resulting from incorporation of Cu into the Au seeds so as to obtain the final AuCu NCs with atomic Au:Cu ratio = 50:50, in the ordered tetragonal phase observed in XRD patterns. First, the volume of an Au NC was calculated considering it as spherical ($V_{Au\ NC}$). Then, considering the number of Au atoms in the unit cell (which is equal to 4) as well as the known unit cell volume of Au ($67.85\ \text{\AA}^3$ in the JCPDS card no. #04-0784), the number of Au atoms per Au NC was calculated from:

$$N_{Au\ atoms\ in\ Au\ NC} = \frac{N_{Au\ atoms\ per\ unit\ cell}}{V_{Au\ unit\ cell}} V_{Au\ NC}$$

The expected volume of the corresponding AuCu NC was calculated considering that the number of Au atoms per NC was constant even after incorporation of Cu. Considering the unit cell volume of AuCu ($29.136\ \text{\AA}^3$ in the JCPDS card no. #01-071-0784) and the number of Au atoms per unit cell of AuCu (which is equal to 1), the AuCu NC volume can be evaluated as follows:

$$V_{AuCu\ NC} = \frac{N_{Au\ atoms\ in\ Au\ NC} * V_{AuCu\ unit\ cell}}{N_{Au\ atoms\ per\ AuCu\ unit\ cell}}$$

To evaluate the diameter of the AuCu NC we assumed that also AuCu NCs were spherical. Hence, starting from 3 nm Au seeds, an enlargement of the particle's diameter of about ~20 % (referred to the starting diameter) should be achieved by incorporation of Cu into the Au seeds. Larger sizes observed on the TEM grids are related to coalescence/sintering of NCs at high temperatures.

Optical absorption characterization: Optical absorption measurements on colloidal solutions were carried out using a Varian Cary 5000 UV-vis-NIR spectrophotometer. NCs were dispersed in hexane before the measurements.

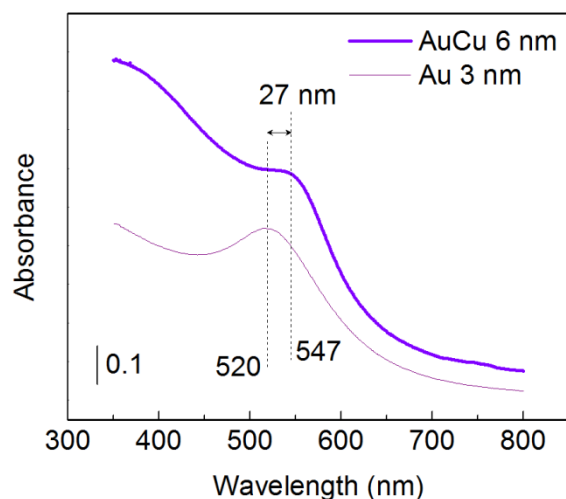


Figure S3. Absorption spectra for Au (thin black line) and AuCu (thick violet line) NCs colloids in hexane.

Comparison of activities between 3 nm Au/Al₂O₃ and 6 nm AuCu/Al₂O₃

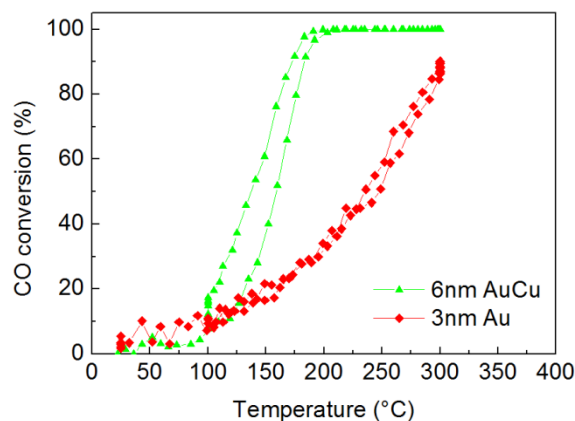


Figure S4. Catalytic activity data for the 1 wt.% AuCu /Al₂O₃ and the 1wt.% Au/Al₂O₃ catalysts in CO oxidation after an oxidative pre-treatment. CO = 1% v/v; O₂ = 10% v/v; GHSV= 3'000'000 Ncc/h/g(AuCu).

Activity of the catalyst without pre-treatment.

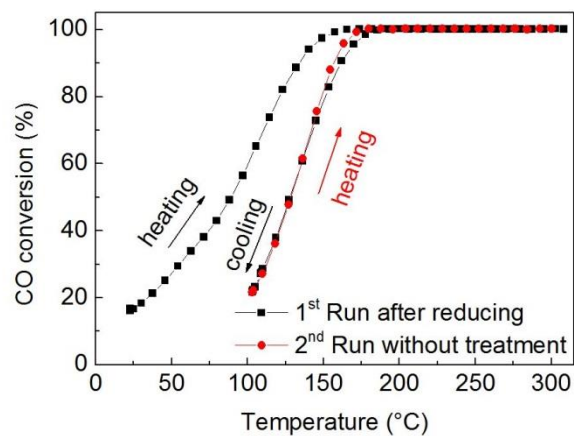


Figure S5. Catalytic activity data for the 1 wt.% AuCu /Al₂O₃ catalyst in CO oxidation after a reducing pre-treatment followed by heating under reaction atmosphere without performing any pre-treatment. CO = 1% v/v; O₂ = 6 % v/v; GHSV= 3'000'000 Ncc/h/g(AuCu).

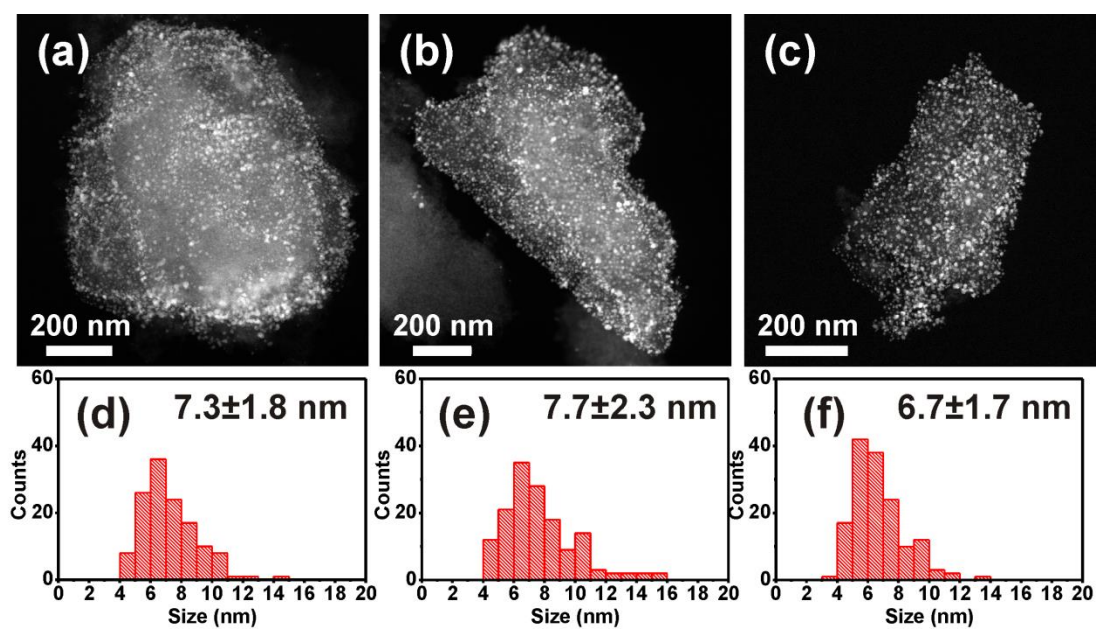


Figure S6. Overview HAADF-STEM images of the catalyst (a) after oxidation, (b) after reduction, (c) after one cycle of reaction and (d-f) corresponding size distribution histograms.

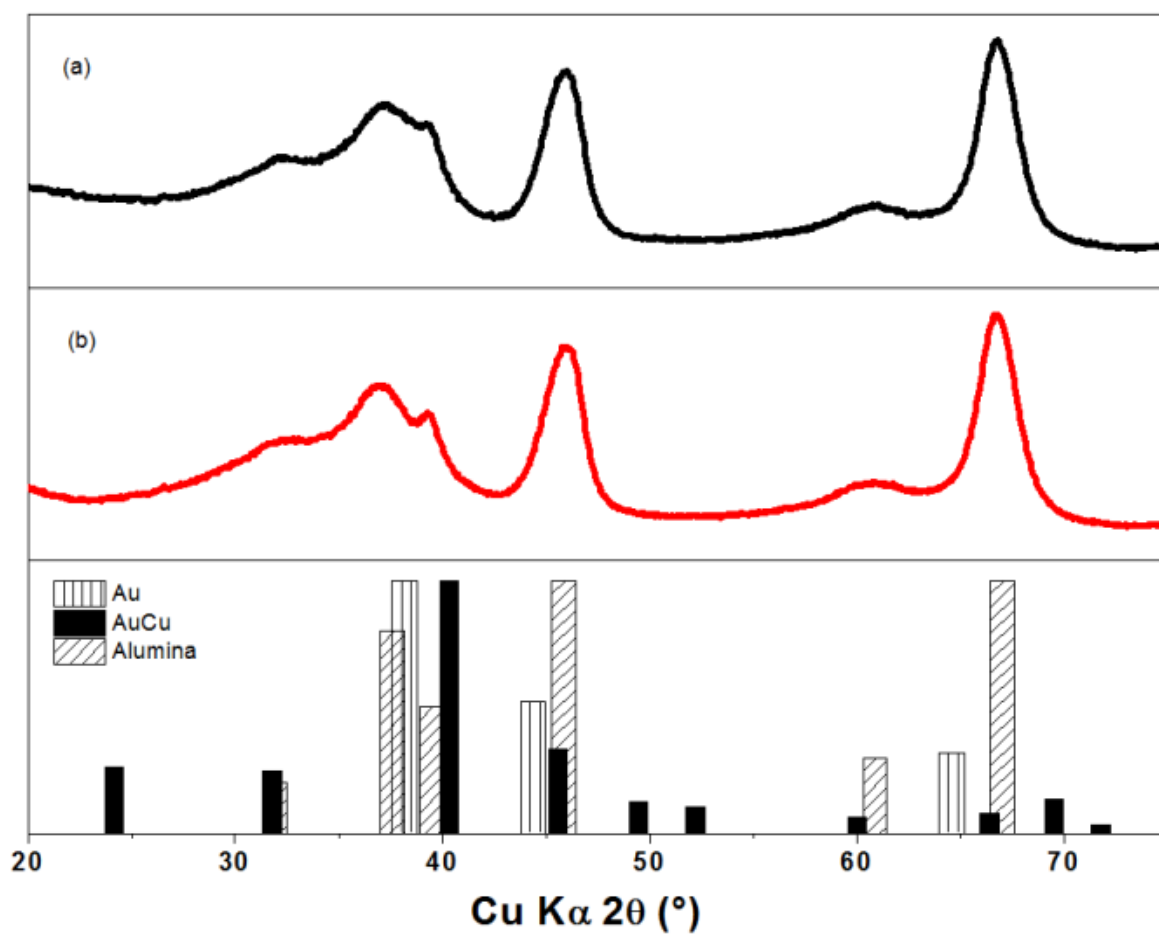


Figure S7. (a) XRD pattern of reduced AuCu /Al₂O₃ catalyst and (b) of gamma-alumina compared with the data base XRD patterns of Au (JCPDS # 00-004-0784), AuCu (JCPDS # 01-071-5024) and gamma-alumina (JCPDS # 00-010-0425).

Temperature Programmed Reduction (TPR)

TPR measurement was carried out over a catalyst batch already oxidized at 350 °C for 1 h in 6% v/v O₂. The catalyst sample was heated to 350 °C in 5% v/v H₂ atmosphere (balance Ar) with a heating rate of 20 °C/min. The test was carried out in a Quantachrome instrument, model Autosorb iQ, equipped with a TCD detector. As shown in Figure S8, two peaks were detected at the temperatures of 155 °C and 205 °C which can be respectively assigned to reduction of Cu²⁺ and Cu⁺.

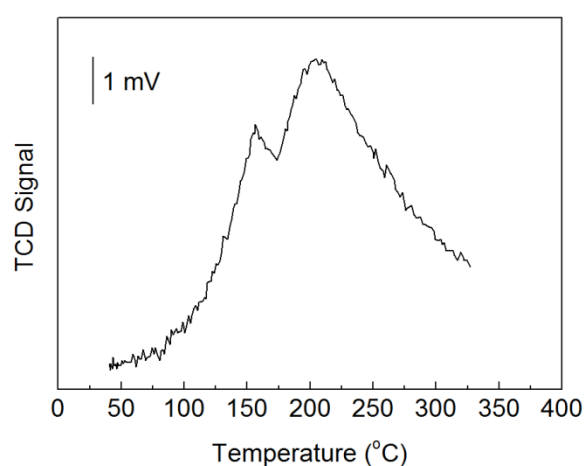


Figure S8. TPR profile of the 1 wt. % AuCu/Al₂O₃ catalyst. Pre-treatment: 1 h at 350°C in 6% v/v O₂. TPR conditions: 5% v/v H₂ in Ar, heating rate = 20 °C/min.

CO & NO DRIFTS on 6nm Au/Al₂O₃ catalyst

In order to check CO and NO adsorption on Au, a catalyst sample was prepared through deposition of 6 nm colloidal Au on alumina. The 6nm Au NCs were prepared in the same manner as the 3 nm Au NCs used as seeds for the synthesis of the AuCu NCs. Compared to what described in the Experimental section for the synthesis of 3nm Au NCs, the temperature of the reaction mixture was lowered to 0°C by means of ice + water mixture. The rest of the synthesis conditions were kept the same. The 6 nm Au/alumina catalyst underwent the same treatment as reported in the paper and exposed to the same CO or NO mixtures for 35 and 42 minutes, respectively.

Figure S9 shows the carbonyl band evolution during 35 min of exposure after oxidizing and reducing pre-treatments. A carbonyl band is formed on Au catalyst at wavenumber of 2141 cm⁻¹ after oxidation while, after reducing pre-treatment, the band is observed at lower wavenumber of 2116 cm⁻¹, in line with reported data on carbonyl bands on Au^{δ+} and Au⁰.¹ Figure S10 shows DRIFTS spectra in the nitrosyl region: NO was not adsorbed on Au NCs neither after reducing nor after oxidizing pre-treatments. After a long time exposure, a broad band that can be assigned to NO⁺ can be observed. As in the case of AuCu/Al₂O₃, the formation of this species is consistent with the presence of NO₂ contamination in the CO stream, arising from the disproportionation reaction of NO: $3 \text{ NO} \leftrightarrow \text{N}_2\text{O} + \text{NO}_2$.²

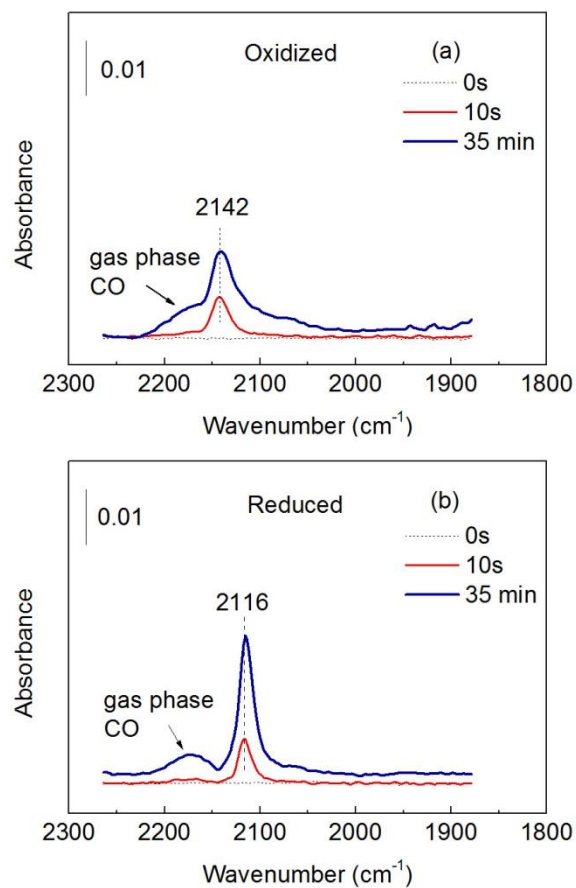


Figure S9. DRIFTS spectra in the carbonyl region obtained during the adsorption of CO at room temperature on the 1 wt.% Au/Al₂O₃ catalyst. Spectra were taken after 0 s, 10s and 35 min of exposure to the probe gas on the same sample that was either oxidized (a) or reduced (b) prior to the adsorption test. Probe gas composition: 0.2% v/v CO, balance He.

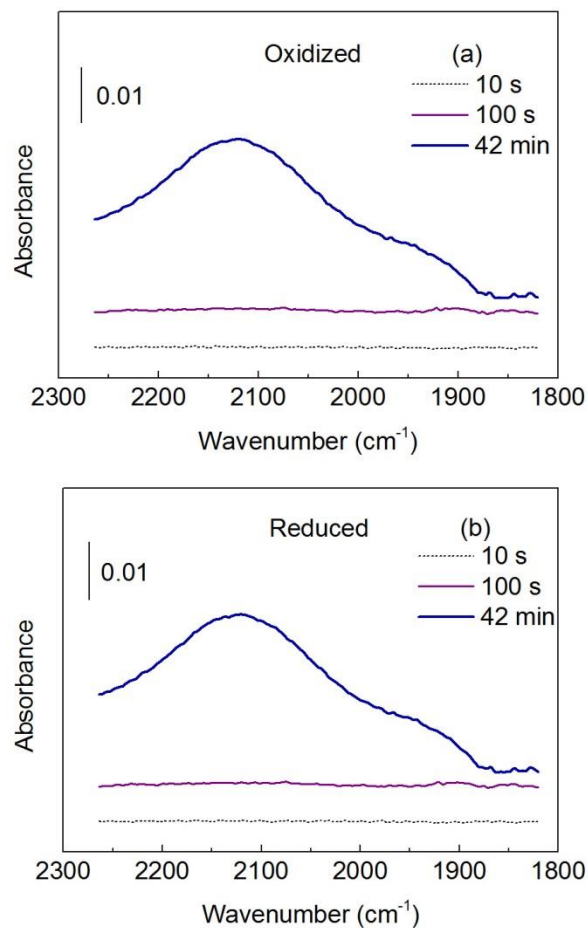


Figure S10. DRIFTS spectra in the nitrosyl region obtained during the adsorption of NO at room temperature on the 1 wt.% Au/Al₂O₃ catalyst . Spectra were taken after 10 s, 100s and 42 min of exposure to the probe gas on the same sample that was either oxidized (a) or reduced (b) prior to the adsorption test. Probe gas composition: 650 ppm NO, balance He.

Thermogravimetric Analysis (TGA) of the AuCu NCs

In order to define the conditions for the successful removal of organic ligands from NCs surface, a TGA analysis was carried out on the parent colloidal AuCu NCs solution. The analysis was performed with a Q500 instrument from TA Instruments. After solvent evaporation, the sample (~1 mg of AuCu NCs) was equilibrated at 30 °C for 30 minutes, then heated to 600 °C with a 10 °C/min heating rate under 50 ml/min of air flow. The weight loss of the sample was monitored in the whole process and its profile is shown in Figure S11. It can be seen that weight loss due to the removal of organic ligands is basically completed at the temperature of 300-350 °C.

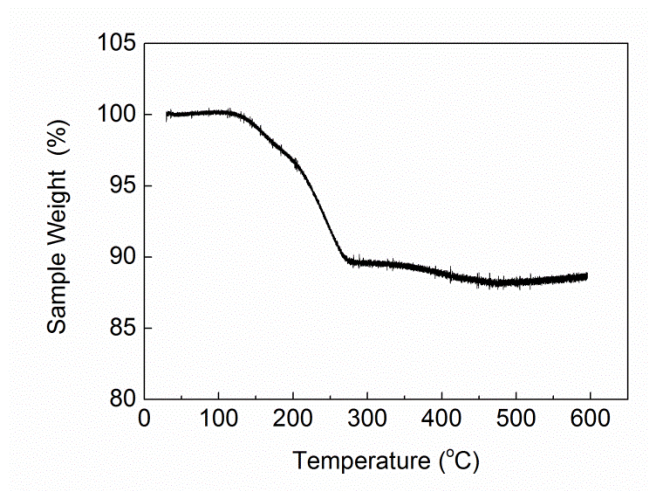


Figure S11. TGA profile of the parent AuCu NCs under air.

REFERENCES

1. Mihaylov, M.; Knözinger, H.; Hadjiivanov, K.; Gates, B. C., *Chem. Ing. Tech.* **2007**, 79, 795-806.
2. (a) Hadjiivanov, K.; Knözinger, H., *Phys. Chem. Chem. Phys.* **2001**, 3, 1132-1137; (b) Hadjiivanov, K.; Saussey, J.; Freysz, J. L.; Lavalley, J. C., *Catal. Lett.* **1998**, 52, 103-108.

Chapter IV¹

Dumbbell-like $\text{Au}_{0.5}\text{Cu}_{0.5}@\text{Fe}_3\text{O}_4$ Nanocrystals: Synthesis, Characterization, and Catalytic Activity in CO Oxidation²

¹ TEM and EDS measurements were done by R. Brescia and A. Scarpellini; XRD by S. Marras; XAS measurement and analyses by T. Midori, P. Destro, M. Prato and D. Zanchet; Magnetic measurement and analysis by A. Lak and T. Pellegrino; All other activities including experimental, data elaboration, results interpretation and manuscript preparation were performed by S. Najafshiri under supervision of M. Colombo (for all characterizations, catalytic experiments, and results interpretation) and L. Manna (for manuscript preparation).

² Reprinted with permission from S. Najafshiri et al., ACS Appl. Mater. Interfaces, 2016, 8 (42), pp 28624–28632. Copyright (2016) American Chemical Society.

Dumbbell-like $\text{Au}_{0.5}\text{Cu}_{0.5}@\text{Fe}_3\text{O}_4$ Nanocrystals: Synthesis, Characterization, and Catalytic Activity in CO Oxidation

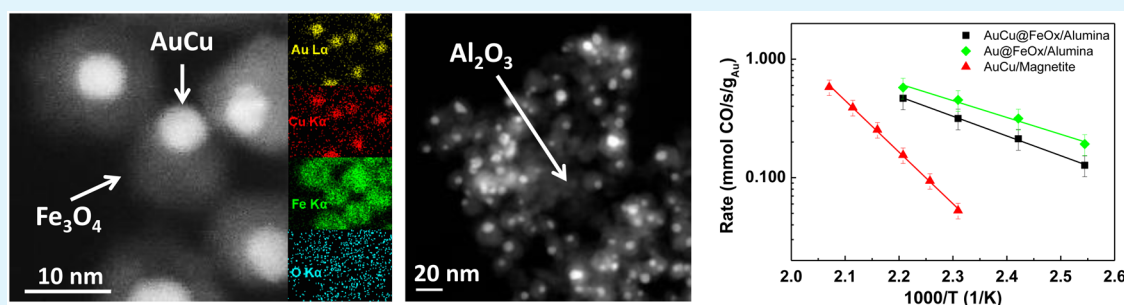
Sharif Najafshirtari,^{†,||} Tathiana Midori Kokumai,[§] Sergio Marras,[†] Priscila Destro,[§] Mirko Prato,[†] Alice Scarpellini,[†] Rosaria Brescia,[†] Aidin Lak,[‡] Teresa Pellegrino,[‡] Daniela Zanchet,[§] Liberato Manna,[†] and Massimo Colombo^{*,†}

[†]Department of Nanochemistry and [‡]Drug Discovery and Development, Istituto Italiano di Tecnologia, Via Morego 30, 16163 Genova, Italy

[§]Institute of Chemistry, University of Campinas (UNICAMP), P.O. Box 6154, 13083-970 Campinas, São Paulo, Brazil

^{||}Dipartimento di Chimica e Chimica Industriale, Università di Genova, via Dodecaneso 31-I, 16146 Genova, Italy

S Supporting Information



ABSTRACT: We report the colloidal synthesis of dumbbell-like $\text{Au}_{0.5}\text{Cu}_{0.5}@\text{Fe}_3\text{O}_4$ nanocrystals ($\text{AuCu}@\text{FeO}_x$ NCs) and the study of their properties in the CO oxidation reaction. To this aim, the as-prepared NCs were deposited on γ -alumina and pretreated in an oxidizing environment to remove the organic ligands. A comparison of these NCs with bulk Fe_3O_4 -supported AuCu NCs showed that the nanosized support was far more effective in preventing the sintering of the metal domains, leading thus to a superior catalytic activity. Nanosizing of the support could be thus an effective, general strategy to improve the thermal stability of metallic NCs. On the other hand, the support size did not affect the chemical transformations experienced by the AuCu NCs during the activation step. Independently from the support size, we observed indeed the segregation of Cu from the alloy phase under oxidative conditions as well as the possible incorporation of the Cu atoms in the iron oxide domain.

KEYWORDS: nanocrystals, dumbbells, bimetallics, CO oxidation, AuCu

1. INTRODUCTION

It is established among the catalysis community that the interaction between the metal and the support has a strong contribution to the catalytic properties of heterogeneous metal supported catalysts.^{1–6} Such catalysts have been typically composed of micrometer-sized grains of support with high surface area (such as metal oxides, active carbon, and zeolites), decorated with clusters or with nanosized metal (and/or metal oxide) domains as the active sites.^{7–12} Different approaches have been followed to enhance the catalytic activity of these materials. Among them are decreasing the size of the metal particles as the most conventional way to increase the metal dispersion and its interface with the support,⁶ tailoring the interface¹³ or the morphology of the support,^{4,14} manipulating the architectural structure,^{7,15–19} or use of nanosized supports.²⁰ The latter has been introduced as a modern way to design more active catalysts and gain fundamental understanding on the interaction between the metal and the support. One important step in this field was made by the

pioneering work of Sun's group, with the successful synthesis of colloidal $\text{Au}/\text{Fe}_3\text{O}_4$ dumbbell-like nanoparticles and their application in CO oxidation.²¹ The dumbbell structure is characterized by an epitaxial connection of a nanosized metallic domain to a nanosized metal oxide domain, with the former being partially nested in the latter.^{22,23} This structure can enhance the charge transfer across the interface between the two nanoparticles and therefore promote the catalytic activity.^{21,24–27} Furthermore, this morphology is reported to ensure structural stability and sintering resistance of the metal phase.²⁸ A severe sintering can indeed affect the dispersion of the metal active sites and is known to cause deactivation and decrease of the catalytic activity in metal supported catalysts. Other hybrid nanostructures have also been developed, such as flower-like $\text{Au}/\text{Fe}_3\text{O}_4$ ²⁹ and $\text{Pd}/\text{Fe}_3\text{O}_4$ ^{30,31} or silica-encapsu-

Received: August 5, 2016

Accepted: October 10, 2016

Published: October 10, 2016

lated Au/Fe₃O₄ dumbbell-like NCs,³² in an attempt to manipulate, adjust, and/or promote the interaction between the metal and the metal oxide at the nanoscale. The work on the dumbbell-like NCs has been extended by synthesizing materials with a bimetallic domain to exploit the possible synergy arising between two metals, as already established for the traditional catalysts.³³ For instance, George et al.²⁶ reported a study on Au_{0.80}Pd_{0.20}-Fe_xO_y dumbbell NCs in CO oxidation, and Sun et al.³⁴ demonstrated an enhanced catalytic electrochemical detection of H₂O₂ using Pt_xPd_{1-x}-Fe₃O₄. Nevertheless, the syntheses of dumbbell-like materials, whether tested for catalysis or for other applications, have been limited mainly to the noble metals for what concerns the metallic domain, e.g., Ag,²⁴ Au,^{21,27–29,35} Pt,^{23,36} Pd,^{30,31} PtPd,³⁴ and AuPd,²⁶ except for a few cases where transition metals or noble metal-transition metal alloys have been reported.^{37–42} The use of noble metal-transition metal alloys in dumbbell-like NCs is thus still widely unexplored.

In this work, we report the synthesis and characterization of dumbbell-like Au_{0.5}Cu_{0.5}@Fe₃O₄ nanocrystals (AuCu@FeOx NCs), exploiting a gold-transition metal alloy as seed to grow an iron oxide domain on top of it. We selected the AuCu alloy since this system is known to be effective in the low temperature CO oxidation reaction and other oxidation reactions.^{43,44} We deposited the NCs on alumina, thoroughly studied their transformations upon an oxidative activation treatment, which was essential to remove the protecting ligands, and further evaluated the synthesized material in the CO oxidation reaction. The oxidation treatment caused the dealloying between Au and Cu, with Cu atoms likely being incorporated in the iron oxide domain. The AuCu@FeOx sample showed CO oxidation reaction rates similar to those measured over a Au@FeOx dumbbell-like catalyst having a similar Au domain size, highlighting the dominant role of the Au-iron oxide interface for this reaction. The nanosized support resulted in a strong thermal stability of the metallic domains and the sintering of the Au domains was effectively prevented. This in turn yielded a higher activity of the AuCu@FeOx dumbbells when compared against a bulk Fe₃O₄ supported AuCu NCs catalyst, where extensive sintering occurred. Nanosizing of the support could thus represent a general yet effective strategy to improve the thermal stability of few nanometer sized metallic domains.

2. EXPERIMENTAL SECTION

2.1. Synthesis of Nanocrystals (NCs). Chemicals. Oleylamine (OLAm, 70%), HAuCl₄·3H₂O, 1-octadecene (Technical grade 90%), oleic acid (OLAc, Technical grade 90%), iron pentacarbonyl (>99.99% trace metals basis), solvents (ethanol, isopropanol, chloroform, and *n*-hexane), and magnetite powder (specific surface area (SSA) = 2.7 m²/g) were purchased from Sigma-Aldrich. CuCl₂ dihydrate (99+%) was purchased from Alfa Aesar while the γ-Al₂O₃ extrudate (SSA = 220 m²/g; average pore diameter = 6.5 nm) was purchased from Strem Chemicals. All chemicals were used as received.

Synthesis of AuCu-Iron Oxide (AuCu@FeOx) and Au-Iron Oxide (Au@FeOx) Dumbbell-Shaped NCs. AuCu@FeOx NCs were synthesized by a seed-mediated growth approach. Premade AuCu NCs, synthesized as thoroughly discussed elsewhere,⁴⁴ were used as seeds, and iron pentacarbonyl was used as the iron source. Typically, 8 mg of the AuCu NCs seeds was mixed with 20 mL of ODE, 3 mL of OLAm, and 1 mL of OLAc and degassed under vacuum at 80 °C for 1 h to remove hexane. Then, a solution of 80 μL of Fe precursor in 1 mL of already degassed ODE was injected in the solution at 150 °C while the temperature was being raised to 205 °C. The mixture was stirred for 1.5 h, and then it was heated up to 300 °C and kept there for 1 h.

The products were washed twice with a mixture of isopropanol and ethanol (3:1 volume ratio), centrifuged, and dispersed in 10 mL of chloroform. Au@FeOx NCs (Au domains of 6.6 ± 1.0 nm) were synthesized according to the procedure reported by Najafshirvari et al.⁴⁵

Catalysts Preparation. The alumina-supported AuCu@FeOx and Au@FeOx catalysts (AuCu@FeOx/Alumina and Au@FeOx/Alumina) were prepared by colloidal deposition. Typically, a specific weight of γ-Al₂O₃ powder (manually crushed and sieved to 90 μm) was dispersed in chloroform. Then a proper amount of colloidal solution (targeting 1.0 wt % Au + Cu for AuCu@FeOx/Alumina and 1.0 wt % of Au for Au@FeOx/Alumina) was added to it, and the suspension was sonicated for 2 h. The magnetite-supported AuCu catalyst (AuCu/Magnetite, 1.0 wt % Au + Cu) was prepared by adding the colloidal solution of AuCu to the magnetite powder (manually pressed, crushed, and sieved to 90 μm) dispersed in hexane, followed by sonication for 2 h. All suspensions were dried under a dry air atmosphere and then calcined in static air at 350 °C for 10 h to remove the ligands from the surface of deposited NCs.⁴⁵ The catalysts were then washed three times with deionized water in order to remove eventual residual chlorine species (see Figures S1 and S2 and related discussion in the Supporting Information) and finally dried again for 3 h at 150 °C.

2.2. Catalytic Experiments. The activity of the catalysts for CO oxidation was measured using a microreactor system coupled with a micro-gas chromatograph (μ-GC) equipped with three modules working in parallel (each consisting of an injector, a column, and a thermal conductivity detector) to analyze CO, O₂, and CO₂ (SRA Instruments model R-3000). Typically, the AuCu@FeOx/Alumina (or Au@FeOx/Alumina) catalyst powder was diluted with alumina (2:1 weight ratio) and loaded into a quartz reactor (i.d. = 8 mm). The AuCu/Magnetite catalyst was not diluted further. The feed gas was a mixture of 1% v/v CO and 6% v/v O₂ balanced with He with a flow rate of 80 Ncc/min corresponding to a weight hourly space velocity (WHSV) of 3 000 000 Ncc/h/(g Au+Cu or Au). After being loaded in the microreactor, the catalysts underwent an activation treatment at 350 °C for 10 h (heat rate 5 °C/min) in an oxidizing atmosphere of 6% v/v O₂ balanced with He. For the activity measurements, the reactor was heated from room temperature to 300 °C with a heating rate of 2 °C/min and kept at 300 °C for 30 min and then cooled down to 100 °C with the same rate and kept at 100 °C for 30 min. Transient activity data were collected every 4 min during the whole experiment. Before each test cycle, the catalyst bed was exposed to a stream of 6% v/v O₂ in He at 350 °C for 1 h. For the kinetics measurements, the CO conversion was measured under steady state conditions (2 h dwell time for each selected temperature) while flowing a mixture of 1% v/v CO and 6% v/v O₂ and balance He. The WHSV was increased to 24 000 000 Ncc/h/(g Au+Cu or Au) in order to keep the CO conversion below 15%. Kinetic measurements were repeated at least three times using different aliquots of the same catalyst batch in order to verify the reproducibility of the data.

2.3. Characterization. Transmission Electron Microscopy (TEM). Overview bright-field (BF) TEM images were recorded using a JEOL JEM-1011 instrument with a thermionic W source operated at 100 kV. The high resolution TEM (HRTEM) images were recorded using an image C_s-corrected JEOL JEM-2200FS TEM with a Schottky emitter, operated at 200 kV. EDS analyses were carried out in high-angle annular dark field-scanning TEM (HAADF-STEM) mode using the same microscope, equipped with a Quantax 400 STEM system and a XFlash 5060 silicon-drift detector (SDD, 60 mm² active area). For EDS analyses, non-Cu grids and an analytical holder with a Be cup were used. The reported EDS maps were obtained by integrating the Au Lα, Cu Kα, Fe Kα, and O Kα peaks in the spectra. Tilt series of HAADF-STEM images were acquired using a FEI Tecnai G2 F20 instrument with a Schottky emitter operated at 200 kV acceleration voltage.

Elemental Analysis. The chemical composition of the colloidal NCs as well as the metal loadings of the catalysts was measured by inductively coupled plasma-optical emission spectroscopy (ICP-OES) using an iCAP 6000 Thermo Scientific spectrometer. A specific weight (in the case of powder catalyst) or volume (in the case of colloidal

solutions) was digested in HCl/HNO₃ 3:1 (v/v) overnight, diluted with deionized water (14 μ S), and filtered using PTFE filter before measurement.

Optical Absorption Spectroscopy. The measurements were performed using a Varian Cary 5000 UV–vis–NIR spectrophotometer in single path configuration within the range of 200–800 nm at a scanning rate of 10 nm/s. The measurement procedure was as follows: first, the solvent was added in a 1.5 mL cuvette, and the background signal was collected. Then, a specific volume of the colloidal solution was added to the cuvette and slowly mixed to get a homogeneous mixture from which the spectrum was collected.

X-ray Diffraction (XRD). XRD patterns were recorded on a Rigaku SmartLab X-ray diffractometer equipped with a 9 kW Cu K α rotating anode (operating at 40 kV and 150 mA) and D/teX Ultra 1D detector set in X-ray reduction mode. The diffraction patterns were collected at room temperature in Bragg–Brentano geometry over an angular range: $2\theta = 20^\circ$ – 85° , with a step size of 0.02° and a scan speed of $0.2^\circ/\text{min}$. XRD data analysis was carried out using PDXL 2.1 software from Rigaku. Semiquantitative analysis based on the reference intensity ratio (RIR) was carried out to estimate the amount of cuprospinel, hematite, and gold in the AuCu/Magnetite sample.

X-ray Absorption Fine Structure Spectroscopy (XAFS). Measurements were performed at the XAFS1 beamline at the Brazilian Synchrotron Light Laboratory (LNLS) with Si(111) as monochromator. The X-ray absorption near edge structure (XANES) spectra were collected at Fe K-edge (7112 eV), Cu K-edge (8979 eV), and Au L₃-edge (11 919 eV) in transmission mode with ion chambers detectors. The samples were packed into pellets after being diluted with boron nitride. The pellets were mounted in a cylindrical quartz reactor connected to a gas flow system, and the tube was placed inside a temperature-controlled furnace. For the in situ activation, the catalyst was heated to 350 $^\circ\text{C}$ (heat rate 5 $^\circ\text{C}/\text{min}$ under 80 Ncc/min of 5% O₂/He gas) and kept at this temperature for 2 h; typically no modification in the spectrum was detected after ~ 30 min. The spectra of references Fe₃O₄ (magnetite), γ -Fe₂O₃ (maghemite), α -Fe₂O₃ (hematite), Fe foil, CuO, Cu₂O, Cu, and Au foils were collected for comparison. The collected data were analyzed using Athena code within Demeter package.⁴⁶

Magnetic Measurements. Field and temperature dependent magnetic measurements were carried out using an ever-cooled Magnetic Property Measurement System (MPMS-XL, Quantum Design) on immobile particles. The immobile samples were prepared by mixing 100 μL of particle solution at an iron concentration of approximately 0.5 g_{Fe}/L with 60 mg gypsum in a designated polycarbonate capsule and letting it to solidify thoroughly. The zero-field-cooled (ZFC) and field-cooled (FC) temperature-dependent magnetization measurements were performed on the identical samples in the cooling field of 5 mT. The magnetization results were corrected with respect to diamagnetic contributions of Au, Cu, water, and gypsum using the automatic background subtraction routine. The curves were normalized to the iron concentration as obtained from the elemental analysis.

3. RESULTS AND DISCUSSION

3.1. Characterization of the Synthesized NCs. Figure 1 and Figure S3 display the results of electron microscopy analyses performed on the as-synthesized AuCu@FeOx dumbbell-like NCs. The synthesis protocol yielded particles with negligible faceting of the oxide domain, which grew isotropically starting from the contact point with the AuCu domain. As a consequence, the particles laid with a preferential orientation over the TEM grid, so that their 2D projection appeared as having a core–shell architecture. However, HAADF-STEM images extracted from the tilted series of Movie IS1 (Figure 1a–c) clearly highlighted that the NCs were actually dumbbell-shaped, i.e., with the metallic domain only partially nested inside the oxide one. They were indeed composed of two nearly spherical domains, with no extended

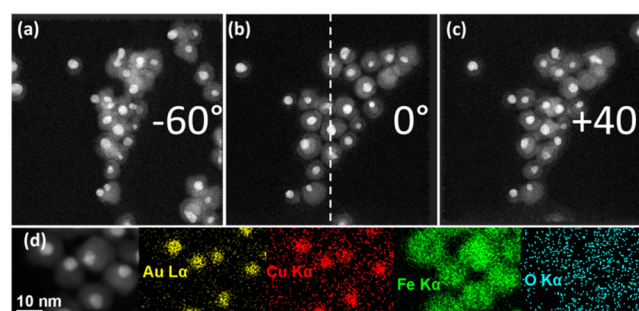


Figure 1. (a–c) HAADF-STEM images extracted from the tilted series of Movie IS1. The dashed line indicates the position of the tilt axis. The full frame size is 327.68 nm. (d) HAADF-STEM image and corresponding quantitative EDS maps (intensity proportional to atomic %) for Au (yellow), Cu (red), Fe (green), and O (blue), showing localization of Au and Cu in the metal domain and distribution of Fe and O in the oxide domain of colloidal dumbbell NCs.

facets, attached to each other. The HAADF-STEM image and the corresponding elemental mapping (Figure 1d) obtained from STEM-EDS revealed that the Au and Cu atoms were localized in the same region of the NC (i.e., the brightest region in the HAADF-STEM image), while the darker region was mainly consisting of Fe and O. The mean size of the Fe-based domain was statistically measured to be 14.6 ± 2.6 nm (Figure S3c), while for the AuCu domain, the mean size was found to be 6.1 ± 1.1 nm (Figure S3d), which corroborates the preservation of the size of the starting AuCu seeds (see Figure S4). The XRD pattern of the AuCu@FeOx NCs, shown in Figure S3e, highlighted the presence of two phases that can be indexed to magnetite and tetra-aurocupride, in agreement with HRTEM analysis (Figure S3b). Therefore, the crystalline structure of the AuCu NCs seeds (Figure S4) was preserved during the synthesis of AuCu@FeOx dumbbells.

The elemental composition of the dumbbell NCs was quantitatively analyzed by ICP-OES, and the results revealed that the Cu/Au atomic ratio was 0.95, close to the value of 0.96 measured in the starting AuCu seeds. Besides TEM imaging, further indication of AuCu attachment to oxide domain was provided by visible light absorption spectroscopy. As shown in Figure S5, the plasmon peak of the AuCu NCs at 546 nm was shifted to 590 nm and broadened. The shift suggests a change of the medium surrounding the AuCu domain resulting in a variation of the local dielectric environment.⁴⁷ This could be attributed to the attachment of the AuCu NCs to the Fe₃O₄ domain as observed in electron microscopy images. On the other hand, broadening and decaying of the intensity is reported to be related to tunneling of the electron at the interface, suggesting a charge transfer between two domains.⁴⁷ Also in this case, the mechanism implies the attachment of the AuCu domain to the Fe₃O₄ domain.

To characterize the magnetic response of the dumbbells, magnetization versus field (M – H curve), zero-field-cooled (ZFC), and field-cooled (FC) temperature-dependent magnetization curves were recorded (see Figure S6). The particles exhibited a high linear susceptibility (χ) and saturation magnetization (M_s) of 80 emu/g, as deduced from the M – H curve (Figure S6a). The superparamagnetic blocking temperature (T_b), estimated from the maximum of the ZFC curve (Figure S6b), was around 220 K, manifesting the superparamagnetic behavior of the particles at room temperature.

The primary results showed that the particles could additionally be promising candidates for a variety of biomedical applications such as magnetic hyperthermia and magnetic resonance imaging.

3.2. Characterization of the AuCu@FeOx/Alumina Catalyst. We supported the as-synthesized dumbbells on alumina and analyzed the sample by HAADF-STEM (Figure 2)

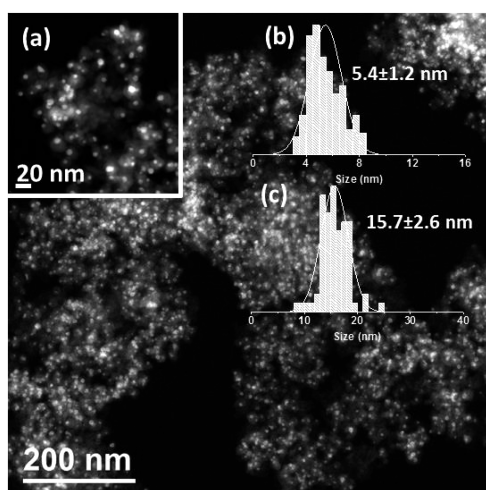


Figure 2. HAADF-STEM image of AuCu@FeOx/Alumina catalyst after activation; 10 h at 350 °C exposed to O₂ = 6% v/v balanced with He; WHSV = 3 000 000 Ncc/h/g(Au+Cu). The insets show (a) a higher magnification image and the size distribution histograms of (b) metal and (c) metal oxide domains.

after the initial activation procedure, necessary to remove the organic ligands from the catalyst surface prior to CO oxidation tests. The dumbbell structure was preserved upon activation of the catalyst and the two distinct domains, as observed in the case of the as-synthesized NCs, were still present in each dimer. Noteworthy, the high surface area of the alumina support could not be exploited to obtain a good NCs dispersion due to the bigger size of the dumbbells (~14 nm) compared to the alumina pore diameter (~6.5 nm). Yet, the dumbbell morphology ensured the physical separation of the metallic domains and effectively prevented their sintering.

A small decrease of the average size of the metallic domain was measured by HAADF-STEM (inset of Figure 2b), which could be ascribed to the dealloying between Au and Cu upon the oxidative activation treatment, as already reported for supported AuCu catalysts.^{44,48–50} Therefore, the activated AuCu@FeOx/Alumina catalyst was analyzed by STEM-EDS in order to study the spatial distribution of elements after the initial activation process. EDS maps showed that both the Fe and the Au atoms were still localized respectively in the oxide and metallic domains of the dumbbells (Figure 3). On the other hand, the Cu atoms had been delocalized and dispersed. It was not possible to determine by this technique whether the Cu atoms were dispersed on the alumina support (as reported by some of us for a AuCu/Al₂O₃ catalyst)⁴⁴ or on the FeOx domain of the dumbbells.

The XRD pattern of the activated AuCu@FeOx/Alumina catalyst (Figure S7) shows the superposition of the AuCu, γ -Fe₂O₃, and γ -Al₂O₃ peaks. Indeed, due to the low metal loading, the small particle sizes, and the presence of alumina, the XRD profile is mostly dominated by the broad γ -Al₂O₃ peaks, limiting the analysis. Nevertheless, at least for the iron

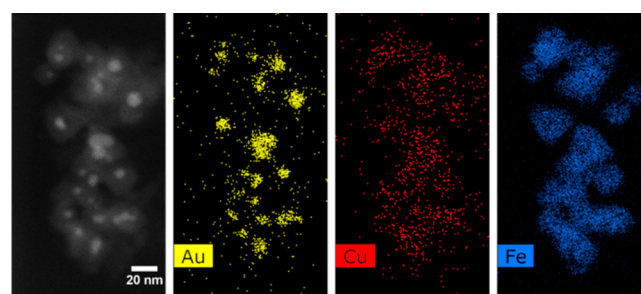


Figure 3. HAADF-STEM images and corresponding quantitative EDS maps for Au, Cu, and Fe after activation (intensity proportional to atomic %).

oxide crystalline phase, the result indicates the transformation of magnetite, as found for the AuCu@FeOx NCs (Figure S3e) to maghemite. It is clear that hematite is not formed after activation.

To shed more light on the transformations caused by the oxidative activation, in situ XAFS measurements were performed on the AuCu@FeOx/Alumina catalyst during such an activation process. Figure 4 shows the XANES spectra collected at different stages of the catalyst activation: (i) initial, at room temperature (blue line), (ii) at 250 °C (red line), (iii) after 1 h at 350 °C (purple line), (iv) after 2 h at 350 °C (green line), and (v) at the end of activation at room temperature (black line). Spectra are reported at the Au L₃-edge (Figure 4a), Cu K-edge (Figure 4b), and Fe K-edge (Figure 4c), and the comparison of the final spectra with the corresponding standards is shown in the insets. Focusing first on the evolution of the XANES Au L₃-edge profile during activation (Figure 4a), it is possible to see that at the initial stage of the activation the fresh catalyst exhibited an increased white line intensity when compared to metallic Au (around 11925 eV). As the activation proceeded, a dampening of this feature was observed, which was attributed to the progressive dealloying of AuCu, thus forming metallic Au.⁴⁸ The similarity between the catalyst after activation and the Au foil standard is clear in the inset of Figure 4a.

In line with the Au L₃-edge results, the XANES spectrum at Cu K-edge (Figure 4b) of the fresh catalyst was consistent to that reported in the literature for AuCu bulk alloys.⁵¹ The spectrum is indeed characterized by the decrease in the intensity of the absorption around 8980 eV compared to Cu foil. Upon activation, the formation of Cu⁺ species occurred at 250 °C, as indicated by the sharp peak at higher energy (8983 eV). These results, in agreement with the Au L₃-edge XANES data, support the dealloying process along with the formation of Cu⁺ species at low temperatures. The inset in Figure 4b evidences the similarity between the spectrum at 250 °C during activation and the Cu₂O standard. As the oxidizing treatment proceeded, the position of the absorption edge shifted to higher energies and approached the value measured on the CuO standard (above 8980 eV). Such a shift was consistent with the increase of copper oxidation state, which suggested the presence of Cu²⁺ species. The absence of sharp features below 8990 eV indicated the coordination of Cu²⁺ ions in a more centrosymmetric configuration compared to the bulk reference.

This observation was in line with the incorporation of the Cu²⁺ ions into the octahedral sites of the spinel structure of the iron oxide domains of the AuCu@FeOx dumbbells to form a

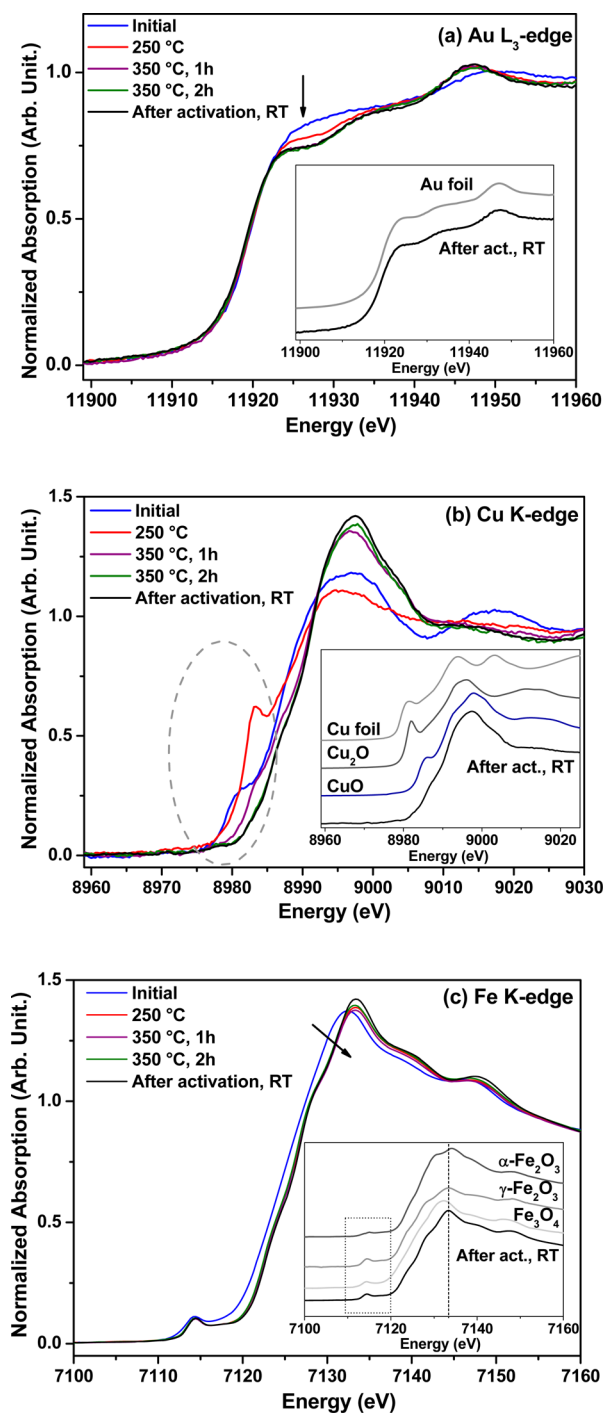


Figure 4. XANES spectra of the AuCu@FeOx/Alumina catalyst during the activation at (a) Au L₃-, (b) Cu K-, and (c) Fe K-edges. In the corresponding insets, the spectrum collected at room temperature at the end of the activation process is compared to the standards (Au foil; Cu foil, Cu₂O, and CuO; α-Fe₂O₃, γ-Fe₂O₃, and Fe₃O₄, respectively).

Cu-poor cuprospinel phase.^{52–54} It is important to note, however, that the absence of well-defined pre-edge features was also observed for highly dispersed Cu²⁺ species on the surface of other oxide supports^{50,55,56} and for Cu(OH)₂.⁵⁷ The differences observed between the spectrum of the catalyst after activation and the CuO standard may thus be accounted for either by the formation of a Cu-poor cuprospinel phase or by the dispersed nature of the Cu²⁺ species interacting with

either the iron oxide, the Au domains, or the alumina support, altering their electronic environment.⁵⁸

The Fe K-edge XANES spectrum of the AuCu@FeOx/Alumina catalyst at the initial stage of the activation process was similar to that of the magnetite (Fe₃O₄) standard (see also Figure S8a). At 250 °C, during activation (Figure 4c), there was a shift in the absorption edge to higher energies, which indicated an increase in the oxidation state of iron already at this temperature. The position of the absorption edge remained then unchanged until the end of the activation. The comparison with the standards showed that the magnetite was transformed to maghemite (γ-Fe₂O₃) (inset of Figure 4c and Figure S8b). The small deviations from the bulk reference patterns were expected due to the nanometric nature of the iron oxide domains. Nevertheless, it was clear from XANES data that magnetite and maghemite were the dominant iron oxide phases before and after the activation, respectively. Concerning the formation of maghemite instead of hematite (α-Fe₂O₃) after activation, as also indicated by XRD (Figure S7), the transition from γ- to α-phase upon heating has been described in the literature to be dependent on factors such as particle morphology and size,⁵⁹ nevertheless, there is no clear threshold of particle size and temperature that would dictate the formation of one or the other structure in nanoparticles. One hypothesis is that the γ- to α-transition may be induced by the increase in particle size upon heating, and the formation of α-Fe₂O₃ would take place once the γ-Fe₂O₃ reaches a critical size (ranging from 10 to 25 nm).^{59,60} Still, the Fe K-edge XANES results presented herein clearly evidenced that the activation of AuCu@FeOx/Alumina catalyst did not lead to the formation of α-Fe₂O₃ as the dominant phase.

3.3. Catalytic Activity Results. The catalytic activity of AuCu@FeOx NCs (1.12 wt % of Au+Cu from ICP) was systematically studied in the CO oxidation reaction. The evolution of catalyst activity during three transient tests is reported in Figure 5a. The sample showed about 10% conversion at room temperature and achieved 100% conversion around 200 °C. The same activity was recorded when repeating the test consecutively for two additional cycles, proving that the catalyst was stable after the first activation treatment.

Steady state kinetic measurements allowed the evaluation of the reaction rates and of the apparent activation energies for the tested samples. To benchmark the catalytic activity of the dumbbells sample, we performed kinetic measurements on a bulk magnetite supported AuCu catalyst (1.05 wt % of Au+Cu from ICP) and on an Au@FeOx/Alumina sample (1.02 wt % of Au from ICP) characterized by gold domains of 6.6 ± 1.0 nm. The stability of these catalysts after the first activation treatment was also experimentally verified (see Figure S9 and ref 45). From Arrhenius-type plots reported in Figure 5b we evaluated the apparent activation energy to be about 32 kJ/mol for the AuCu@FeOx/Alumina and 27 kJ/mol for the Au@FeOx/Alumina, while we estimated a value of 83 kJ/mol for the AuCu/Magnetite catalyst. Considering the transformations observed during the activation step over the AuCu@FeOx catalyst and the oxidizing nature of the catalytic test's atmosphere, it is not surprising that the AuCu@FeOx and Au@FeOx samples showed similar reaction rates and activation energy. The turnover frequencies (TOF) for the dumbbell catalysts were also evaluated at 120 °C based on the method described in the Supporting Information, taking into account the estimated exposure of metal domain in the dumbbell morphology. The values of 0.23 and 0.43 s⁻¹ were obtained for

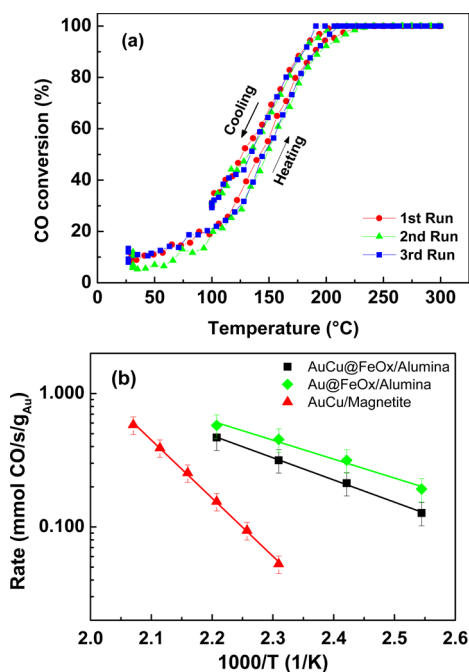


Figure 5. (a) Transient CO oxidation activity profiles for AuCu@FeOx/Alumina and (b) steady-state CO oxidation rates for AuCu@FeOx/Alumina (black square), Au@FeOx/Alumina (green diamonds), and AuCu/Magnetite (red triangle) catalysts. Experimental conditions: CO = 1% v/v; O₂ = 6% v/v; (a) WHSV = 3 000 000 and (b) 24 000 000 Ncc/h/g(metal).

AuCu@FeOx/Alumina and Au@FeOx/Alumina, respectively, which is in the same order of magnitude as the TOFs reported for Au-based catalysts.^{45,61} This experimental evidence suggests that also in the case of AuCu@FeOx dumbbells the catalytic activity is associated with the gold/iron oxide interface,^{45,62} with an apparently negligible role of the Cu presence in the nanosized iron oxide support. Moreover, the comparison against the bulk magnetite supported AuCu catalyst highlighted how the nanosizing of the support resulted in an enhanced catalytic activity and significant decrease of the activation energy.

3.4. Characterization of AuCu/Magnetite. In order to understand the nature of the difference between the catalytic activity of AuCu@FeOx/Alumina and AuCu/Magnetite samples, we analyzed the latter one by means of different techniques. The results of the XRD analyses performed on the AuCu/Magnetite catalyst before and after the activation process are displayed in Figure 6. The magnetite phase was detected in the fresh catalyst (Figure 6a) while the diffraction peaks associated with the AuCu NCs could not be easily seen compared to the support, due to the low NCs loading (~1 wt %) and the small crystals' size (~6 nm). However, the magnification of the 2θ region between 39° and 42° revealed a broad peak at 2θ of ~41°, which was attributed to the presence of tetragonal tetra-auricupride phase (as for the starting colloidal NCs, see Figure S4). The broadness of this peak compared to the ones assigned to magnetite was due to the large difference in the sizes of the crystalline phases. The XRD pattern of the activated AuCu/Magnetite catalyst (Figure 6b) highlighted that the magnetite phase of the support was largely transformed into hematite upon the oxidative activation treatment, in line with the previous discussion regarding the formation of the α phase as a function of the particle size. The

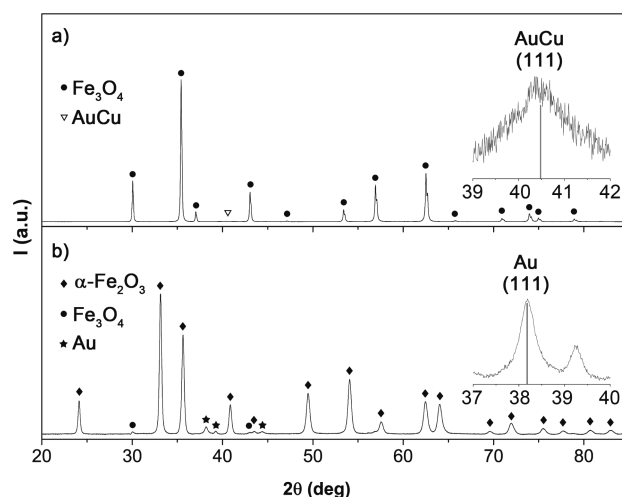


Figure 6. X-ray diffraction (XRD) patterns of AuCu/Magnetite (a) before and (b) after in situ activation treatment (10 h at 350 °C exposed to O₂ = 6% v/v balanced with He; WHSV = 3 000 000 Ncc/h/g(Au+Cu)). Experimental data are compared with the database powder XRD patterns for tetragonal AuCu (ICSD code: 42574), Au (ICSD code: 44362), magnetite (ICSD code: 65341), and hematite (ICSD code: 82136).

magnification of the 2θ region between 37° and 40° (inset of Figure 6b) highlighted a shift in the (111) peak position due to dealloy and segregation of Cu from Au which resulted in the formation of Au NCs, in analogy with the AuCu@FeOx/Alumina catalyst. The Au (111) peak also became narrower, indicating the sintering of the NCs. Since no Cu or Cu oxide phases could be detected by XRD, the possible incorporation of Cu in the iron oxide structure was also evaluated. Such an incorporation would result in the formation of a cuprospinel phase, which has the same crystalline structure of magnetite and, as a consequence, a similar diffraction pattern (see comparison of reference patterns in Figure S10). To verify this hypothesis, we carried out a semiquantitative analysis based on the reference intensity ratio (RIR) over the activated AuCu/Magnetite sample. The amount of cuprospinel phase evaluated according to this method was about 1 order of magnitude higher than the theoretical amount that could be actually formed considering the Cu loading of the sample (see Table S1). While this calculation indicated the certain presence of residual magnetite, it did not rule out the presence of the cuprospinel phase. We thus repeated the XRD analysis after further annealing the sample for 10 h at 350 °C in air in order to force the oxidation of the residual magnetite phase and its transformation to hematite. As shown in Figure S11, a residual peak was still present in the sample, and the RIR analysis (Table S1) resulted in a quantification of the cuprospinel phase consistent with the amount of Cu in the sample. Noteworthy, the phase assignment was further confirmed by the XRD analysis performed over an Au/Magnetite sample that underwent the same annealing treatment. In this case, no residual magnetite phase could be detected as clearly shown in Figure S11.

The AuCu/Magnetite was further analyzed by the HAADF-STEM imaging, before and after activation. The AuCu NCs were not well dispersed on the grains of the magnetite support (Figure 7a,c), as a higher number of NCs was found in vicinity of each other in some areas of the support. The size distribution of the NCs was statistically measured by analyzing TEM images

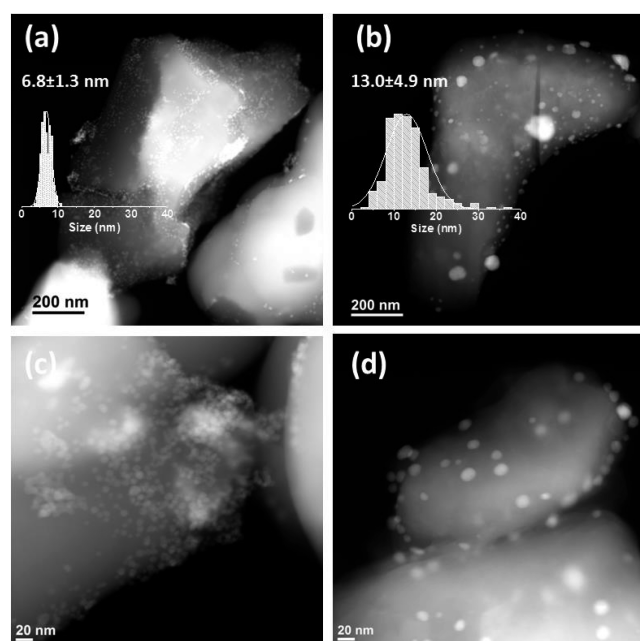


Figure 7. HAADF-STEM images of AuCu/magnetite catalyst (a, c) before and (b, d) after activation; 10 h at 350 °C exposed to O₂ = 6% v/v balanced with He; WHSV = 3 000 000 Ncc/h/g(Au+Cu). NCs size distribution histograms are displayed as insets.

(inset of Figure 7a) and the obtained value of 6.8 ± 1.3 nm (close to the starting size of 6.5 ± 1.7 nm) confirmed that the colloidal deposition procedure did not cause sintering. However, it was clear from TEM analyses that the deposition method and the low surface area of the support prevented a good dispersion of the NCs on the support, unlike the case of the dumbbells sample where the morphology of the NCs guaranteed the physical separation of the metallic particles. The activated AuCu/magnetite was found to have suffered from severe sintering, as can be seen from Figure 7b,d. In this case, the NCs' mean size increased indeed to 13.0 ± 4.9 nm with few NCs as large as ~ 40 nm. This was a consequence of the poor NCs dispersion and could indirectly suggest a poor interaction of the NCs with the support, which can be the main cause of the lower catalytic activity measured compared to the AuCu@FeOx/alumina catalyst.

4. CONCLUSIONS

To sum up, we have shown that AuCu NCs can be used as seeds to prepare Au_{0.5}Cu_{0.5}@Fe₃O₄ dumbbell-like NCs, with the bimetallic domain being preserved during the synthesis step. Dealloying between Au and Cu was observed upon an oxidative activation treatment, performed in order to remove the organic ligands and to study the synthesized material in the CO oxidation reaction. In this regard, the comparison of the catalytic performances of the synthesized material against an Au@FeOx dumbbell-like catalyst (having similar Au domain size) and against a bulk magnetite supported AuCu catalyst provided us different information. Comparable reaction rates per unit mass of gold and similar activation energies were obtained over the AuCu@FeOx and Au@FeOx samples. These results suggested that the presence of highly dispersed Cu²⁺ species on the nanosized iron oxide support had an apparently negligible effect on the catalytic activity of CO oxidation. This oxidative reaction was thus most likely dominated by the gold/

iron oxide interface. It should be noted, however, that the dealloying resulted in a decreased average size of the metallic domain, which is known to be beneficial for the CO oxidation over Au catalysts. Notably, this phenomenon could provide a strategy to prepare Au-based dumbbell-like catalysts with reduced Au size and thus enhanced CO oxidation activity. It is also worth to mention that catalytic reactions conducted in a more reducing environment will probably reveal different performances of the AuCu@FeOx and Au@FeOx dumbbell-like NCs. In this case, the dealloying process may be partially reversed, as in the case of AuCu NCs,^{44,48} and differences in activity due to the alloy formation may be evidenced. We have shown that the activation treatment did not cause any change in the morphology of the AuCu@FeOx dumbbell NCs, and yet more importantly, the catalyst did not suffer from sintering of the metallic domains, most likely thanks to the dumbbell morphology. On the other hand, we found that the AuCu NCs on magnetite support suffered from severe sintering. Furthermore, upon activation the initial phase of iron oxide, i.e., magnetite, was transformed mainly into maghemite in the nanosized support, while the bulk magnetite support was transformed to hematite as the dominant phase. In both cases, the Cu was found to be dealloyed from the AuCu domain upon activation, and we found indications of Cu incorporation into the iron oxide domain. These results strongly highlighted the enhanced structural stability of the metallic domains in the dumbbells morphology. Therefore, and regardless of the similarity of the transformations at the nanoscale, it was indeed the nanosized support which prevented the sintering of the Au domains and resulted in a higher activity of the nanosized supported catalyst.

■ ASSOCIATED CONTENT

Supporting Information

The Supporting Information is available free of charge on the ACS Publications website at DOI: 10.1021/acsami.6b09813.

Removal of Cl species from catalyst's surface, detailed characterization of AuCu@FeOx and AuCu seeds, optical absorption spectroscopy results, XRD of AuCu@FeOx/Alumina catalyst, magnetic measurement of as-prepared AuCu@FeOx NCs, XANES spectrum of the fresh AuCu@FeOx/Alumina catalyst against bulk magnetite, XANES spectrum of the activated AuCu@FeOx/Alumina catalyst against bulk maghemite and hematite, stability test of AuCu/Magnetite, reference XRD patterns for cuprospinel and magnetite, semiquantitative analysis of AuCu/Magnetite based on reference intensity ratio (RIR), further XRD analysis of AuCu/Magnetite and Au/Magnetite (PDF)

Aligned tilt series of HAADF-STEM images (AVI)

■ AUTHOR INFORMATION

Corresponding Author

*E-mail: massimo.colombo@iit.it (M.C.).

Notes

The authors declare no competing financial interest.

■ ACKNOWLEDGMENTS

The authors acknowledge Pablo Guardia for his contribution to the synthesis of the colloidal NCs. The authors acknowledge financial support from European Union through the EU-ITN network Mag(net)icFun (PITN-GA-2012–290248). T.M.K.

and P.D. were supported by CAPES (Coordenação de Aperfeiçoamento de Pessoal de Nível Superior, 99999.013076/2013-02) scholarship. P.D. and D.Z. were supported by CNPq (Conselho Nacional de Desenvolvimento Científico e Tecnológico, 870359/1997-5 and 309373/2014-0) funding. The authors gratefully acknowledge LNLS (Brazilian Synchrotron Light Laboratory) for access to the XAFS1 beamline.

REFERENCES

- (1) Tauster, S. J.; Fung, S. C. Strong Metal-Support Interactions: Occurrence Among the Binary Oxides of Groups IIA–VB. *J. Catal.* **1978**, *55* (1), 29–35.
- (2) Hayek, K.; Kramer, R.; Paál, Z. Metal-Support Boundary Sites in Catalysis. *Appl. Catal., A* **1997**, *162* (1–2), 1–15.
- (3) Overbury, S. H.; Ortiz-Soto, L.; Zhu, H.; Lee, B.; Amiridis, M.; Dai, S. Comparison of Au Catalysts Supported on Mesoporous Titania and Silica: Investigation of Au Particle Size Effects and Metal-Support Interactions. *Catal. Lett.* **2004**, *95* (3–4), 99–106.
- (4) Liu, J. Advanced Electron Microscopy of Metal-Support Interactions in Supported Metal Catalysts. *ChemCatChem* **2011**, *3* (6), 934–948.
- (5) Cargnello, M.; Doan-Nguyen, V. V. T.; Gordon, T. R.; Diaz, R. E.; Stach, E. A.; Gorte, R. J.; Fornasiero, P.; Murray, C. B. Control of Metal Nanocrystal Size Reveals Metal-Support Interface Role for Ceria Catalysts. *Science* **2013**, *341* (6147), 771–773.
- (6) Munnik, P.; de Jongh, P. E.; de Jong, K. P. Recent Developments in the Synthesis of Supported Catalysts. *Chem. Rev.* **2015**, *115* (14), 6687–6718.
- (7) Wu, Z.; Deng, J.; Liu, Y.; Xie, S.; Jiang, Y.; Zhao, X.; Yang, J.; Arandian, H.; Guo, G.; Dai, H. Three-Dimensionally Ordered Mesoporous Co_3O_4 -Supported Au–Pd Alloy Nanoparticles: High-Performance Catalysts for Methane Combustion. *J. Catal.* **2015**, *332*, 13–24.
- (8) Wang, F.; Xu, L.; Zhang, J.; Zhao, Y.; Li, H.; Li, H. X.; Wu, K.; Xu, G. Q.; Chen, W. Tuning the Metal-Support Interaction in Catalysts for Highly Efficient Methane Dry Reforming Reaction. *Appl. Catal., B* **2016**, *180*, 511–520.
- (9) Wu, Q.; Zhang, C.; Zhang, B.; Li, X.; Ying, Z.; Liu, T.; Lin, W.; Yu, Y.; Cheng, H.; Zhao, F. Highly selective Pt/Ordered Mesoporous TiO_2 – SiO_2 Catalysts for Hydrogenation of Cinnamaldehyde: The Promoting Role of Ti^{2+} . *J. Colloid Interface Sci.* **2016**, *463*, 75–82.
- (10) Julkapli, N. M.; Bagheri, S. Graphene Supported Heterogeneous Catalysts: An Overview. *Int. J. Hydrogen Energy* **2015**, *40* (2), 948–979.
- (11) Cheng, N.; Liu, J.; Banis, M. N.; Geng, D.; Li, R.; Ye, S.; Knights, S.; Sun, X. High Stability and Activity of Pt Electrocatalyst on Atomic Layer Deposited Metal Oxide/Nitrogen-Doped Graphene Hybrid Support. *Int. J. Hydrogen Energy* **2014**, *39* (28), 15967–15974.
- (12) Sartipi, S.; Alberts, M.; Meijerink, M. J.; Keller, T. C.; Pérez-Ramírez, J.; Gascon, J.; Kapteijn, F. Towards Liquid Fuels from Biosyngas: Effect of Zeolite Structure in Hierarchical-Zeolite-Supported Cobalt Catalysts. *ChemSusChem* **2013**, *6* (9), 1646–1650.
- (13) Moon, S. Y.; Naik, B.; Jung, C.-H.; Qadir, K.; Park, J. Y. Tailoring Metal–Oxide Interfaces of Oxide-Encapsulated Pt/Silica Hybrid Nanocatalysts with Enhanced Thermal Stability. *Catal. Today* **2016**, *265*, 245–253.
- (14) Li, Y.; Shen, W. Morphology-Dependent Nanocatalysts: Rod-Shaped Oxides. *Chem. Soc. Rev.* **2014**, *43* (5), 1543–1574.
- (15) Rolison, D. R. Catalytic Nanoarchitectures – The Importance of Nothing and the Unimportance of Periodicity. *Science* **2003**, *299* (5613), 1698–1701.
- (16) Pietron, J. J.; Stroud, R. M.; Rolison, D. R. Using Three Dimensions in Catalytic Mesoporous Nanoarchitectures. *Nano Lett.* **2002**, *2* (5), 545–549.
- (17) Yu, Y.; Sun, K.; Tian, Y.; Li, X. Z.; Kramer, M. J.; Sellmyer, D. J.; Shield, J. E.; Sun, S. One-Pot Synthesis of Urchin-Like FePd – Fe_3O_4 and Their Conversion into Exchange-Coupled Li_0 – FePd – Fe Nanocomposite Magnets. *Nano Lett.* **2013**, *13* (10), 4975–4979.
- (18) Bao, S.; Yan, N.; Shi, X.; Li, R.; Chen, Q. High and Stable Catalytic Activity of Porous $\text{Ag}/\text{Co}_3\text{O}_4$ Nanocomposites Derived from MOFs for CO Oxidation. *Appl. Catal., A* **2014**, *487*, 189–194.
- (19) Cui, C.-H.; Yu, S.-H. Engineering Interface and Surface of Noble Metal Nanoparticle Nanotubes toward Enhanced Catalytic Activity for Fuel Cell Applications. *Acc. Chem. Res.* **2013**, *46* (7), 1427–1437.
- (20) Carabineiro, S. A. C.; Bogdanchikova, N.; Tavares, P. B.; Figueiredo, J. L. Nanostructured Iron Oxide Catalysts with Gold for The Oxidation of Carbon Monoxide. *RSC Adv.* **2012**, *2* (7), 2957–2965.
- (21) Yu, H.; Chen, M.; Rice, P. M.; Wang, S. X.; White, R. L.; Sun, S. Dumbbell-like Bifunctional Au – Fe_3O_4 Nanoparticles. *Nano Lett.* **2005**, *5* (2), 379–382.
- (22) Wang, C.; Xu, C.; Zeng, H.; Sun, S. Recent Progress in Syntheses and Applications of Dumbbell-like Nanoparticles. *Adv. Mater.* **2009**, *21* (30), 3045–3052.
- (23) Wang, C.; Daimon, H.; Sun, S. Dumbbell-like Pt – Fe_3O_4 Nanoparticles and Their Enhanced Catalysis for Oxygen Reduction Reaction. *Nano Lett.* **2009**, *9* (4), 1493–1496.
- (24) Li, Y.; Zhang, Q.; Nurmikko, A. V.; Sun, S. Enhanced Magneto-optical Response in Dumbbell-like Ag – CoFe_2O_4 Nanoparticle Pairs. *Nano Lett.* **2005**, *5* (9), 1689–1692.
- (25) Zhao, J.; Liu, H.; Ye, S.; Cui, Y.; Xue, N.; Peng, L.; Guo, X.; Ding, W. Half-Encapsulated Au Nanoparticles by Nano Iron Oxide: Promoted Performance of The Aerobic Oxidation of 1-Phenylethanol. *Nanoscale* **2013**, *5* (20), 9546–9552.
- (26) George, C.; Genovese, A.; Casu, A.; Prato, M.; Povia, M.; Manna, L.; Montanari, T. CO Oxidation on Colloidal $\text{Au}_{0.80}\text{Pd}_{0.20}$ – Fe_xO_y Dumbbell Nanocrystals. *Nano Lett.* **2013**, *13* (2), 752–757.
- (27) Wang, C.; Yin, H.; Dai, S.; Sun, S. A General Approach to Noble Metal–Metal Oxide Dumbbell Nanoparticles and Their Catalytic Application for CO Oxidation. *Chem. Mater.* **2010**, *22* (10), 3277–3282.
- (28) Wu, B.; Zhang, H.; Chen, C.; Lin, S.; Zheng, N. Interfacial Activation of Catalytically Inert Au (6.7 nm)– Fe_3O_4 Dumbbell Nanoparticles for CO Oxidation. *Nano Res.* **2009**, *2* (12), 975–983.
- (29) Lin, F.-h.; Doong, R.-A. Bifunctional Au – Fe_3O_4 Heterostructures for Magnetically Recyclable Catalysis of Nitrophenol Reduction. *J. Phys. Chem. C* **2011**, *115* (14), 6591–6598.
- (30) Chen, S.; Si, R.; Taylor, E.; Janzen, J.; Chen, J. Synthesis of Pd/ Fe_3O_4 Hybrid Nanocatalysts with Controllable Interface and Enhanced Catalytic Activities for CO Oxidation. *J. Phys. Chem. C* **2012**, *116* (23), 12969–12976.
- (31) Kim, M.; Song, H. Precise Adjustment of Structural Anisotropy and Crystallinity on Metal– Fe_3O_4 Hybrid Nanoparticles and Its Influence on Magnetic and Catalytic Properties. *J. Mater. Chem. C* **2014**, *2* (25), 4997–5004.
- (32) Wu, B.; Tang, S.; Chen, M.; Zheng, N. Amphiphilic Modification and Asymmetric Silica Encapsulation of Hydrophobic Au – Fe_3O_4 Dumbbell Nanoparticles. *Chem. Commun.* **2014**, *50* (2), 174–176.
- (33) Tao, F. Synthesis, Catalysis, Surface Chemistry and Structure of Bimetallic Nanocatalysts. *Chem. Soc. Rev.* **2012**, *41* (24), 7977–7979.
- (34) Sun, X.; Guo, S.; Liu, Y.; Sun, S. Dumbbell-like PtPd – Fe_3O_4 Nanoparticles for Enhanced Electrochemical Detection of H_2O_2 . *Nano Lett.* **2012**, *12* (9), 4859–4863.
- (35) Yin, H.; Wang, C.; Zhu, H.; Overbury, S. H.; Sun, S.; Dai, S. Colloidal Deposition Synthesis of Supported Gold Nanocatalysts Based on Au – Fe_3O_4 Dumbbell Nanoparticles. *Chem. Commun.* **2008**, *36*, 4357–4359.
- (36) George, C.; Dorfs, D.; Bertoni, G.; Falqui, A.; Genovese, A.; Pellegrino, T.; Roig, A.; Quarta, A.; Comparelli, R.; Curri, M. L.; Cingolani, R.; Manna, L. A Cast-Mold Approach to Iron Oxide and Pt/Iron Oxide Nanocontainers and Nanoparticles with a Reactive Concave Surface. *J. Am. Chem. Soc.* **2011**, *133* (7), 2205–2217.
- (37) Figuerola, A.; Fiore, A.; Di Corato, R.; Falqui, A.; Giannini, C.; Micotti, E.; Lascialfari, A.; Corti, M.; Cingolani, R.; Pellegrino, T.;

Cozzoli, P. D.; Manna, L. One-Pot Synthesis and Characterization of Size-Controlled Bimagnetic FePt–Iron Oxide Heterodimer Nanocrystals. *J. Am. Chem. Soc.* **2008**, *130* (4), 1477–1487.

(38) Figueroa, S. J. A.; Stewart, S. J.; Rueda, T.; Hernando, A.; de la Presa, P. Thermal Evolution of Pt-Rich FePt/Fe₃O₄ Heterodimers Studied Using X-Ray Absorption Near-Edge Spectroscopy. *J. Phys. Chem. C* **2011**, *115* (13), 5500–5508.

(39) Schladt, T. D.; Graf, T.; Köhler, O.; Bauer, H.; Dietzsch, M.; Mertins, J.; Branscheid, R.; Kolb, U.; Tremel, W. Synthesis and Magnetic Properties of FePt@MnO Nano-Heteroparticles. *Chem. Mater.* **2012**, *24* (3), 525–535.

(40) Nakhjavan, B.; Tahir, M. N.; Panthöfer, M.; Gao, H.; Gasi, T.; Ksenofontov, V.; Branscheid, R.; Weber, S.; Kolb, U.; Schreiber, L. M.; Tremel, W. Controlling Phase Formation in Solids: Rational Synthesis of Phase Separated Co@Fe₂O₃ Heteroparticles and CoFe₂O₄ Nanoparticles. *Chem. Commun.* **2011**, 47 (31), 8898.

(41) Nakhjavan, B.; Tahir, M. N.; Natalio, F.; Panthöfer, M.; Gao, H.; Dietzsch, M.; Andre, R.; Gasi, T.; Ksenofontov, V.; Branscheid, R.; Kolb, U.; Tremel, W. Ni@Fe₂O₃ Heterodimers: Controlled Synthesis and Magnetically Recyclable Catalytic Application for Dehalogenation Reactions. *Nanoscale* **2012**, *4* (15), 4571.

(42) Nakhjavan, B.; Tahir, M. N.; Natalio, F.; Gao, H.; Schneider, K.; Schladt, T.; Ament, I.; Branscheid, R.; Weber, S.; Kolb, U.; Sönnichsen, C.; Schreiber, L. M.; Tremel, W. Phase Separated Cu@Fe₃O₄ Heterodimer Nanoparticles from Organometallic Reactants. *J. Mater. Chem.* **2011**, *21* (24), 8605.

(43) Bracey, C. L.; Ellis, P. R.; Hutchings, G. J. Application of Copper-Gold Alloys in Catalysis: Current Status and Future Perspectives. *Chem. Soc. Rev.* **2009**, *38* (8), 2231–2243.

(44) Najafshiri, S.; Brescia, R.; Guardia, P.; Marras, S.; Manna, L.; Colombo, M. Nanoscale Transformations of Alumina-Supported AuCu Ordered Phase Nanocrystals and Their Activity in CO Oxidation. *ACS Catal.* **2015**, *5* (4), 2154–2163.

(45) Najafshiri, S.; Guardia, P.; Scarpellini, A.; Prato, M.; Marras, S.; Manna, L.; Colombo, M. The Effect of Au Domain Size on the CO Oxidation Catalytic Activity of Colloidal Au–FeOx Dumbbell-like Heterodimers. *J. Catal.* **2016**, *338*, 115–123.

(46) Ravel, B.; Newville, M. ATHENA, ARTEMIS, HEPHAESTUS: Data Analysis for X-Ray Absorption Spectroscopy Using IFEFFIT. *J. Synchrotron Radiat.* **2005**, *12* (4), 537–541.

(47) Wei, Y.; Klajn, R.; Pinchuk, A. O.; Grzybowski, B. A. Synthesis, Shape Control, and Optical Properties of Hybrid Au/Fe₃O₄ “Nanoflowers”. *Small* **2008**, *4* (10), 1635–1639.

(48) Bauer, J. C.; Mullins, D.; Li, M.; Wu, Z.; Payzant, E. A.; Overbury, S. H.; Dai, S. Synthesis of Silica Supported AuCu Nanoparticle Catalysts and The Effects of Pretreatment Conditions for The CO Oxidation Reaction. *Phys. Chem. Chem. Phys.* **2011**, *13* (7), 2571–2581.

(49) Bauer, J. C.; Mullins, D. R.; Oyola, Y.; Overbury, S. H.; Dai, S. Structure Activity Relationships of Silica Supported AuCu and AuCuPd Alloy Catalysts for the Oxidation of CO. *Catal. Lett.* **2013**, *143* (9), 926–935.

(50) Destro, P. Gold-copper Colloidal Nanoparticles: Insights About the Alloy Formation and Application in CO Oxidation Reaction. PhD Thesis, Chemistry Institute, University of Campinas, 2016.

(51) Kuhn, M.; Sham, T. K. Charge Redistribution and Electronic Behavior in a Series of Au–Cu Alloys. *Phys. Rev. B: Condens. Matter Mater. Phys.* **1994**, *49* (3), 1647–1661.

(52) Krishnan, V.; Selvan, R. K.; Augustin, C. O.; Gedanken, A.; Bertagnolli, H. EXAFS and XANES Investigations of CuFe₂O₄ Nanoparticles and CuFe₂O₄–MO₂ (M = Sn, Ce) Nanocomposites. *J. Phys. Chem. C* **2007**, *111* (45), 16724–16733.

(53) Estrella, M.; Barrio, L.; Zhou, G.; Wang, Q.; Wen, W.; Hanson, J. C.; Frenkel, A. I.; Rodriguez, J. A. In Situ Characterization of CuFe₂O₄ and Cu/Fe₃O₄ Water–Gas Shift Catalysts. *J. Phys. Chem. C* **2009**, *113* (32), 14411–14417.

(54) Frenkel, A. I.; Wang, Q.; Marinkovic, N.; Chen, J. G.; Barrio, L.; Si, R.; Cámara, A. L.; Estrella, A. M.; Rodriguez, J. A.; Hanson, J. C. Combining X-ray Absorption and X-ray Diffraction Techniques for in

Situ Studies of Chemical Transformations in Heterogeneous Catalysis: Advantages and Limitations. *J. Phys. Chem. C* **2011**, *115* (36), 17884–17890.

(55) Belin, S.; Bracey, C. L.; Briois, V.; Ellis, P. R.; Hutchings, G. J.; Hyde, T. I.; Sankar, G. CuAu/SiO₂ Catalysts for The Selective Oxidation of Propene to Acrolein: The Impact of Catalyst Preparation Variables on Material Structure and Catalytic Performance. *Catal. Technol.* **2013**, *3* (11), 2944–2957.

(56) Gervasini, A.; Manzoli, M.; Martra, G.; Ponti, A.; Ravasio, N.; Sordelli, L.; Zaccheria, F. Dependence of Copper Species on The Nature of the Support for Dispersed CuO Catalysts. *J. Phys. Chem. B* **2006**, *110* (15), 7851–7861.

(57) Scariot, M.; Francisco, M. S. P.; Jordão, M. H.; Zanchet, D.; Logli, M. A.; Vicentini, V. P. An Investigation of The Activation Process of High Temperature Shift Catalyst. *Catal. Today* **2008**, *133–135*, 174–180.

(58) Zhang, R.; Miller, J. T.; Baertsch, C. D. Identifying The Active Redox Oxygen Sites in a Mixed Cu and Ce Oxide Catalyst by *in Situ* X-Ray Absorption Spectroscopy and Anaerobic Reactions with CO in Concentrated H₂. *J. Catal.* **2012**, *294*, 69–78.

(59) Machala, L.; Tuček, J.; Zbořil, R. Polymorphous Transformations of Nanometric Iron(III) Oxide: A Review. *Chem. Mater.* **2011**, *23* (14), 3255–3272.

(60) Belin, T.; Millot, N.; Bovet, N.; Gailhanou, M. In Situ and Time Resolved Study of The γ/α -Fe₂O₃ Transition in Nanometric Particles. *J. Solid State Chem.* **2007**, *180* (8), 2377–2385.

(61) Schubert, M. M.; Hackenberg, S.; van Veen, A. C.; Muhler, M.; Plzak, V.; Behm, R. J. CO Oxidation over Supported Gold Catalysts—“Inert” and “Active” Support Materials and Their Role for the Oxygen Supply during Reaction. *J. Catal.* **2001**, *197* (1), 113–122.

(62) Zhao, K.; Tang, H.; Qiao, B.; Li, L.; Wang, J. High Activity of Au/ γ -Fe₂O₃ for CO Oxidation: Effect of Support Crystal Phase in Catalyst Design. *ACS Catal.* **2015**, *5* (6), 3528–3539.

Supporting Information

Dumbbell-like $\text{Au}_{0.5}\text{Cu}_{0.5}@\text{Fe}_3\text{O}_4$ Nanocrystals: Synthesis, Characterization and Catalytic Activity in CO Oxidation

*Sharif Najafshirtari,^{a,c} Tathiana Midori Kokumai,^b Sergio Marras,^a Priscila Destro,^b Mirko Prato,^a
Alice Scarpellini,^a Rosaria Brescia,^a Aidin Lak,^d Teresa Pellegrino,^d Daniela Zanchet,^b Liberato
Manna,^a Massimo Colombo^{*a}*

a) Department of Nanochemistry, Istituto Italiano di Tecnologia, Via Morego 30, 16163, Genova, Italy.

b) Institute of Chemistry, University of Campinas (UNICAMP), P.O. Box 6154, 13083-970 Campinas,
São Paulo, Brazil.

c) Dipartimento di Chimica e Chimica Industriale, Università di Genova, via Dodecaneso 31- I-16146
Genova, Italy.

d) Drug Discovery and Development, Istituto Italiano di Tecnologia, Via Morego 30, 16163 Genova,
Italy.

massimo.colombo@iit.it (corresponding author email)

Movie IS1: Aligned tilt series of HAADF-STEM images on the AuCu@FeO_x heterostructures, collected from -70° to +50°. in steps of 2° at high angles and 5° from -30° to +30°. The full frame size is 327.68 nm and the rotation axis is vertical and centered in the image.

Removal of Chlorine species from catalyst surface

The presence of Cl on the dumbbell catalyst even after the calcination step was verified by two different methods. We firstly washed the catalyst sample with warm water ($\sim 40\text{ }^{\circ}\text{C}$), collected the supernatant solution and mixed it with a AgNO_3 solution: precipitation of AgCl was clearly observed in case of AuCu@FeOx/Alumina (see Figure S1) and Au@FeOx/Alumina (not shown), while no precipitate was formed in case of AuCu/Magnetite sample. We also obtained indirect evidence of the presence of residual Cl in the non-washed catalysts by collecting the catalytic activity data in CO oxidation. As shown in Figure S2, the non-washed AuCu@FeOx/Alumina catalyst showed much lower activity than the washed sample, in line with the well-known poisoning effect of Cl on the CO oxidation activity of Au based catalysts¹⁻². The same trend was observed over the Au@FeOx/Alumina sample (not shown). In case of AuCu/Magnetite catalyst, no significant difference in the catalytic activity was observed between the washed and non-washed samples. Compared to the AuCu/Magnetite sample, the only additional source of Cl in case of the dumbbells samples was the solvent in which the dumbbell NCs were dispersed (i.e. chloroform). Based on these results, it seems plausible that the calcination step in the static air caused the decomposition/combustion of residual chloroform and consequently Cl poisoning of the AuCu@FeOx/Alumina and Au@FeOx/Alumina samples. Another possibility is that the Cl had a different affinity for the different supports (i.e. alumina vs. magnetite), leading thus to a different effect of the washing procedure. Though the detailed understanding of this phenomenon is not in the scope of the present work, washing of the dumbbell catalyst was nevertheless essential to attain the highest level of activity in CO oxidation.

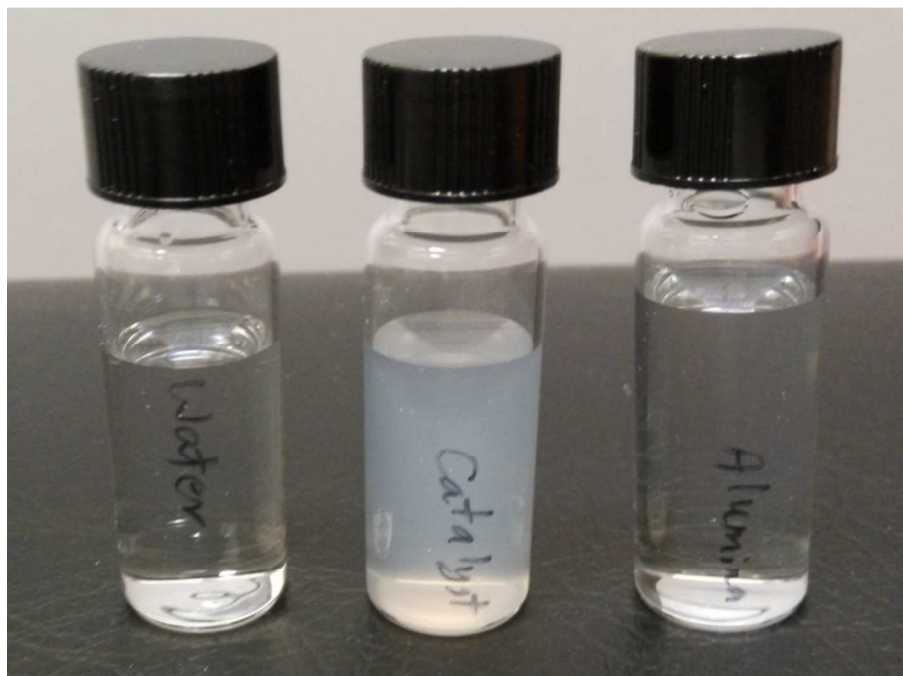


Figure S1. Successful removal of the Cl from the calcined dumbbell catalyst. The left vial contains plain deionized water used for the washing step; the middle vial contains the supernatant recovered after the first washing step of the AuCu@FeOx/Alumina dumbbell catalyst and addition of 400 μ l of AgNO₃ (0.5 M). The right vial contains the supernatant recovered after washing of the bare Alumina support and addition of the same AgNO₃ solution.

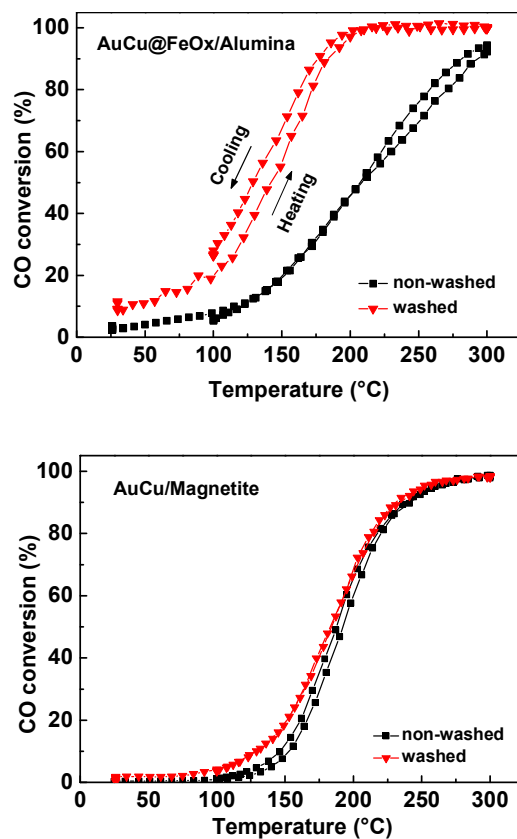


Figure S2. Comparison of the CO oxidation activity for the washed and non-washed AuCu@FeOx/Al₂O₃ and AuCu/Magnetite catalysts. Experimental conditions: CO = 1% v/v; O₂ = 6% v/v; WHSV= 3'000'000 Ncc/h/g(Au+Cu).

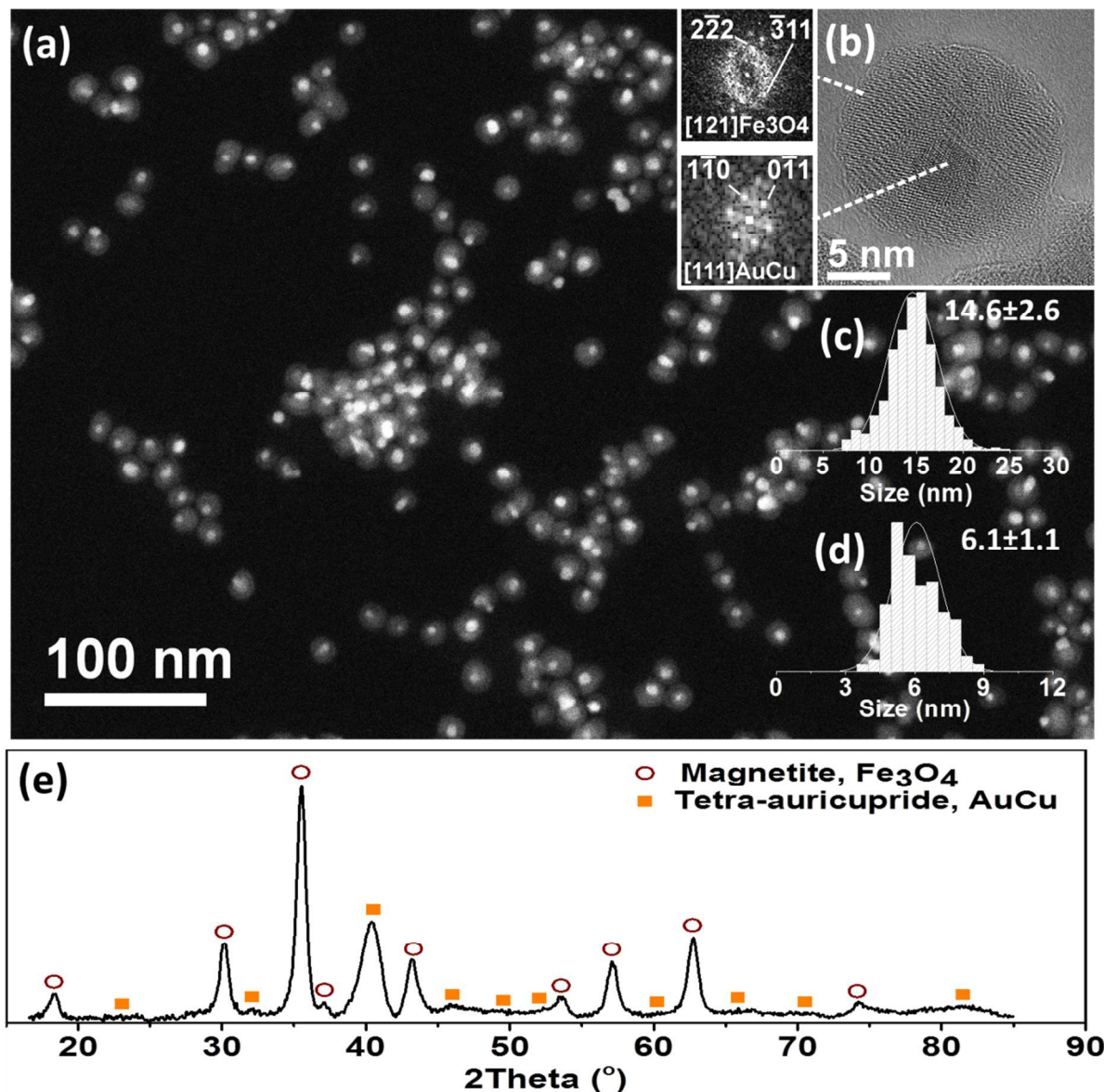


Figure S3. (a) Typical HAADF-STEM image of the as-prepared AuCu@FeOx colloidal NCs. (b) HRTEM image of a single NC. (c) Size distribution histograms of FeOx and (d) AuCu domains obtained by graphical analysis. (e) X-ray diffraction (XRD) pattern of the as-synthesized AuCu@FeOx dumbbell NCs. Experimental data are compared with the database powder XRD patterns for tetragonal AuCu (ICSD code: 42574) and magnetite Fe₃O₄ (ICSD code: 65341).

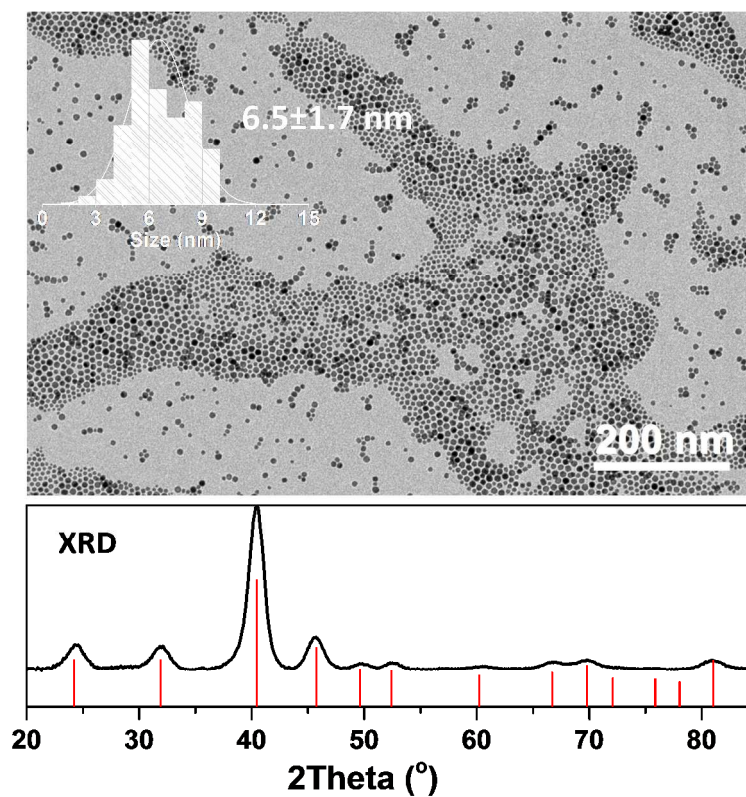


Figure S4. Typical bright-field (BF)-TEM image of the as-prepared AuCu colloidal NCs; top left inset: size distribution obtained by measuring ~3500 NCs; the XRD pattern of AuCu seeds at the bottom. Experimental data are compared with the database powder XRD pattern for tetragonal AuCu (ICSD code: 42574);

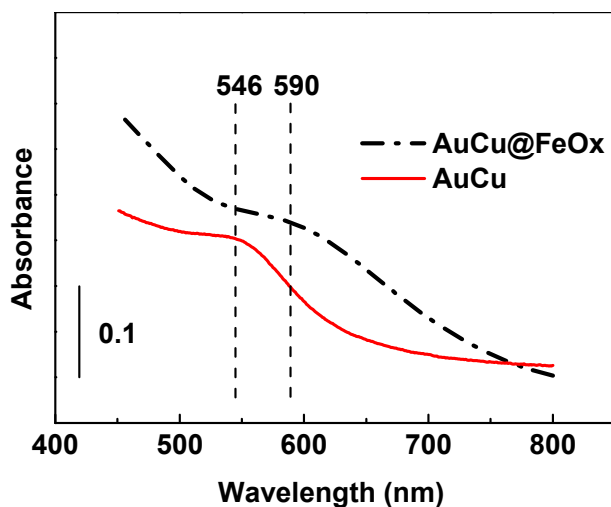


Figure S5. Absorption spectra for AuCu (thin red line) and AuCu@FeOx (thick black dash-dot line) NCs dispersed in hexane and chloroform, respectively. The background spectrum of the solvent was collected before each measurement.

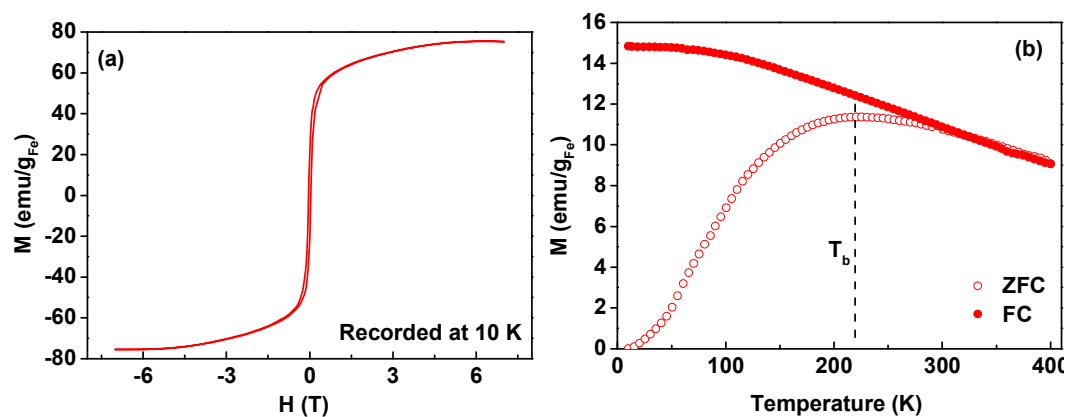


Figure S6. (a) Magnetization versus field (M - H) measured at 10 K and (b) zero-field-cooled (ZFC) and field-cooled (FC) temperature dependent magnetization curves recorded on the dumbbell NCs in the cooling field of 5 mT .

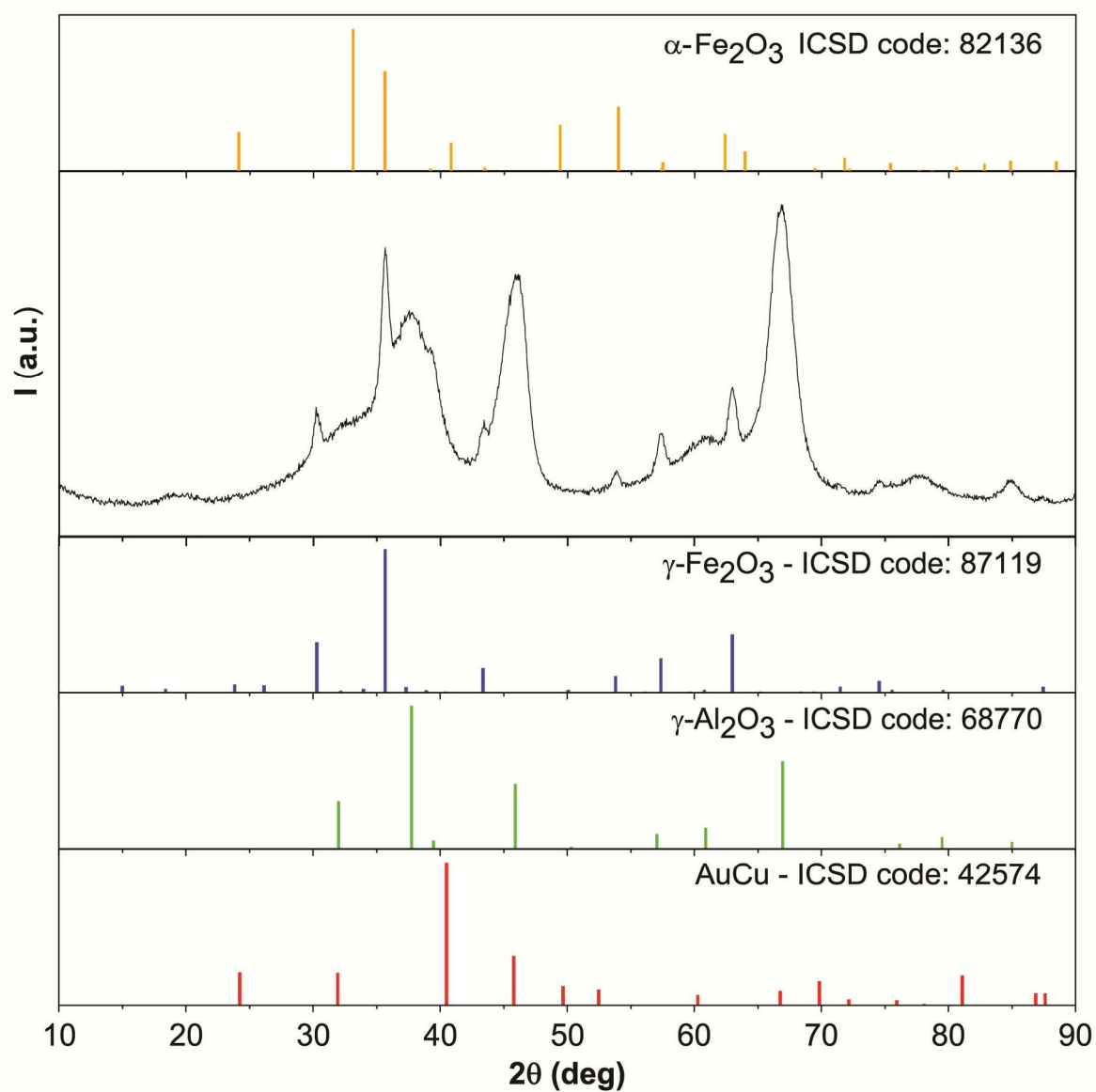


Figure S7. X-ray diffraction (XRD) patterns of AuCu@FeOx/Alumina catalyst after activation. Experimental data are compared with the database powder XRD patterns for maghemite (ICSD code: 87119), hematite (ICSD code: 82136), γ -Al₂O₃ (ICSD code: 68770) and AuCu (ICSD code: 42574).

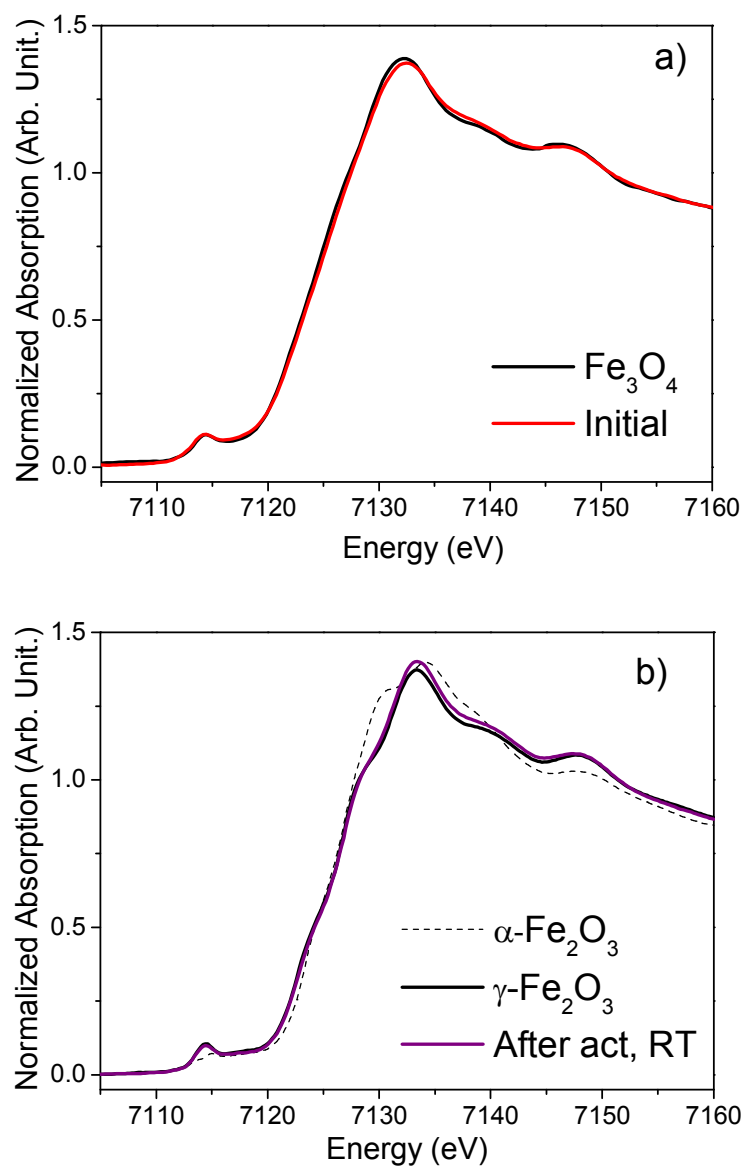


Figure S8. Comparison of the Fe K-edge XANES spectra of a) the fresh AuCu@FeOx/Alumina catalyst against bulk magnetite and b) the activated AuCu@FeOx/Alumina catalyst against bulk maghemite (γ -Fe₂O₃) and hematite (α -Fe₂O₃).

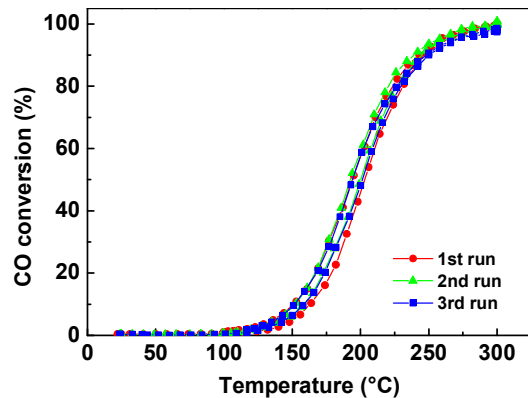


Figure S9. Stability of the AuCu/Magnetite catalysts proved by reproducibility of the catalytic activity data in CO oxidation in three consecutive cycles of transient test after oxidative pre-treatment; Experimental conditions: CO = 1% v/v; O₂ = 6% v/v; WHSV= 3'000'000 Ncc/h/g(Au+Cu).

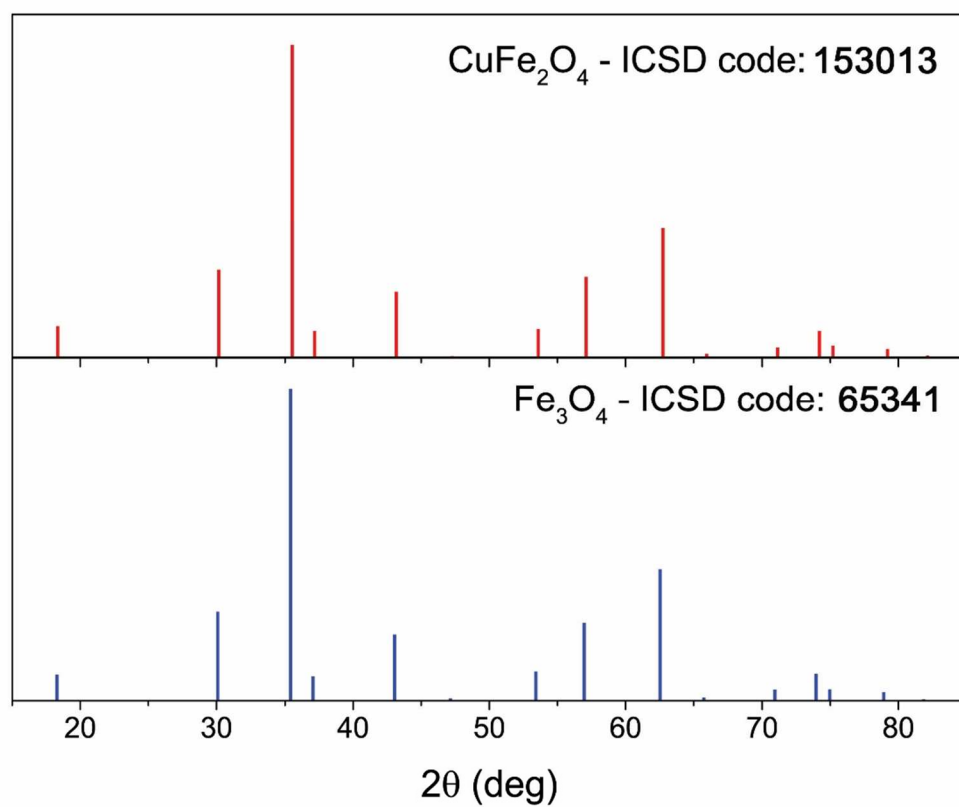


Figure S10. XRD reference patterns for magnetite (ICSD code 65341) and cuprospinel (ICSD code 153013).

Table S1. Semi-quantitative analysis based on Reference Intensity Ratio (RIR).

Sample	Cuprospinel (ICSD code 153013)	Gold (ICSD code 44362)	Hematite (ICSD code 82136)	Cu moles from RIR	Cu moles from ICP
Activated AuCu/Magnetite	6.8 ± 0.1 wt. %	1.1 ± 0.01 wt. %	92.1 ± 0.01 wt. %	0.0284	0.0041
AuCu/Magnetite further annealed for 10h at 350°C in air	0.8 ± 0.3 wt. %	0.9 ± 0.04 wt. %	98.3 ± 0.01 wt. %	0.0033	0.0041

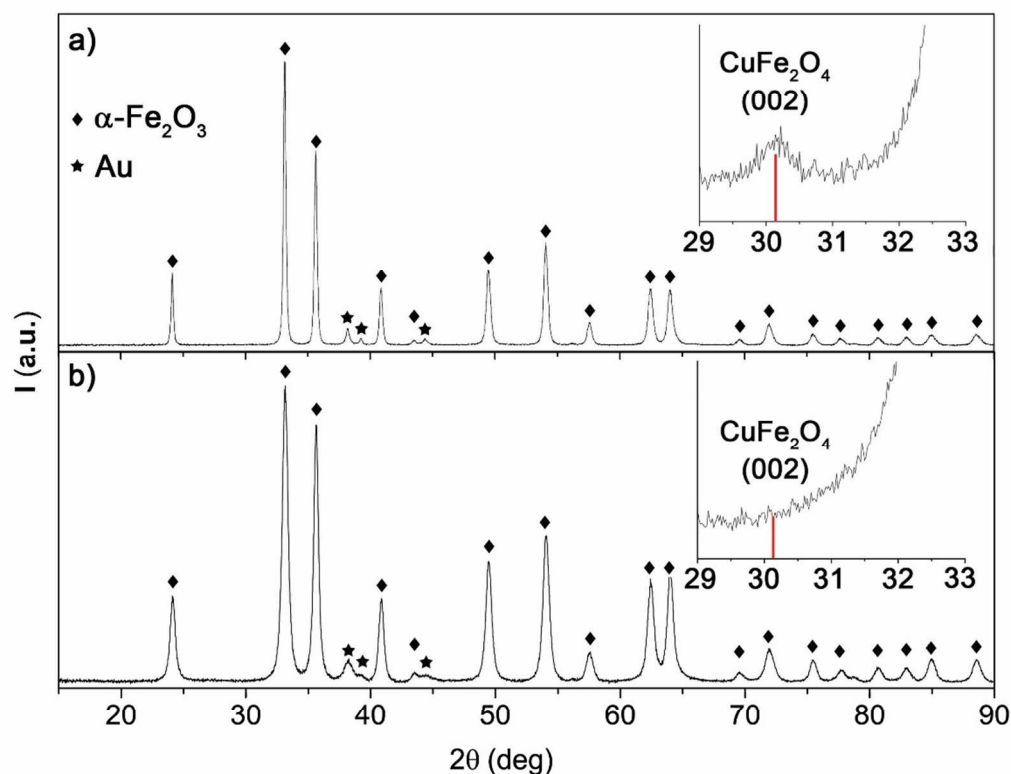


Figure S11. X-ray diffraction (XRD) patterns of (a) AuCu/Magnetite and (b) Au/Magnetite after further calcination in air for 10 h at 350 °C. Experimental data are compared with the database powder XRD patterns for hematite (ICSD code: 82136), cuprospinel (ICSD code: 153013) and Au (ICSD code:

44362). The data presented in the insets were obtained using a reduced scan speed of 0.01 °/min. The reduced scan speed was necessary in order to increase the signal to noise ratio and resolve the weak pattern of the cuprospinel phase.

Evaluation of Turn over Frequency (TOF):

We report the rate of reaction as:

$$\frac{molCO_2produced}{s} = \frac{CO_{feed} (N_{cc}/min) \cdot CO_{conversion}}{60 (s/min) \cdot 22.414 (cc/mol)}$$

We assumed spherical Au domains and considered that only half of the sphere was exposed to the reacting atmosphere (i.e. half of the sphere is embedded in the iron oxide domain). The content of gold was measured by ICP. We consider bulk gold density and the area occupied by surface gold atoms to be 1.9 E-5 mol/m² [3]. TOF was thus calculated as:

$$TOF = \frac{molCO_2produced}{s} \cdot \frac{1}{molAu}$$

References

- (1) Oh, H. S.; Yang, J. H.; Costello, C. K.; Wang, Y. M.; Bare, S. R.; Kung, H. H.; Kung, M. C. Selective Catalytic Oxidation of CO: Effect of Chloride on Supported Au Catalysts, *J Catal.* **2002**, 210 (2), 375-386.
- (2) Broqvist, P.; Molina, L. M.; Grönbeck, H.; Hammer, B. Promoting and Poisoning Effects of Na and Cl Coadsorption on CO Oxidation over MgO-Supported Au Nanoparticles, *J. Catal.* **2004**, 227 (1), 217-226.
- (3) Güttel, R.; Paul, M.; Galeano, C.; Schüth, F. Au, @ZrO₂ Yolk–Shell Catalysts for CO Oxidation: Study of Particle Size Effect by Ex-post Size Control of Au Cores, *J. Catal.* **2012**, 289, 100-104

Chapter V

Metal-support interaction in Au catalysis: the effect of the morphology of a nano-oxide domain in CO oxidation activity

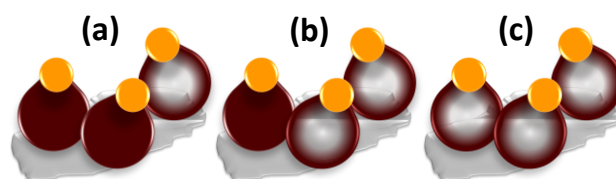
5.1. Introduction

From the pioneering works of Haruta in low temperature CO oxidation [1] and of Hutchings in hydrochlorination of acetylene [2], extensive studies and developments have been carried out on Au based catalysts [3,4]. In this regard, CO oxidation has been studied not only as a target reaction but also as a model one in order to understand the nature of the active sites and further to design more efficient catalysts [5]. Among many reported catalytic materials, the Au-Iron oxide system has been reported among the most active ones for CO oxidation [6,7]. Various important parameters have been studied and reported to contribute in the activity of such catalytic materials; among them are: the size of the Au, the surface charge of the Au species, the nature of the support and the Au-support interaction [8-10]. For example, Herzing et al. [11] suggested that there is a direct correlation between higher CO oxidation activity with decreasing of the Au domain size to 2-5 nm as a critical size. On the other hand, Carabineiro et al. [5] observed that the catalyst with the smallest size of the Au had not been the most active one and attributed the highest activity to the presence of Au^+ in the system. In contrast, Guo et al. [10] have reported that the charge state of the Au species has more significant contribution to the activity regardless of their sizes i.e. metallic Au species are more active than the ionic ones. But, Herzing et al. [11] have also suggested that the activity can be mostly related to the sub-nanometer Au species beyond the resolution of the electron microscopy measurements. More recently, it has been proposed by He et al. [12] that the catalytic properties are the result of complex population versus activity hierarchy relationships, and the observed activity is a weighted average from the contributions of all Au species having different sizes i.e. atoms, clusters and nanoparticles (NPs). Regarding the support effect at the same Au size, Mizera et al. [13] attributed the higher CO oxidation activity observed for maghemite support to the increase of weakly bound oxygen compared to magnetite due to a different structural properties. As another example, Huang et al. [9] have shown that the catalytic oxidation of 1,4-butanediol to γ -butyrolactone is also greatly affected by the nature of iron oxide supports. Due to complexity of these catalytic systems, it is challenging yet very important to effectively study the contribution of each of these factors by careful isolation of their effects [8]. This is hardly achieved by studying the catalyst prepared by conventional methods as obtaining a uniform set of active species could be quite difficult and challenging. The application of colloidal chemistry on the other hand, provides the opportunity to obtain targeted materials with well-defined structural properties. Such materials can then be used to gain fundamental understandings of the catalytic functions [14]. Among different types of colloidal nanocrystals (NCs), those with a dumbbell-like

morphology represent a very important class of materials characterized by a nanosized metal (M) and a metal oxide (MOx) domain epitaxially attached to each other [15-17]. This morphology provides materials with superior catalytic activity, thanks to enhanced charge transfer and sintering resistance of metal domains [15,16,18-20]. Additionally, it is possible using this morphology to isolate and study the different aspects of metal-support interaction [16]. For example, we had previously shown that the CO oxidation activity is essentially related to the interface between Au and iron oxide, which is promoted by decreasing of the Au domain size at similar Au surface charge and same nanosized support [19]. In another work, we showed the superior thermal stability of the metallic NPs when attached to a nanosized support resulting in a significant improvement of the activity compared to bulk-supported NPs [16].

In this work, we studied how the morphology of the nanosized oxide support in a nanodumbbell structure influences the stability of the metal domain and the catalytic activity in CO oxidation. Specifically we investigated the effects resulting from making the oxide domains hollow. Through colloidal synthesis, we prepared a set of dumbbell-like NCs each one consisting of an AuCu NCs attached to an iron oxide based one. A fraction of the NCs were characterized by a core-shell morphology in the oxide domain having an Fe-rich core, with their population being tunable by simply adjusting one of the synthesis parameters. These NCs were deposited on alumina to prepare the catalysts and exposed to an oxidizing pretreatment, essential to activate the metal domain through the removal of the protecting ligands, before being tested in CO oxidation. Upon activation, the NCs with the Fe-rich core were transformed to dumbbell-like NCs having a hollow oxide domain. We thus prepared different catalyst batches consisting of dumbbell-like NCs having the same size and crystalline structures for the M and MOx domains, while the population of the NCs with hollow oxide domain was different among the batches (as schematically shown in Scheme 1). The NCs and catalysts were extensively characterized in order to establish a structure-activity correlation. Indeed, we observed a difference in the activity i.e. the catalyst with more hollow oxide NCs was less active. As the sizes of both domains were similar in all cases, we evaluated the charge transfer between the two domains by means of surface sensitive spectroscopy techniques such as CO DRIFT. Both measurements revealed the similar charge transfer between two domains. Structural properties of the catalysts and NCs were then studied by XRD and XAFS which revealed the same crystalline structure in both M and MOx domains for the activated catalysts. On the other hand, XAFS measurements suggested that the MOx domain was more disordered in the catalyst sample having more NCs with

hollow MOx. The effect of the hollow morphology on the reducibility of the oxide domain is currently under investigation.



Scheme 1. The schematic illustration of different batches of activated catalysts having different population of dumbbell-like NCs with hollow oxide domain. The yellow sphere represents the metal (M) domain while the brown spheres are representative of metal oxide (MOx) domains. The hollow oxide domains are illustrated with the same color but more transparent. The gray sheet is the alumina support used as inert carrier for the NCs.

5.2. Experimental

5.2.1. Chemicals

Oleylamine (OlAm, 70%), $\text{HAuCl}_4 \cdot 3\text{H}_2\text{O}$, 1-Octadecene (Technical grade 90%), Oleic acid (OlAc, technical grade 90%), Iron pentacarbonyl (>99.99% trace metals basis), solvents (ethanol, isopropanol, toluene and n-hexane) were purchased from Sigma Aldrich. CuCl_2 dihydrate (99+%) was purchased from Alfa Aesar while the $\gamma\text{-Al}_2\text{O}_3$ extrudate ($\text{SSA} = 220 \text{ m}^2/\text{g}$; average pore diameter = 6.5 nm) was purchased from Strem Chemicals and silica was obtained from Sigma Aldrich. All chemicals were used as received without further purifications.

5.2.2. Synthesis of AuCu- Iron Oxide (AuCu@FeOx) NCs

AuCu@FeOx NCs were typically synthesized by a seed mediated growth approach [16], using pre-made AuCu NCs, synthesized based on the protocols described in [21], and iron pentacarbonyl as the iron source. Typically, a specific volume of AuCu colloidal solution corresponding to 8 mg of the AuCu was mixed with 20 ml of ODE, 3 ml of OlAm, 1.0 ml of OlAc. The amount of OlAc was adjusted to different levels of 0.5 and 0.2 ml to induce less oxidation of the Fe in the oxide domain and to manipulate the population of dumbbells with Fe-rich core in the oxide domain. The mixture was then degassed under vacuum at 80 °C for 1 h to remove hexane i.e. the solvent dispersing AuCu NCs. Then, the atmosphere was switched to N_2 and the temperature was raised to 205 °C. Meanwhile, a solution of 80 μl Fe precursor in 1 ml of already degassed ODE was injected in the solution at 150 °C. The mixture was stirred for 1.5 h and then it was heated up to 300 °C and kept there for 1 h. The products were

washed twice with a mixture of isopropanol and ethanol (3:1 vol. ratio), centrifuged and dispersed in 10 ml of toluene. The samples were tagged as D1, D2 and D3 corresponding the NCs synthesized using 1.0, 0.5 and 0.2 ml of OIAc, respectively.

5.2.3. Catalyst Preparation

The alumina supported catalysts were prepared by colloidal deposition of as-prepared dumbbell NCs. Typically, a specific weight of γ -Al₂O₃ powder (manually crushed and sieved to 90 μ m) was dispersed in toluene and then a proper amount of colloidal solution (targeting either 1.0 wt.% or 2.0 wt.% Au+Cu) was added to it and the suspension was sonicated for 2 h. All suspensions were dried under dry air atmosphere and tagged as D1-F, D2-F and D3-F corresponding to fresh catalysts right after the deposition of NCs synthesized using 1.0, 0.5 and 0.2 ml of OIAc, respectively. The catalysts were also calcined in static air for 10 h at 350 °C to activate the catalyst by removing the protecting ligands from the surface of the NCs [16]. In this case, the samples were labeled as D1-A, D2-A and D3-A, representing of the activated catalysts.

5.2.4. Activity Measurements

The activity of the catalysts for CO oxidation was measured using a micro-reactor system coupled with a micro-Gas Chromatographer (μ -GC) equipped with three modules working in parallel (each consisting of an injector, a column and a thermal conductivity detector) to analyze CO, O₂ and CO₂ (SRA Instruments model R-3000). Two sets of measurement were performed, transient and step-wise steady state to obtain respectively the light-off curve and the kinetic parameters. Typically for the transient tests, the catalyst powders (1.0 wt.% Au+Cu) were diluted with alumina (2:1 weight ratio) and loaded into a quartz reactor (internal diameter = 8 mm). The feed gas was a mixture of 1% v/v CO and 6% v/v O₂ balanced with He with a flow rate of 80 Ncc/min corresponding to a weight hourly space velocity (WHSV) of 3'000'000 Ncc/h/(g Au+Cu). After being loaded in the micro-reactor, the catalysts underwent an initial pre-treatment at 350 °C for 10 h (heat rate 5 °C/min) in an oxidizing atmosphere of 6% v/v O₂ balanced with He. The reactor was then heated from room temperature to 300 °C with a heating rate of 2 °C/min while the activity data were being collected every 4 min.

For the kinetic measurements, the catalysts powder (2.0 wt.% Au+Cu) were mixed with silica powder (manually crushed and sieved to 90 μ m, 1:9 weight ratio) and loaded into the reactor. The same initial pre-treatment was performed before starting the test followed by CO conversion measurement

under steady state conditions (2 h dwell time for each selected temperature). The feed gas was the same one used for the transient tests, while the WHSV was increased to 12'000'000 Ncc/h/(g Au+Cu) in order to keep the CO conversion below 15%. Kinetic measurements were repeated two times for the same loaded batch and three times using different aliquots of the same catalyst batch, in order to verify the reproducibility and the dispersion of the data.

5.2.5. Characterization

5.2.5.1. Transmission Electron Microscopy (TEM)

Overview bright-field (BF) TEM images were recorded using a JEOL JEM-1011 instrument with a thermionic W source operated at 100 kV. The high resolution TEM (HRTEM) images were recorded using an image C_s -corrected JEOL JEM-2200FS TEM with a Schottky emitter, operated at 200 kV. EDS analyses were carried out in high-angle annular dark field-scanning TEM (HAADF-STEM) mode using the same microscope, equipped with a Quantax 400 STEM system and a XFlash 5060 silicon-drift detector (SDD, 60 mm² active area). For EDS analyses, non-Cu grids and an analytical holder with a Be cup were used. The reported EDS maps were obtained by integrating the Au $L\alpha$, Cu $K\alpha$, Fe $K\alpha$ and O $K\alpha$ peaks in the spectra. HAADF-STEM images of the calcined catalysts were acquired using a FEI Tecnai G2 F20 instrument with a Schottky emitter operated at 200 kV acceleration voltage.

5.2.5.2. Elemental Analysis

The chemical composition of the colloidal NCs as well as the metal loadings of the catalysts were measured by Inductively Coupled Plasma-Optical Emission Spectroscopy (ICP-OES) using an iCAP 6000 Thermo Scientific spectrometer. A specific weight (in case of powder catalyst) or volume (in case of colloidal solutions) was digested in HCl/HNO₃ 3:1 (v/v) overnight, diluted with deionized water (14 μ S) and filtered using PTFE filter before measurement.

5.2.5.3. X-Ray Diffraction (XRD)

XRD patterns of the NCs were recorded on a Rigaku SmartLab X-Ray diffractometer equipped with a 9 kW Cu $K\alpha$ rotating anode (operating at 40 kV and 150 mA) and D\teX Ultra 1D detector set in X-ray reduction mode. The diffraction patterns were collected at room temperature in Bragg-Brentano geometry over an angular range: $2\theta = 20^\circ$ – 85° , with a step size of 0.02° and a scan speed of $0.2^\circ/\text{min}$. XRD data analysis was carried out using PDXL 2.1 software from Rigaku. Two different sets of sample were measured, namely as-prepared NCs and calcined ones. Initially, fresh NCs were deposited

on the wafer and XRD patterns were collected. Later, the wafer was removed and placed in a furnace where it was exposed to a heat treatment under air atmosphere for 10 h at 350 °C (heating rate of 5 °C/min). The XRD patterns were then collected in this way from the calcined NCs.

5.2.5.4. X-Ray Absorption Fine Structure Spectroscopy (XAFS)

Measurements were performed at the XAFS beamline at the Eletterra synchrotron light source [22] in Trieste, Italy. The catalysts samples, total 6 samples including fresh and activated of D1-D3, were diluted with polyvinylpyrrolidone (PVP) powder and packed into pellets. Then these pellets were mounted column-wise in a special motorized sample holder which allowed for selecting a desired sample without opening the sample chamber. The X-ray absorption near edge structure (XANES) and the extended X-ray absorption fine structure (EXAFS) spectra were collected at Fe K-edge (7112 eV), Cu K-edge (8979 eV) and Au L₃-edge (11919 eV) in transmission mode with ion chambers detectors. The spectra of references Fe₃O₄ (magnetite), γ -Fe₂O₃ (maghemite), α -Fe₂O₃ (hematite), CuFe₂O₄ (cuprospinel), Fe foil, Cu and Au foils were collected for comparison and signal calibration. The collected data was normalized using Athena code within Demeter package (version 0.9.25) [23]. The EXAFS part of the spectra were obtained by converting the normalized data in energy space into k space and weighted by k^2 , then Fourier transformed in the selected k range using a Hanning window.

5.2.5.5. *In-situ* Diffuse Reflectance Infrared Fourier Transform Spectroscopy (DRIFTS)

Spectra were collected on the activated catalysts unloaded after the reaction test using a Vertex 70 infrared spectrometer (Brüker Optics) equipped with a DRIFTS cell (Praying Mantis, Harrick) and a Mercury Cadmium Telluride detector (MCT) cooled with liquid nitrogen. The outlet of the DRIFTS cell was connected to an on-line mass spectrometer (Pfeiffer Vacuum Omnistar GSD 320). Using a 4 ports selector valve, the inlet gas was switched between two different gas streams, one used for purging and/or pretreatments (6% v/v O₂ and balance He) and the other containing the probe gas (0.25% v/v CO and balance He) both with the flowrate of 80 Ncc/min. The loaded sample was pretreated prior to the measurements at 350 °C for 1 h (the heating rate of 20 °C/min) after which the cell was cooled down to room temperature at the same rate. Once the temperature and the signal became stable, the background spectrum was collected under the same atmosphere. Then, the sample was exposed to the probe gas and the spectra were collected every 10 s for the first 100 s of adsorption. The adsorption was monitored for further 35 min, by collecting a spectrum every 5 min. The samples were subsequently

purged after the measurement for 40 min while the spectra were monitored every 5 min. Each test was performed two times to verify the reproducibility of the measurement.

5.3. Results and Discussion

5.3.1. Characterization of the NCs

We had already reported the successful synthesis of dumbbell-like AuCu@FeO_x NCs and fully characterized them with several techniques [16]. We had shown that these NCs will transform upon activation to a new nanocomposite having Au in the metal domain and a Cu-poor cuprospinel phase in the oxide domain, while the dumbbell morphology could be preserved. In this work, we manipulated the synthesis conditions using the same AuCu seeds in order to obtain nanostructures with different properties in the oxide domain. Keeping all the synthesis conditions the same, we reduced the amount of the OlAc to two lower different levels which resulted in the formation of a number of NCs having a seemingly core-shell structure in the oxide domain. The population of such NCs was indeed tunable with decreasing the amount of OlAc. Figure 1 displays the TEM images of as-synthesized NCs using different levels of OlAc along with the size distributions of both M and MO_x domains of dumbbell-like NCs in insets. The mean size of M domain in the samples were obtained by statistical analysis on the TEM images and found to be the same: 5.7 ± 1.4 nm for D1 i.e. the sample with highest amount of OlAc, 5.5 ± 0.8 nm for D2 i.e. the sample with intermediate level of OlAc and 5.7 ± 1.2 nm for D3 i.e. the sample with lowest amount of OlAc. The size of M domain was also close the values obtained from the AuCu seeds (5.8 ± 1.3 nm) proving the preservation of the size (see Figure S1) as already reported elsewhere [16]. The mean size of the MO_x domain of the samples was found also to be very similar among each other: 15.2 ± 2.4 nm for D1, 16.4 ± 5.4 nm for D2 and 15.5 ± 3.6 nm for D3. To characterize the observed core of the NCs, one typical NC was analyzed by HAADF-STEM. As shown in Figure S2, the corresponding elemental mapping of a NC highlighted that the core was rich in Fe. This can suggest a lower oxidation extent of the Fe precursor from D1 to D3 as a result of using less OlAc, as reported in literature for the synthesis of Fe NPs [24].

Further and substantial proof for the different oxidation extent among the samples was found by XRD analysis on the as-prepared NCs. As shown in Figure S3, XRD patterns of all three samples were representative of two major phases i.e. tetra-auricupride (a tetragonal AuCu phase) and magnetite (an inverse spinel iron oxide phase). Nevertheless, the intensity of the 100% peak of magnetite compared to that of AuCu was decreasing from D1 to D3, as evident after normalization of the intensities based

on the 100% peak of AuCu. Noteworthy, the samples contained the same (Au+Cu)/Fe ratio, as proven by ICP analysis (see Table 1). At the same time, no traces of additional iron containing phases could be found in the XRD patterns, suggesting the amorphous nature of the Fe rich cores. Further evidence of the different oxidizing character of the synthesis environment is provided by the careful analysis of the diffraction peak assigned to the AuCu alloy. It should be mentioned indeed that the position of the AuCu main peak was slightly shifted to lower 2θ (less than 1°) with the increase of the OIAc content, which is indicative of a partial, minor dealloying between Au and Cu [25]. Nevertheless, the elemental composition of the samples were analyzed by ICP-OES and revealed that the Au:Cu ratio was the same as the initial seeds, as summarized along with the other measured properties of the NCs in Table 1.

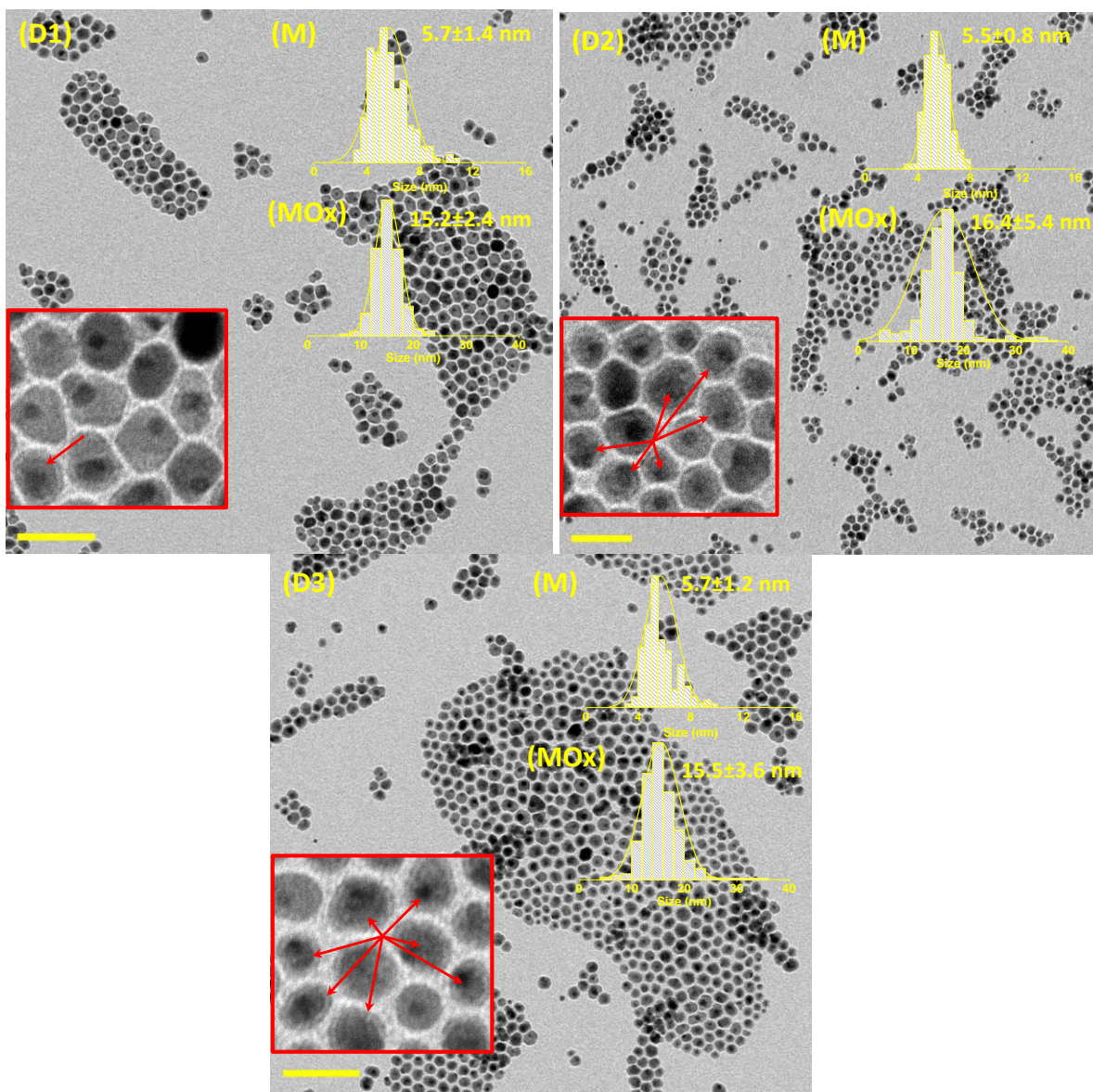


Figure 1. Typical bright-field (BF)-TEM image of the as-prepared AuCu@FeOx colloidal NCs with the size distribution of metal domain (M) and metal oxide domain (MOx); the scale bars = 100 nm. Zoom-in sections of the images are shown as insets where some of the NCs having Fe-rich core in MOx domains are marked with red arrows.

Table 1. Summary of NCs properties from elemental analyses.

Sample Tag	D1	D2	D3
M mean size	5.7±1.4 nm	5.5±0.8 nm	5.7±1.2 nm
MOx Mean size	15.2±2.4 nm	16.4±5.4 nm	15.5±3.6 nm
Au:Cu (molar)	54.3:45.7	53.5:46.5	54.3:45.7
(Au+Cu)/Fe (molar)	0.14	0.14	0.13

5.3.2. Initial characterization of the catalysts

The as-prepared NCs were further deposited on the alumina according to the procedure discussed in the Experimental section and calcined to remove the protecting ligands and activate the M domains. The elemental loadings of the fresh catalysts i.e. before activation were measured by ICP-OES which proved the same loadings for the three catalytic samples as reported in Table 2. Needless to say, the loading of Au+Cu in all cases were almost 2.0 wt.%, very close to the targeted value. A different set of samples were also prepared targeting 1.0 wt.% loading of Au+Cu for transient catalytic tests for which the same accuracy was obtained.

Table 2. Results of ICP-OES on the elemental loadings of the nominal 2 wt.% (Au+Cu) fresh catalysts in terms of wt.%.

Sample Tag	Au loading (%)	Cu loading (%)	Fe loading (%)
D1-F	1.44	0.55	6.19
D2-F	1.46	0.54	6.44
D3-F	1.45	0.55	6.7

The activated catalysts were examined by electron microscopy and the results are shown in Figure 2. Apart from a good dispersion of the metal domains (distinguishable by the spheres with brighter contrast), an interesting feature was also observed particularly for the D2 and D3 samples: the formation of dumbbell NCs having a hollow oxide domain. Nevertheless, the dumbbell morphology was preserved whether having full or hollow oxide domain. In addition, several properly tilted NCs were found in all three samples proving the existence of dumbbell rather than core-shell NCs. The population of NCs with hollow oxide domain, though not statistically measured, seemed to increase from D1 to D3 in line with the increase of NCs having a Fe-rich core in the fresh samples. This suggested that the hollow oxide NCs were formed by the oxidation of Fe in those NCs having Fe-rich cores via a mechanism known as Kirkendall effect, as thoroughly explained for a number of NPs [26-29]. While the mean sizes of M and MO_x domains were found to be the same among the samples (see insets in Figure 2), a small decrease was found in the M domain compared to the fresh NCs. We had reported for a sample similar to the D1 herein reported that dealloying of Cu occurred upon activation [16], which seemed to took place as well here for the D2 and D3 samples. The decrease of the size is in line with the estimated values from structural transformation of AuCu domain of the fresh NCs to Au domain of the activated NCs (see SI for details of calculation).

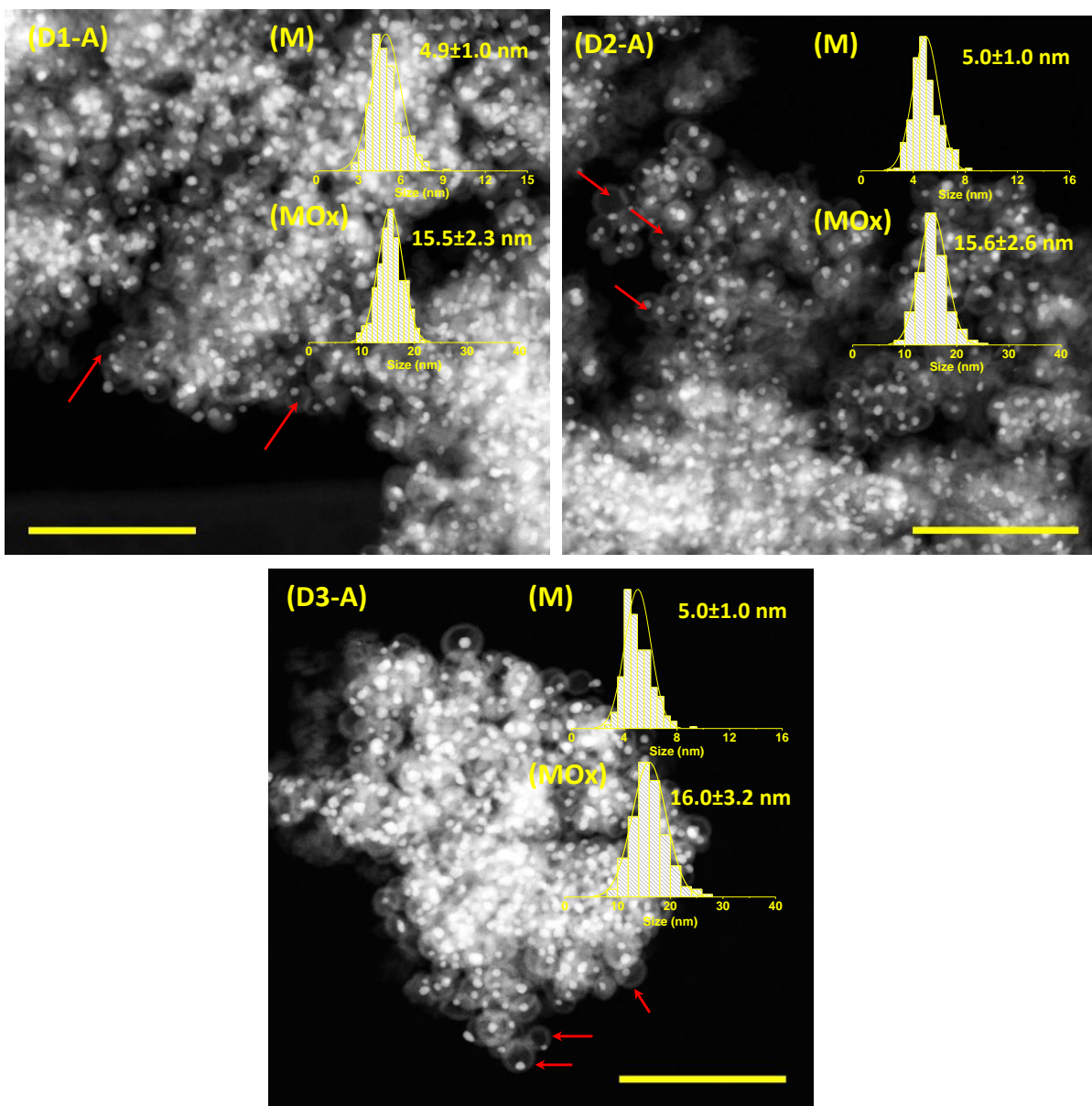


Figure 2. Typical HAADF-STEM images of the activated catalysts with the size distribution of metal (M) and metal oxide domain (MOx) as insets. The red arrows show of the NCs with hollow oxide domain; the scale bars = 100 nm.

5.3.3. Catalytic activity results

The catalytic properties of the catalysts were systematically studied in CO oxidation reaction. The light-off curves were obtained using the activated catalysts having 1.0 wt.% loading of Au+Cu. As shown in Figure 3-a, all samples had the same activity at low temperature range and achieving 100% conversion at temperature above 200 °C. But interestingly, the samples showed difference in the mid temperature range in the order of D1>D2>D3. For example, at the temperature of 150 °C, the D1

showed 58.1% of conversion while D2 and D3 gave 44.5% and 38.8%, respectively. To quantify the observed difference, kinetic measurements were performed using other batches of catalysts with 2.0 wt.% Au+Cu loadings. The same trend was observed in the kinetic tests. Indeed, D1 sample, i.e. the sample with the least population of dumbbell NCs having hollow oxide domains, exhibited the highest CO oxidation rate (see Figure 3-b). Noteworthy to mention, the activation energy (E_a) was estimated using the Arrhenius equation and found to be similar among the samples, in the order of 40 kJ/mol. In addition, turn over frequencies (TOF) were also evaluated at 140 °C according to the method described in SI taking into account the estimated exposure of M domain in the dumbbell morphology. The values were found to be 0.21, 0.13 and 0.05 s⁻¹ for D1, D2 and D3 catalysts, respectively, comparable with the reported values for Au-based catalysts [16,19,30] yet still highlighting the difference between the catalytic properties of the samples.

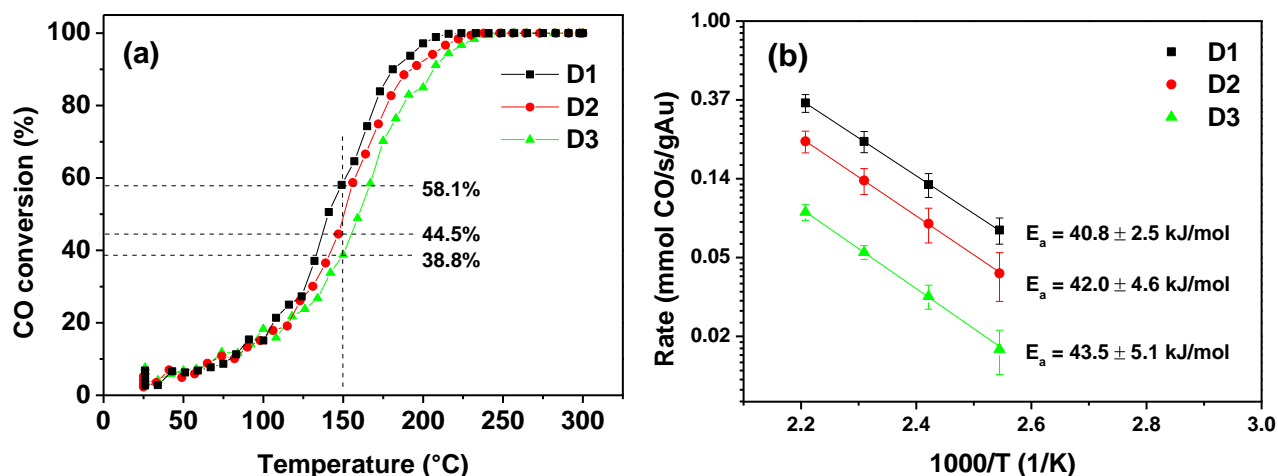


Figure 3. (a) Light-off curves and (b) kinetic data of the catalyst. Experimental conditions: CO = 1% v/v; O₂ = 6% v/v; WHSV= 3'000'000 for (a) and 12'000'000 Ncc/h/g(Au+Cu) for (b).

As detailed in the following, further characterization techniques were employed shed light on the observed differences.

5.3.4. Charge transfer between M and MO_x

One interesting feature of the dumbbell NCs is the fact that there can be an enhanced charge transfer between the two nanosized domains that are attached together [15,17,20], which can promote the catalytic properties compared to those of bulk supported metal catalysts. This phenomenon is indeed able to alter the strength of the adsorbed species on the active sites since it has a direct correlation with

the surface charge of the active sites. In this regard, CO adsorption monitored by DRIFT spectroscopy has been shown to be a powerful technique to differentiate between the existing active sites, being able to identify a slight change of the surface charge, especially for Au-based catalysts [10,21,31]. Therefore, the catalysts after kinetic measurements were unloaded from the reactor and examined by CO DRIFT after an oxidizing pretreatment and the results are shown in Figure 4. All three catalysts showed an evolution of a carbonyl band at the wavenumber of $\sim 2121\text{ cm}^{-1}$ during 35 min of exposure. There was also another shoulder-like feature at about 2 cm^{-1} higher than the main band for D1, causing the peak to be slightly asymmetrical. This feature gradually diminished in D2 and D3. The results were comparable with the carbonyl band already observed on the Au-iron oxide dumbbell-like catalyst [19] and alumina supported Au catalysts [21]. Interestingly, when compared to literature [10,21], the band in these catalysts occurred at a wavenumber which is close to the band observed at reduced Au species (2116 cm^{-1}) rather than the oxidized ones (2142 cm^{-1}). Therefore, it was concluded that the Au domain, was slightly positive yet less positive compared to the corresponding Au-iron oxide catalyst (having the same size of the Au domain). In order to further verify if the band is related to Au species, we also monitored the spectra during 40 min of desorption and, as shown in Figure S4, the carbonyl band totally disappeared in all samples. This excluded the possibility of the presence of species such as Cu^+ , which can form more stable carbonyl species [21,32].

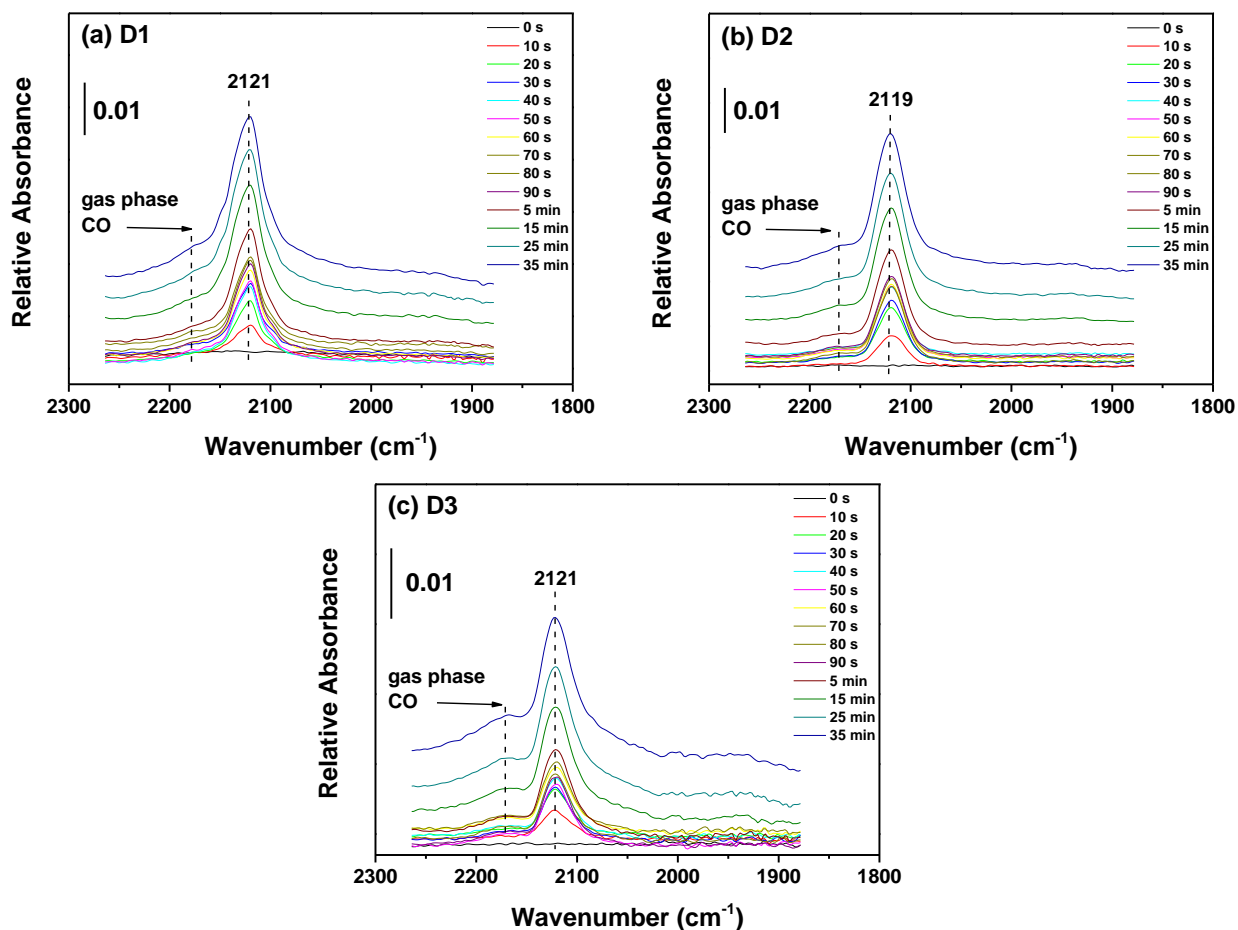


Figure 4. DRIFTS spectra in the carbonyl region recorded during the adsorption of CO at room temperature using 0.25% v/v CO in He as probe gas after oxidizing pretreatment in 6% v/v O₂ in He, at 350 °C for 1 h.

5.3.5. Structural properties

As mentioned above in the text, from the XRD patterns collected over the as-prepared NCs we understood the change between the ratio of AuCu and magnetite as the dominant phases in the fresh samples (see Table 1). In order to gain insights into the transformation of the NCs on the support, the fresh NCs deposited on the XRD wafer were exposed to a similar heat treatment as in the case of the catalysts. As shown in Figure S5-a, all activated samples had similar patterns samples, with the intensities of the peaks related to iron oxide phase which were different among the samples, suggesting the existence of different crystallite sizes. Reduction of the intensity for the iron oxide phases was in correlation with increasing of the population of NCs with a hollow MO_x domain. In addition, no residual AuCu phase was found in any of the patterns, while its corresponding 100% peak was shifted to a 2 θ which is indicative of Au phase. It was thus concluded that the AuCu phase of M domain of the NCs was completely dealloyed in all samples resulting in formation of Au phase. On the other hand,

the iron oxide phase was found to be mainly maghemite for all three samples while a small contribution from a hematite phase was also found for D3 sample.

XAFS spectroscopy is another powerful tool to understand the relation between structure and reactivity of active sites in heterogeneous catalysts [33,34] and therefore it was applied in this work to study the structural properties of both fresh and activated catalysts. The spectra were collected at different absorption edges, namely Au L₃-edge (11919 eV), Cu K-edge (8979 eV) and Fe K-edge (7112 eV), corresponding to the elements present in our system. The XANES spectra of the catalysts at different edges were compared first (see Figure S6). Looking at the data related to Au L₃-edge (Figure S6-1&b), it was evident that the samples, either fresh or activated, had almost similar absorptions profiles without a shift in the absorption edge suggesting the same oxidation state for the Au among the samples. All fresh samples resembled XANES spectrum of an AuCu alloy, while the activated samples were representative of that of metallic Au [16]. The dealloying after activation was clear for all samples by observing a dampening of the white line intensity at the energy ~11925 eV [16,35]. Interestingly and with respect to the high sensitivity of XANES to small structural and electronic changes [36], a very small decrease of the white line intensity was observed from D3-F to D1-F, suggesting a partial dealloying in the fresh sample by increasing the OIac content, in-line with the XRD results where a tiny shift of the 100% peak of AuCu had been observed. The same trend for partial dealloying by increasing of OIac was observed and eventually more visible in the XANES spectra of the fresh samples at Cu K-edge (Figure S6-c). Indeed, D1-F showed a less intense pre-edge peak at the energy of 8980 eV compared to those of D2 and D3. This decrease of intensity suggested a decrease in the fraction of Cu alloyed with the Au, in line with the increase of the OIac content which acted as the oxidizing agent during the synthesis. Comparing each fresh sample with its corresponding activated one highlighted the same increase of oxidation state for Cu among all samples, practically to Cu²⁺ and as a result of the oxidation pretreatment [16]. Comparing the XANES spectra of the activated samples at Cu K-edge (Figure S6-d), on the other hand revealed that the Cu in three activated samples have the same oxidation state. Moreover, the absence of sharp features below 8990 eV indicated Cu²⁺ ions are coordinated in a more centrosymmetric configuration compared to the bulk reference (such as octahedral sites). XANES spectra of the fresh samples at Fe K-edge, are compared in Figure S6-e all representative of magnetite [16] with a decrease in the intensity of the white lines from D1-F to D3-F. This decrease could be attributed to the lower crystallinity of the sample or a lower contribution of the magnetite phase due to the presence of more NCs with Fe-rich cores in MOx domain, in-line with the

result of XRD and TEM. All samples also featured a pre-edge peak at energy of ~ 7114 eV which could be attributed to the 1s to 3d transition, suggesting the existence of some non-centrosymmetric absorption sites such as tetrahedral positions [37,38] which is expected in the magnetite crystalline structure. The XANES spectra of the activated samples at Fe K-edge (Figure S6-f) proved a higher oxidation state for Fe in all samples, while the spectra were resembling to that of maghemite [16].

In order to understand the structural properties of the catalytic samples, the absorption spectra were further converted into the k space and the EXAFS functions were extracted from the post edge region (see Figure S7). The k^2 -weighted EXAFS functions were then Fourier transformed to isolate the contribution of different scatterings from neighboring atoms as a function of radial distance (see Figure 5).

The k^2 -weighted EXAFS functions of the fresh samples at Au L_3 -edge as well as the magnitude of their Fourier transforms ($|FT|$) are shown in Figure S7-a and Figure 5-a, respectively. While both EXAFS functions and $|FT|$ were quite similar, a small shift was observed in the data in the k space suggesting a slightly different environment around the Au absorbers. This is also supported by the $|FT|$ results where a slightly more intense peak was observed for the first shell of Au-Cu indicative of AuCu alloy. This is in line with the observation from XRD analysis using which we found AuCu phase was totally preserved at minimum level of OIAc i.e. for D3-F. On the other hand, the activated samples showed similar oscillations in the k space in line with XANES results suggesting the formation of Au phase after activation (see Figure S7-b and Figure 5-b). The peaks in Figure 5-b could be attributed to different Au-Au shells around the Au absorbers.

The same trend for partial dealloying of AuCu in the fresh samples was also observed by analyzing the data at Cu K-edge. As shown in Figure S7-c, the oscillations were slightly shifted to higher energies from D1-F to D3-F samples. This indicates slightly less scattering contributions from the atoms in the first shell in vicinity of Cu absorbers. Indeed, the $|FT|$ of the EXAFS functions revealed a peak at a low radial distance of 1.4 Å (see Figure 5-c), typically observed for oxygen-coordinated metal absorber [39-42]. Noteworthy, the presence of CuO could be discarded for all fresh samples with respect to the XANES results particularly the position of pre-edge feature of the spectra.

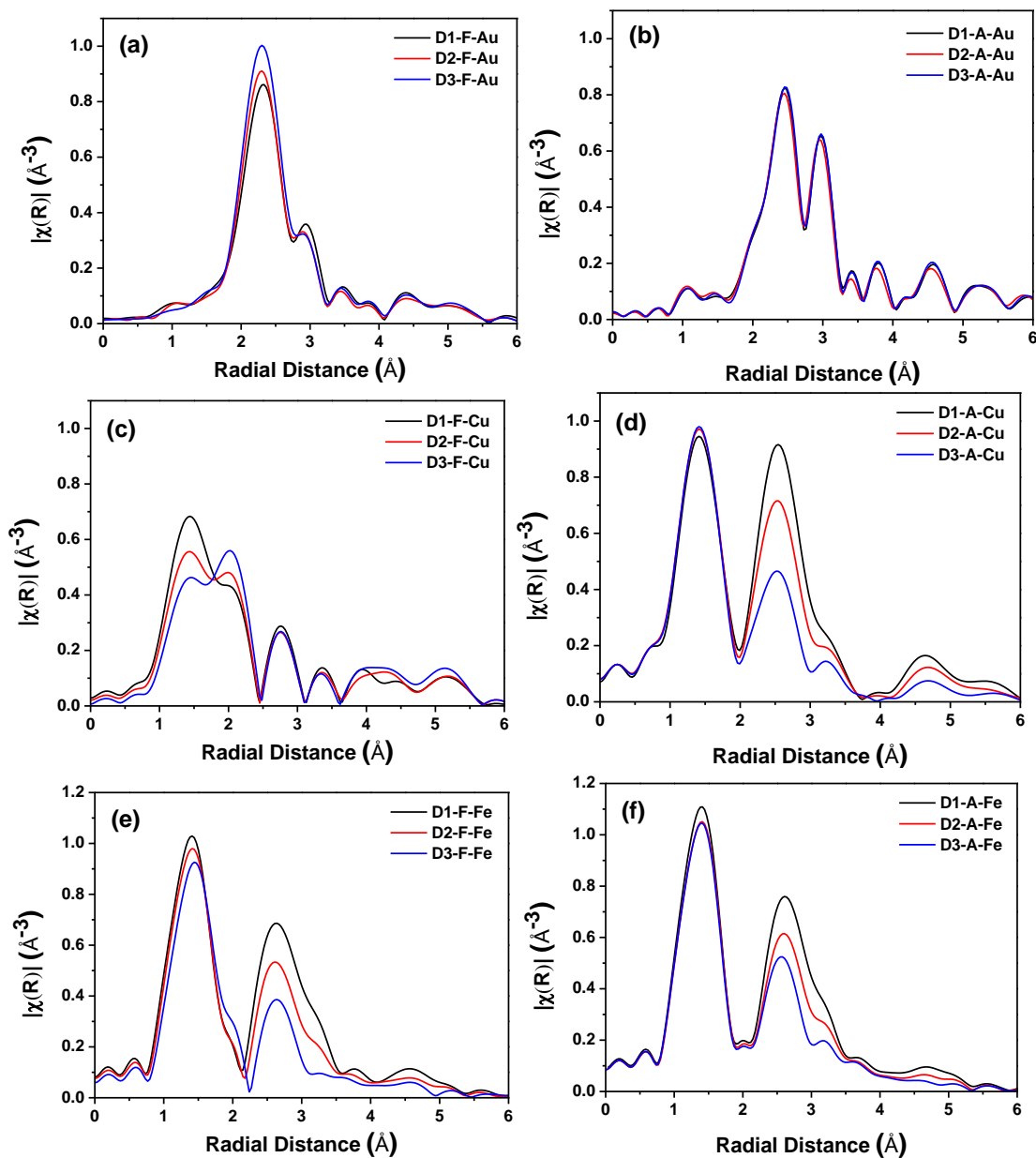


Figure 5. The magnitude of the Fourier transforms of the k^2 -weighted EXAFS function for the fresh and activated catalysts at different edges of (a & b) Au-L3, (c & d) Cu-K and (e & f) Fe-K; F and A designate fresh and activated catalysts, respectively.

The EXAFS functions of the activated samples at Cu K-edge (Figure S7-d) indicated the same pattern among the samples, i.e. the oscillations occurring at the same k , while the amplitudes were decreasing from D1-A to D3-A. This could be attributed to a more disordered nature [43] of the sample, or the decrease of average coordination number due to termination effect in NCs with smaller size [44,45], both consistent with the formation of more hollow MOxs. On the other hand, Figure 5-d

showed the presence of a shell for all activated samples at low radial distance, typical of metal-O shell, while two more shells with different intensities in form of a main peak with a clear shoulder could be observed at higher radial distances. In principle, these two shells can be attributed to presence of metal cations at octahedral and tetrahedral positions of a cubic oxide having a spinel structure [43]. As we had proved the formation of Cu^{2+} upon activation as well as their possible incorporation into the octahedral vacancies of the resulted oxide domain [16], we assumed the presence of a spinel structure i.e. maghemite in which the octahedral cation vacancies are partially filled with Cu atoms. However, due to increase of disorder as well as reducing of the crystallite size at the higher population of hollow MOx, the intensities of the Cu-metal peak in the |FT| was decreasing from D1-A to D3-A. Nevertheless, both peaks in oxide region of the |FT| can be as well attributed to the presence of Fe atoms in both octa and tetrahedral positions which can contribute to the scattering at those radial distances around Cu absorbers. .

Similar to the case of Cu K-edge, the EXAFS functions at the Fe K-edge (Figure S7-e) showed a small shift to higher energies in line with the higher oxidation extent for the Fe from D3-F to D1-F, as found out by XRD and EDS results. A similar situation was observed for the |FT| as in the case of data of the activated samples at Cu K-edge consistent with the structure of magnetite having both octa and tetrahedral cation positions. Needless to say, in this case only Fe atoms can be present in the cation positions as Cu atoms were found to be mostly in the alloy phase. A shoulder was observed at the radial distance of $\sim 2 \text{ \AA}$ which was more intensified from D1-F to D3-F. This could be related to amorphous iron phase which was increasing from D1-F to D3-F in line with the observation in |FT|. EXAFS functions of the activated samples at Fe K-edge (Figure S7-f) were also representing a similar pattern as in the case of Cu K-edge i.e. the amplitude of oscillation was decreasing from D1-A to D3-A. This again suggested the similarity between the crystalline structure of the samples, while the increased disorder or the termination effect due to further reducing of the size of the nano MOx domains was prevailing in the case of a higher population of NCs with hollow oxide. The |FT| also in this case revealed a typical profile for the oxides containing of both octahedral and tetrahedral positions.

5.4. Summary and Conclusions

To sum up, we prepared a set of dumbbell-like NCs consisting of AuCu and iron oxide while a fraction of the NCs had Fe-rich core in the oxide domain. Indeed, it was possible to manipulate the population of such NCs by tuning the synthesis conditions. Their presence could be attributed to less

oxidation extent for Fe as a result of using less amount O source in the synthesis. A set of catalysts was prepared from these NCs and further studied in CO oxidation after an initial activation pretreatment which was necessary to remove the protecting ligands. A number of nanoscale transformations were observed upon activation which essentially defined the final catalytic properties of the NCs. While the dumbbell-like morphology was preserved upon activation in all samples, it was observed that the NCs having Fe-rich core would evolve to have a hollow oxide domain. In this regard, the final NCs were consisting of Au in the metal domain and a Cu-poor cuprospinel phase in the oxide domain or from another perspective, a maghemite structure with Cu incorporated in its octahedral vacancies. Interestingly, the samples showed different CO oxidation activity and a trend was obtained for decreasing of the activity by increasing the number of NCs with hollow oxide domain. As the sizes of both metal and metal oxide domains as well as the morphologies of the NCs with and without hollow oxide domains were similar in all cases, we tried to correlate the difference in the activity with possible difference in structural properties. The charge transfer between the two domains was studied by CO-DRIFT and XPS, both suggesting a similarity for the Au species in the system regardless of having NCs with hollow oxide domain. On the other hand, XAFS results revealed that despite having similar crystalline systems in the samples, the oxide domain would become more disordered as the population of NCs with hollow oxide domain increased. One explanation for the observed difference in activity could be a different reducibility of the nano MO_x domains as a result of reducing crystallite sizes by increasing the population of NCs with hollow MO_x. In addition, the distribution of the Cu can be different in the full MO_x versus hollow ones which can affect the activity of the catalysts. These issues are currently under investigation as they require further evaluations. In addition, the qualitative interpretation of the EXAFS data will be confirmed by quantitative analyses and modeling.

Reference

1. Haruta, M., N. Yamada, T. Kobayashi, and S. Iijima, *Gold catalysts prepared by coprecipitation for low-temperature oxidation of hydrogen and of carbon monoxide*. J. Catal., 1989. **115**(2): p. 301-309.
2. Hutchings, G.J., *Vapor phase hydrochlorination of acetylene: Correlation of catalytic activity of supported metal chloride catalysts*. J. Catal., 1985. **96**(1): p. 292-295.
3. Hutchings, G.J., *Catalysis by gold*. Catal. Today, 2005. **100**(1-2): p. 55-61.
4. Hashmi, A.S.K. and G.J. Hutchings, *Gold Catalysis*. Angew. Chem. Int. Ed., 2006. **45**(47): p. 7896-7936.
5. Carabineiro, S.A.C., N. Bogdanchikova, P.B. Tavares, and J.L. Figueiredo, *Nanostructured iron oxide catalysts with gold for the oxidation of carbon monoxide*. RSC Adv., 2012. **2**(7): p. 2957-2965.
6. Lin, H.-Y. and Y.-W. Chen, *Low-Temperature CO Oxidation on Au/FeO_x Catalysts*. Ind. Eng. Chem. Res., 2005. **44**(13): p. 4569-4576.
7. Lopez, N., T.V.W. Janssens, B.S. Clausen, Y. Xu, M. Mavrikakis, T. Bligaard, and J.K. Nørskov, *On the origin of the catalytic activity of gold nanoparticles for low-temperature CO oxidation*. J. Catal., 2004. **223**(1): p. 232-235.
8. Guo, Y., D. Gu, Z. Jin, P.-P. Du, R. Si, J. Tao, W.-Q. Xu, Y.-Y. Huang, S. Senanayake, Q.-S. Song, C.-J. Jia, and F. Schuth, *Uniform 2 nm gold nanoparticles supported on iron oxides as active catalysts for CO oxidation reaction: structure-activity relationship*. Nanoscale, 2015. **7**(11): p. 4920-4928.
9. Huang, J., W.-L. Dai, and K. Fan, *Remarkable support crystal phase effect in Au/FeO_x catalyzed oxidation of 1,4-butanediol to γ -butyrolactone*. J. Catal., 2009. **266**(2): p. 228-235.
10. Guo, L.-W., P.-P. Du, X.-P. Fu, C. Ma, J. Zeng, R. Si, Y.-Y. Huang, C.-J. Jia, Y.-W. Zhang, and C.-H. Yan, *Contributions of distinct gold species to catalytic reactivity for carbon monoxide oxidation*. Nat. Commun., 2016. **7**: p. 13481.

11. Herzing, A.A., C.J. Kiely, A.F. Carley, P. Landon, and G.J. Hutchings, *Identification of Active Gold Nanoclusters on Iron Oxide Supports for CO Oxidation*. Science, 2008. **321**(5894): p. 1331-1335.
12. He, Q., S.J. Freakley, J.K. Edwards, A.F. Carley, A.Y. Borisevich, Y. Mineo, M. Haruta, G.J. Hutchings, and C.J. Kiely, *Population and hierarchy of active species in gold iron oxide catalysts for carbon monoxide oxidation*. Nat. Commun., 2016. **7**: p. 12905.
13. Mizera, J., N. Spiridis, R. Socha, R. Grabowski, K. Samson, J. Korecki, B. Grzybowska, J. Gurgul, L. Kępiński, and M.A. Małecka, *Au/FeOx catalysts of different degree of iron oxide reduction*. Catal. Today, 2012. **187**(1): p. 20-29.
14. Meunier, F.C., *Bridging the Gap between Surface Science and Industrial Catalysis*. ACS Nano, 2008. **2**(12): p. 2441-2444.
15. George, C., A. Genovese, A. Casu, M. Prato, M. Povia, L. Manna, and T. Montanari, *CO Oxidation on Colloidal Au_{0.80}Pd_{0.20}-Fe_xO_y Dumbbell Nanocrystals*. Nano Lett., 2013. **13**(2): p. 752-757.
16. Najafshirtari, S., T.M. Kokumai, S. Marras, P. Destro, M. Prato, A. Scarpellini, R. Brescia, A. Lak, T. Pellegrino, D. Zanchet, L. Manna, and M. Colombo, *Dumbbell-like Au_{0.5}Cu_{0.5}@Fe₃O₄ Nanocrystals: Synthesis, Characterization, and Catalytic Activity in CO Oxidation*. ACS Appl. Mater. Interfaces, 2016. **8**(42): p. 28624-28632.
17. Yu, H., M. Chen, P.M. Rice, S.X. Wang, R.L. White, and S. Sun, *Dumbbell-like Bifunctional Au-Fe₃O₄ Nanoparticles*. Nano Lett., 2005. **5**(2): p. 379-382.
18. Wu, B., H. Zhang, C. Chen, S. Lin, and N. Zheng, *Interfacial activation of catalytically inert Au (6.7 nm)-Fe₃O₄ dumbbell nanoparticles for CO oxidation*. Nano Res., 2009. **2**(12): p. 975-983.
19. Najafshirtari, S., P. Guardia, A. Scarpellini, M. Prato, S. Marras, L. Manna, and M. Colombo, *The effect of Au domain size on the CO oxidation catalytic activity of colloidal Au-FeOx dumbbell-like heterodimers*. J. Catal., 2016. **338**: p. 115-123.

20. Zhao, J., H. Liu, S. Ye, Y. Cui, N. Xue, L. Peng, X. Guo, and W. Ding, *Half-encapsulated Au nanoparticles by nano iron oxide: promoted performance of the aerobic oxidation of 1-phenylethanol*. *Nanoscale*, 2013. **5**(20): p. 9546-9552.
21. Najafshirtari, S., R. Brescia, P. Guardia, S. Marras, L. Manna, and M. Colombo, *Nanoscale Transformations of Alumina-Supported AuCu Ordered Phase Nanocrystals and Their Activity in CO Oxidation*. *ACS Catal.*, 2015. **5**(4): p. 2154-2163.
22. Andrea Di, C., A. Giuliana, M. Marco, P. Emiliano, N. Nicola, C. Andrea, and O. Luca, *Novel XAFS capabilities at ELETTRA synchrotron light source*. *J. Phys.: Conf. Ser.*, 2009. **190**(1): p. 012043.
23. Ravel, B. and M. Newville, *ATHENA, ARTEMIS, HEPHAESTUS: data analysis for X-ray absorption spectroscopy using IFEFFIT*. *J. Synchrotron Radiat.*, 2005. **12**(4): p. 537-541.
24. Farrell, D., S.A. Majetich, and J.P. Wilcoxon, *Preparation and Characterization of Monodisperse Fe Nanoparticles*. *J. Phys. Chem. B*, 2003. **107**(40): p. 11022-11030.
25. Bauer, J.C., D. Mullins, M. Li, Z. Wu, E.A. Payzant, S.H. Overbury, and S. Dai, *Synthesis of silica supported AuCu nanoparticle catalysts and the effects of pretreatment conditions for the CO oxidation reaction*. *Phys. Chem. Chem. Phys.*, 2011. **13**(7): p. 2571-2581.
26. Yin, Y., R.M. Rioux, C.K. Erdonmez, S. Hughes, G.A. Somorjai, and A.P. Alivisatos, *Formation of Hollow Nanocrystals Through the Nanoscale Kirkendall Effect*. *Science*, 2004. **304**(5671): p. 711-714.
27. Wang, W., M. Dahl, and Y. Yin, *Hollow Nanocrystals through the Nanoscale Kirkendall Effect*. *Chem. Mater.*, 2013. **25**(8): p. 1179-1189.
28. Peng, S. and S. Sun, *Synthesis and Characterization of Monodisperse Hollow Fe₃O₄ Nanoparticles*. *Angew. Chem. Int. Ed.*, 2007. **46**(22): p. 4155-4158.
29. Cabot, A., V.F. Puentes, E. Shevchenko, Y. Yin, L. Balcells, M.A. Marcus, S.M. Hughes, and A.P. Alivisatos, *Vacancy Coalescence during Oxidation of Iron Nanoparticles*. *J. Am. Chem. Soc.*, 2007. **129**(34): p. 10358-10360.

30. Schubert, M.M., S. Hackenberg, A.C. van Veen, M. Muhler, V. Plzak, and R.J. Behm, *CO Oxidation over Supported Gold Catalysts—“Inert” and “Active” Support Materials and Their Role for the Oxygen Supply during Reaction*. J. Catal., 2001. **197**(1): p. 113-122.
31. Mihaylov, M., H. Knözinger, K. Hadjiivanov, and B.C. Gates, *Characterization of the Oxidation States of Supported Gold Species by IR Spectroscopy of Adsorbed CO*. Chem. Ing. Tech., 2007. **79**(6): p. 795-806.
32. Hadjiivanov, K. and H. Knozinger, *FTIR study of CO and NO adsorption and coadsorption on a Cu/SiO₂ catalyst: Probing the oxidation state of copper*. Phys. Chem. Chem. Phys., 2001. **3**(6): p. 1132-1137.
33. Bordiga, S., E. Groppo, G. Agostini, J.A. van Bokhoven, and C. Lamberti, *Reactivity of Surface Species in Heterogeneous Catalysts Probed by In Situ X-ray Absorption Techniques*. Chem. Rev., 2013. **113**(3): p. 1736-1850.
34. Herbert, J.J., P. Senecal, D.J. Martin, W. Bras, S.K. Beaumont, and A.M. Beale, *X-ray spectroscopic and scattering methods applied to the characterisation of cobalt-based Fischer-Tropsch synthesis catalysts*. Catal. Sci. Technol., 2016. **6**(15): p. 5773-5791.
35. Kuhn, M. and T.K. Sham, *Charge redistribution and electronic behavior in a series of Au-Cu alloys*. Physical Review B, 1994. **49**(3): p. 1647-1661.
36. Krishnan, V., R.K. Selvan, C.O. Augustin, A. Gedanken, and H. Bertagnolli, *EXAFS and XANES Investigations of CuFe₂O₄ Nanoparticles and CuFe₂O₄–MO₂ (M = Sn, Ce) Nanocomposites*. J. Phys. Chem. C, 2007. **111**(45): p. 16724-16733.
37. Westre, T.E., P. Kennepohl, J.G. DeWitt, B. Hedman, K.O. Hodgson, and E.I. Solomon, *A Multiplet Analysis of Fe K-Edge $1s \rightarrow 3d$ Pre-Edge Features of Iron Complexes*. J. Am. Chem. Soc., 1997. **119**(27): p. 6297-6314.
38. Yao, Y., Y. Hu, and R.W.J. Scott, *Watching Iron Nanoparticles Rust: An in Situ X-ray Absorption Spectroscopic Study*. J. Phys. Chem. C, 2014. **118**(38): p. 22317-22324.

39. Thanh, N.K., T.T. Loan, L.N. Anh, N.P. Duong, S. Soontaranon, N. Thammajak, and T.D. Hien, *Cation distribution in CuFe₂O₄ nanoparticles: Effects of Ni doping on magnetic properties*. J. Appl. Phys., 2016. **120**(14): p. 142115.
40. Kwon, S.G., S. Chattopadhyay, B. Koo, P.C. dos Santos Claro, T. Shibata, F.G. Requejo, L.J. Giovanetti, Y. Liu, C. Johnson, V. Prakapenka, B. Lee, and E.V. Shevchenko, *Oxidation Induced Doping of Nanoparticles Revealed by in Situ X-ray Absorption Studies*. Nano Lett., 2016. **16**(6): p. 3738-3747.
41. Aritani, H., T. Tanaka, T. Funabiki, S. Yoshida, M. Kudo, and S. Hasegawa, *Structure of Mo–Mg Binary Oxides in Oxidized/Reduced States Studied by X-ray Absorption Spectroscopy at the Mo K Edge and Mg K Edge*. J. Phys. Chem., 1996. **100**(13): p. 5440-5446.
42. Komlev, A.A., T.L. Makarova, E. Lahderanta, P.V. Semenikhin, A.I. Veinger, T.V. Tisnek, G. Magnani, G. Bertoni, D. Pontiroli, and M. Ricco, *Magnetism of aniline modified graphene-based materials*. J. Magn. Magn. Mater., 2016. **415**: p. 45-50.
43. Calvin, S., *XAFS for Everyone*. 2013: Taylor & Francis.
44. Calvin, S., M.M. Miller, R. Goswami, S.-F. Cheng, S.P. Mulvaney, L.J. Whitman, and V.G. Harris, *Determination of crystallite size in a magnetic nanocomposite using extended x-ray absorption fine structure*. J. Appl. Phys., 2003. **94**(1): p. 778-783.
45. Wang, X., M. Zhu, L.K. Koopal, W. Li, W. Xu, F. Liu, J. Zhang, Q. Liu, X. Feng, and D.L. Sparks, *Effects of crystallite size on the structure and magnetism of ferrihydrite*. Environ. Sci.: Nano, 2016. **3**(1): p. 190-202.

Supporting Information

Metal-support interaction in Au catalysis: the effect of
the morphology of a nano-oxide domain in CO
oxidation activity

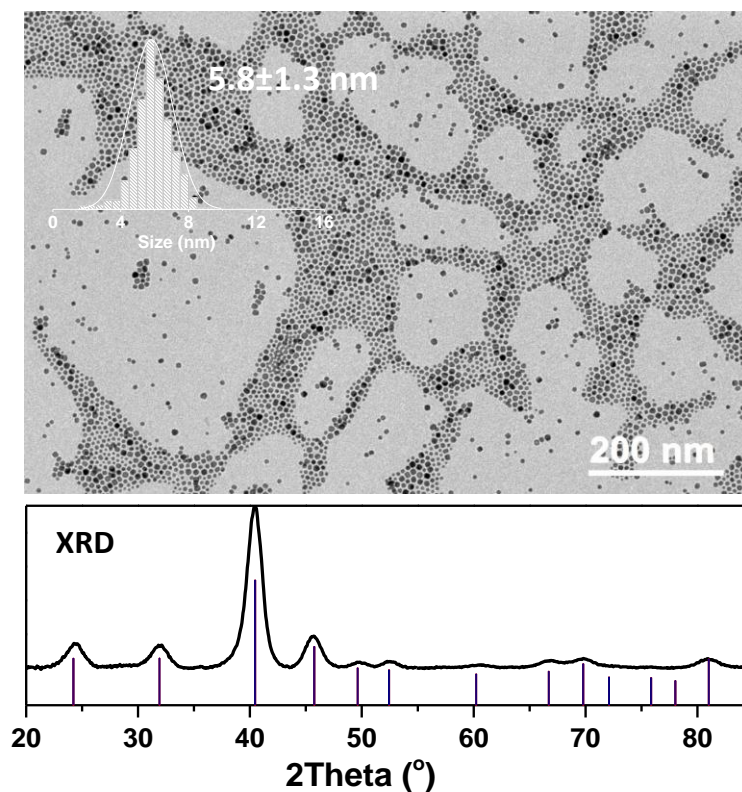


Figure S1. Typical bright-field (BF)-TEM image of the as-prepared AuCu colloidal NCs; top left inset: size distribution obtained by measuring ~650 NCs; the XRD pattern of AuCu seeds at the bottom. Experimental data are compared with the database powder XRD pattern for tetragonal AuCu (ICSD code: 42574).

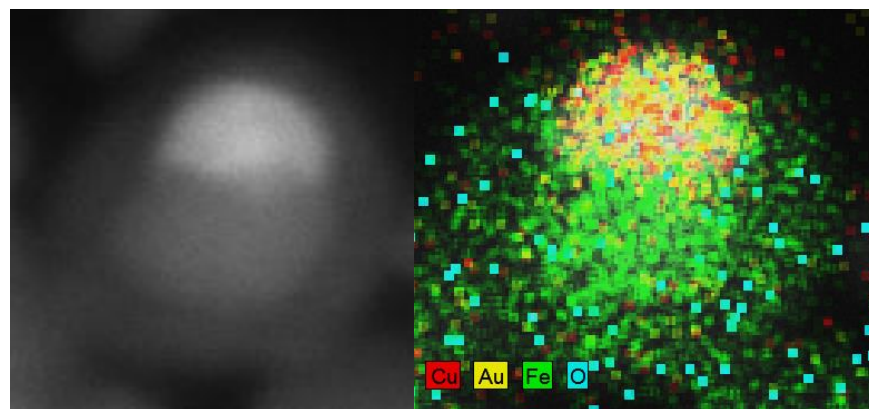


Figure S2. HAADF-STEM image and corresponding quantitative EDS maps (intensity proportional to atomic %) for of Au (yellow), Cu (red), Fe (green), and O (blue), showing localization of Au and Cu in the metal domain and Fe-rich core in the metal oxide domain.

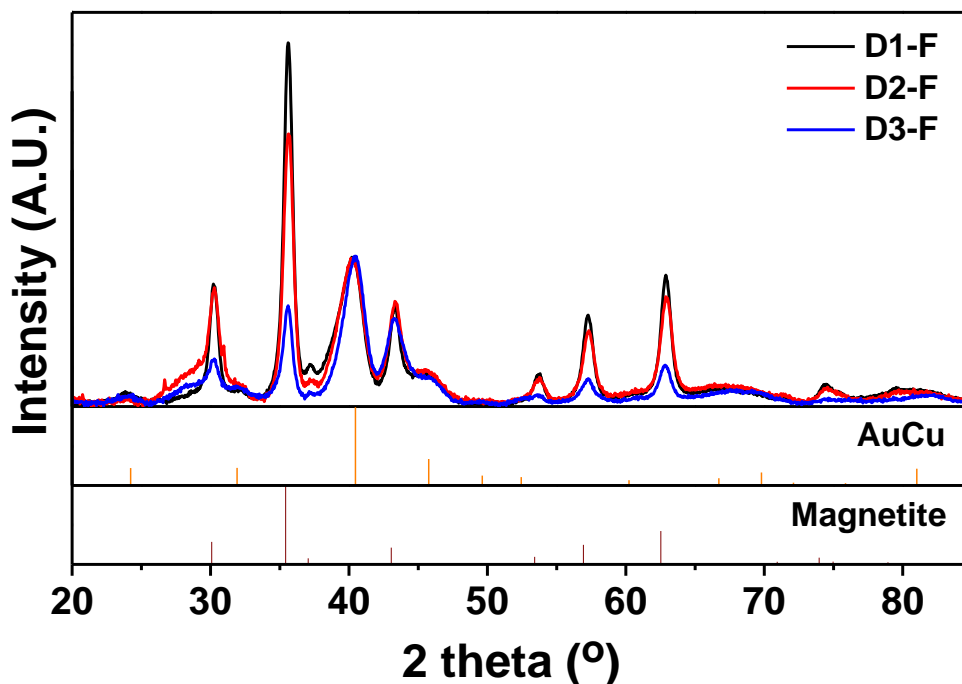


Figure S3. X-ray diffraction (XRD) pattern of the as-synthesized AuCu@FeOx dumbbell NCs. Experimental data are compared with the database powder XRD patterns for tetragonal AuCu (ICSD code: 42574) and magnetite Fe₃O₄ (ICSD code: 65341).

Calculation of Au domain size from dealloying of AuCu domain of AuCu@FeOx NCs:

We estimated the size of Au domain resulting from dealloying of Cu from AuCu domains of dumbbells into Au. We considered the initial AuCu domain as sphere with atomic Au:Cu ratio = 50:50 (as per the ICP results), in the ordered tetragonal phase as observed by XRD. First, the number of Au atoms in the resulted Au domains would be equal to the number of Au atoms in the initial AuCu domains of dumbbell NCs before activation. Therefore, considering the unit cell volume of AuCu (28.72 Å³ in the JCPDS card No. #98-004-2574) and the number of Au atoms per unit cell of AuCu (which is equal to 1), we have:

$$N_{\text{Au atoms in Au domain}} = N_{\text{Au atoms in AuCu domain}} = \frac{V_{\text{AuCu domain}} \times N_{\text{Au atoms per AuCu unit cell}}}{V_{\text{AuCu unit cell}}}$$

where $V_{\text{AuCu domain}}$ can be calculated considering the diameter obtained from image analysis (i.e. ~ 5.7 nm). Then, the volume of an Au domain and subsequently its diameter can be calculated considering it as spherical ($V_{\text{Au NC}}$). Then, considering the number of Au atoms in the unit cell (which is equal to 4) as well as the known unit cell volume of Au (67.92 \AA^3 in the JCPDS card No. #98-004-4362), the number of Au atoms per Au NC was calculated from:

$$V_{\text{Au domain}} = \frac{V_{\text{Au unit cell}} \times N_{\text{Au atoms in AuCu domain}}}{N_{\text{Au atoms per AuCu unit cell}}}$$

To resulting value for size of resulted Au domain is 4.8 nm which is similar to the measured value of 5.0 nm obtained from image analysis of the activated catalysts.

Evaluation of Turn over Frequency (TOF):

We report the rate of reaction as:

$$\frac{\text{molCO}_2\text{produced}}{s} = \frac{\text{CO}_{\text{feed}} (N_{\text{cc}} / \text{min}) \cdot \text{CO}_{\text{conversion}}}{60 (s / \text{min}) \cdot 22.414 (cc / \text{mol})}$$

We assumed spherical Au domains and considered that only half of the sphere was exposed to the reacting atmosphere (i.e. half of the sphere is embedded in the iron oxide domain). The content of gold was measured by ICP. We consider bulk gold density and the area occupied by surface gold atoms to be $1.9 \text{ E-}5 \text{ mol/m}^2$ [1]. TOF was thus calculated as:

$$\text{TOF} = \frac{\text{molCO}_2\text{produced}}{s} \cdot \frac{1}{\text{molAu}}$$

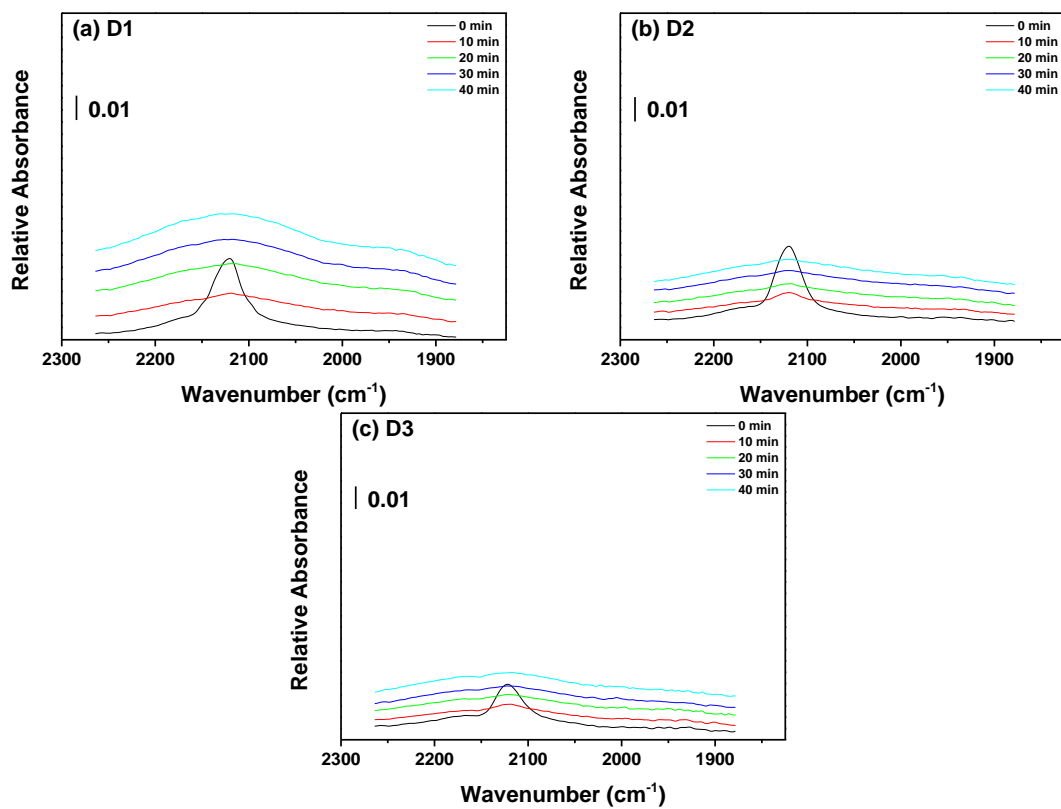


Figure S4. DRIFTS spectra in the carbonyl region recorded during the desorption of CO at room temperature using 6% v/v O_2 in He.

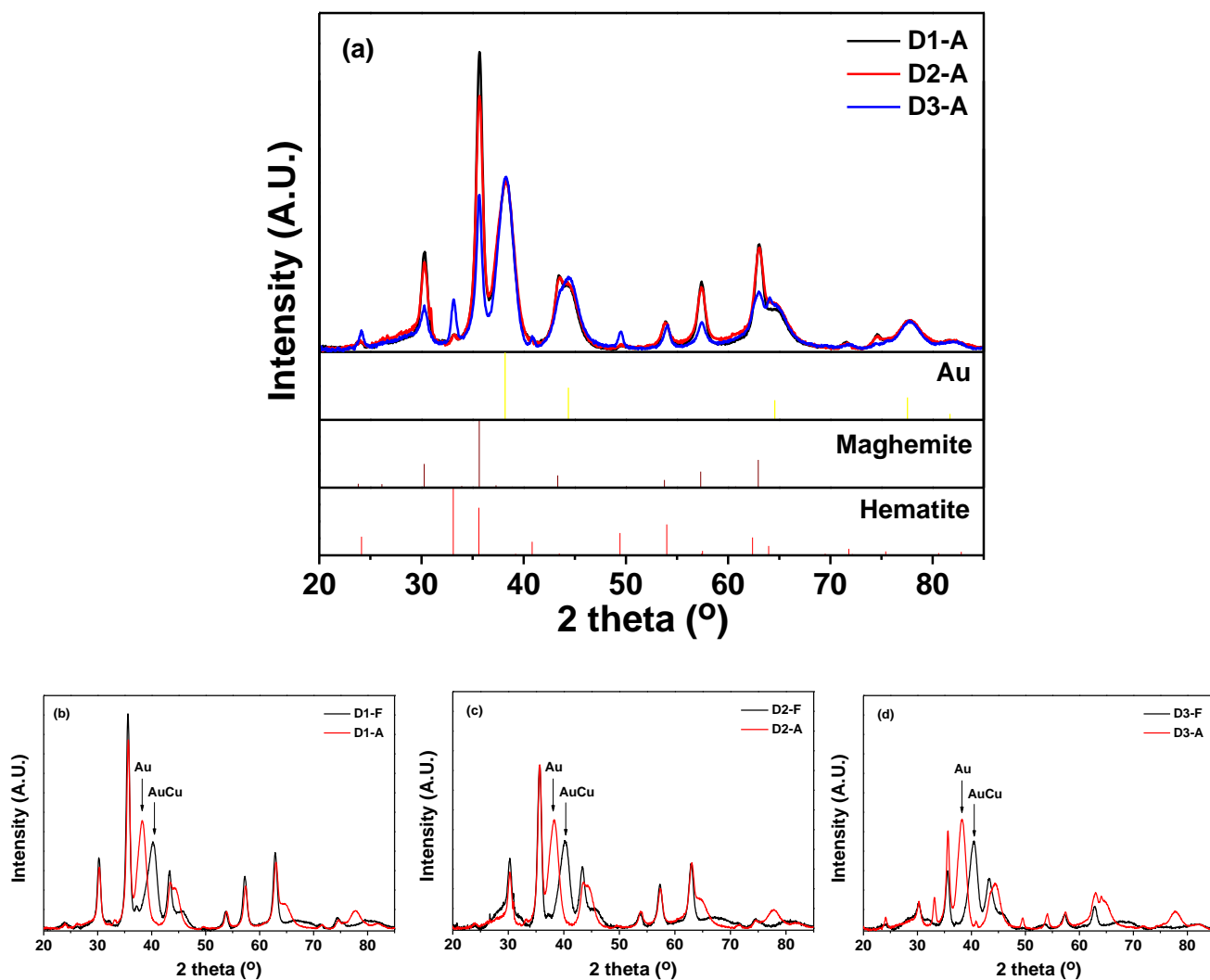


Figure S5. (a) comparison of the X-ray diffraction (XRD) patterns for the calcined AuCu@FeO_x dumbbell NCs. (b) – (d) provide the comparison between the fresh and calcined NCs for each set of samples. Experimental data are compared with the database powder XRD patterns for tetragonal Au (ICSD code: 44362), maghemite (ICSD code:87119) and hematite (ICSD code:82136).

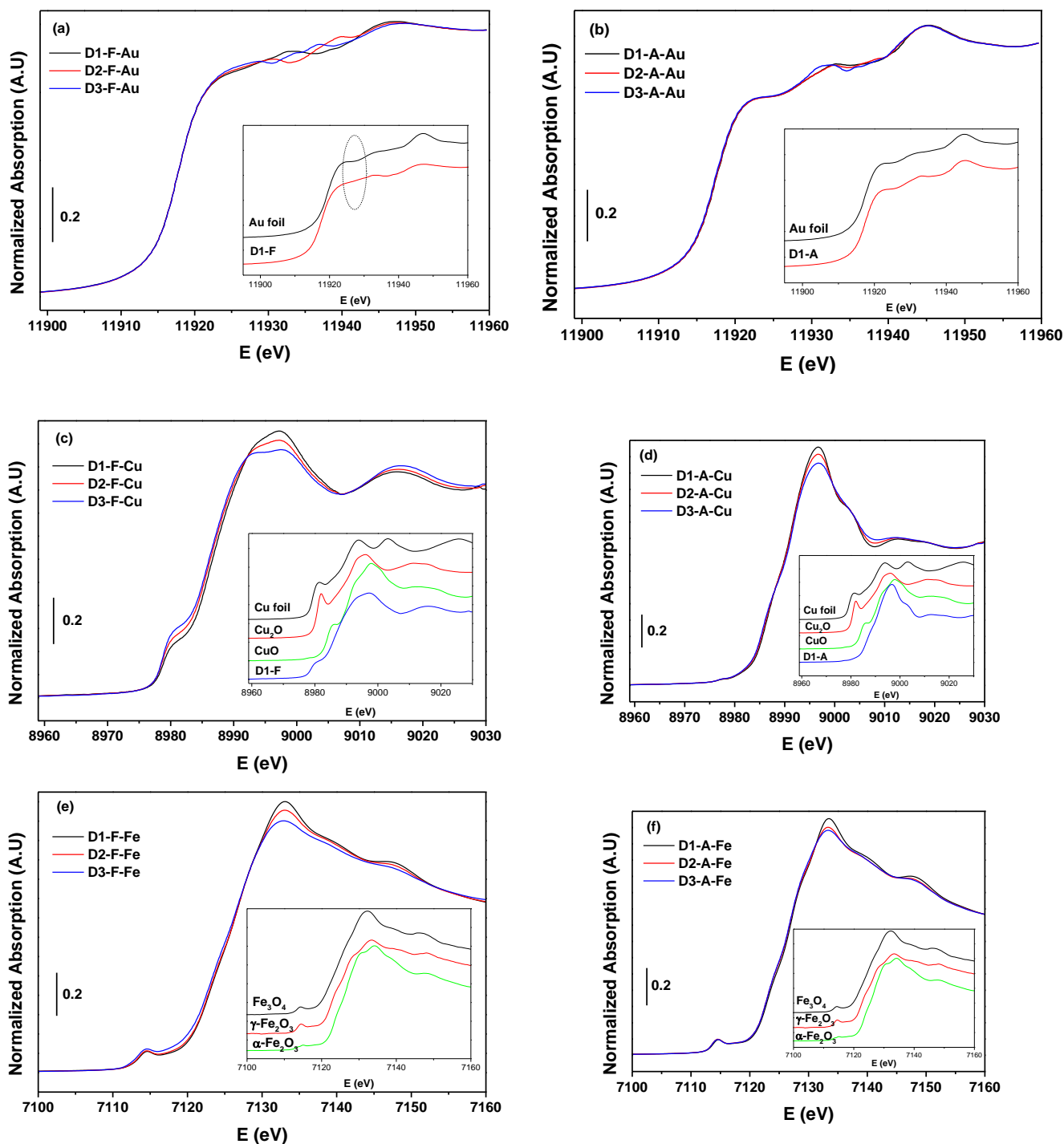


Figure S6. XANES spectra of fresh and activated catalysts at different edges of (a & b) Au-L3, (c & d) Cu-K and (e & f) Fe-K; F and A designate fresh and activated catalysts, respectively. The reference spectra are shown as insets.

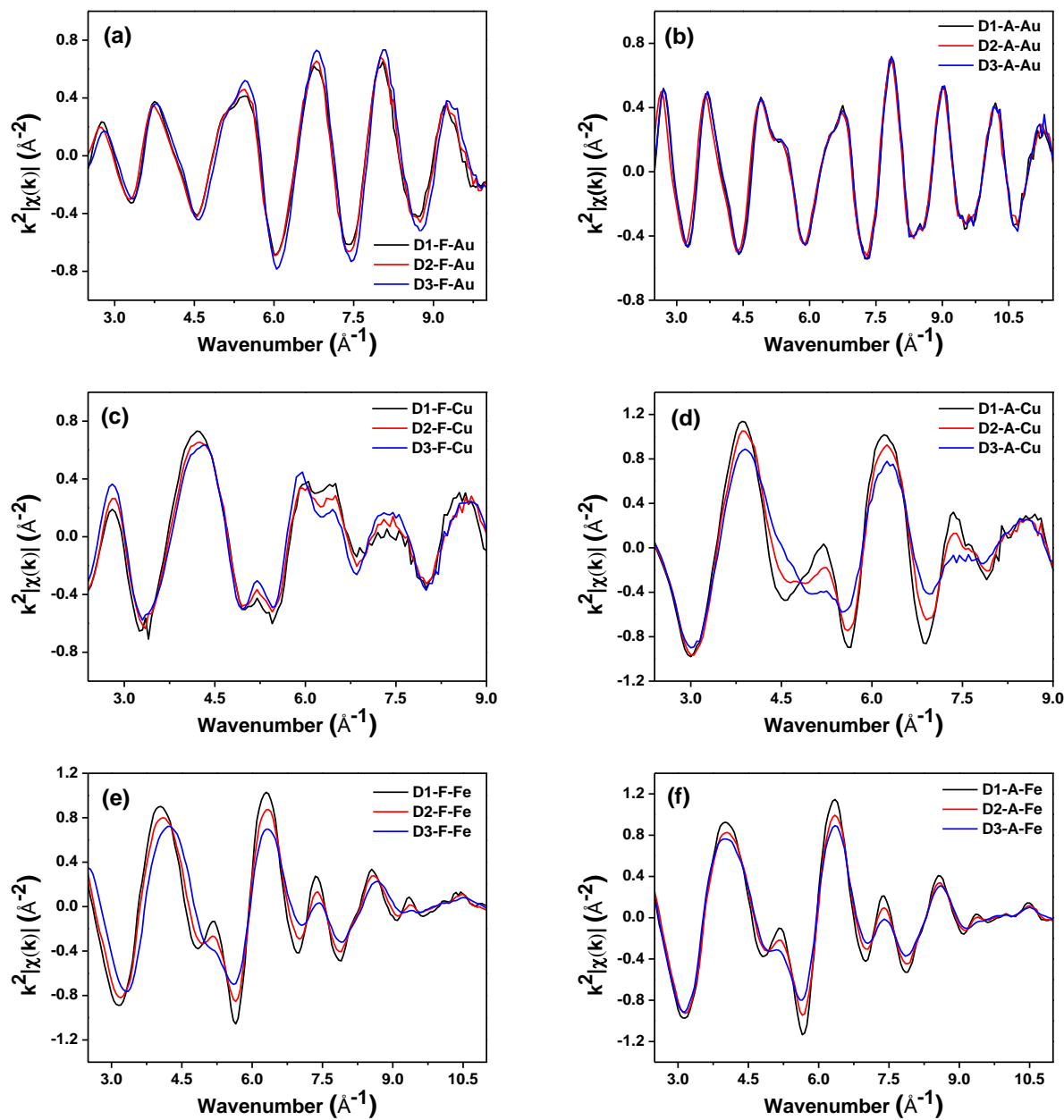


Figure S7. k^2 -weighted EXAFS functions of fresh and activated catalysts at different edges of (a & b) Au-L3, (c & d) Cu-K and (e & f) Fe-K; F and A designate fresh and activated catalysts, respectively.

References

- [1] Güttel, R.; Paul, M.; Galeano, C.; Schüth, F. Au, @ZrO₂ Yolk–Shell Catalysts for CO Oxidation: Study of Particle Size Effect by Ex-post Size Control of Au Cores, *J. Catal.* **2012**, 289, 100-104

Appendix I

Application of NCs in liquid phase hydrogenation of model compounds

Table of Contents

1. Introduction.....	3
2. Experimental.....	4
3. Results and discussion	6
3.1. Au/Turbobeads	6
3.2. Pd/Turbobeads.....	7
3.3. AuCu/Turbobeads	8
3.4. AuCu@FeOx/Turbobeads.....	10
4. Concluding remarks on application of colloidal NCs in liquid phase reactions.....	11

1. Introduction

There has been an emerging demand for green chemical routes in the synthesis of organic compounds due to environmental concerns, particularly when homogeneous catalysis is involved. Generally, homogeneous catalysts provide high activity and better selectivity due to their high level of exposure and spatial configuration at the molecular level. However, they suffer from a major drawback which is the fact that the catalyst needs to be separated from the reaction mixture in order to isolate the product [1]. This is not a very trivial task yet important for economic and environmental reasons. To overcome this problem, one possible approach involves the immobilization of the homogeneous metal-based catalysts on a support, which can be more easily separated from the reaction mixture by means of filtration or other techniques. Application of magnetic supports in this regard gives the advantage of facile separation using an external magnet [1,2]. In this way, the catalysts can be further recycled and be used again, providing an economic and practical synthesis route.

Different approaches have been taken to immobilize the metallic active sites; most of them involved the initial modification of the surface of the magnetic support in order to anchor the metallic active sites [3]. The metal NCs can be also encapsulated within a porous polymeric shell which is formed around the magnetic NPs as the core of the composite catalyst to provide the possibility of magnetic separation [4]. In this class of materials, metallic NCs are typically formed by reduction of a metal precursor after impregnation of the support and the polymeric matrix [5]. Indeed, such nanocomposite can offer a very good dispersion of the metallic active sites which consequently results in a high level of activity.

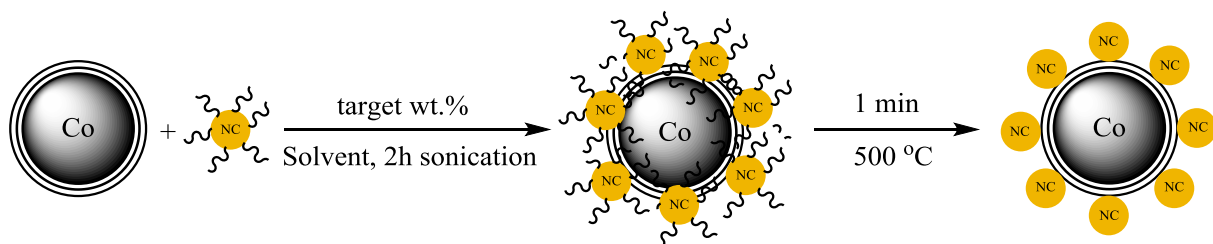
Within this context, catalysts can be also prepared by deposition of pre-made colloidal nanocrystals (NCs) on magnetic supports. The use of pre-made NCs in catalyst preparation offers an additional possibility to finely tune the size and the properties of the active sites (such as shape, morphology, composition and crystalline structure) and to exploit synergetic effects between different constituents.

Considering the above discussion, I started a work in the third year of my PhD in the group of Prof. Reiser in the Institut für Organische Chemie, Institut für Pharmazie und Chemie, Universität Regensburg, where I stayed for 9 month in the context of a cotutelle agreement (from Dec 2015 till September 2016). There, I explored the catalytic activities of some of the NCs synthesized in IIT for liquid phase hydrogenation and oxidation reactions. In this regard, I developed a procedure to prepare magnetically recyclable catalysts using Turbobeats magnetic NPs as support (i.e. commercially

available carbon coated Co NPs [6]) and pre-made colloidal NCs. I prepared a number of catalysts and applied them in liquid phase oxidation and hydrogenation reactions. The most promising results were observed for the hydrogenation of cinnamaldehyde to its corresponding unsaturated (or saturated) alcohol using AuCu (or AuCu@FeOx) NCs. We have checked the effect of different parameters on the extent of the reaction and found that the reaction takes place at moderately high H₂ pressure of 20 bar, the temperature of 50 °C and 24 h reaction time. The method for catalyst preparation is straightforward and can be applied for other colloidal NCs of interest as long as they are stable under harsh conditions of sonication. In order to complete this work, it should be extended further in different directions. Briefly, some few more tests are needed in order to fully understand the effects of the reaction parameters on the extent of cinnamaldehyde hydrogenation as well as the product distribution. The catalysts should be also characterized further before and after reactions. Considering the magnetic nature of the catalyst, some consecutive trials should be performed in order to study the recyclability of the catalyst. The work will be hopefully finalized by the time of the defense.

2. Experimental

The catalysts were prepared using colloidal deposition method. Different colloidal NCs were synthesized including Au, Pd, AuCu and AuCu@FeOx and were used as catalysts for the tested reactions. To achieve a targeted loading, a specific amount of colloidal NCs with known concentrations were taken and added to specified weight of Turbobeeds magnetic NPs dispersed in a solvent. The solvent used in the preparation of the catalysts was identical to the dispersing solvent of the colloidal solutions. The suspension in a vial was then sonicated for 1 h after which the solvent was removed and the solid catalyst was dried at 80 °C or 2 h. A number of catalysts were also prepared in the same manner using alumina as support to check some engineering aspects of the testing protocol, as will be discussed in the text. In order to see the effect of the ligands around the deposited NCs, the catalysts were also rapidly calcined before using, at high temperature of 500 °C in air atmosphere [7]. The fast calcination procedure was indeed applied to limit the burning of the carbon coating of the Turbobeeds NPs. The procedure applied for the preparation of the catalyst is schematically shown in Scheme 1.



Scheme 1. Sketch of the catalyst preparation procedure.

The batch reaction tests were performed in two ways depending on the applied pressure. For the tests under atmospheric pressure, a standard 10 ml reaction tube equipped with a valve was used. Through the valve, either O₂ or H₂ was provided by a balloon to perform oxidation or hydrogenation reactions at atmospheric pressure. The hydrogenation reaction was also performed under high pressure using an autoclave where high pressure H₂ was provided from a cylinder. The vessels in both cases were evacuated and/or purged at least 3 times prior to reaction test. To do so, a specific weight of the catalyst was introduced into the reaction vessel and then a specific volume of an already-prepared solution of the substrate was added to it. The reaction media was mixed using a magnetic bar throughout the applied time. After completion of the reaction, the catalyst was separated either by using an external magnet (in case of the Turbobeeds support) or by filtration (in case of the alumina support). The catalyst inside the reaction tube under mixing, as well as the effectiveness of the magnetic separation of the catalyst is shown in Figure 1. The extent of the reaction was then monitored offline by GC, measuring the concentration of the substrate before and after the reaction. An internal standard i.e. dodecane was used in order to quantify the GC results. The substrates used in the experiments are reported in Table 1.

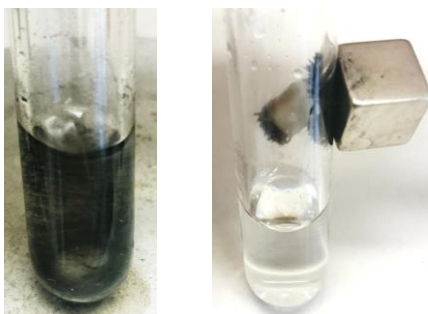
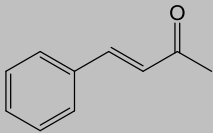
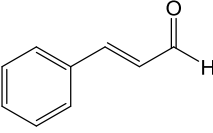
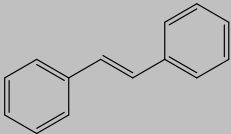
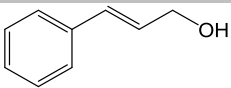


Figure 1. (Left) catalyst under mixing (right) magnetic separation of the catalysts by external magnet.

Table 1. list of the substrate used in my experiments.

	Compound	Formula	Structure
1	Benzalacetone	C ₁₀ H ₁₀ O	
2	Cinnamaldehyde	C ₉ H ₈ O	
3	Trans-stilben	C ₁₄ H ₁₂	
4	Cinnamyl alcohol	C ₉ H ₁₀ O	

3. Results and discussion

The results are summarized here being categorized with respect to the different catalysts used in the experiments.

3.1. Au/Turbobeads

This sample was initially prepared in order to understand the applicability of the preparation method as well as the potential application of such catalysts in liquid phase hydrogenation. Pre-made colloidal solution of 3 nm Au NPs (synthesized based on the procedure reported by us in [8]) was used in order to have the catalyst with a nominal loading of 0.2 and 0.5 wt.%. In both cases, it was found that the loading of the catalysts were ~50% less than the targeted values. The reason would be the instability of Au colloidal NCs under sonication. So basically, the NCs were getting aggregated under harsh sonication conditions. The aggregation was even visually observable after sonication, forming a layer of Au deposited on the surface of the vial used for catalyst preparation. Nevertheless, the catalyst was tested in the hydrogenation of benzalacetone (an unsaturated ketone) and cinnamaldehyde (an unsaturated aldehyde) to explore the activity of the catalyst in hydrogenation of C=C double bond, and/or aldehyde or ketone functional groups in such compounds. The conditions of the tests are summarized in Table 2.

Table 2. Results of the hydrogenation reactions using Au/Turbobeads catalyst (room temperature, solvent: isopropanol)

Substrate	Cat. mol% *	t (h)	P (bar)	Conversion (%)
1	0.09	3	1	0
1	0.22	3	1	0
2	0.38	3	1	0
2	0.38	3	20	0

* Defined as the total moles of the metal on the loaded catalyst / the total moles of substrate.

3.2. Pd/Turbobeads

This sample was prepared with respect to the fact that the Pd is known to be very effective for hydrogenation of the C=C bond even at room temperature [4,5]. So the idea was to see if the ligands around Au NCs are blocking (or limiting) the access to the Au atoms and thus hindering the reaction though the Au based catalyst are typically reported to be active at moderately high temperature and pressure [9].

In this regard, I prepared a batch of Pd NPs based on a procedure reported in [10], quite similar to the procedure I adopted to prepared Au NPs. Briefly, Pd(acac)₂ was dissolved in a mixture of olyelamine and Tetralin® and mixed under inert atmosphere for 10 min. Then, the stoichiometric amount of the reducing agent TBAB (tertiary butylamine borane complex) was added to the mixture. The temperature was raised to 60 °C where the formation of NPs was observed by sudden change of the color to black. The reaction was mixed at this temperature for an hour. After that the NPs were washed twice with isopropanol and separated with centrifuge and finally dispersed in hexane. In this way, a batch of Pd NPs was prepared having exactly the same ligands as the Au.

The catalyst was prepared by colloidal deposition under sonication in the same way as for the Au catalyst. Also in this case, the Pd NCs were found to be unstable under such harsh conditions and the loading was ~30% less than the targeted value. Nevertheless, the catalyst was tested in a number of hydrogenation reactions. Three reaction tests were performed as specified in

Table 3 and the catalyst was found to be promising in hydrogenation of the C=C bond. Noteworthy, the catalyst was not active in hydrogenation of the aldehyde functional group at these conditions as

checked by comparing of the GC results against the reference materials i.e. saturated / unsaturated aldehyde and alcohols.

Table 3. Results of the hydrogenation reactions using Pd/Turbobeads catalyst (room temperature, solvent: isopropanol);

Substrate	Cat. mol%	t (h)	P (bar)	Conversion (%)	TOF (h ⁻¹)
1	0.11	3	1	30	93.9
1	0.41	3	1	92	74
3	0.07	3	1	83	400

These results suggested that the catalyst made from this simple route showed a TOF for the conversion of (**3**) comparable to the previous Pd catalysts reported in literature [5].

3.3. AuCu/Turbobeads

The colloidal AuCu NCs were synthesized according to the procedure we published before [11]. The as-prepared NCs were then used to prepare the catalyst under the same conditions reported above in the text. The loading of the metals was checked by ICP and found to match the targeted value. This proved the stability of the AuCu NCs under harsh sonication conditions as we had seen also before in case of other supports (for instance bulk magnetite). The catalysts were then tested in a number of oxidation and hydrogenation reactions as shown in Table 4. It should be mentioned that the temperature of the reactions was also increased in some cases (either using an oil bath equipped with an external temperature controller or a heating mantel in case of high pressure trials).

Table 4. Results of the oxidation reactions using AuCu/Turbobeads catalyst.

Substrate	Cat. mol%	t (h)	T (°C)	P (bar)	Solvent	Conversion (%)
2	0.85	3	50	1	isopropanol	0
2	3.5	3	50	1	isopropanol	0
2	3.5	3	50	1	Toluene	0
4	1.7	3	50	1	Toluene	0

One trial was also performed for the oxidation of (4) to the corresponding aldehyde (2) using the calcined catalyst under the same conditions as in the last entry of Table 4. The reason was to see if removal of ligands can have a positive effect on the activity of the catalyst. Also in this case, no conversion was observed. The catalyst was then tested before and after calcination in hydrogenation of (2) with the aim to obtain its corresponding unsaturated alcohol (4).

Table 5. Results of the hydrogenation reactions using AuCu/Turbobeads catalyst (isopropanol was used as solvent in all trials).

Substrate	Cat. mol%	t (h)	T (°C)	P (bar)	Conversion (%)
2	0.85 (non-calcined)	3	50	20	0
2	1.7 (non-calcined)	24	50	20	100
2	0.7 (calcined)	24	50	20	100
2	0.36 (calcined)	24	50	20	0

It was observed that 100% conversion can be achieved either by calcined or non-calcined catalyst. However, at catalyst/substrate molar ratio as low as 0.36, no conversion was observed. Two additional tests were also performed; one using toluene as the solvent to see the effect of the solvent and a blank run (without using the catalyst) to check contribution of the uncatalyzed reaction. In both cases, the temperature was 50 °C and the reaction time was set to 24 h. No conversion was observed in neither of the tests proving that the catalyst was the active agent for the conversion of (2). It was also inferred from the tests that apparently there was an induction period and so probably the reaction was not taking place in the initial time of the reaction (see for example [12]; though it should be mentioned that this issue requires further careful examinations if it will be a matter of interest). This might be also due to the fact the catalyst was not properly dispersible in the reaction media especially in the first hours of the reaction. This could lead to an improper mixing of the catalyst in the liquid media and therefore decrease the accessibility of the catalyst active sites to the substrate. Indeed, after some time the catalyst particles were more dispersed in the liquid media under the mixing and therefore the reaction was conducted. To double check the issue of mixing, some reaction tests were performed under sonication while in another trial, alumina supported catalyst was used. The oxidation of (4) dissolved in toluene at room temperature and atmospheric pressure was carried out as an index reaction. In general, conversion was observed to a small extent upon enhancement of the contact between the catalyst and

the substrate, whether provided by alumina support or due to sonication. Nevertheless, the results were not interesting from catalytic point of view as it seemed that the limiting step for this reaction was not the mixing but the solubility of the gas phase reactant in the liquid phase. Indeed, reaction carried out at 20 bar of H₂ could achieve 100% conversion, even at the seemingly improper mixing conditions.

In the next step, I characterized the product of this hydrogenation reaction to see if we were selectively hydrogenating the aldehyde functional group. The product of the reaction test at which we had 100% conversion was characterized initially by Thin Layer Chromatography (TLC) which showed the hydrogenation of aldehyde group as well as hydrogenation of C=C. I also checked the product by MS as well as GC, comparing the retention time of the product against the reference samples. Both techniques revealed that the product is the saturated alcohol and so the catalyst was able to hydrogenize both aldehyde functional group and the C=C.

3.4. AuCu@FeOx/Turbobeads

The colloidal NCs used to prepare this catalyst were prepared according to a method which was developed in our group in IIT [13]. The dumbbell like NCs are composed of a metal domain of AuCu (similar alloy NCs that were introduced before), attached to an iron oxide domain. Before using this catalyst, the loading of the catalyst was checked by ICP and it was found that also in this case, the measured values were identical to the targeted loadings. This proved the stability of dumbbell NCs under sonication and also the applicability of the method for catalyst preparation.

Using this catalyst, a number of reaction tests were conducted as summarized in Table 6. It was found out that also in this case, the high pressure of H₂ was the most important factor to achieve full conversion. Interestingly, it was found that there was a product distribution at full conversion in such a way that only ~50% of the product was the saturated alcohol. The other product was the unsaturated alcohol (**4**). This suggested that there were two reactions in series i.e. hydrogenation of aldehyde functional group followed by hydrogenation of C=C. This can be a very interesting subject to study further as it can be related to the different redox properties of AuCu domain when attached to iron oxide. The existence of a charge transfer between the two domains of the dumbbell NCs have been shown in our previous studies which can be the explanation for the observed catalytic properties. Interestingly, when the reaction was performed at lower pressure of 10 bar, no conversion was observed proving again the importance of this parameter in the extent of reaction. Nevertheless, the

reaction should be also checked at this lower pressure but prolonged time to make sure about the effect of the pressure.

Table 6. Results of the hydrogenation reactions using AuCu@FeOx/Turbobeads catalyst (isopropanol was used as solvent in all trails).

Substrate	Cat. mol%	t (h)	T (°C)	P (bar)	Conversion (%)
2	1.7 (calcined)	3	50	1	0
2	0.7 (calcined)	6	50	20	0
2	0.7 (calcined)	24	50	20	100
2	0.7 (calcined)	18	50	10	0

4. Concluding remarks on application of colloidal NCs in liquid phase reactions

We have applied a procedure to prepare magnetically recyclable catalysts for liquid phase reactions. Using Turbobeads magnetic NPs and pre-made colloidal NCs, I prepared different batches of catalysts and applied them in a number of oxidation and hydrogenation reactions. The most promising results were the hydrogenation of cinnamaldehyde to its unsaturated corresponding alcohol or the saturated alcohol using AuCu/Turbobeads or AuCu@FeOx/Turbobeads. We have checked the effect of different parameters on the extent of the reaction and found that the reaction takes place at a moderately high pressure of 20 bar, the temperature of 50 °C and 24 h reaction time. The method for catalyst preparation is straightforward and can be applied for other colloidal NCs of interest as long as they are stable under harsh conditions of sonication.

References

1. Polshettiwar, V., R. Luque, A. Fihri, H. Zhu, M. Bouhrara, and J.-M. Basset, *Magnetically Recoverable Nanocatalysts*. Chem. Rev., 2011. **111**(5): p. 3036-3075.
2. Baeza, A., G. Guillena, and D.J. Ramón, *Magnetite and Metal-Impregnated Magnetite Catalysts in Organic Synthesis: A Very Old Concept with New Promising Perspectives*. ChemCatChem, 2016. **8**(1): p. 49-67.
3. Tan, C.G. and R.N. Grass, *Suzuki cross-coupling reactions on the surface of carbon-coated cobalt: expanding the applicability of core-shell nano-magnets*. Chemical Communications, 2008(36): p. 4297-4299.
4. Kainz, Q.M., R. Linhardt, R.N. Grass, G. Vilé, J. Pérez-Ramírez, W.J. Stark, and O. Reiser, *Palladium Nanoparticles Supported on Magnetic Carbon-Coated Cobalt Nanobeads: Highly Active and Recyclable Catalysts for Alkene Hydrogenation*. Adv. Funct. Mater., 2014. **24**(14): p. 2020-2027.
5. Linhardt, R., Q.M. Kainz, R.N. Grass, W.J. Stark, and O. Reiser, *Palladium nanoparticles supported on ionic liquid modified, magnetic nanobeads - recyclable, high-capacity catalysts for alkene hydrogenation*. RSC Adv., 2014. **4**(17): p. 8541-8549.
6. Grass, R.N., E.K. Athanassiou, and W.J. Stark, *Covalently Functionalized Cobalt Nanoparticles as a Platform for Magnetic Separations in Organic Synthesis*. Angewandte Chemie International Edition, 2007. **46**(26): p. 4909-4912.
7. Cargnello, M., C. Chen, B.T. Diroll, V.V.T. Doan-Nguyen, R.J. Gorte, and C.B. Murray, *Efficient Removal of Organic Ligands from Supported Nanocrystals by Fast Thermal Annealing Enables Catalytic Studies on Well-Defined Active Phases*. J. Am. Chem. Soc., 2015. **137**(21): p. 6906-6911.
8. Najafshirtari, S., P. Guardia, A. Scarpellini, M. Prato, S. Marras, L. Manna, and M. Colombo, *The effect of Au domain size on the CO oxidation catalytic activity of colloidal Au-FeOx dumbbell-like heterodimers*. J. Catal., 2016. **338**: p. 115-123.
9. Milone, C., R. Ingoglia, A. Pistone, G. Neri, F. Frusteri, and S. Galvagno, *Selective hydrogenation of α,β -unsaturated ketones to α,β -unsaturated alcohols on gold-supported catalysts*. Journal of Catalysis, 2004. **222**(2): p. 348-356.

10. Mazumder, V. and S. Sun, *Oleylamine-Mediated Synthesis of Pd Nanoparticles for Catalytic Formic Acid Oxidation*. Journal of the American Chemical Society, 2009. **131**(13): p. 4588-4589.
11. Najafshirtari, S., R. Brescia, P. Guardia, S. Marras, L. Manna, and M. Colombo, *Nanoscale Transformations of Alumina-Supported AuCu Ordered Phase Nanocrystals and Their Activity in CO Oxidation*. ACS Catal., 2015. **5**(4): p. 2154-2163.
12. Relvas, J., R. Andrade, F.G. Freire, F. Lemos, P. Araújo, M.J. Pinho, C.P. Nunes, and F.R. Ribeiro, *Liquid Phase hydrogenation of nitrobenzene over an industrial Ni/SiO₂ supported catalyst*. Catalysis Today, 2008. **133–135**: p. 828-835.
13. Najafshirtari, S., T.M. Kokumai, S. Marras, P. Destro, M. Prato, A. Scarpellini, R. Brescia, A. Lak, T. Pellegrino, D. Zanchet, L. Manna, and M. Colombo, *Dumbbell-like Au_{0.5}Cu_{0.5}@Fe₃O₄ Nanocrystals: Synthesis, Characterization, and Catalytic Activity in CO Oxidation*. ACS Appl. Mater. Interfaces, 2016. **8**(42): p. 28624-28632.

Name: Sharif Najafishirtari
Date of Birth: Aug. 4th, 1982
Nationality: Iranian
Marital Status: Single
Address: Vico Boccadoro 9/7, Genova, Italy
Cell: +39-3453481431/+98-9127982195
Email: sharif.najafishirtari@iit.it / sharif.najafi@gmail.com



Education:

- ❖ **PhD (2014-current):** Chemical Science and Technology, Istituto Italiano di Tecnologia in collaboration with University of Genova (Italy) and University of Regensburg (Germany) under supervision of Prof. Liberato Manna and Dr. Massimo Colombo in IIT, Prof. Fabio Canepa in Unige, and Prof. Oliver Reiser in Universität Regensburg.
- ❖ **Master of Science (2007-2010):** Chemical Engineering (Minor in Catalyst), University of Tehran, Iran (GPA: 17.91/20); **Thesis title:** Investigation of performance of the FCC catalyst in fixed bed reactor under periodic operation. **Advisors:** Prof. Abbas Ali Khodadadi, Prof. Yadollah Mortazavi.
- ❖ **Bachelor of Science (2000-2005):** Chemical Engineering (Minor in Process Engineering), Azad University Southern Branch of Tehran, Iran (GPA: 15.49/20); **Thesis title:** Chemical Recycling of Polyethylene Terephthalate by Means of Water Steam. **Advisor:** Prof. Mehdi Rafizadeh.

Working Experiences:

- ❖ **Istituto Italiano di Tecnologia (IIT), from 12th May 2013 up to now**
 - ★ Fellow researcher working on colloidal nanocomposites for CO oxidation, Catalysis group, Nanochemistry Department.
 - ★ Admitted as a PhD student in University of Genova within a dual PhD program and Mag(net)ic Fun network funded by Marie Curie action.
- ❖ **Institut für Organische Chemie, Institut für Pharmazie und Chemie, Universität Regensburg , from 1st Dec 2015 up to 31st Aug 2016**
 - ★ Guest PhD student working on application of colloidal NPs in liquid phase reactions.
- ❖ **Chagalesh Consultant Co., as a Process Engineer, from February 2011 up to May 2013**
 - ★ Detail design of units including chemical storage, sea water intake and distribution, sea water desalination and distribution, demineralization, potable water, cooling water (by means of refrigeration cycle) and instrument air, gas refinery complex, Phase 14 of Assaluye, South Pars Field.
 - ★ Participation in HAZOP study meetings of the above-mentioned units as the process expert of the consultant party.
 - ★ Technical bid evaluation of suppliers of Claus and tail gas treatment catalysts for SRU unit in gas refinery complex, Phase 14 of Assaluye.
- ❖ **Laboratory of Catalyst and Nanostructured Materials, Department of Chemical Engineering, Faculty of Engineering, University of Tehran, from March 2008 till February 2011.**
 - ★ Synthesis of FCC catalyst ingredients (Y-zeolite, amorphous silica-alumina, binder, filler and some additives such as ceria-zirconia) and preparation of catalytic composite by incorporation method.
 - ★ Designing and construction of a spray drier to be used in drying of FCC catalyst slurry.
 - ★ Designing and construction of a new laboratory setup for determination of FCC catalyst activity in periodic operation.
 - ★ Designing and construction of a standard equipment for testing the CO and CH₄ gas sensors for NIGC.

- ★ Designing and construction of an apparatus to perform Temperature Programmed Analysis and Measure BET surface area.
- ❖ **DSP Consultants, from August 2005 till January 2007 full time and up to December of 2007 part time.**
 - ★ Designing of instructional multimedia softwares for training of the field operators in petrochemical plants.
 - ★ Modeling and simulation of the 1st urea reactor for Razi petrochemical complex.
 - ★ Thermodynamic modeling of methane steam reforming by means of Gibbs minimization method.
 - ★ Development of a program to model mass and heat transfer in polyamid hollow fiber membrane modules for separation of light hydrocarbons from gaseous mixtures.
 - ★ Simulation of gas separation in hollow fiber membrane modules by means of RBF neural network.
 - ★ Thermodynamic modeling of single-phase urea reactor.
 - ★ Thermodynamic modeling of two-phase urea reactor with a new mathematical algorithm.

Publications

- ★ **Sharif Najafishirtari**, Alice Scarpellini, Sergio Marras, Mirko Prato, Clara Guglieri, Liberato Manna, Massimo Colombo; “Metal-support interaction in Au catalysis: the effect of the morphology of a nano-oxide domain in CO oxidation activity”, manuscript under preparation.
- ★ **Sharif Najafishirtari**, Tathiana Midori Kokumai, Sergio Marras, Priscila Destro, Mirko Prato, Alice Scarpellini, Rosaria Brescia, Aidin Lak, Teresa Pellegrino, Daniela Zanchet, Liberato Manna, Massimo Colombo; “Dumbbell-like $\text{Au}_{0.5}\text{Cu}_{0.5}@\text{Fe}_3\text{O}_4$ Nanocrystals: Synthesis, Characterization and Catalytic Activity in CO Oxidation”; Submitted to ACS applied Materials and Interfaces
- ★ **S. Najafishirtari**, P. Guardia, Alice Scarpellini, Mirko Prato, S. Marras, L. Manna, M. Colombo, “The effect of Au domain size on the CO oxidation catalytic activity of colloidal Au-FeOx dumbbell-like heterodimers”, Journal of Catalysis 338 (2016) 115–123. **This paper was selected as Editor-in-Chief’s Featured Article in June 2016.**
- ★ **S. Najafishirtari**, R. Brescia, P. Guardia, S. Marras, L. Manna, M. Colombo, “Nanoscale transformations of alumina-supported AuCu ordered phase nanocrystals and their activity in CO oxidation”, ACS Catalysis 2015, 5, 2154–2163.
- ★ Zahra Hosseinpour, Alice Scarpellini, **Sharif Najafishirtari**, Sergio Marras, Massimo Colombo, Abdolali Alemi, Michaël De Volder, Chandramohan George, and Vladimir Lesnyak; “Morphology Dependent Electrochemical Properties of CuS Hierarchical Super-Structures”; ChemPhysChem 2015, 16, 3418 –3424.
- ★ M.S. Aghakhani, A.A. Khodadadi, **Sh. Najafi**, Y. Mortazavi, “Enhanced Triisopropylbenzene Cracking and Suppressed Coking on Tailored Composite of Y-Zeolite/Amorphous Silica-Alumina Catalyst”, Journal of Industrial and Engineering Chemistry 20 (2014), 3037-3045.

Conferences

- ★ 16th International Congress on Catalysis (ICC 16), Place: Beijing (China), Date: 03/07/2016-08/07/2016, Contribution: Poster. “AuCu@FeOx dumbbell like heterodimers as catalysts for the CO oxidation: when support size matters”; **Sharif Najafishirtari**, Alice Scarpellini, Mirko Prato, Sergio Marras, Priscila Destro, Tathiana Midori, Daniela Zanchet, Liberato Manna, Massimo Colombo.
- ★ Gold World Conference, 26-28 July 2015, Cardiff, UK “AuCu ordered tetragonal phase nanocrystals: the effects of nanoscale transformations on CO oxidation catalytic activity”, **S. Najafishirtari**, R. Brescia, P. Guardia, S. Marras, L. Manna, M. Colombo.
- ★ 24th North American Catalysis Society Meeting (NAM24), 14-19 June 2015, Pittsburgh, Pennsylvania, US “Nanoscale Transformations of Alumina-Supported AuCu Ordered Phase Nanoparticles upon CO Oxidation”, **S. Najafishirtari**, R. Brescia, M. Colombo, L. Manna,.
- ★ 8th International Conference in Environmental Catalysis (ICEC), 24-27 August 2014, Asheville, North Carolina, US “CO oxidation over dumbbell like Au@FeOy nanoparticles: catalytic activity, thermal stability and effect of gold domain size”, **S. Najafishirtari**, M. Colombo, L. Manna.

- ★ 15th International Congress on Catalysis (15th ICC), 1-7 July 2012, Munich, Germany, “Investigation of performance of the FCC catalyst in fixed bed reactor under periodic operation”, **Sh. Najafi**, M.S. Aghakhani, A.A. Khodadadi, Y. Mortazavi.
- ★ 16th international of zeolite conference (16th IZC), 4-9 July 2010, Sorrento, Italy, “Y-zeolite/amorphous silica-alumina core-shell catalyst for cracking of TIPB as a heavy model compound for FCC”, M.S. Aghakhani, **Sh.Najafi**, A.A. Khodadadi, Y. Mortazavi, M. Beyramali,.
- ★ 16th international of zeolite conference (16th IZC), 4-9 July 2010, Sorrento, Italy, “Modified kaolin as an alternative and more proper matrix for pre-cracking of TIPB as a resid FCC feed model compound”, M.S. Aghakhani, Y. Mortazavi, **Sh.Najafi**, A.A. Khodadadi, , M. R. Afife,.
- ★ 17th international congress of chemical and process engineering (CHISA), 2006, Prague, Czech, “How to study the Urea synthesis reactor”, M. Changiz, **Sh. Najafi**, M. Goharrokhi.

Technical Skills:

- ★ Software design and visual programming.
- ★ Familiar with applying numerical methods of constrained or non-constrained optimization.
- ★ Familiar with different techniques for synthesis of catalytic materials.
- ★ Familiar with synthesis of zeolitic materials and enhancement of their hydrothermal stability.
- ★ Experienced in colloidal synthesis of nanocrystals (metals, bimetals, metal oxides and their composites).
- ★ Experienced in using characterization equipment for temperature programmed tests such as TPR, TPD, and TPO as well as BET surface area measurement.
- ★ Experienced in online and off line analysis with Gas chromatograph.
- ★ Experienced in online FTIR spectroscopy of gaseous mixtures and of solid surfaces by means of DRIFT.
- ★ Experienced in designing and construction of laboratory scale furnaces and microreactors.
- ★ Familiar with XRD, XANEX, EXAFS, FESEM & TEM imaging & EDS, ICP, Spectroscopy techniques.

Language Skills:

- ★ PBT TOEFL: 623/669 (2006).
- ★ IBT TOEFL: 100/120 (2012); Reading: 27, Listening: 27, Speaking: 22 and Writing: 24.
- ★ Familiar with Italian through self-study.

Computer Skills:

- ★ General: Microsoft Office (Word, Excel, Powerpoint, Visio), Endnote.
- ★ Engineering: Aspen Plus, Aspen Properties, HYSYS, PIPESYS, HTFS+, Pipephase.
- ★ Programming: Visual Basic, Visual C, C++, MATLAB.
- ★ Specials: Origin, Athena, Artemis, Clemex, Gatan Digital Micrograph, Imagej2x, HighScore.

Declaration

Herewith I declare that this present thesis is a presentation of my original work prepared singlehanded. Wherever contributions from others are involved, all of them are marked clearly, with reference to the literature, license and acknowledgment of collaborative research.

Genoa, 14 February 2017

Sharif Najafishirtari